VON KARMAN INSTITUTE FOR FLUID DYNAMICS
AERONAUTICS AND AEROSPACE DEPARTMENT

VRIJE UNIVERSITEIT BRUSSEL
RESEARCH GROUP ELECTROCHEMICAL AND SURFACE ENGINEERING

POLITECNICO DI MILANO
DIPARTIMENTO DI SCIENZE E TECNOLOGIE AEROSPAZIALI

Development of an Ablation Model for Rarefied Flows with Application to Meteoroid Entry

---

Thesis presented by Federico Bariselli in order to obtain the degree of:

Doctor of Philosophy in Engineering Sciences (Vrije Universiteit Brussel, Belgium)
Doctor of Philosophy in Aerospace Engineering (Politecnico di Milano, Italy)

Supervisors:

Prof. Thierry Magin (von Karman Institute for Fluid Dynamics, Belgium) and
Prof. Annick Hubin (Vrije Universiteit Brussel, Belgium) and
Prof. Aldo Frezzotti (Politecnico di Milano, Italy)

Doctoral Committee:

Prof. Philippe Claeys (Vrije Universiteit Brussel, Belgium), President
Prof. Rik Pintelon (Vrije Universiteit Brussel, Belgium), Vice president
Dr Mesfin Haile Mamme (Vrije Universiteit Brussel, Belgium), Secretary
Prof. Luigi Vigevano (Politecnico di Milano, Italy), Reviewer
Prof. Margaret Campbell-Brown (University of Western Ontario, Canada), Reviewer
Prof. Anne Bourdon (École Polytechnique, France), Reviewer

Development of an Ablation Model for Rarefied Flows with Application to Meteoroid Entry

Keywords: Meteor – Gas-surface interactions – Hypersonics – Aerothermodynamics – DSMC

D/2020/0238/726, T. Magin, Editor-in-Chief
Published by the von Karman Institute for Fluid Dynamics with permission.

ISBN 978-2-87516-157-4

A Grace e alla mia famiglia.

"La montagna più alta rimane sempre dentro di noi."
– Walter Bonatti

Abstract

About 100 tonnes of small meteoroids enter the terrestrial atmosphere every day. As a meteoroid interacts with the atmosphere, its surface temperature can reach several thousands of Kelvins, causing its ablation. Among the various strategies for the observation of meteors, radio-based techniques have proved to be a simple yet valuable tool for collecting large amounts of data. Ground-radio stations can detect free electron densities in the meteoroid trail, which are initially produced by the hyperthermal collisions of the ablated species with the incoming freestream. Therefore, the ability to predict the ionisation intensity and the rate of dissipation of the plasma trail becomes essential for the correct interpretation of the radio signal. However, the current models are drastically simplified; they use zero-dimensional approaches and disregard nonequilibrium phenomena, such as rarefied gas effects.

This work aims to provide a detailed description of the degradation process of a meteoroid and the physico-chemical dynamics driving the ablated vapour around the body and in the extended plasma trail. Each improvement in the modelling is expected to impact not only our understanding of the physical problem but also the estimates on mass fluxes and the statistical outcome of the collected observational data.

Chapter 3 describes the nonequilibrium collisional processes around millimetre-sized meteoroids, at certain selected conditions along the entry path. These conditions are chosen in agreement with the trajectory and flow regime analysis performed in Chapter 2. Particular attention is given to the production of free electrons, on which the intensity of the radio signal depends. We carry out the investigation in the framework of the Direct Simulation Monte Carlo (DSMC) method, where we include specific models to tackle both gas-surface interactions and gas-phase encounters. With respect to classical meteor theory, the introduced evaporation boundary condition can take into account condensation fluxes and the backscattering of molecules at the wall. Moreover, a database of elastic and reactive cross sections is developed for the ablated vapour. This set of data may be useful to scientists as a reference database for future theoretical and numerical studies. Collisional processes and shielding effects prove to be meaningful for events below 100 km or intense ablation rates, and they could be even more significant for bigger meteoroids. Ionisation comes mainly from the hyperthermal encounters between air and vapour, rather than from thermalised metal-metal collisions.

Chapter 4 deals with the experimental characterisation of the material response of some meteorite samples. These experiments allow testing the evaporation model from Chapter 3 and yield insight into the ablation mechanisms. We present the results from two campaigns, carried out in the VKI Plasmatron wind tunnel and the NASA Ames laser ablation facility, so as to span a range

of evaporation conditions. Both tests confirm strong degassing of light species and oxidation, and they indicate that accurate ablation modelling requires describing the mechanical removal of the molten layer into the hypersonic flow. Geochemical characterisation of the recovered material demonstrates the successful use of these type of facilities to reproduce fusion crusts similar to those collected on the ground. Finally, measurements of the surface temperatures, coupled with thermal response modelling of the material, help in refining the understanding of the surface energy balance. Despite the simplicity of the numerical model, simulations and pyrometry data are found to agree reasonably well in laser experiments, while they needed a tuned contribution of the oxidation heat flux in the Plasmatron tests.

In Chapter 5, we study the processes which lead to the extinction of the plasma trail. For this purpose, we employ the simulations obtained in Chapter 3 as initial conditions to carry out detailed chemical and multicomponent diffusion calculations of the extended trail (up to several kilometres) using a Lagrangian approach. In this approach, a fluid element reactor marches along assigned streamlines, calculating multicomponent mass diffusion in the radial direction and detailed chemical reactions. Chemical reactions have negligible effects in the neutralisation process of underdense trails, which are dominated by mass diffusion. Also, a constant diffusion coefficient, as used in standard models, is sufficient to reproduce the numerical profiles. The influence of chemistry and differential diffusion could be enhanced in overdense meteors. Therefore this aspect deserves future investigation. Finally, we link the dissipation of the electrons to the reflected radio echo, so as to estimate the resulting signal in the framework of the classical underdense meteor theory. On the whole, the procedure presented represents a standalone methodology, which can provide meteor physical parameters at given trajectory conditions, without the need to rely on standard lumped models.

Finally, in light of the experimental results of Chapter 4, in Chapter 6, we present a numerical procedure that allows studying melting in the presence of a rarefied gas phase. In these flows, the condensed phase can be treated as a continuous medium, whereas a kinetic treatment is needed for the gas. We propose a computational approach in which both phases are simulated by particle schemes: the DSMC method for the vapour and the Smoothed Particle Hydrodynamics (SPH) method for the solid and the liquid. This approach is computationally more intensive than the one of Chapter 3, as it proposes to describe the dynamics of the three phases comprehensively. In this case, a two-way coupling between phases is pursued, at the expense of other possibly relevant phenomena such as evaporation or chemical nonequilibrium of the gas, which are not taken into account. We show the details of the thermal and dynamic coupling methodology, along with some verification test cases in simplified configurations. Finally, as a proof-of-concept, we consider the melting of a solid cylinder immersed in a rarefied hypersonic stream. The dynamics of the molten layer under the influence of the external flow is analysed.

Abstract in layman's terms

About 100 tonnes of small meteoroids enter the terrestrial atmosphere every day. Due to their small size and tremendous speeds, meteoroids burn up at high altitudes, where they are responsible for the metal-rich layers in the mesosphere and lower thermosphere that play an essential role in atmospheric chemical processes. Among the various strategies for the observation of shooting stars, radio techniques have proved to be a simple yet valuable tool for collecting large amounts of data, 24 hours a day regardless of the visibility conditions. Ground-radio stations can detect the plasma in the glowing trail, which is produced by the fast collisions of the vaporised rock with the incoming airflow. Therefore, the ability to predict the ionisation intensity and the dissipation rate of the plasma trail becomes essential for the correct interpretation of the radio signal. However, current approaches are drastically simplified and disregard collisional effects in the rarefied gas.

This work aims to provide a detailed description of the meteoroid degradation process and those physico-chemical phenomena that drive the dynamics of the ablated vapour around the body and in its plasma trail. First, we study the gas behaviour by simulating the molecules directly at the kinetic scale. In a second step, a procedure to examine the neutralisation of the extended trail is designed. Also, we devote particular attention to the investigation of gas-surface interactions. This investigation is supported by ground experiments in a plasma wind tunnel and laser facility. Finally, a computational methodology, which accounts for the thermal and dynamic coupling of the vapour with the condensed phase, is developed and verified.

We are confident that this dissertation has put together the fundamental tiles of a broader and ambitious modelling effort that will help astronomers to reduce uncertainties in the interpretation of radio echoes, paving the way towards the adoption of more sophisticated computer simulations in the field of meteor science.

Acknowledgements

> *Once upon a time, in an Indian village, an elephant had been brought. Six blind men were so curious to know about its aspect and nature that they rushed to inspect it by palpation. The first man put his hand on the trunk and said, "This being is like an enormous snake". For the second man, whose hand had landed on the ear, this creature seemed like a fan. The third man, who was touching its leg, imagined the elephant like a tree trunk. The blind man who placed his hand upon its chest conceived the animal like a wall. Another man held its tail and described it as a rope. The last man reached one of its tusks and stated, "This beast is hard and smooth like a spear!".*
>
> – The parable of the Blind Men and an Elephant

It was probably at a project meeting with my supervisors and collaborators during my first year of PhD when I realised what meteor science was about. It wan an *elephant*! Sitting around the table of that meeting room, I understood that we were all there for a different reason. For someone, shooting stars represented a gateway to the formation of the Solar System. For others, they could unveil the mechanisms behind the development of life on Earth. Meteors were worth studying to learn more about space debris demise or the detailed plasma chemistry in a thruster for someone else. And for still others, they closely resembled evaporating fuel droplets, such as those in the combustion chamber of an engine.

It took me a while to understand what to look for in this multifaceted, fascinating topic. Only at that point, when I learned what meteors represented to me, I recognised what this PhD would have been about.

First of all, I would like to acknowledge my mentors Thierry Magin, Aldo Frezzotti, and Annick Hubin. The three of you have been precious to my work and personal growth in such a complementary way. Thanks for sharing your wisdom and for giving me this opportunity.

Second, I desire to thank my companion in this adventure, Bruno Dias. It has been an incredible ride. You have helped me continuously, encouraged, and constructively criticised. More than a colleague, I have found a friend. Always believe in yourself, because you will be an excellent researcher!

I am thankful to Stefano Boccelli. It has been fun and challenging to be your advisor, and I swear I have learned from you much more than what you have from me. I am lucky to be your friend, and thanks for all the help!

I cannot forget Erik Torres, my Research Master advisor. I have learned the importance of the details working with you. Thanks for your sharp guidance,

the days in Minneapolis and all the excellent explanations on Kinetic Theory.

I am very grateful to Hermes Scandelli and Pietro Parodi. Hermes, you bought into the SPH-DSMC coupling, worked with enthusiasm, and helped me develop the solver during your months at VKI. Pietro, you opened me the world of RAM-EP and the Particle-in-Cell method. Guys, I wish you brilliant future careers.

Thanks to Bernd Helber for performing the experiments in the VKI Plasmatron and George Bellas for the discussion on gas-surface interactions and state-to-state models. Thanks to JB Scoggins, Alessandro Turchi, Vincent Leroy, and Alejandro Alvarez Laguna. You have been scientific role models. Thanks to David Henneaux, for the feedback you gave me on the draft of this thesis. I am honoured I could be part of such a research group. I wish all of you good luck in life and career.

I am indebted with Eric Stern for the incredible experience and opportunity at NASA Ames and Francesco Panerai who welcomed and took care of me as an older brother. Thanks to Laura, Clara and George, I will remember the days in Palo Alto as some of the happiest of my life.

Thanks to Lidia Pittarello for helping me see the world of meteors from another perspective, the passion you have transmitted me, and for sharing your ideas in the drafting of Chapter 4.

I thank Hervé Lamy to help me understand the topic and design the BRAMS network that has given the origin and motivation to this thesis.

I am much obliged to Oscar Steenhaut, Priya Laha, and Kitty Baert at SURF for assisting me with SEM-EDS and Raman Spectroscopy.

I want to thank the jury members of this dissertation. Their comments and suggestions allowed me to improve the quality of the final manuscript considerably.

I express my gratitude to Peter Brown and Margaret Campbell-Brown for the appreciation shown for my work after the last *Meteoroid* conference in Bratislava. This has been the fuel for the last months of work and real motivation.

The research presented in the next pages has been funded by a PhD fellowship of the Research Foundation Flanders (FWO). I acknowledge the FWO for the trust and the generous grant that has allowed me to spend my last four years in complete freedom in doing something that I loved. I hope somehow, someday this research will be useful to the economy in Flanders (sic!).

I am thankful to Bogdan, Claudia, Fabio, Stefano V., Roberto, Giulia, Elissavet, and Giacomo in any particular order. You have been like a second family here in Belgium for me, and I keep in my heart countless joyful memories.

Thanks to Charline, Gunther, Tania, Anabel, Maria Teresa, Francisco, Andrea A., Ivàn, Ludovico, Zuheyr, Andrea F., Adriana, Damien, and the whole VKI family for all the chats and the companionship in the coffee breaks.

Gracias a July por cuidarme el verano pasado, por el entrenamiento de español y todas las cenas peruanas que me distrajeron mucho.

Thanks to Grace for being a constant source of inspiration and my first fan. Your attention to the details and the love you put into things has enriched my everyday life and sweeten my journey.

Infine, un ringraziamento speciale va alla mia famiglia. Anche se ci separano quasi 1000 km vi ho sempre sentiti vicino con il cuore e la mente. Grazie per il vostro supporto e l'amore incondizionato.

Federico Bariselli
Brussels, June 2020

Contents

List of Publications

Journal articles

1. F. Bariselli, S. Boccelli, B. Dias, A. Hubin, T. E. Magin, A self-consistent method for the simulation of meteor trails with application to radio observations, *Astronomy & Astrophysics*, 641, A100, 2020

2. F. Bariselli, A. Frezzotti, A. Hubin, T. E. Magin, Aerothermodynamic modelling of meteor entry flows, *Monthly Notices of the Royal Astronomical Society*, 492(2):2308-2325, 2020

3. B. Helber, B. Dias, F. Bariselli, L. F. Zavalan, L. Pittarello, S. Goderis, B. Soens, S. J. McKibbin, P. Claeys, T. E. Magin, Analysis of meteoroid ablation based on plasma wind-tunnel experiments, surface characterization, and numerical simulations, *The Astrophysical Journal*, 876(2):120-134, 2019

4. L. Pittarello, S. Goderis, B. Soens, S. J. McKibbin, G. Giuli, F. Bariselli, B. Dias, B. Helber, G. O. Lepore, F. Vanhaecke, C. Koeberl, T. E. Magin, P. Claeys, Meteoroid atmospheric entry investigated with plasma flow experiments: Petrography and geochemistry of the recovered material, *Icarus*, 331:170-178, 2019

5. S. Boccelli, F. Bariselli, B. Dias, T. E. Magin, Lagrangian diffusive reactor for detailed thermochemical computations of plasma flows, *Plasma Sources Science and Technology*, 28(6):065002, 2019

Conference proceedings

1. F. Bariselli, S. Boccelli, A. Frezzotti, A. Hubin, T. E. Magin, Aerothermodynamic modelling of meteor entry flows in the rarefied regime, *2018 Joint Thermophysics and Heat Transfer Conference*, Atlanta, Georgia, USA, 2018-4180, 2018

2. B. Dias, F. Bariselli, A. Turchi, A. Frezzotti, P. Chatelain, T. E. Magin, Development of a melting model for meteors, *30th International Symposium on Rarefied Gas Dynamics*, Victoria, British Columbia, Canada, 1786(1):160004, 2016

3. F. Bariselli, E. Torres, T. E. Magin, State-specific catalytic recombination boundary condition for DSMC methods in aerospace applications, *30th International Symposium on Rarefied Gas Dynamics*, Victoria, British Columbia, Canada, 1786(1):190009, 2016

List of Figures

List of Tables

List of Symbols

Symbols with multiple definitions should be clear from the context in which they are used.

Constants

h	[J s]	Planck constant
k_B	[J/K]	Boltzmann constant
R	[J/K/kg]	gas constant
σ_S	[W/m^2/K^4]	Stefan-Boltzmann constant

Roman symbols

$\boldsymbol{a}$	[m^2/s]	generic acceleration term
a_0	[m]	Bohr radius
b	[m]	impact parameter
$\mathbf{B}$	[-]	SPH gradient renormalisation matrix
$\boldsymbol{B}$	[T]	Earth's magnetic field
$\mathcal{C}$	[s^2/m^6]	nonreactive collisional source term,
	[-]	Fresnel integral
c_p	[J/K/kg]	specific heat capacity
C_1	[1/J]	TCE model parameter
C_2	[-]	TCE model parameter
C_3	[-]	TCE model parameter
C_4	[m^3/mol/s]	Arrhenius pre-exponential factor
C_5	[-]	Arrhenius temperature exponent
C_6	[-]	ionisation efficiency parameter

d	[m]	molecular diameter,
	[m]	diameter of the experimental sample
D	[m]	diameter of the meteoroid,
	[m^2/s]	multicomponent diffusion coefficient,
	[m]	thickness
$\mathcal{D}$	[m^2/s]	binary diffusion coefficient
e	[J/kg]	thermal energy per unit mass
E	[J/kg]	energy per unit mass
$\boldsymbol{E}$	[V/m]	electric field
E_0	[J]	activation/ionisation energy
E_c	[J]	collision energy
f	[s^3/m^6]	molecular velocity distribution function
Fo	[-]	Fourier number
g	[s^3/m^6]	Maxwellian velocity distribution function
$\boldsymbol{g}$	[m/s]	collisional relative velocity
l	[K/s]	generic energy source term
h	[J/kg]	enthalpy per unit mass,
	[m]	SPH smoothing length
h_0	[J/kg]	formation enthalpy
H	[m]	altitude
$\mathcal{I}$	[-]	ensemble of SPH/DSMC particles
k	[m/s]	chemical rate coefficient
$\mathcal{K}$	[$m^2/V/s$]	zero-field mobility factor
$\mathcal{K}_B$	[s^3/m^3]	scattering kernel
Kn	[-]	Knudsen number
l	[m]	representative macroscopic scale,
	[m]	length of the experimental sample
L	[J/kg]	latent heat
m	[kg]	mass of the meteoroid,
	[kg]	mass of the experimental sample,
	[kg]	mass of one SPH particle
$\dot{m}$	[kg/s]	mass flow rate
M	[-]	meteoric atom
M	[kg/mol]	molar mass

Ma	[-]	Mach number
n	[1/m^3]	number density
$\boldsymbol{n}$	[-]	normal unit vector
$\hat{n}$	[1/m]	line number density
$n_{\mathrm{w}}^{\mathrm{eq}}$	[1/m^3]	equilibrium vapour number density
$\mathcal{N}$	[-]	number of particles in a DSMC cell
$\mathcal{N}_{\mathrm{pair}}$	[-]	maximum number of collisions in a DSMC cell
N_{s}	[-]	number of sampling timesteps
$\dot{N}_{\mathrm{coll}}$	[1/s]	total number of collisions per unit time
Nu	[-]	Nusselt number
p	[Pa]	pressure
P	[W]	power
$\mathcal{P}$	[-]	probability of a binary collision
Pr	[-]	Prandtl number
q	[C]	electric charge
$\boldsymbol{q}$	[W/m^2]	heat flux
$\mathcal{Q}$	[-]	Heaviside step function
r	[m]	radial coordinate,
	[m]	distance between molecules,
	[m]	radius
R	[m]	radius of the meteoroid,
	[m]	distance of reflection point from radio station
$\mathcal{R}$	[s^2/m^6]	reactive collisional source term
r_0	[m]	initial meteor radius
Re	[-]	Reynolds number
s	[m]	streamline curvilinear abscissa
$\mathcal{S}$	[-]	set of species,
	[-]	Fresnel integral
S_{c}	[m^2]	cross section of the meteoroid
t	[s]	time
T	[K]	temperature
$\boldsymbol{v}$	[m/s]	macroscopic velocity
V	[m/s]	module of the macroscopic velocity
$\mathcal{V}$	[m^3]	volume of a DSMC cell
V_0	[m/s]	ionisation threshold velocity

$\boldsymbol{V}^{\mathrm{d}}$	[m/s]	diffusion velocity
V_{t}	[m/s]	thermal velocity
$\mathcal{W}$	[$1/\mathrm{m}^2$]	SPH smoothing kernel
W_{p}	[-]	DSMC particle weight
x	[m]	axial coordinate
$\boldsymbol{x}$	[m]	physical space coordinate
X	[-]	chemical symbol for a species
X	[-]	molar fraction
Y	[-]	mass fraction
z	[-]	elementary charge,
	[m]	spatial coordinate
z_{R}	[deg]	angle of the radiant from the zenith

Greek symbols

α	[-]	scattering exponent of the VSS model,
	[-]	evaporation/condensation coefficient,
	[m^3]	dipole polarisability
β	[-]	ionisation efficiency,
	[deg]	angle between wave propagation plane and entry trajectory
β_0	[-]	ionisation steric factor
β_E	[1/s]	boundary layer velocity gradient
γ	[-]	heat capacity ratio,
	[-]	reduced variable for relative velocity
	[deg]	angle between electric field and receiver line of sight
γ_r	[-]	recombination coefficient
Γ	[-]	free molecular drag coefficient,
	[-]	Euler Gamma function,
	[K/s]	energy source term
δ	[-]	Dirac impulse function
Δ	[m]	molten layer
ϵ	[-]	emissivity,
	[J]	depth of the Lennard-Jones potential well
ϵ_0	[F/m]	free-space permittivity
$\epsilon_\star$	[N/m]	surface tension
η	[Pa s]	shear viscosity,
	[-]	nondimensional coordinate
θ		microscopic property,
	[deg]	angular coordinate,
	[deg]	local streamline slope
κ	[1/m]	mean local curvature
λ	[W/m/K]	thermal conductivity
$\tilde{\lambda}$	[m]	mean free path
λ_D	[m]	Debye length
$\lambda_\star$	[m]	electromagnetic wavelength
Λ	[-]	heat transfer coefficient

μ	[kg]	molecular mass
μ^{R}	[kg]	reduced mass
ν	[1/s/m^3]	molecular collision frequency,
	[m^2/s]	kinematic viscosity
$\nu_\star$	[1/s]	electromagnetic frequency
ν'	[-]	forward stoichiometric coefficient
ν"	[-]	backward stoichiometric coefficient
$\boldsymbol{\xi}$	[m/s]	molecular velocity
ξ_0	[-]	number of equivalent electrons in the outer shell
$\mathbf{\Pi}$	[Pa]	stress tensor
ρ	[kg/m^3]	mass density
σ	[m^2]	total collision cross section
σ_{e}	[m^2]	scattering cross section
$\bar{\sigma}$	[m]	Lennard-Jones potential parameter
Σ		generic surface
τ	[s]	duration of the experiment,
	[s]	exponential decay constant,
	[Pa]	shear stress
ϕ	[kg/s/m^2]	mass flux
	[deg]	half angle between transmitter and receiver
		at reflection point
φ	[deg]	angular coordinate
χ	[deg]	scattering angle
$\boldsymbol{\chi}$	[m^2/s]	acceleration term
ψ	[J]	interatomic potential
Ψ		macroscopic property
ω	[-]	temperature exponent VHS/VSS model
$\dot{\omega}$	[kg/s/m^3]	chemical production rate
ω_{c}	[rad/s]	cyclotron frequency
ω_{p}	[rad/s]	plasma frequency
Ω	[m^3/s]	collision integral,
	[m^2]	smoothing kernel support domain

Subscripts and superscripts

a	ambipolar,
	air
A	atom
b	backward
c	condensed phase,
	condensation
chem	chemical
cg	condensed-gas interface
conv	convective
cr	critical
cw	cold-wall stagnation point
e	electron,
	evaporation
E	boundary layer edge
el	electric
f	forward
fl	flight
g	gas phase
i	ion,
	interface
I	ionisation
l	liquid phase
m	melting
new	post gas-surface-interaction property
old	pre gas-surface-interaction property
ox	oxidation
R	receiver
rad	radiative
ref	reference value
rot	rotational
s	solid phase,
	sample

sl	solid-liquid interface
sp	stagnation point
t	trail
T	transmitter
tr	translational
v	vapour phase
vib	vibrational
w	wall
∞	freestream
’	post-collision property

Acronyms

AB	Alkali Basalt
AMOR	Advanced Meteor Orbit Radar
ATAP	Asteroid Threat Assessment Project
AV	Acceleration Voltage
BRAMS	Belgian RAdio Meteor Stations network
CCD	Charge-Coupled Device
CFL	Courant-Friedrichs-Lewy
CMOR	Canadian Meteor Orbit Radar
DSMC	Direct Simulation Monte Carlo
EDS	Energy-Dispersive X-ray Spectroscopy
FD	Finite Differences
FDTD	Finite-Difference Time-Domain
ICP	Inductively Coupled Plasma
IRS	Institut für Raumfahrtsysteme
LA-ICP-MS	Laser Ablation-Inductively Coupled Plasma-Mass Spectrometry
LARSEN	LAgrangian Reactor for StrEams in Nonequilibrium
LEO	Low Earth Orbit
LHMEL	Laser Hardened Materials Evaluation Laboratory

LHTS	Local Heat Transfer Simulation
LIBS	Laser-Induced Breakdown Spectroscopic
MSSWG	Japanese Meteor Science Seminar Working Group
MUTATION++	MUlticomponent Thermodynamic And Transport Properties for IoNized plasmas
NASA	National Aeronautics and Space Administration
NRLMSISE	Naval Research Laboratory Mass Spectrometer Incoherent Scatter radar Empirical
OC	Ordinary Chondrite
OES	Optical Emission Spectroscopy
PIC	Particle-In-Cell
SEM	Scanning Electron Microscope
SPARTA	Stochastic PArallel Rarefied-gas Time-accurate Analyzer
TCE	Total Collision Energy
TPS	Thermal Protection System
UV	Ultraviolet
VHS	Variable Hard Spheres
VKI	von Karman Institute for Fluid Dynamics
VSIE	Volume-Surface Integral Equation
VSS	Variable Soft Spheres
VUB	Vrije Universiteit Brussel
WD	Working Distance
XRF	X-Ray Fluorescence

CHAPTER 1

Introduction

"Even very great men sometimes indulge in wishful thinking."

– Theodore von Kármán

1.1. Radio-based meteor observations

About 100 tonnes of small meteoroids enter the terrestrial atmosphere every day [Love and Brownlee, 1993, Vondrak et al., 2008]. These bodies, from one-meter diameter to micron-size grains, originate either from sublimating comets or disintegrated asteroids. In their rush to the ground, they intersect the atmosphere at hypersonic velocities from 11.2 to 72.5 km/s. As a meteoroid interacts with the atmosphere, its surface temperature can reach several thousands of Kelvins, causing its ablation. Bodies up to a few millimetres mainly ablate through melting, i.e. spraying of the molten layer [Girin, 2017] and evaporation. The latter is responsible for the metal-rich layers in the mesosphere and lower thermosphere that play an essential role in atmospheric chemical processes [Plane, 1991, Plane et al., 2015].

Among the various experimental strategies for the observation of meteors, radar- and radio-based techniques [Kaiser, 1953, McKinley, 1961] have proved to be a simple yet valuable tool for collecting large amounts of data, 24 hours a day regardless of the visibility conditions. The data obtained comprise trajectory information, such as the flight velocity, quantities related to the physical

Parts of this chapter have been published or are submitted for publication in

1. F. Bariselli, S. Boccelli, A. Frezzotti, A. Hubin, T. E. Magin, **Aerothermodynamic modelling of meteor entry flows in the rarefied regime**, *2018 Joint Thermophysics and Heat Transfer Conference*, Atlanta, Georgia, USA, 2018-4180, 2018

2. F. Bariselli, A. Frezzotti, A. Hubin, T. E. Magin, **Aerothermodynamic modelling of meteor entry flows**, *Monthly Notices of the Royal Astronomical Society*, 492(2):2308-2325, 2020

3. F. Bariselli, S. Boccelli, B. Dias, A. Hubin, T. E. Magin, **A self-consistent method for the simulation of meteor trails with application to radio observations**, *Astronomy & Astrophysics*, 641, A100, 2020

state of the meteor vapour, e.g. its degree of ionisation [Hocking et al., 2001, Weryk and Brown, 2013], or indirect measurements of the atmospheric conditions, such as pressure and temperature [Hocking et al., 1997, Cervera and Reid, 2000].

The Belgian Institute for Space Aeronomy has put in place an experiment, the Belgian RAdio Meteor Stations (BRAMS) network, to measure velocity, trajectory, and mass of meteors. This network (see Figure 1.1) consists of a radio transmitter emitting at 49.97 MHz and a series of receivers spread all over Belgium to collect and standardise meteor observations [Lamy et al., 2011]. Employing the forward-scattering technique [Forsyth and Vogan, 1955], these radio stations can detect free electron densities in the meteoroid trail, which are initially produced by the hyperthermal collisions of the ablated species with the incoming freestream air-jet [Dressler and Murad, 2001].

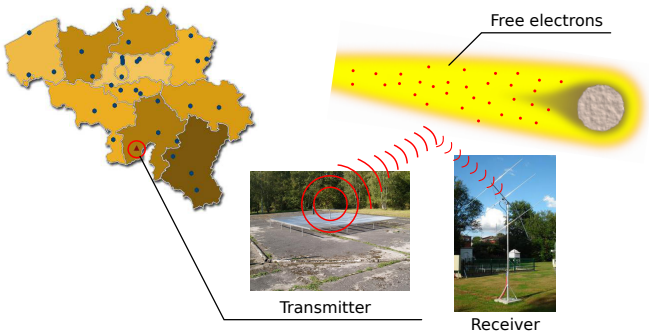

Figure 1.1.: *The map of the BRAMS network in Belgium and a schematic showing the principle behind the forward-scattering technique.*

When the density of the free electrons is weak, the incident radio wave can propagate in the ionised gas, where it is scattered by the individual electrons. Astronomers refer to this condition as an *underdense reflection*. Signals from underdense meteors last no more than a few tenths of a second, and they are the most observed. For these events, the theory indicates: i) the mass of the object is proportional to the amplitude of the echo; ii) its duration, which is strictly linked to the deionisation process in the plasma trail, is proportional to the electron line density at the reflection point [McKinley, 1961]. Figure 1.2 shows the example of a spectrogram recorded by BRAMS, obtained performing a discrete Fourier transform of the raw audio signal over a period of 5 minutes, where nine underdense meteor echoes have been detected.

Therefore, the ability to calculate i) the ionisation intensity and distribution; ii) the rate of dissipation of the plasma trail becomes essential for the correct interpretation of the radio signal. Each improvement in the modelling is expected to impact not only the comprehension of the physical problem but also the estimates on mass fluxes and the statistical outcome of the collected meteor

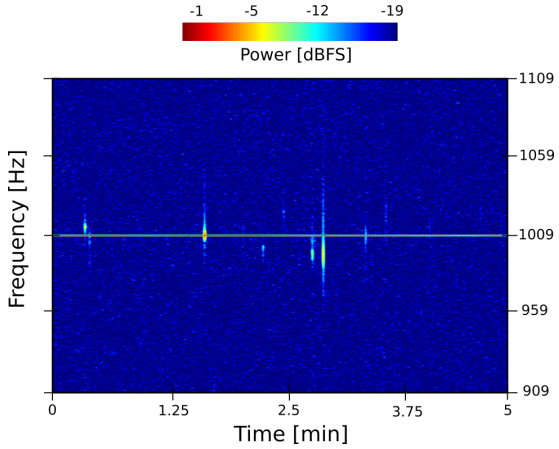

Figure 1.2.: *Example of a BRAMS spectrogram recorded for 5 minutes, after processing of the signal. The spectrogram displays how the power of the signal is distributed among the frequencies as a function of time. The horizontal line is the direct tropospheric beacon coming from the transmitter. All the vertical traces (we can count up to nine in this plot) are underdense meteor echoes. Credits of the Royal Belgian Institute for Space Aeronomy.*

data.

1.2. The meteor phenomenon

Meteoroid flux into Earth's atmosphere

Figure 1.3 illustrates the mass flux of meteoroids into Earth's atmosphere as a function of their mass. One can see that the bulk of meteoric material vaporising in the atmosphere is formed by small particles in the range between 5×10^{-5} and 2×10^{-2} m [Ceplecha et al., 1998]. Radar and radio waves techniques are able to sample meteoroids smaller than optical systems, but big enough to ablate and generate a trail of plasma sufficiently intense to be detected. According to Baggaley [1980, 2002], this corresponds to a rough limit of 10^{-5} m in diameter for meteoroids travelling at a speed of about 30 km/s. Particles smaller than several hundredths of a millimetre decelerate before reaching the melting temperature. This class of micrometeoroids, for which most of the heat is dissipated by radiation, is detected neither by radar nor optical techniques and disappear into the atmosphere without the possibility of being tracked. This class of particles takes the name of *cosmic dust*.

Meteor physics

Due to their small size and tremendous speeds, radio/radar meteoroids often burn up at high altitudes above 80 km, where the atmosphere is rarefied

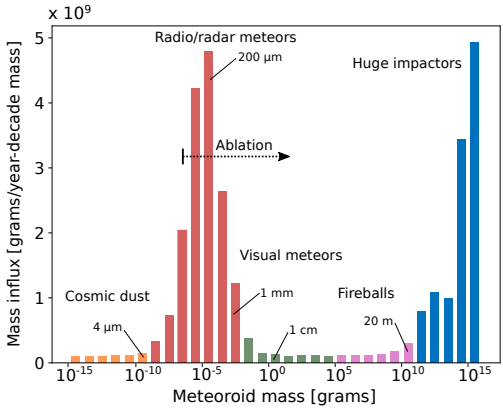

Figure 1.3.: *Mass influx per decade of mass with respect to the mass of the meteoroid. The histogram reveals a bimodal contribution in the flux distribution, where one peak corresponds to particles of about 200 μm, while the other is associated with impactors that can produce damages at the ground or craters. Figure adapted from Flynn [2002] and Trigo-Rodríguez [2019].*

[Ceplecha et al., 1998]. Here, the gas cannot be treated as if it was in thermodynamic equilibrium (*continuum assumption*), and the Navier-Stokes equations usually employed in gasdynamics fail [Bird, 1994]. Travelling at geocentric speeds from 11.2 to 72.5 km/s, meteoroids experience velocities which can be hundreds of times higher than the local speed of sound [Boyd, 1998]. The high energies involved activate coupled physico-chemical phenomena (strong departure from thermo-chemical equilibrium, radiative heating, and complex gas-surface interactions), which make the prediction of these flows a challenging task [Anderson, 2000, Brun, 2009].

Figure 1.4 shows the first-ever observed shock-like structure in front of a meteoroid [Stenbaek-Nielsen and Jenniskens, 2004], and it represents an excellent example of how complex physics is involved in this phenomenon. The meteor is initially a point source, with only a faint trace of wake. Around frame "250" a distinct spatial structure, reminiscent of a shock, develops. The spatial scale size is surprisingly large ($\approx$ 500 m), leading the authors to think that it is associated with photo-chemical processes driven by the intense UV radiation from the hot gas. Moreover, a bright and extended trail develops behind the object, which is a sign of phenomena such as material ablation; collisional processes leading to vibrationally and electronically excited internal energy modes; dissociation, ionisation, and subsequent diffusion and recombination of the ions; possible plasma instabilities as charged species interact with the Earth's magnetic field.

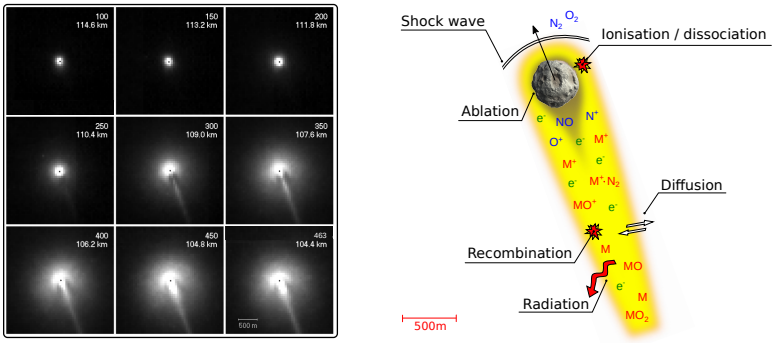

Figure 1.4.: *On the left, development of a large shock-like structure in front of a Leonid meteoroid flying at 71.6 km/s (-3 magnitude), caught by a CCD camera at 1000 frames/s [Stenbaek-Nielsen and Jenniskens, 2004]. On the right, a schematic with some of the coupled physico-chemical phenomena taking place in meteors. The drawing is not to scale.*

1.3. State-of-the-art in meteor modelling

In this section, an overview of the state-of-the-art in meteor modelling is given. We focus our attention on radio meteors, for which hydrodynamic approaches cannot be used, and we highlight the critical limits of currently employed methodologies.

1.3.1. Classical lumped-parameter models

A summary of classical meteor models is given in Bronshten [1983] or Ceplecha et al. [1998]. These models are agile and based on algebraic relations that condense the complexity of the problem into a few physical parameters. This simplicity makes them suitable for parametric studies and fitting of observational curves. However, they all suffer from common drawbacks. In particular, they are i) utterly deficient in the gas dynamical description of the phenomenon; ii) based on zero-dimensional approaches (in this sense they are "lumped"); iii) derived under the assumption of free molecular flow, i.e. the aerothermodynamic environment, including the possible formation of shock waves, is disregarded.

Traditionally, radio meteors have been modelled as a sequence of three distinct phases: i) the material degradation and mass loss process, also known as *ablation*; ii) the production of free electrons as a consequence of energetic collisions of the ablated vapour with the air coming from the freestream[1]; iii) the diffusion and recombination of ions in the trail driving the extinction of the radio event.

[1] Ceplecha et al. [1998] estimated that 90% of the meteor light originates from inelastic collisions of vaporised metallic atoms with air.

Ablation process

The ablation process is represented as a cartoon in Figure 1.5. Energetic gas-surface interactions heat the material, causing melting and evaporation. The liquid can be sprayed away in the form of droplets by aerodynamic and inertial loads. Volatilisation and degassing of light elements lead the melt phase to boil, with the consequent formation of vesicles of various size, that are characteristic of the quenched stony meteorites found on the ground [Genge and Grady, 1999, Genge, 2017] (see Figure 1.5). Above 130 km, *sputtering* can also play a role [Popova et al., 2007]. Moreover, fragmentation has been observed as part of the degradation process by both optical [Stokan and Campbell-Brown, 2014a] and radar techniques [Kero et al., 2008, Zhu et al., 2016]. However, the treatment of boiling, sputtering, and fragmentation is beyond the scope of this work. Therefore, a review about their modelling will not be part of this section.

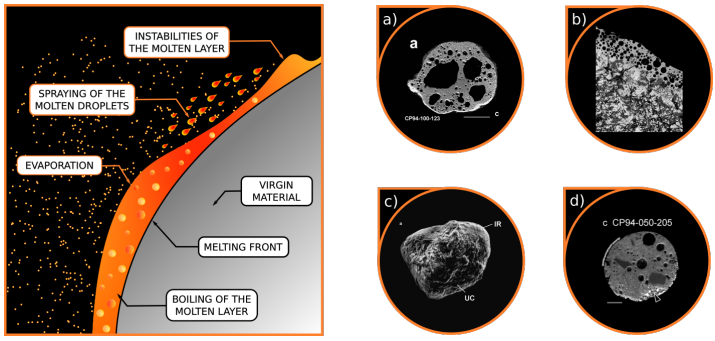

Figure 1.5.: *On the left, a graphical representation of the ablation process. On the right, the result of this process is shown by micrographs of meteorites and micrometeorites which survived atmospheric entry. References: a) Genge et al. [2008]; c) Genge [2006]; d) Genge [2017].*

The physical theory of meteor ablation was first laid down by Öpik [1936, 1958]. The Estonian astronomer evaluated the relevance of a number of phenomena, such as vaporisation and fusion, spraying of the molten phase, stability of liquid drops, and the role of rotation in mass removal.

The simplest among the ablation models assumes that the mass loss rate is proportional to the kinetic energy imparted to the meteoroid, with the ablation beginning when the surface of the meteoroid reaches its boiling point. From Bronshten [1983], if density and velocity of the freestream are respectively defined as ρ_∞ and V_∞, we can write the ablation rate for an object of mass m as

$$\dot{m}_\mathrm{e} = \frac{S_\mathrm{c} \Lambda \rho_\infty V_\infty^3}{2 L_\mathrm{e}}, \tag{1.1}$$

where $S_\mathrm{c} = \pi R^2$ represents the cross section of the meteoroid, R being its radius, while Λ is the *heat transfer coefficient*, and L_e is the latent heat of evaporation.

Standard evaporation models were derived under the assumption of free molecular flow (expansion into the vacuum). Love and Brownlee [1991] proposed an ablation model applying the Knudsen-Langmuir formula, coupled with the Clausius-Clapeyron relation to compute the equilibrium vapour density of the melt-vapour phase transition. Campbell-Brown and Koschny [2004] inferred that this model is best suited for meteoroids of lower densities for which the ablation may start before the boiling temperature is reached. This model was adapted by McNeil et al. [1998] to treat the differential evaporation of volatile species. Vondrak et al. [2008] adopted a similar approach, with the equilibrium properties of the silicate-vapour system computed by means of mass balance and mass action calculations (MAGMA code) [Fegley and Cameron, 1987].

In the context of evaporation, MAGMA was also employed to model unsteady vaporisation by incrementally removing the vapour after complete equilibration with its condensed phase [Fegley and Cameron, 1987, Schaefer and Fegley, 2004]. The authors proceeded as follows: i) compute the bulk elemental composition of the magma and the vapour; ii) equilibrate the system; iii) remove the vapour and go back to Point i). The authors called this procedure *fractional vaporisation*. With this approach, the system is losing mass in a step-wise fashion, as a sequence of states in thermodynamic equilibrium.

Free electron production

Classical theory assumes that a cylindrical column of ionised metal atoms with radius r_0 instantaneously forms upon the passage of the meteoroid. This characteristic length was named *initial meteor radius*, and it was defined by Manning [1958] as the half-width of the initial Gaussian distribution of electrons. For the initial radius r_0, a variety of approximate formulas exist, but significant scatter has been identified between theoretical and observational values. Theoretical analysis of collision cooling indicated a dependence of the radius on flight velocity and atmosphere density $\sim V_\infty^{0.8}/\rho_\infty$, whereas experimental values for faint meteors can be described using the empirical relation $\sim V_\infty^{0.6}/\rho_\infty^{0.25}$ [Ceplecha et al., 1998].

The formula that describes the formation of the ionised trail reads as

$$\hat{n}_\mathrm{e} = \frac{\beta}{\mu V_\infty}\dot{m}_\mathrm{e}, \tag{1.2}$$

where quantity $\hat{n}_\mathrm{e}$ describes the number of electrons produced per meter by an ablating meteoroid of mass m, moving at speed V_∞, only as a function of the ablation rate and the nondimensional *ionisation efficiency* β. Quantity μ is the average meteoric atom mass. Therefore, the physico-chemical processes leading to the excitation and ionisation of metallic atoms are lumped into the ionisation efficiency β in function of V_∞, that is defined as the ratio between the number of electrons produced and the number of vaporised atoms. In his theoretical work, Jones [1997] provides species-specific values for some atoms of interest, showing that this coefficient can be decomposed into two contributions: the

first represents the proportion of particles $\beta_0(V_\infty)$ ionising at the first collision; the second is proportional to $(1-\beta_0)$ and mimics the dynamics of the gas phase, hence the probability with which a collision subsequent to the first one can lead to the formation of an ion. Moreover, for $V_\infty < 35$ km/s, Jones [1997] proposes a global ionisation efficiency for faint meteors equal to

$$\beta = 9.4 \times 10^{-6}(V_\infty - 10)^2 V_\infty^{0.8}, \tag{1.3}$$

where the freestream velocity is expressed in km/s.

Free electron dissipation

For low-density plasma columns, the neutralisation of the trail is mainly driven by mass diffusion. Upon trail formation, charged particles start spreading in the surrounding atmosphere. If we neglect the effect of chemistry, then the electron density distribution $n_\mathrm{e}(r,t)$ in the radial direction r is Gaussian at any time t [McKinley, 1961] and reads as

$$n_\mathrm{e} = \frac{\hat{n}_\mathrm{e}}{\pi r_\mathrm{t}^2} \exp\left\{ -\frac{r^2}{r_\mathrm{t}^2} \right\}. \tag{1.4}$$

In this equation, the trail is a cone with radius $r_\mathrm{t} = \sqrt{r_0^2 + 4D_\mathrm{a}t}$ (see Figure 1.6), and the electron line density $\hat{n}_\mathrm{e}$ is conserved in time, due to the absence of recombination reactions.

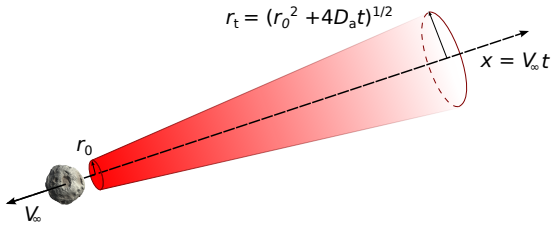

Figure 1.6.: *In the classical approximation, the trail is expanding with a conical shape in the surrounding atmosphere.*

Equation 1.4 assumes that ions and electrons diffuse at the same rate governed by the common and constant *ambipolar diffusion coefficient* D_a

$$D_\mathrm{a} = \left[1 + \frac{T_\mathrm{e}}{T_\mathrm{i}}\right] D_\mathrm{i}, \tag{1.5}$$

where T_e and T_i are the electron temperature and the ion temperature, respectively. The factor between brackets comes from the presence of the *ambipolar electric field*[2] that accelerates the rate of diffusion of the ions D_i in the neutral

[2]Light electrons would diffuse much faster than heavy ions. Charge separation leads to the formation of a self-generated electric field that keeps charge neutrality.

background gas [Kaiser, 1953].

Jones [1991] and Robson [2001] considered the effect of the Earth's magnetic field $\boldsymbol{B}$. In particular, the diffusion perpendicular to the magnetic field lines is inhibited by a factor $\nu^2/(\nu^2+\omega_c^2)$, ν being the collision frequency of the charge particles with the background atmosphere and ω_c their frequency of spinning around magnetic lines

$$\omega_c = \frac{qB}{\mu}. \tag{1.6}$$

Here, μ is the mass of the charged particle and q its charge. Although ions are always dominated by collisions (their collision frequency ν_i is much larger than $\omega_{c,i}$ up to 140 km), for electrons the frequency of collision ν_e becomes comparable with $\omega_{c,e}$ at 80 km. At around 100 km, the magnetised electrons control transverse diffusion instead of the ions, leading to a distortion of the trail cross section into an elliptical shape [Baggaley, 2002].

1.3.2. Flowfield modelling and simulations

Beside classical lumped models, different authors have studied the formation and extinction of the plasma trail by more sophisticated numerical analysis. However, as reported by Silber et al. [2018b] in their comprehensive review, computational studies in the field of meteor shock waves are relatively sparse with a consequent lack of understanding of the relevant rarefied hypersonic flow. Concerning the trail, existing studies focus either on the plasma dynamics or the recombination process of the metallic compounds and free electrons. Ablation and ionisation are lumped to input conditions for the simulations. Moreover, only simplified kinetics is taken into account [Vinković et al., 2016].

Ablated vapour dynamics and plasma formation

Boyd [1998] was the first to address the problem of the ablation of meteoroids in the rarefied regime by giving a detailed description of the phenomenon from the flowfield perspective using the Direct Simulation Monte Carlo (DSMC) method [Bird, 1994]. He treated the meteoroid material as made of a single species, i.e. magnesium, using a phenomenological ablation model accounting for evaporation of the metal, and assuming a vaporisation temperature of 2500 K. No chemical reactions were considered in the gas phase. Preliminary results indicated that a cloud of ablated material surrounds the meteoroid and that an extensive high-temperature region in near-thermal equilibrium is present in the meteor trail. This result is in qualitative agreement with spectral measurements of meteor wakes, but it is not able to predict their composition and ablation rate quantitatively. A DSMC approach was also used by Vinković [2007] to predict the emission of light by very high altitude meteors detected from the ground, not explainable through classical ablation theory. The study focused on the sputtering of atoms from the meteoroid surface [Rogers et al., 2005]. Strong assumptions were made, such as no distinction between atomic and molecular species in the gas phase. Other physical processes like vaporisation, ionisation,

dissociation, and excitation were not included. A simplified particle-based approach was developed by Stokan and Campbell-Brown [2014b] to model the space resolved trail luminosity of faint meteors in direct connection to the local number of collisions.

With application to radar head-echo, Dimant and Oppenheim [2017a,b] developed a simplified kinetic equation to describe the formation of a quasi-neutral plasma around an ablating submilligram meteoroid. They obtained analytical expressions for the spatial and velocity distributions of ions and neutrals, through which they could compute gas and plasma densities as a function of the distance from the meteoroid. Their findings were supported by Particle-In-Cell (PIC) simulations [Sugar et al., 2018]. This type of analysis is valuable to assess the assumptions at the foundations of the classical theory for radio scattering. For example, the degree of attenuation of a radio echo depends on the radial distribution of the electron density within the train. Different authors have argued that the ionisation profile is instantaneously formed after the passage of the meteoroid, and it follows a Gaussian distribution around the body [Manning, 1958, Greenhow and Hall, 1960]. A numerical investigation by Jones [1995], who performed some Monte Carlo simulations in the framework of elastic interactions, showed that the ions reach thermal equilibrium in about ten collisions. Moreover, he found that the initial ionisation distribution is far from being Gaussian. According to this author, a more refined description, which takes into account ionising collisions, is desirable.

Trail evolution

The decay of the signal is mostly linked to the evolution of the free electrons in the trail, and classically it has been studied considering constant ambipolar diffusion and a thermalised chemistry mechanism [Baggaley, 2002]. In their pioneering work, Baggaley and Cummack [1974] solved a system of diffusion equations in cylindrical coordinates. There, the initial condition was assumed to be a Gaussian radial distribution of the meteoritic atomic ions, which were left as the only constituents of the starting mixture.

The same approach, along with a simplified mixture composed of one single synthetic meteoric element, M, and its oxide ions, MO^+, MO_2^+, was used to study the echo duration produced in overdense meteors [Baggaley, 1978]. In these studies, the role of ozone as the controlling neutral gas was recognised, and two-body dissociative recombination was identified as the leading reaction for chemical neutralisation. The initial explanation for which electron attachment could play a significant role in this process was dispelled. Moreover, chemistry was found to be a relevant dissipation mechanism only at altitudes below 80 km, where collisions are more frequent, with diffusion becoming dominant high in the atmosphere.

Although a fairly complete chemical mechanism was considered in these works, the diffusion process was modelled by assuming a common and constant ambipolar diffusion coefficient computed for positive ions moving through a N_2-O_2 mixture. The treatment on ionic diffusion in meteor trains was dis-

cussed in another work by Jones and Jones [1990] for a binary mixture of ions as they suggested that differential diffusion among species may influence ion chemistry in dense plasma trails. However, no numerical solutions based on the presented results were attained. Dimant and Oppenheim [2006] solved the diffusion equation of the thermalised trail by considering the spatial distribution and evolution of the ambipolar electric field. Additionally, they treated the effects of the background plasma, neutral atmosphere, and geomagnetic field. Ion and electron temperatures were considered constant. In this regard, the thermalisation of the trail was studied by Baggaley and Webb [1977], considering a two-temperature model. The authors showed how free electrons seem to achieve thermal equilibrium with the ambient gas at timescales lower than a tenth of a second.

Numerical computations of the trail offer a set of challenges. An important one concerns its vast extent, which can reach kilometres in length, while the transverse dimension stays of the order of meters. The resulting computational grids are likely to be extremely heavy, if not heavily deformed, and computational resources are easily overwhelmed. Therefore, plasma and gas dynamics simulations have been performed following a variety of methodologies, ad-hoc assumptions and different levels of approximation, depending on the focus of the study. The DSMC method was employed by Boyd [1998] to obtain nonequilibrium simulations of the vapour in a 40 m trail in order to investigate the relaxation of the rotational degrees of freedom. Zinn et al. [2004] developed a coupled radiative-hydrodynamic code for the cylindrical expansion of the gas in the trail of a fireball, tracking the chemical evolution and temperature distributions in the first 200 m. Finally, Oppenheim and Dimant [2015] studied the diffusion of the plasma column and the development of turbulence in the presence of a background wind using a three-dimensional PIC code over a 100 m long domain.

1.4. Objectives and outline of the thesis

The current state-of-the-art models are drastically simplified, often based on a zero-dimensional approach, and disregarding nonequilibrium phenomena, such as rarefied gas effects. On the other hand, past computational studies have tackled the formation and the dissipation of the plasma trail as two separate problems, and they never account for the whole picture in a self-consistent way. Also, past simulations have included only basic kinetics and simplified vapour mixtures.

The goal of this work is to develop comprehensive physico-chemical models and methodologies for the description of the meteor phenomenon in the rarefied regime, with application to radio detection (see Figure 1.7). By doing so, we would like to reduce the initial uncertainties relevant to i) the input of metals in the chemistry of the upper atmosphere, ii) the resulting ionisation efficiencies and plasma dissipation rates, which are necessary for a correct interpretation of radar and radio detection measurements.

The two main technical/modelling objectives of this work can be synthesised as follows:

- **Objective 1. Modelling of the gas-surface interactions. a)** A classical evaporation boundary condition is implemented in a DSMC code, accounting for condensation fluxes and the backscattering of molecules at the wall. **b)** The thermal response of some meteorite samples tested via plasma wind-tunnel and laser experiments is characterised. These experiments provide validation of the evaporation model and insight into the material behaviour, which, in turn, allows for the refinement of the developed methodology. **c)** A computational methodology is developed to simulate melting in the presence of a nonequilibrium gas phase.

- **Objective 2. Modelling of the ablated vapour and free electrons. a)** The hyperthermal chemistry of meteoric metal species in the rarefied gas phase is taken into account. Transport and chemical kinetic properties of the ablated vapour are considered by constructing a database of relevant elastic and reactive cross sections. Then, we study the resulting plasma formation using the DSMC method. **b)** The evolution of the free electrons and metal compounds is simulated in the trail, employing a Lagrangian fluid approach. Multicomponent diffusion, including the ambipolar electric field, and thermalised chemistry are included to provide accurate inputs for the reconstruction of the radio echo.

To make the link with the overarching goal, in Figure 1.7 we show the radio-echo signal received upon reflection from underdense trails, along with the technical objectives just described. A very steep rise of a few hundredths of a second, which corresponds to ablation and free electron production, is followed by an exponential decay of the received power (free electron dissipation).

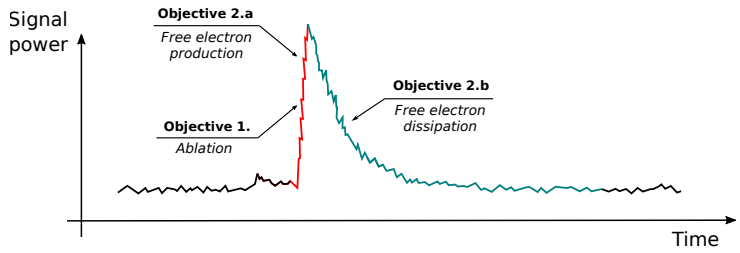

Figure 1.7.: *Sketch of an underdense radio echo in relationship to meteor modelling. The technical objectives of the thesis are highlighted.*

The thesis is divided into seven chapters including introduction and conclusions. The body of the manuscript is structured as follows:

In **Chapter 2**, we analyse the entry trajectory coupled with the thermal response of the meteoroid, and we investigate the flow regimes experienced by the meteoroid in its rush to the ground. This analysis helps to identify those

points along the entry path for which the dynamics of the vapour phase plays a significant role. Moreover, it allows us to extract relevant freestream and wall boundary conditions for the subsequent flowfield analysis performed in Chapter 3 and Chapter 5.

Starting from the results obtained in Chapter 2, **Chapter 3** (**Objectives 1.a and 2.a**) aims to provide a detailed description of the ablated vapour dynamics around millimetre-sized meteoroids at certain selected conditions along the entry path. Particular attention is given to the production of free electrons, on which the intensity of the radio signal depends. The investigation is developed in the framework of the DSMC method to account for the dynamics of the rarefied gas. Specific physico-chemical models are included to tackle both gas-surface interactions and gas-phase encounters in detail.

Chapter 4 (**Objective 1.b**) deals with the experimental characterisation of the material response of some meteorite samples. These experiments allow i) testing the evaporation model resulting from the theoretical/numerical effort of Chapter 3 and ii) yielding insight into the mechanisms which characterise meteoroid ablation. Two different experiments have been considered so as to span a range of evaporation conditions: the von Karman Institute for Fluid Dynamics (VKI) Plasmatron wind-tunnel for mild evaporation; the NASA Ames laser ablation facility for intense evaporation. Experiments are followed by a multiscale analysis of the surface which permits us to gain a better understanding of the thermo-chemical mechanisms occurring during the degradation of the material.

In **Chapter 5** (**Objective 2.b**), we study the processes which lead to the extinction of the plasma trail. For this purpose, we employ the simulations obtained in Chapter 3 as initial conditions in order to carry out detailed chemical and multicomponent diffusion calculations of the extended trail (up to several kilometres). Finally, we link the dissipation of the electrons to the reflected radio echo, so as to estimate the resulting signal in the framework of the classical underdense meteor theory.

Chapter 4 has highlighted that accurate ablation modelling requires describing the entrainment of the molten layer into the hypersonic flow. In these flows, the condensed phase can be treated as a continuous medium, whereas a kinetic treatment is needed for the gas. Therefore, in **Chapter 6** (**Objective 1.c**), we present a numerical procedure that allows us to study melting in the presence of a rarefied gas phase. We propose a computational approach in which both phases are simulated by particle schemes: the DSMC method for the vapour and the Smoothed Particle Hydrodynamics (SPH) method for the solid and the liquid. We show the details of the coupling methodology, along with some verification test cases.

Chapter 7 summarises the main results obtained in this work. In particular, we draw conclusions concerning those scientific questions and technical

objectives addressed in this chapter. Finally, suggestions for future investigations are given.

The structure of this thesis and the dependencies among the different chapters are highlighted in Figure 1.8.

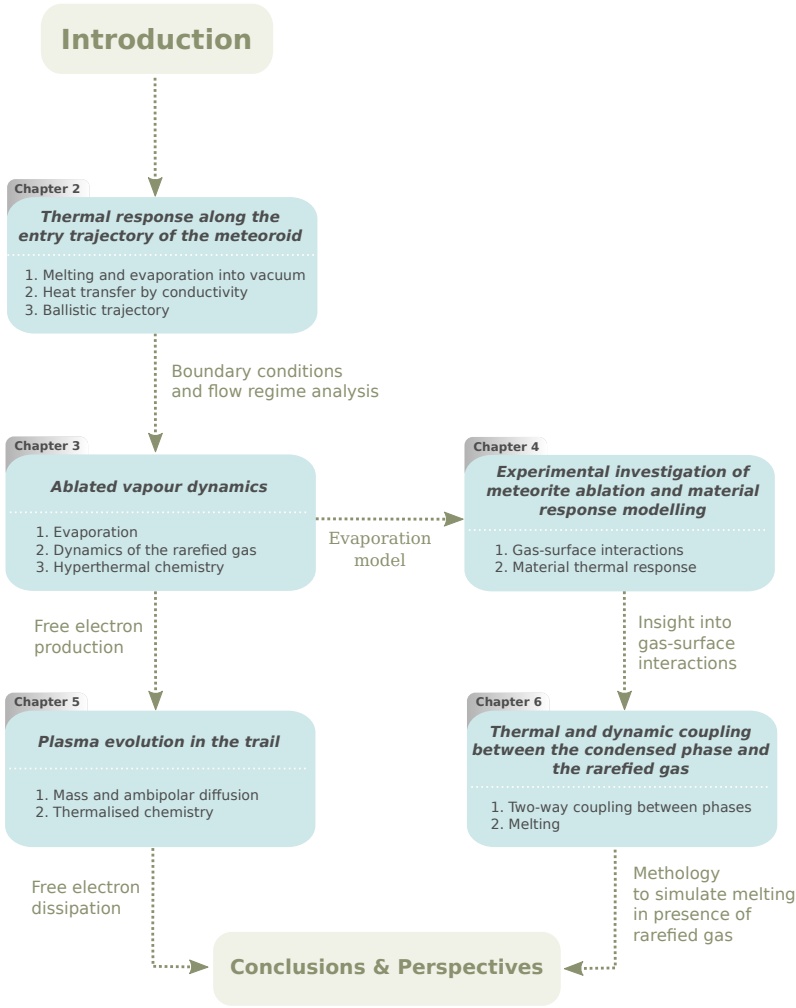

Figure 1.8.: *Structure of the thesis. The aim and the dependencies among the different chapters are highlighted. For each chapter, a list of the phenomena investigated is presented.*

CHAPTER 2

Meteoroid Entry Trajectory

"Le premier était de ne recevoir jamais aucune chose pour vraie que je ne la connusse évidemment être telle; c'est-à-dire, d'éviter soigneusement la précipitation et la prévention, et de ne comprendre rien de plus en mes jugements que ce qui se présenterait si clairement et si distinctement à mon esprit, que je n'eusse aucune occasion de le mettre en doute. Le second, de diviser chacune des difficultés que j'examinerais, en autant de parcelles qu'il se pourrait, et qu'il serait requis pour les mieux résoudre."

– René Descartes (Discours de la Méthode)

2.1. Introduction

In the picture of a destruction process mainly driven by evaporation and mechanical removal, ablation only starts after a pre-heating phase in the thermosphere, in which the surface of the body is heated up to the melting condition. In this phase, since the atmospheric density is low, the meteoroid essentially conserves both its mass and flight velocity. The onset of intense evaporation takes place at the altitude at which the surface starts melting. This altitude is a function of the velocity and dimensions of the body, with the smallest and fastest meteoroids being vaporised earlier along their trajectory.

In this chapter, we consider the thermal response of the meteoroid along its entry trajectory, obtained by compiling the works by Ceplecha et al. [1998] and Bonacina et al. [1973]. This synthetic analysis has the aim of providing relevant boundary conditions for the gas-phase simulations (which will be the

Parts of this chapter have been published in

1. F. Bariselli, S. Boccelli, A. Frezzotti, A. Hubin, T. E. Magin, **Aerothermodynamic modelling of meteor entry flows in the rarefied regime**, *2018 Joint Thermophysics and Heat Transfer Conference*, Atlanta, Georgia, USA, 2018-4180, 2018

2. F. Bariselli, A. Frezzotti, A. Hubin, T. E. Magin, **Aerothermodynamic modelling of meteor entry flows**, *Monthly Notices of the Royal Astronomical Society*, 492(2):2308-2325, 2020

core of Chapters 3 and 5), for both the freestream and the surface. This analysis is important for two reasons. First, the rate of evaporation of metallic species, which is the primary source of free electrons, is a strong function of the temperature of the body. Secondly, we are interested in estimating the altitudes (and thus the pressures and densities) at which the evaporation begins and for which the dynamics of the vapour could play a significant role.

The chapter is structured as follows. In the following section, we review the methodology used for the modelling of the material response of a meteoroid along its entry trajectory. In Section 2.3, we explain the numerical procedure, and the numerical tool developed is verified. Section 2.4 is devoted to the analysis of the trajectory, performed for a range of relevant sizes and entry flight velocities. Finally, we estimate the flow regimes encountered during the hypersonic flight, using basic kinetic theory, and we highlight the critical limits of currently employed approaches.

2.2. Methodology

2.2.1. Thermal equation

For a rapidly tumbling[1] sphere of radius R [Ceplecha et al., 1998], the heat equation reads as

$$\frac{\partial T}{\partial t} = \frac{\lambda}{\rho c_\mathrm{p}} \frac{\partial^2 T}{\partial r^2} + \frac{2\lambda}{\rho c_\mathrm{p}} \frac{1}{r} \frac{\partial T}{\partial r}, \tag{2.1}$$

where quantities λ, ρ, and c_p respectively represent the thermal conductivity, density, and specific heat of the meteoroid. The heat equation in this form is obtained by applying a transformation into spherical coordinates $T = T(r, \theta, \varphi, t)$, dropping the angular dependencies due to the symmetry of the problem. Figure 2.1 shows a sketch of the one-dimensional domain approximation employed in this chapter.

2.2.2. Phase-change models

Equation 2.1 is solved with the following boundary condition at the vapour-liquid interface (indicated with subscript "w")

$$\frac{\Lambda \rho_\infty V_\infty^3}{8} = \lambda \left.\frac{\partial T}{\partial r}\right|_\mathrm{w} + \epsilon \sigma_\mathrm{S} (T_\mathrm{w}^4 - T_\infty^4) + \phi_\mathrm{e} L_\mathrm{e}, \tag{2.2}$$

which represents a surface energy balance where the thermal energy received by the meteoroid (left-hand side term) is balanced by the heat conduction, gray-body radiation, and vaporisation losses on the right-hand side. In Equation 2.2,

[1] We assume that the only effect of tumbling is to level out the heat load over the whole surface of the body. This justifies the one-dimensional approximation. In reality, tumbling influences the dynamics of the molten layer and the mechanical removal of the droplets.

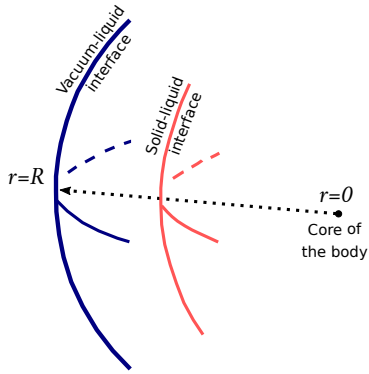

Figure 2.1.: *Representation of the one-dimensional approximation employed for the solution of the heat equation in spherical coordinates, under the assumption of rapidly tumbling sphere.*

quantity Λ is the heat transfer coefficient, ϵ the emissivity, σ_S the Stefan-Boltzmann constant, and L_e the latent heat of evaporation. The evaporation mass flux ϕ_e is computed through the Knudsen-Langmuir formula as

$$\phi_e = n_w^{eq} \sqrt{\frac{\mu k_B T_w}{2\pi}}, \tag{2.3}$$

which was already introduced in Chapter 1. The symbol k_B denotes the Boltzmann constant, μ the average meteoric atom mass, and n_w^{eq} the equilibrium vapour number density. Equation 2.3 is set different from zero only when the surface temperature is close to or above the melting condition. The recession velocity V_w is linked to the evaporation mass flux by the following relation

$$V_w = \frac{\phi_e(T_w)}{\rho}. \tag{2.4}$$

The liquid-solid transition is dealt with through the *apparent heat capacity method* by Bonacina et al. [1973]. Dias et al. [2016] used this technique to assess the thickness of the liquid layer, which can be taken away by the incoming jet. In this method, only one equation is solved for both the condensed phases without the need for tracking the melting front, which is obtained a posteriori. The latent heat of melting L_m at the interface is taken into account by assuming a temperature dependency of the heat capacity of the following type

$$c_p = \begin{cases} c_{p,s} & \text{if } T \leq T_m - \Delta T \\ \frac{c_{p,s}+c_{p,l}}{2} + \frac{L_m}{2\Delta T} & \text{if } T_m - \Delta T < T < T_m + \Delta T \\ c_{p,l} & \text{if } T \geq T_m + \Delta T \end{cases} \tag{2.5}$$

where T_m is the melting temperature, and ΔT defines the range in which the

molten layer and solid coexist, a typical feature of melting problems in mixed substances.

2.2.3. Trajectory equation

The freestream velocity V_∞ in the boundary condition is updated along the trajectory by decelerating the body according to the ballistic law

$$\frac{\partial V_\infty}{\partial t} = -\frac{3}{4}\frac{\rho_\infty}{\rho}\frac{\Gamma}{R}V_\infty^2, \tag{2.6}$$

where Γ is the free molecular drag coefficient. Finally, the change in altitude with time $H(t)$ is a function of the angle of the radiant from the zenith z_R, as follows

$$\frac{\partial H}{\partial t} = -V_\infty \cos z_\mathrm{R}. \tag{2.7}$$

Note that Equation 2.7 couples back to Equations 2.2 and 2.6 through the value of the atmospheric density ρ_∞, that is a function of the altitude.

Freestream properties are computed according to the Naval Research Laboratory Mass Spectrometer Incoherent Scatter radar Empirical atmospheric model (NRLMSISE-00) developed by Picone et al. [2002].

2.3. Numerical method

The integration in time of Equation 2.1, coupled with that of Equations 2.6 and 2.7 is performed via an explicit Euler method. We employ a finite differences (FD) scheme for the spatial discretisation of Equation 2.1 over the domain represented in Figure 2.1, with Equation 2.2 as boundary condition. Equation 2.1 is solved in a fixed reference frame, with the vapour-liquid interface that moves at each timestep in agreement with the recession velocity of the wall. At each timestep, the mesh is regenerated in order to keep it uniform. If the node at the interface overlaps its neighbour, a node is dropped, so that the space discretisation remains nearly constant throughout the simulation. At each timestep, the solution previously obtained is re-mapped on the new grid.

We report the verification of the developed numerical code in Appendix A.

2.4. Results and discussion

Ordinary chondrites represent more than 90% of meteorites collected on the ground. Similar to magmatic rocks such as basalt, these meteorites are composed of a mixture of metal oxides with a composition close to the one reported in Table 2.1, extracted directly from Vondrak et al. [2008]. For our modelling, from here on, this will be considered as the meteoroid prototype.

Though the chemical composition of the ordinary chondrites has been widely studied, much less attention has been devoted to characterising their physical

properties, especially at high temperatures [Loehle et al., 2017a]. The list of the properties employed in this work to model the material is given in Table 2.2. These properties are assumed in line with those of Vondrak et al. [2008] and Campbell-Brown and Koschny [2004]. Finally, thermal conductivity is set according to the work of Yomogida and Matsui [1983], where the authors computed values between 0.415 and 3.85 W/m/K.

2.4.1. Trajectory and material response analysis

Trajectory simulations are run for different diameters (1, 2, and 5×10^{-3} m) and velocities spanning from 12 to 72 km/s. The simulations are compared with data stored in the Japanese Meteor Science Seminar Working Group (MSSWG) Orbit Database, where multi-station video meteor data have been collected over 26 years. These data are freely available for download on the International Meteor Organisation website (`https://www.imo.net/resources/databases/`). Some data are reported in Figure 2.2, showing the onset of the meteor phenomenon and its extinction. As a modelling assumption, we assumed that these two points correspond respectively to the beginning and the end of the ablation process. Average values and standard deviations are also reported. A radiant angle $z_R = 40$ deg, which turns out to be the most probable from the database, has been chosen along with drag coefficient $\Gamma = 1$, and heat transfer coefficient $\Lambda = 0.5$ [Campbell-Brown and Koschny, 2004].

In Figure 2.2, results from the synthetic model appear in the range of two standard deviations of the MSSWG observation. Slower simulated meteoroids seem to present longer trajectories than the observed ones. A possible explanation could reside in the fact that, for slower bodies, characterised by lower rates of evaporation, the entrainment of the molten layer by the surrounding gas may represent a significant mechanism of mass loss, which is not modelled here.

Table 2.1.: *Chemical composition chosen as reference for the modelling of an ordinary chondrite [Vondrak et al., 2008].*

SiO_2	MgO	FeO	Al_2O_3	CaO	Na_2O	K_2O	TiO_2
			[wt %]				
34.0	24.2	36.3	2.5	1.89	1.1	0.1	0.01

Table 2.2.: *Physical properties assumed to model an ordinary chondrite.*

ρ	λ	ϵ	$c_{p,l}$	$c_{p,s}$	T_m	L_m	L_e
[kg/m^3]	[W/m/K]	[-]	[J/kg/K]		[K]	[J/kg]	
3500	3.5	1.0	1050	1100	2000	4×10^5	4×10^6

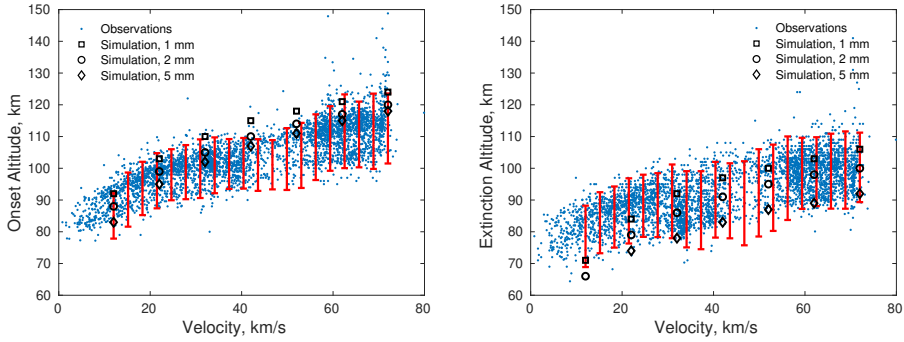

(a) **(b)**

Figure 2.2.: *Altitude of onset (a) and extinction (b) of the meteor from the visual detections stored in the MSSWG Orbit Database (https://www.imo.net/resources/databases/). The comparison with the simulated trajectories shows a good agreement with the observational data. Bars indicate a range of two standard deviations around the average value.*

When a meteoroid enters the atmosphere, it starts heating up very quickly. However, down to 200 km, the rise in temperature of the body is generally small. Particles of size 10^{-4} m are characterised by fast and uniform heating with negligible temperature gradients between the surface and the core of the body. The cooling effect due to the re-radiation of the surface is evident for the smaller and slower particles. For this condition, the melting temperature is not reached, and the body cools down as soon as the meteoroid starts decelerating. As shown in Figures 2.3 (b) and 2.3 (c), the thermal nonequilibrium inside the material is enhanced by increasing the velocity and the diameter. For bigger bodies (Figure 2.3 (c)), the thermal response is delayed, and the rise in temperature occurs abruptly.

When the surface starts melting, evaporation can commence. The altitude at which this occurs defines the *line of intensive evaporation*. From this point of the trajectory on, the energy is dissipated mostly by evaporation, and the material does not heat up any more. Only higher heat fluxes (Figure 2.3 (d)), encountered at greater velocities, lead the surface temperature to overcome the melting condition. This plateau could also be due to the chemical composition of the meteorite, kept constant along the trajectory. A depletion in volatile elements in the first part of the simulation would probably result in a drop of the vapour pressure (because dominated by the refractory elements) with a consequent increase of the surface temperature [McNeil et al., 1998, Janches et al., 2009]. On the other hand, Figure 2.3 (a) reveals a condition for which the object stops ablating before being completely disintegrated and glides down to the lower atmosphere layer as it loses momentum.

When small particles start melting, they immediately become molten droplets (see Figure 2.3 (a)). In this condition, the effect of the flow shear may play

an important role, with the mass being lost mainly through mechanical removal [Girin, 2017]. In particles of intermediate size (see Figure 2.3 (a) and (b)), a layer of liquid develops over the solid particle. This layer seems not to be present in the largest and fastest class of bodies under study (see Figure 2.3 (d)), where the evaporation front consumes the molten film, and the two fronts turn out to coincide. Moreover, in this class of meteoroids, heat conduction does not have time to level out the temperature inside the body, and the core remains unaffected. It is reasonable to think that this class of meteoroids fragments due to the large thermal stresses at the surface.

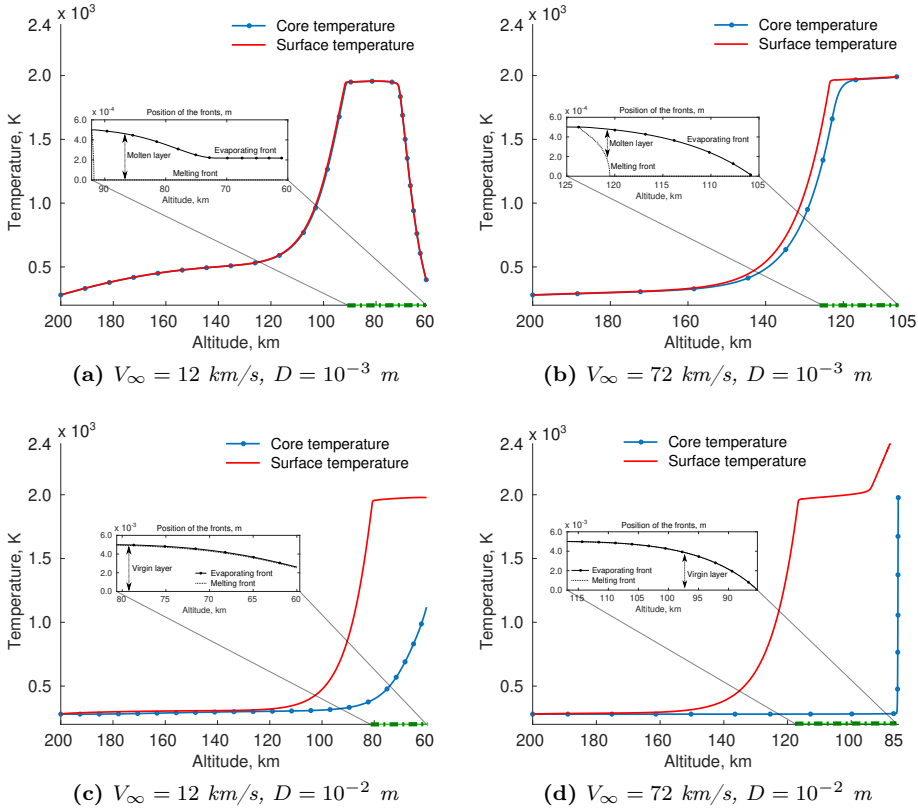

(a) $V_\infty = 12\ km/s,\ D = 10^{-3}\ m$ **(b)** $V_\infty = 72\ km/s,\ D = 10^{-3}\ m$

(c) $V_\infty = 12\ km/s,\ D = 10^{-2}\ m$ **(d)** $V_\infty = 72\ km/s,\ D = 10^{-2}\ m$

Figure 2.3.: *Temperature and front evolution along the simulated trajectories, for a range of diameters D and velocities V_∞, typical of meteoroid entry. The ablation phase is highlighted with a green line -·-·- on the abscissas. The positions of the melting and evaporation fronts are computed from the core of the body, and they are shown in the subwindow of each plot.*

2.4.2. Analysis of the flow regime

In meteors, the dynamics of the vapour cloud and its role in the formation of the shock wave is still unclear. In general, the collisional regime of a gas can be identified by a nondimensional parameter, the Knudsen number [Kogan, 1969, Bird, 1994], which is defined as the ratio between the kinetic and the macroscopic scale

$$\mathrm{Kn} = \frac{\tilde{\lambda}}{l}. \tag{2.8}$$

The kinetic scale $\tilde{\lambda}$ represents the average distance that a particle travels between successive collisions and is called the *mean free path*. For a gas composed of rigid elastic spheres of diameter d, length $\tilde{\lambda}$ is

$$\tilde{\lambda} = \frac{1}{\sqrt{2} n \sigma}, \tag{2.9}$$

and it depends on the local number density of the gas n and on the *collision cross section*[2], $\sigma = \pi d^2$. In Figure 2.4, we show a schematic of the mean free path and the collision cross section for a hard-sphere molecule travelling in a background gas.

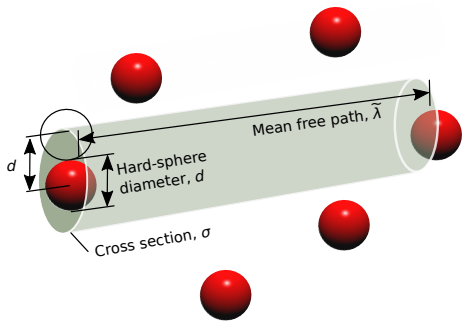

Figure 2.4.: *Graphical representation of the mean free path $\tilde{\lambda}$ and the collision cross section for a hard-sphere molecule σ travelling in a background gas of density n.*

For flows characterised by Kn << 1, the gas-phase collisions dominate the dynamics of the gas. The ablated vapour shields the meteoroid, and an intense bow shock wave develops in front of the body. These flows are characterised by local thermodynamic equilibrium, and hydrodynamic approaches can be used. On the other extreme, in the *free molecular regime* (Kn >> 1), the effect of gas-phase encounters can be neglected. Thus, gas particles move past each other without energy or momentum exchange and only interact with the surface of the body. As seen in Chapter 1, this regime constitutes a standard assumption in the modelling of meteoroid entry flows. If the two scales are comparable

[2]The collision cross section defines the sphere of influence of a molecule along its path.

(i.e. $\mathrm{Kn} \approx 1$), then the flow is in the *transitional regime*, and the effect of the collisions in the gas is considerable, but not sufficient to take the system to local thermodynamic equilibrium. For the correct modelling of this regime, gas encounters cannot be disregarded, and a kinetic equation must be used. This topic will be at the core of Chapter 3.

In the field of meteor flows, Silber et al. [2018b] collected the main analytical, observational, and computational efforts on this topic in their review. Bronshten [1983] extensively analysed the role of the collisions under subsequent levels of approximation to study the effect of screening due to the reflected or evaporated molecules under different conditions. As a result, he obtained values for the drag and heat transfer coefficients (respectively Γ and Λ) to be used under the approximation of free molecular flow.

In Figure 2.5, we show a diagram of the characteristic conditions encountered by a meteoroid in terms of Knudsen number and normalised ablation rate, as a function of diameter and altitude. In particular, we have chosen: i) the freestream Knudsen number, $\mathrm{Kn}_\infty = \tilde{\lambda}_\infty / D$, where the diameter of the meteoroid D is used as representative macroscopic scale; ii) the ablation rate of Equation 1.1, normalised by the initial mass of the object as follows

$$\frac{\dot{m}_\mathrm{e}}{m} = \frac{3}{16} \frac{\rho_\infty}{\rho} \frac{\Lambda V_\infty^3}{D L_\mathrm{e}}. \tag{2.10}$$

Equation 2.10, that is expressed as a function of the size of the body and the altitude of detection, tells how much of its initial mass the meteoroid would lose in one second at a certain given condition. For example, a 1 mm body falling at 32 km/s, detected by a radar at an altitude of 90 km experiences free molecular flight, considering that $\mathrm{Kn}_\infty > 10$. However, the collisional regime experienced by the vapour can differ significantly from the one suggested by the nominal condition [Silber et al., 2017, 2018a], as evaporation has already been triggered (the point lies below the line of intensive evaporation computed in Section 2.4.1), and the meteoroid is ablating fast at a normalised rate above 100. In Figure 2.5, we also report four bright meteor events among the ones selected by Moreno-Ibáñez et al. [2018]. These events are all characterised by an entry velocity around 30 km/s. Combining infrasound and photometric information with theoretical considerations, three of them were categorised in the slip flow regime ($0.001 < \mathrm{Kn}_\infty < 0.1$) and one of them (ID-20100530) at the limit between the slip and transitional flows. Here, their position in the diagram places them at a nominal condition of transitional regime ($\mathrm{Kn}_\infty > 0.1$), but in a situation of intense evaporation ($1 < \dot{m}_\mathrm{e}/m < 10$) for ID-20100530, and very intense evaporation ($10 < \dot{m}_\mathrm{e}/m < 100$) for the others.

Due to the large enough number of collisions taking place in the meteor head and vapour cloud, Popova et al. [2000] stressed the importance of taking into account metal-metal interactions in addition to air-metal particle collisions. They stated that, when the vapour pressure is much higher than the atmospheric pressure, the ablated vapour expands similarly to a hydrodynamic flow into a vacuum. In contrast with this suggestion, the methodologies developed

by Stokan and Campbell-Brown [2014b] and Dimant and Oppenheim [2017a] disregarded the interactions of the evaporated particles with each other. Therefore, we can try to verify this hypothesis by writing the number of collisions per unit time which occur in the vapour cloud as made up by two contributions, air-vapour $\dot{N}_{\text{coll}}^{\text{av}}$ and vapour-vapour $\dot{N}_{\text{coll}}^{\text{vv}}$ interactions. It reads

$$\begin{aligned}\dot{N}_{\text{coll}} &= \dot{N}_{\text{coll}}^{\text{av}} + \dot{N}_{\text{coll}}^{\text{vv}} \\ &= 4\pi \int_R^{R^\star} \left(n_\infty n_{\text{v}} \sigma V_\infty + \frac{n_{\text{v}}^2}{2} \sigma V_{\text{t}} \right) r^2 dr \\ &= 4\pi \frac{1-\sqrt{\kappa}}{\sqrt{\kappa}} \left[n_\infty V_\infty + \frac{\sqrt{\kappa}}{2} n_{\text{w}}^{\text{eq}} V_{\text{t}} \right] n_{\text{w}}^{\text{eq}} \sigma R^3,\end{aligned} \tag{2.11}$$

which has been obtained by integrating the collision frequency of the molecules characterised by an average cross section σ, over a spherical volume around the object of radius R, which spans from its surface to a point in the space where the vapour number density n_{v} has decayed by a factor κ[3] (at $r = R^\star$). Quantities V_{t} and n_∞ represent respectively the thermal velocity of the vapour and the freestream number density.

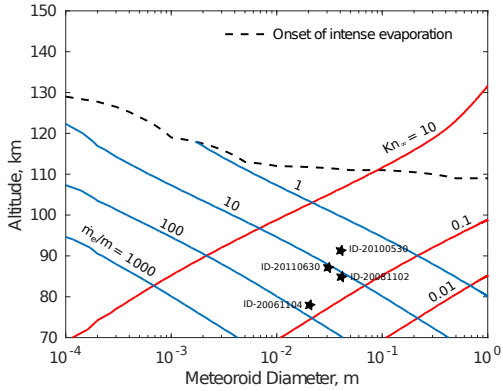

Figure 2.5.: *Diagram of the rarefaction regimes encountered by a meteoroid flying at 32 km/s is shown by plotting the Knudsen number (Kn_∞, ——) and normalised ablation rate ($\dot{m}_e/m$, ——) contours in relation to the diameter of the body and the altitude of the detection. The onset of evaporation has been computed through the trajectory analysis performed in this chapter. In the plot, four bright meteor events classified between the slip and transitional regimes are reported [Moreno-Ibáñez et al., 2018].*

In Figure 2.6, quantitative values are given for $\kappa = 10^{-3}$. The contributions of air-vapour and vapour-vapour collisions are studied separately. Above

[3]The underlined hypothesis is that the number density of the vapour decays from its value in equilibrium at the surface temperature, $n_{\text{w}}^{\text{eq}}(T_{\text{w}})$, with the square of the distance r to the wall $n_{\text{v}} = n_{\text{w}}^{\text{eq}} R^2/r^2$, thus $\kappa = (R/R^\star)^2$.

105 km, vapour-vapour interactions in thermal equilibrium are found to be more important than the interactions with the freestream air molecules. Conversely, hyperthermal air-vapour collisions become dominant at lower altitudes, where the density of the atmosphere is higher.

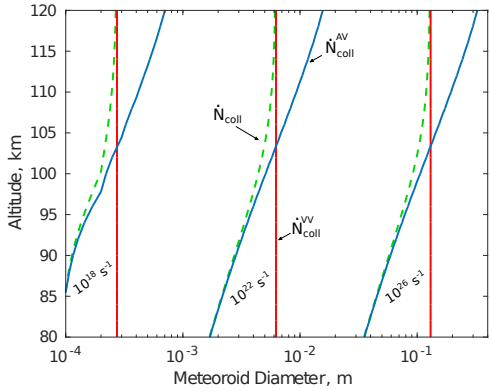

Figure 2.6.: *Contribution of air-vapour ($\dot{N}_{coll}^{av}$, ——) and vapour-vapour ($\dot{N}_{coll}^{vv}$, ——) collisions to the total number of collisions ($\dot{N}_{coll}$, - - -) experienced per unit time by the ablated molecules. Contour lines are shown in relation to the diameter of the body and the altitude of detection. Vapour-vapour collisions seem to be very important only above 105 km.*

2.5. Concluding remarks

We have analysed the thermal response of the meteoroids along their entry trajectory and selected those conditions that will be used at the boundaries of the domain, for the detailed flowfield analysis performed in Chapters 3 and 5.

Simulations have been run for a range of diameters and velocities characteristic of radio/radar meteors so as to identify freestream conditions, between the onset and the end of intense evaporation, for which the dynamics of the vapour phase cannot be disregarded. Moreover, when evaporation commences, the surface of the body reaches a temperature plateau not far from the material melting point.

Small particles are characterised by fast and uniform heating. In particles of intermediate size, a layer of liquid develops over the solid particle. Therefore, for this class of meteoroids, the effect of the external gas on the molten material may play an important role, with part of the mass being lost through mechanical removal. This topic will be at the core of the methodology developed in Chapter 6.

Finally, we have examined the flow regimes experienced by the meteoroid along its entry trajectory, using basic kinetic theory analysis. After the onset of intense evaporation, the collisional regime experienced by the vapour differs

from the one suggested by the freestream Knudsen number. We have also evaluated the relative contribution of air-vapour and vapour-vapour collisions, with the latter becoming dominant only above 105 km, where the density of the atmosphere is lower.

CHAPTER 3

Aerothermodynamics of Meteoroid Entry Flows

"Ceci n'est pas une pipe."

– René Magritte

3.1. Introduction

In this chapter, we intend to describe in detail the ablated vapour dynamics around millimetre-sized meteoroids, with particular focus on the formation of the plasma around the meteoroid. We are interested in providing a picture of the steady flowfield at a certain instant along the trajectory, for a given chemical composition and temperature of the condensed phase.

Particular attention is dedicated to the modelling of gas-surface interactions and chemical reactions leading to the production of free electrons from heavy-particle and electron-impact ionisation of metallic species, as well as ionisation of air, usually neglected in conventional works. Our analysis is developed in the framework of the Direct Simulation Monte Carlo (DSMC) method to account for rarefied gas effects. In particular, an evaporation boundary condition suitable to model multicomponent silicate materials is introduced. The transport properties of the ablated vapour are computed using the Chapman-Enskog theory, and the DSMC phenomenological parameters are retrieved by fitting the collision integrals over a wide range of temperatures. Finally, inelastic cross sections for heavy- and electron-impact ionisation of metals are computed in order to obtain DSMC steric factors.

Parts of this chapter have been published in

1. F. Bariselli, S. Boccelli, A. Frezzotti, A. Hubin, T. E. Magin, **Aerothermodynamic modelling of meteor entry flows in the rarefied regime**, *2018 Joint Thermophysics and Heat Transfer Conference*, Atlanta, Georgia, USA, 2018-4180, 2018

2. F. Bariselli, A. Frezzotti, A. Hubin, T. E. Magin, **Aerothermodynamic modelling of meteor entry flows**, *Monthly Notices of the Royal Astronomical Society*, 492(2):2308-2325, 2020

The chapter is structured as follows. Physical and mathematical models are introduced in Section 3.2, starting from a brief introduction to the Boltzmann equation and the relevant boundary conditions. After, transport properties of the ablated vapour and ionisation reactions are reviewed and derived. In Section 3.3, we briefly present the DSMC method and those phenomenological models for elastic and reactive cross sections that are used along with this numerical method. Employed cross section data are computed and presented. In Section 3.4, the flow around a 1 mm evaporating meteoroid is analysed at different altitudes and velocities so to span different rarefaction regimes.

3.2. Physico-chemical models

3.2.1. Statistical description of the gas

As long as the hypothesis of continuum is valid, a hydrodynamic model can be applied [Josyula and Burt, 2011]. However, under rarefied conditions, the collision rate is too low for the gas to reach local thermodynamic equilibrium. Also, the high energies involved in meteors (above 100 eV) enhance thermo-chemical nonequilibrium effects. Hence, the gas has to be described at the gas *kinetic scale*, rather than by the Navier-Stokes equations. At this scale, the gas is comprised of particles exchanging momentum and energy during collisions. Such a scale does not employ a fully deterministic approach, but a statistical description.

We can introduce the function $f_i(\boldsymbol{x}, \boldsymbol{\xi}, t)$ that is defined as the *one-particle velocity distribution function* for the species $i \in \mathcal{S}$, in the physical and velocity space $(\boldsymbol{x}, \boldsymbol{\xi})$[1]. This function has a physical interpretation, $f_i \, d\boldsymbol{x} \, d\boldsymbol{\xi}$ being the expected number of molecules of species i in the volume element $d\boldsymbol{x}$ located at $\boldsymbol{x}$, whose velocities lie in the velocity element $d\boldsymbol{\xi}$ about velocity $\boldsymbol{\xi}$ at time t.

The Boltzmann equation

The evolution over time of f_i is described by an integro-differential equation, the Boltzmann equation [Cercignani, 1969, Ferziger and Kaper, 1972], which for a gas mixture can be written, in the absence of external forces, as

$$\partial_t f_i + \boldsymbol{\xi} \cdot \boldsymbol{\nabla} f_i = \mathcal{C}_i(f) + \mathcal{R}_i(f) \qquad i \in \mathcal{S}. \tag{3.1}$$

The left-hand side describes the effect of macroscopic gradients on the velocity distribution function; on the the right-hand side, the collisional source terms $\mathcal{C}_i(f)$ and $\mathcal{R}_i(f)$ respectively model elastic scattering and reactive encounters [Giovangigli, 1999]. These operators take into account the collisional processes experienced by pairs of particles due to local binary encounters, and they are responsible for the evolution of f_i in the velocity space, without affecting the position of the molecules in the physical space.

[1] For the sake of simplicity, we are not including the internal energy degrees of freedom of the molecules in the treatment of Sections 3.2.1 and 3.2.2.

Macroscopic properties

In gasdynamics, we are often interested in averaged fields and their spatial distribution. Any quantity of interest at the macroscopic level, such as density, bulk velocity, and total energy of the gas $\Psi(\boldsymbol{x},t)=\{\rho,\rho\boldsymbol{v},\rho E\}$, can be obtained from the related quantities at molecular scale $\theta_i(\boldsymbol{x},\boldsymbol{\xi},t)=\{\mu_i,\mu_i\boldsymbol{\xi},\frac{1}{2}\mu_i|\boldsymbol{\xi}|^2\}$ as a moment of the probability distribution function

$$\Psi=\sum_{i\in\mathcal{S}}\int\theta_i f_i\ d\boldsymbol{\xi}, \tag{3.2}$$

where μ_i is the atomic mass of species i.

3.2.2. Kinetic boundary condition for evaporation

From a microscopic point of view, the vapour-liquid interface is a finite region whose thickness is 10-20 nominal molecular diameters [Frezzotti, 2011]. At a kinetic scale, its detailed physical structure is neglected and reduced to a surface Σ bounding the vapour. The molecular flux of the species i emerging from Σ, which moves at velocity $\boldsymbol{v}_{\rm w}$ and is characterised by a normal unit vector $\boldsymbol{n}$ can be modelled by the following inhomogeneous linear boundary condition

$$\begin{aligned}[\boldsymbol{\xi}-\boldsymbol{v}_{\rm w}]\cdot\boldsymbol{n}\ f_i \;&=\; [\boldsymbol{\xi}-\boldsymbol{v}_{\rm w}]\cdot\boldsymbol{n}\ g_i\\ &+\int_{[\boldsymbol{\xi}'-\boldsymbol{v}_{\rm w}]\cdot\boldsymbol{n}<0}[\boldsymbol{\xi}'-\boldsymbol{v}_{\rm w}]\cdot\boldsymbol{n}\ \mathcal{K}_{B_i}(\boldsymbol{\xi}'\to\boldsymbol{\xi})\ f_i\ d\boldsymbol{\xi}',\\ &\qquad\qquad [\boldsymbol{\xi}-\boldsymbol{v}_{\rm w}]\cdot\boldsymbol{n}>0\quad i\in\mathcal{S}.\end{aligned} \tag{3.3}$$

This comprises two contributions (see Figure 3.1 (a)): i) the particles coming from the liquid and evaporating into the vapour phase with a half-range Maxwellian; ii) the molecules in the gas phase which, interacting with the wall and not condensing, are scattered back.

Concerning the first contribution, at the equilibrium vapour number density $n^{\rm eq}_{{\rm w}_i}$(wall composition, $T_{\rm w}$), and temperature $T_{\rm w}$, the half-range Maxwellian distribution reads as

$$g_i=\frac{\alpha_{{\rm e}_i}\ n^{\rm eq}_{{\rm w}_i}}{(2\pi R_i T_{\rm w})^{3/2}}\ \exp\left\{-\frac{|\boldsymbol{\xi}-\boldsymbol{v}_{\rm w}|^2}{2R_iT_{\rm w}}\right\},\quad [\boldsymbol{\xi}-\boldsymbol{v}_{\rm w}]\cdot\boldsymbol{n}>0, \tag{3.4}$$

in which R_i is the gas constant defined as $k_{\rm B}/\mu_i$, $k_{\rm B}$ being the Boltzmann constant. Departures from equilibrium are taken into account via an evaporation coefficient $0\le\alpha_{{\rm e}_i}\le 1$.

The second contribution describes the molecules in the gas phase which, interacting with the wall and not condensing, are scattered back and whose velocity is instantaneously changed from $\boldsymbol{\xi}'$ to $\boldsymbol{\xi}$ (denoted by $\boldsymbol{\xi}'\to\boldsymbol{\xi}$) with

probability driven by the *scattering kernel*

$$\mathcal{K}_{B_i}(\boldsymbol{\xi}' \to \boldsymbol{\xi}) = (1-\alpha_{\mathrm{c}_i})\frac{[\boldsymbol{\xi}-\boldsymbol{v}_{\mathrm{w}}]\cdot\boldsymbol{n}}{2\pi(R_i T_{\mathrm{w}})^2}\,\exp\left\{-\frac{|\boldsymbol{\xi}-\boldsymbol{v}_{\mathrm{w}}|^2}{2R_i T_{\mathrm{w}}}\right\}. \tag{3.5}$$

In this case, the kernel is written as if the impinging particles were fully thermalised to the temperature of the liquid. The condensation coefficient $0 \leq \alpha_{\mathrm{c}_i} \leq 1$ represents the probability to condense for a molecule of the species i as shown by Figure 3.1 (b) that provides a graphical representation of the fluxes of molecules at the surface.

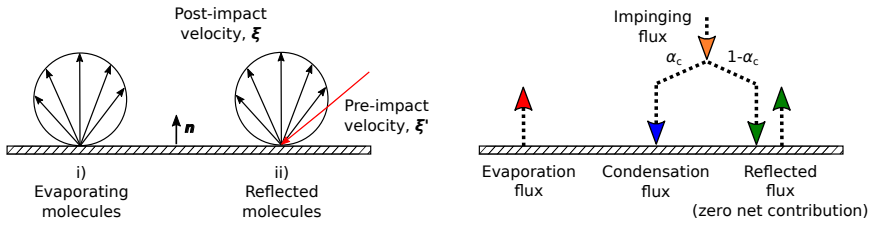

(a) **(b)**

Figure 3.1.: *(a) Graphical representation of the two different contributions composing the right-hand side of Equation 3.3. (b) Schematic showing the balance of fluxes at the surface from the vapour side.*

Link to classical evaporation models

The expression for the net evaporation flux ϕ_{e} reads as

$$\phi_{\mathrm{e}} = \sum_{i\in\mathcal{S}}\left(\alpha_{\mathrm{e}_i}\, n_{\mathrm{w}_i}^{\mathrm{eq}}\sqrt{\frac{\mu_i k_{\mathrm{B}} T_{\mathrm{w}}}{2\pi}} + \alpha_{\mathrm{c}_i}\int_{[\boldsymbol{\xi}-\boldsymbol{v}_{\mathrm{w}}]\cdot\boldsymbol{n}<0}\mu_i f_i\,[\boldsymbol{\xi}-\boldsymbol{v}_{\mathrm{w}}]\cdot\boldsymbol{n}\,d\boldsymbol{\xi}\right), \tag{3.6}$$

where the first term, the evaporation flux, is obtained by integrating over the proper velocity space the first term in the right-hand side of Equation 3.3, and the second term, the condensation flux, can be computed from the solution of the Equation 3.1. If the condensation flux in Equation 3.6 is zero, then we retrieve the Knudsen-Langmuir relation that we had previously introduced in Chapters 1 and 2

$$\phi_{\mathrm{e}} = \sum_{i\in\mathcal{S}}\alpha_{\mathrm{e}_i}\, n_{\mathrm{w}_i}^{\mathrm{eq}}\sqrt{\frac{\mu_i k_{\mathrm{B}} T_{\mathrm{w}}}{2\pi}}, \tag{3.7}$$

that models the evaporation process into a vacuum. Instead, if the vapour phase is in equilibrium at the surface at its own temperature T, number density

$n = \sum_{i \in \mathcal{S}} n_i$, and zero bulk velocity, from Equation 3.6 one obtains

$$\phi_{\mathrm{e}} = \sum_{i \in \mathcal{S}} \left(\alpha_{\mathrm{e}_i} \, n_{\mathrm{w}_i}^{\mathrm{eq}} \sqrt{\frac{\mu_i k_{\mathrm{B}} T_{\mathrm{w}}}{2\pi}} - \alpha_{\mathrm{c}_i} \, n_i \sqrt{\frac{\mu_i k_{\mathrm{B}} T}{2\pi}} \right), \tag{3.8}$$

which is known as Hertz-Knudsen formula.

Melt-vapour system equilibrium properties

According to Equation 3.4, the distribution functions of evaporating species are determined by the equilibrium vapour partial densities $n_{\mathrm{w}_i}^{\mathrm{eq}}$. The latter is computed by the multiphase and multicomponent equilibrium solver developed by Fegley and Cameron [1987], MAGMA. Using a mass-action mass-balance algorithm, MAGMA has been widely employed to model silicate lavas and has been extensively validated against experimental data [Schaefer and Fegley, 2004].

In the present model formulation, the molten phase is assumed to have constant and uniform temperature T_{w} as well as constant chemical composition. Therefore, the computed flowfield around the meteoroid is affected by evaporation through the equilibrium vapour densities obtained by MAGMA, but the molten phase composition and temperature are not affected by the computed flowfield.

Evaporation and condensation coefficients

Evaporation and condensation coefficients are left as free parameters in the model. For monatomic metal vapours, evaporation coefficients are close to unity [Ogasawara et al., 1998]. However, in the case of silicate and oxides, evaporation and condensation involve decomposition and recombination of molecules and atoms. Hence, an activation barrier, associated with the breaking of bonds in a dissociating and evaporating molecule, may result in rates which are lower than those predicted by the theory. Schaefer and Fegley [2004] reviewed some of the experimental works in which evaporation coefficients for silicate and oxides were computed as the departure of the evaporation rate into vacuum from the equilibrium one. As an example, Hashimoto [1990] reported very low values for the coefficients in forsterite, MgO, and SiO_2. Moreover, numerical efforts by Alexander [2001] and Fedkin et al. [2006] to reproduce experiments by Hashimoto [1983] resulted in species-specific evaporation coefficients far from unity.

In general, little is known about the factors that influence evaporation coefficients and there is no theory for calculating them from first principles. For this reason, we decide to set evaporation and condensation coefficients equal to one for all the metallic species. For nitrogen compounds (e.g. N_2, NO, etc.), the possibility to condense is assumed to be zero. On the other hand, O and O_2, which are both present in the vapour and the freestream, are treated differently: gas-phase oxygen originating from evaporation is assigned a con-

densation probability equal to one, upon colliding with the meteoroid surface; zero condensation probability is assigned to atmospheric oxygen. In the context of the one-way coupling between molten and vapour phases mentioned above, this rule implements in a very simplified way the assumption that the molten phase is allowed to accommodate by condensation the amount of oxygen lost by evaporation.

3.2.3. Transport properties of the ablated vapour

Experimental data on transport properties of alkali metal vapours are scarce due to the high temperatures required, low vapour pressures, and corrosive nature [Ghatee and Niroomand-Hosseini, 2007].

Kinetic theory provides the mathematical framework which allows linking interatomic forces to transport coefficients. As a result of the Chapman-Enskog perturbative solution method [Bird et al., 1960], the binary viscosity coming from the interaction between species i and j reads as

$$\eta_{ij} = \frac{5}{8}\frac{k_{\mathrm{B}}T}{\Omega_{ij}^{(2,2)}}. \tag{3.9}$$

Quantity $\Omega_{ij}^{(2,2)}$ is the so-called *collision integral*, defined as

$$\Omega_{ij}^{(2,2)} = \sqrt{\frac{2\pi k_{\mathrm{B}}T}{\mu_{ij}^{\mathrm{R}}}}\int_0^{+\infty}\int_0^{+\infty} e^{-\gamma_{ij}^2}\gamma_{ij}^7(1-\cos^2\chi)b db\, d\gamma, \tag{3.10}$$

in which b is the impact parameter characterising the binary collision, $\mu_{ij}^{\mathrm{R}} = \frac{\mu_i\mu_j}{\mu_i+\mu_j}$ the reduced mass, and $\gamma_{ij}^2 = \frac{\mu_{ij}^{\mathrm{R}}|\boldsymbol{\xi}_i-\boldsymbol{\xi}_j|^2}{2k_{\mathrm{B}}T}$ a reduced variable for the relative velocity $(\boldsymbol{\xi}_i - \boldsymbol{\xi}_j)$. The scattering angle, $\chi = \chi(b, |\boldsymbol{\xi}_i - \boldsymbol{\xi}_j|, \psi)$, resulting from the dynamic of the binary collision (see Figure 3.2 (a)), directly depends on the relevant interatomic potential, ψ. Each type of collision (e.g. neutral-neutral, ion-neutral, etc.) would require a different type of potential. However, this procedure quickly becomes cumbersome. In this work, we employ the Lennard-Jones potential

$$\psi(r_{ij}) = 4\epsilon_{ij}\left[\left(\frac{\bar{\sigma}_{ij}}{r_{ij}}\right)^{12} - \left(\frac{\bar{\sigma}_{ij}}{r_{ij}}\right)^{6}\right], \tag{3.11}$$

which consists of two parts: a steep repulsive term and a smoother attractive term (see Figure 3.2 (b)). Quantity ϵ_{ij} is the depth of the potential well, $\bar{\sigma}_{ij}$ is the finite distance at which the inter-particle potential is zero, and r_{ij} is the distance between the particles.

In order to obtain theoretical viscosity curves for single species vapours, we compute $\Omega_{ii}^{(2,2)}$. For this procedure, the Lennard-Jones (6-12) parameters of Table 3.1 have been employed. Combination rules for polyatomic species, whose potential parameters are not available in the literature, are used as proposed

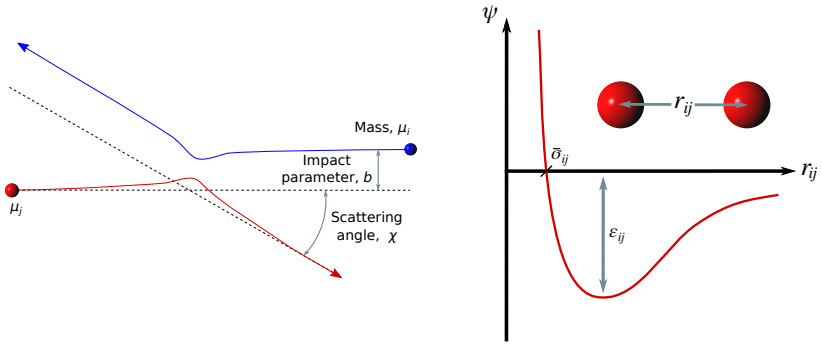

Figure 3.2.: *On the left, graphical representation of a binary elastic collision characterised by impact parameter b and resulting in scattering angle χ. On the right, Lennard-Jones potential: a steep repulsive part and a smoother attractive part can be identified.*

in their work by André et al. [2010]

$$\begin{aligned} \bar{\sigma}_{\mathrm{SiO_2\text{-}SiO_2}} &= (\bar{\sigma}^3_{\mathrm{Si\text{-}Si}} + \bar{\sigma}^3_{\mathrm{O\text{-}O}} + \bar{\sigma}^3_{\mathrm{O\text{-}O}})^{1/3}, \\ \epsilon_{\mathrm{SiO_2\text{-}SiO_2}} &= (\epsilon_{\mathrm{Si\text{-}Si}}\ \epsilon_{\mathrm{O\text{-}O}}\ \epsilon_{\mathrm{O\text{-}O}})^{1/3}. \end{aligned} \tag{3.12}$$

In Figure 3.3, a comparison between our prediction and a few sets of available experimental results [Lee and Bonilla, 1968, Vargaftik et al., 1991, Briggs, 1968, Stefano et al., 1966] is provided. Differences between theory and experiments may come from the presence of molecules and ions in the vapours or from uncertainties in the potential parameters. One could also argue that the Lennard-Jones potential (6-12) does not apply to alkali metals such as potassium. Ghatee and Niroomand-Hosseini [2007] stated that it fails in the prediction of transport properties of K, Rb, and Cs metals' vapour, especially in the low-temperature range. Nonetheless, in our study, the comparison turns out to be fair, with sodium viscosity lying between the two sets of data and the potassium one extremely close.

For atomic potassium, we also compare the thermal conductivity. Following the definition of Prandtl number, which is equal to 2/3 in the absence of internal energy modes, one obtains

$$\lambda_{ii} = \frac{c_{\mathrm{p}_i}\eta_{ii}}{\mathrm{Pr}}, \tag{3.13}$$

where $c_{\mathrm{p}_i} = \frac{5}{2}R_i$ is the specific heat at constant pressure. In Figure 3.3 (b), the comparison for the thermal conductivity of K with the available data is excellent.

Table 3.1.: *Lennard-Jones interatomic potential parameters employed to compute collision integrals for neutral-neutral collisions of metallic species. References: (1) Svehla [1962]; (2) McGee et al. [1998].*

Interaction	$\bar{\sigma}$ [A]	ϵ/k_B [K]	Reference
Si-Si	2.91	3036.0	1
Mg-Mg	2.93	1614.0	1
Al-Al	2.66	2750.0	1
Fe-Fe	2.47	7556.0	2
Ca-Ca	4.52	50.0	2
Na-Na	3.58	1375.0	1
K-K	4.25	850.0	2
SiO-SiO	3.52	461.0	Combination rules
SiO_2-SiO_2	3.96	245.94	Combination rules
MgO-MgO	3.53	336.12	Combination rules
Al_2-Al_2	3.35	2750.0	Combination rules
AlO-AlO	3.35	542.0	Combination rules
Al_2O_2-Al_2O_2	4.22	438.75	Combination rules
FeO-FeO	3.24	727.27	Combination rules
CaO-CaO	4.81	59.16	Combination rules
Na_2-Na_2	4.5	1375.0	Combination rules
NaO-NaO	4.0	310.24	Combination rules
Na_2O-Na_2O	4.79	509.61	Combination rules
K_2-K_2	5.35	850.0	Combination rules
KO-KO	4.57	243.93	Combination rules
K_2O-K_2	5.57	369.81	Combination rules

3.2.4. Ionisation reactions due to hyperthermal collisions

At collision energies above 100 eV, chemical reactions which lead to breaking and formation of new chemical bonds are no longer important processes [Dressler and Murad, 2001]. Instead, inelastic collisions consisting in transitions to electronically excited atoms are more probable. In particular, in meteors, free electrons are assumed to be mostly produced by collisions of metal atoms with atmospheric molecules through heavy-impact reactions of the following type

$$\mathrm{M} + \mathrm{N_2} \rightarrow \mathrm{M^+} + \mathrm{N_2} + \mathrm{e^-}, \tag{3.14}$$

where N_2 can be substituted by O_2. Meteor spectra give an indication in this sense, as they are dominated by atomic lines of meteoric origin, mostly neutral atoms, but also singly ionised ions [Berezhnoy and Borovička, 2010]. When a sufficient number of electrons has been produced, ionisation by electron-impact

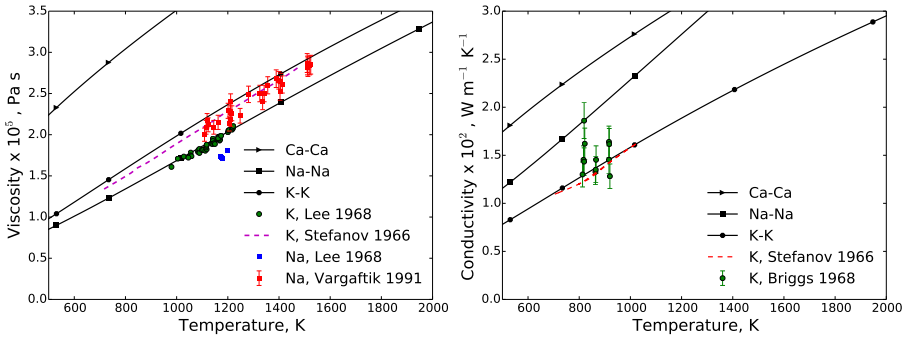

(a) **(b)**

Figure 3.3.: *Shear viscosity (a) and thermal conductivity (b) for some alkali atoms and comparison with available experimental data. Ca, which is not an alkali metal, is kept as a reference.*

can take over as the dominant process

$$\mathrm{M} + \mathrm{e}^- \rightarrow \mathrm{M}^+ + 2\mathrm{e}^-. \tag{3.15}$$

Moreover, a substantial contribution to the production of free electrons can be given by photoionisation processes of the following type

$$\mathrm{M} + h\nu_\star \rightarrow \mathrm{M}^+ + \mathrm{e}^-, \tag{3.16}$$

h and $\nu_\star$ being the Plank constant and the light frequency respectively, and in minor part by secondary impact ionisation reactions, involving doubly ionised species. However, only the mechanisms of Equations 3.14 and 3.15 will be considered in this study.

The most extensive review on the gas-phase chemical dynamics involving metallic species was provided by Dressler and Murad [2001]. Although a considerable body of literature exists for thermalised metal chemistry, reliable cross sections for hyperthermal collisions (1 to 1000 eV, corresponding to relative velocities of 3-100 km/s) seem to exist only for Na and K, and a substantial experimental effort would be required [Plane et al., 2015]. While ion beam generators are standard technology and the knowledge about metal-ion inelastic collisions is relatively established, the same cannot be said of metal-neutral interactions, given the associated experimental difficulties. Friichtenicht et al. [1967] measured the degree of ionisation of fast particles injected into a thick gas target. They found an approximate $\sim V_\infty^4$ dependence of the ionisation cross sections, higher than the semi-empirical relation $\sim V_\infty^{3.42}$ from Bronshten [1983], but in agreement with the observational investigations by Verniani and Hawkins [1964]. The experiments of Bydin and Bukhteev [1960] and Cuderman [1972] provided data on fast alkali neutral metal beams with N_2 and O_2 gases.

Although leading to different results, these works showed a similar trend with the O_2 cross sections more than an order of magnitude higher than those for N_2. Very few studies [Bukhteev and Bydin, 1963, Boitnott and Savage, 1971] report measurements of fast Ca, Mg, Si, and Fe collisions in N_2 and O_2 gases, producing cross sections generally lower than those observed for the alkali metals, whose ionisation potentials are inferior. However, the accuracy of these data is questionable.

From the analytical point of view, Kunc and Soon [1991] summarised the available approaches. They show that a reliable theory to predict heavy-impact ionisation is not available yet. In this work, we employ Drawin semi-empirical cross sections [Drawin and Emard, 1973] to obtain an estimate of heavy- and electron-impact ionisation processes. For the former, the cross section reads

$$\sigma_{\mathrm{I}} = \begin{cases} 0 & \text{if } W_0 < 1 \\ 4\pi a_0^2 \left(\frac{E_{\mathrm{H}}}{E_0}\right)^2 \frac{\mu_{\mathrm{A}}}{\mu_{\mathrm{H}}} \xi_0^2 \frac{2\mu_{\mathrm{e}}}{\mu_{\mathrm{e}}+\mu_{\mathrm{A}}} (W_0 - 1) & \\ \qquad \times \left[1 + \frac{2\mu_{\mathrm{e}}}{\mu_{\mathrm{e}}+\mu_{\mathrm{A}}} (W_0 - 1)\right]^{-2} & \text{if } W_0 \geq 1 \end{cases} \tag{3.17}$$

where $W_0 = E_{\mathrm{c}}/E_0$, E_{c} being the energy of the collision, E_0 the ionisation energy, μ_{A} and μ_{e} the mass of the incident atom and of an electron. E_{H}, μ_{H}, and a_0 are respectively the ionisation energy, the mass, and the first Bohr radius of atomic hydrogen. Finally, ξ_0 represents the number of equivalent electrons in the outer (ground state) shell of the target atom.

In Figure 3.4 and 3.5, we provide a comparison of the cross sections obtained in this work with the experimental results of Bydin and Bukhteev [1960] and Cuderman [1972] for heavy-impact ionisation and the data recommended by Lennon et al. [1988] for electron-impact ionisation. Results are in reasonable agreement with those reported in the literature. In particular, electron-impact cross sections by Drawin seem to perform well close to the ionisation threshold for all the species. For Si, Na, and K, however, the analytic cross sections seem to under-predict the recommended values at higher impact energies. Moreover, electron-heavy ionisation cross sections are characterised by a peak not far from the ionisation threshold, and after that they decrease (Figure 3.5). Similarly, this maximum is present in heavy-heavy cross sections, but it occurs at energy values which are higher than those of interest in this work.

3.3. The Direct Simulation Monte Carlo method

DSMC [Bird, 1963, 1994] is a particle-based method for the numerical solution of Equation 3.1. This technique has been widely used in the aerospace community over the last 50 years to simulate hypersonic flows [Ivanov et al., 1998, LeBeau, 1999] with a high degree of thermo-chemical nonequilibrium. The trajectories of a representative number of molecules $\mathcal{I}$ are simulated in the physical space. Each simulated particle corresponds to a certain number of real

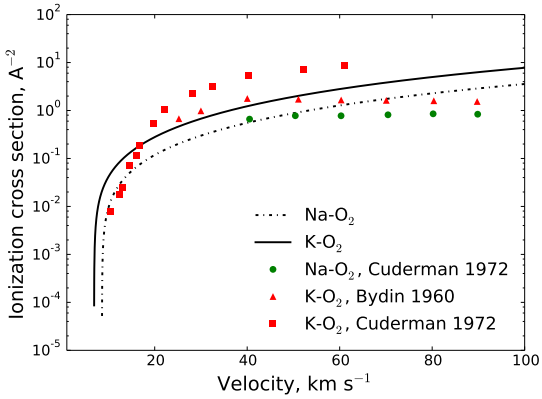

Figure 3.4.: *Drawin cross sections computed for heavy-impact ionisation are compared with available experimental data [Bydin and Bukhteev, 1960, Cuderman, 1972].*

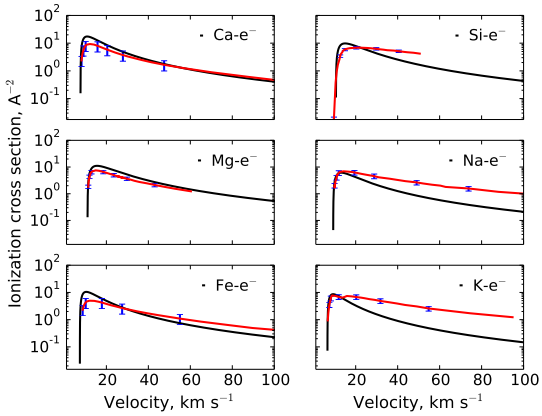

Figure 3.5.: *Drawin cross sections computed for electron-impact ionisation — are compared with available recommended data — [Lennon et al., 1988].*

molecules according to a statistical weight W_p and is characterised by position $\boldsymbol{x}_i$ and velocity $\boldsymbol{\xi}_i$. As shown in Figure 3.6, each timestep alternates the execution of the collisionless motion of particles and the computation of collisions: the particle advection phase is treated deterministically integrating in time the ballistic trajectories, whereas the collisional source terms of Equation 3.1 are solved by means of Monte Carlo stochastic evaluation of the collision pairs. The splitting of the left- and right-hand side of Equation 3.1 leads to accurate results only if the employed timestep Δt is a fraction of the mean collision time existing between two consecutive collisions. The physical domain is discretised with a grid, whose cells have a characteristic length which must be a fraction of the mean free path. This background mesh is used for the efficient choice of

collisions partners.

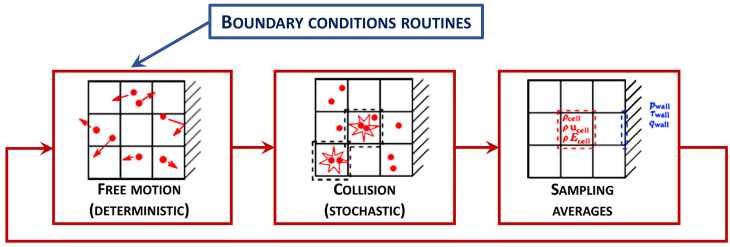

Figure 3.6.: *Schematic of the DSMC algorithm. Each timestep alternates the execution of the collisionless motion of particles and the computation of collisions. The molecules can interact with the boundaries in the free advection phase.*

3.3.1. DSMC algorithm

Advection step and boundary conditions

In the absence of external forces, the collisionless Boltzmann equation is equivalent to the solution of the following system of differential equations. For $i \in \mathcal{I}$,

$$\dot{\boldsymbol{x}}_i = \boldsymbol{\xi}_i \tag{3.18}$$

$$\dot{\boldsymbol{\xi}}_i = 0, \tag{3.19}$$

which can be integrated using an explicit Euler scheme. If the trajectory of the molecule is interrupted by a boundary, then the timestep is splitted into two smaller intervals. The interaction with a surface causes the velocity of the molecule to be instantaneously updated according to the scattering kernel in Equation 3.5, before completing the particle motion for the remaining time. Also, in this step, evaporating molecules are injected at the wall according to the distribution of Equation 3.4. Analogously, the molecules coming from the freestream are generated sampling from a Maxwell distribution function at the local gas properties n_∞, $\boldsymbol{v}_\infty$, and T_∞.

Collision step

The collision step is based on the local homogeneous relaxation equation

$$\partial_t f_i = \mathcal{C}_i(f) + \mathcal{R}_i(f) \qquad i \in \mathcal{S}. \tag{3.20}$$

In DSMC, only the molecules belonging to the same cell can potentially collide, and the collision partners are computed by the algorithm regardless of their

position in the cell. Therefore, the probability of a pair of molecules to collide $\mathcal{P}_{ij}$ is proportional to the volume swept by their total cross section σ_{ij} as follows

$$\mathcal{P}_{ij} = \frac{\sigma_{ij}\ |\boldsymbol{\xi}_i - \boldsymbol{\xi}_j|\ W_\mathrm{p}\ \Delta t}{\mathcal{V}_k}, \tag{3.21}$$

where $\mathcal{V}_k$ is the volume of the k-th cell.

The maximum number of binary collisions in a cell is given by

$$\mathcal{N}_k^\mathrm{pair} = \frac{1}{2}\ \mathcal{N}_k(\mathcal{N}_k - 1)\ \frac{(\sigma_{ij}|\boldsymbol{\xi}_i - \boldsymbol{\xi}_j|)_k^\mathrm{max}\ W_\mathrm{p}\ \Delta t}{\mathcal{V}_k}, \tag{3.22}$$

for which we have used $\mathcal{N}_k$ to indicate the number of molecules present in a computational cell at an instant in time. The scheme selects $\mathcal{N}_k^\mathrm{pair}$ random pairs and accepts the collision between a given pair with a probability $\sigma_{ij}|\boldsymbol{\xi}_i - \boldsymbol{\xi}_j|/(\sigma_{ij}|\boldsymbol{\xi}_i - \boldsymbol{\xi}_j|)_k^\mathrm{max}$, where the denominator is an estimate of the maximum expected value for $\sigma_{ij}|\boldsymbol{\xi}_i - \boldsymbol{\xi}_j|$.

Macroscopic variables

The macroscopic properties of the gas in the k-th cell can be obtained by averaging the microscopic properties $\theta_i(\boldsymbol{\xi}, t)$, i being the index of the molecule over a sample of particles $\mathcal{I}_k^\mathrm{s}$. This procedure is the discrete analogue of the one defined by Equation 3.2. For example, for cell k, we can write the density as

$$\rho_k = \frac{W_\mathrm{p} \sum_{i \in \mathcal{I}_k^\mathrm{s}} \mu_i}{\mathcal{V}_k N_\mathrm{s}}, \tag{3.23}$$

where N_s is the number of timesteps over which the sample is accumulated. In an unsteady simulation, $N_\mathrm{s} = 1$ and the sample is made up of those molecules which belong to the same cell at a certain instant in time. After the onset of steady flow conditions, the sample can be accumulated over multiple timesteps. The bulk velocity reads as

$$\boldsymbol{v}_k = \frac{\sum_{i \in \mathcal{I}_k^\mathrm{s}} \boldsymbol{\xi}_i}{\mathcal{N}_k^\mathrm{s}}, \tag{3.24}$$

where $\mathcal{N}_k^\mathrm{s}$ is the number of molecules present in the cell over N_s sampling timesteps.

3.3.2. DSMC elastic cross sections

In dilute gases, the transport properties introduced in Section 3.2.3 are the natural result of the simulated binary collisions. DSMC relies on a phenomenological potential to make molecules interact. Although apparently simplistic, these models are able to reproduce to some extent the most salient physics of the collision process, with the advantage of being computationally cheap. In the Variable Soft Sphere (VSS) model, molecules are approximated as rigid spheres of diameter d, which depends on the relative velocity of the impact. The total

cross section is written as a function of the relative velocity $\boldsymbol{g} = \boldsymbol{\xi}_i - \boldsymbol{\xi}_j$ as follows

$$\sigma = \pi d_{\text{ref}}^2 \left(\frac{g_{\text{ref}}}{|\boldsymbol{g}|} \right)^{2\omega - 1}. \tag{3.25}$$

The quantities with subscript "ref" are reference values evaluated at a reference temperature T_{ref}, and ω is the temperature exponent which allows the variation of the particle diameter with temperature. In this way, molecules with higher impact energies spend less time interacting on the potential energy surface. In the VSS model, the scattering law (see its graphical representation in Figure 3.2 (a) for a generic potential and in Figure 6.1 for the hard-sphere potential) reads as

$$\chi = 2 \cos^{-1} \left\{ \left(\frac{b}{d} \right)^{\frac{1}{\alpha}} \right\}, \tag{3.26}$$

which allows us to model anisotropic scattering events through the exponent α (where $\alpha = 1$ corresponds to an isotropic scattering law). It is well known that such a model fails in the attempt of capturing diffusion processes in mixtures of gases, and that the anisotropy of neutral-charged collisions in weakly ionised gases is not accurately described [Swaminathan-Gopalan and Stephani, 2015]. The collision parameters are obtained by averaging the properties of the collision partners: $d_{\text{ref}_{ij}} = (d_{\text{ref}_i} + d_{\text{ref}_j})/2$, $\omega_{ij} = (\omega_i + \omega_j)/2$, $\alpha_{ij} = (\alpha_i + \alpha_j)/2$.

Dataset

The collision integrals of Equation 3.10, $\Omega_{ii}^{(2,2)}$ can be expressed as function of the VSS model parameters as follows

$$\Omega_{ii}^{(2,2)}\Big|_{\text{VSS}} = \frac{4\alpha_i}{(\alpha_i + 1)(\alpha_i + 2)} \frac{\pi d_{\text{ref}_i}^2}{2} \sqrt{\frac{k_{\text{B}} T}{2\pi \mu_{ii}^{\text{R}}}} \left(\frac{T_{\text{ref}_i}}{T} \right)^{\omega_i - \frac{1}{2}} \frac{\Gamma\left(\frac{9}{2} - \omega_i\right)}{\Gamma\left(\frac{5}{2} - \omega_i\right)}, \tag{3.27}$$

where Γ is the Euler gamma function. Through Equation 3.27, least squares fitting is performed to obtain the VSS parameters for each collision pair (see Figure 3.7). Quantity $T_{\text{ref}} = 1000$ K is chosen as reference temperature. The fitting minimises the error in the range of temperatures between 800 and 4000 K. Table 3.2 reports the VSS parameters obtained through this procedure.

Finally, the VSS model coefficients for air neutrals and their ions, usually employed in the literature, can be found in Appendix B, Table B.1.

3.3.3. DSMC reactive cross sections

Chemistry is accounted for through the Total Collision Energy (TCE) method by Bird [1994]. This method consists of assuming an analytic form for the

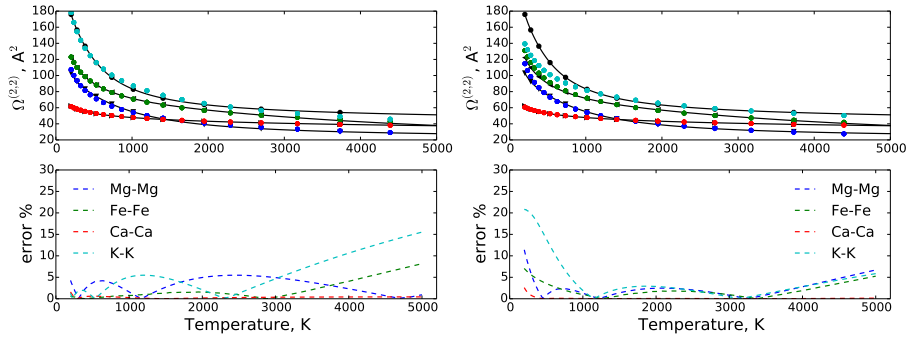

Figure 3.7.: *Fitting procedure of the VSS collision integrals with their exact formulation for some metallic atoms. Two possible choices are proposed, (a) to minimise the error between 200 and 5000 K or (b) to minimise the error between 800 and 4000 K.*

collision-dependent reaction cross section

$$\sigma_{\mathrm{I}} = \begin{cases} 0 & \text{if } E_{\mathrm{c}} < E_0 \\ \sigma C_1 (E_{\mathrm{c}} - E_0)^{C_2} \left(1 - \frac{E_0}{E_{\mathrm{c}}}\right)^{C_3} & \text{if } E_{\mathrm{c}} \geq E_0. \end{cases} \tag{3.28}$$

When averaging this cross section over a Maxwellian velocity distribution, it is possible to equate it to the known rate coefficient in Arrhenius form. The forward rate coefficients in Arrhenius form reads as

$$k_{\mathrm{f}}(T) = C_4 T^{C_5} \exp\left\{ -\frac{E_0}{k_{\mathrm{B}} T} \right\}, \tag{3.29}$$

where constants C_4 and C_5 are determined experimentally. Backward rates, k_{b}, are computed from *detailed balance*, starting from the available forward rate coefficients and equilibrium constants based on thermodynamic properties.

Dataset

Chemical reactions from the NASA Air-11 mixture, which includes air neutrals and their ions, are accounted for by Park's mechanism [Park, 1993, Park et al., 2001]. This mechanism considers dissociation reactions, in addition to the Zel'dovich process, which can lead to the formation of nitric oxide. The presence of NO in meteor flows has been studied in the past [Menees and Park, 1976, Park and Menees, 1978, Silber et al., 2018b]. Here, it does not represent our focus, as it only marginally influences the electron density. Also, Park's mechanism involves associative and electron-impact ionisation of air species and consequent charge exchange reactions (see Table B.2 in Appendix B for

Table 3.2.: *Variable Soft Sphere (VSS) parameters obtained by fitting the collision integral $\Omega_{ii}^{(2,2)}$ for T_{ref} = 1000 K. This procedure is equivalent to tuning VSS parameters to the viscosity curve. The average fitting error is reported for the range between 800 and 4000 K.*

Interaction	d_{ref} [A]	ω [-]	α [-]	Error [%]
Si-Si	5.99	0.99	1.29	0.99
Mg-Mg	5.09	0.96	1.37	1.53
Al-Al	5.36	0.99	1.38	0.77
Fe-Fe	5.61	0.87	1.23	1.09
Ca-Ca	4.12	0.65	1.17	0.04
Na-Na	5.87	0.93	1.25	1.86
K-K	5.86	0.83	1.18	2.04
SiO-SiO	4.07	0.72	1.22	1.23
SiO_2-SiO_2	4.14	0.67	1.18	0.48
MgO-MgO	3.85	0.69	1.21	0.8
Al_2-Al_2	6.77	0.99	1.23	0.77
AlO-AlO	4.02	0.74	1.25	1.48
Al_2O_2-Al_2O_2	4.84	0.72	1.17	1.16
FeO-FeO	4.23	0.8	1.28	1.89
CaO-CaO	4.43	0.65	1.18	0.03
Na_2-Na_2	7.38	0.93	1.36	1.86
NaO-NaO	4.32	0.68	1.18	0.71
Na_2O-Na_2O	5.68	0.74	1.18	1.38
K_2-K_2	7.36	0.83	1.45	2.04
KO-KO	4.77	0.67	1.18	0.47
K_2O-K_2	6.18	0.7	1.17	0.92

the complete chemical mechanism).

Heavy-heavy and electron-heavy ionisation processes of metals have been added to Park's mechanism. The semi-empirical cross sections of Equation 3.17 have been fitted into the phenomenological cross section of Equation 3.28. The DSMC algorithm computes the probability with which a collision can result in a reaction according to a steric factor obtained as the ratio σ_{I}/σ which, in turn, can be expressed as the efficiency of ionisation at the first collision β_0. This efficiency was previously defined in Section 1.3.1. Efficiencies β_0 for different species were given by Jones [1997] in the form

$$\beta_0 = \frac{C_6\ (V_\infty - V_0)^2\ V_\infty^{0.8}}{1 + C_6\ (V_\infty - V_0)^2\ V_\infty^{0.8}}, \tag{3.30}$$

where the parameter C_6 is a constant calibrated by experimental data and V_0 the ionisation threshold velocity. A comparison between the values of β_0 provided by Jones [1997] and the DSMC steric factors obtained in this work is

given in Figure 3.8, and a fair agreement is found.

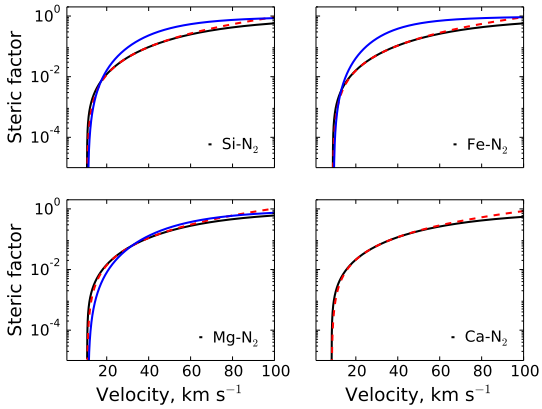

Figure 3.8.: *The steric factors computed in this work* ▬ *and their fitting into a DSMC form* - - - *are compared with* β_0 *coefficients* ▬ *[Jones, 1997].*

TCE coefficients obtained from the fitting procedure for heavy- and electron-impact ionisation are presented in Tables 3.3 and 3.4.

Table 3.3.: *TCE coefficients obtained from the fitting procedure of M-*N_2 *ionisation cross sections. These values can be used for the comparison of the DSMC steric factors with* β_0 *coefficients, as provided in Figure 3.8.*

Interaction	C_1 [1/J]	C_2 [-]	C_3 [-]	E_0 [eV]
Si-N_2	1.0×10^{-6}	1.23	0.64	8.15
Mg-N_2	7.04×10^{-7}	1.22	0.65	7.65
Fe-N_2	7.49×10^{-8}	1.17	0.7	7.87
Al-N_2	6.01×10^{-7}	1.26	0.64	5.99
Ca-N_2	1.25×10^{-9}	1.09	0.81	6.11
Na-N_2	2.01×10^{-7}	1.24	0.67	5.14
K-N_2	2.75×10^{-8}	1.21	0.72	4.34

3.3.4. Inelastic collisions and plasma effects

The translational-internal energy exchanges for air molecules are modelled according to the classical Larsen-Borgnakke phenomenological model [Borgnakke and Larsen, 1975]. In this approach, the post-collision properties of the two colliding molecules are sampled from a joint equilibrium distribution of translational and internal modes, and the equilibrium relaxation rates are captured

Table 3.4.: *TCE coefficients obtained from the fitting procedure for electron-impact ionisation.*

Interaction	C_1 [1/J]	C_2 [-]	C_3 [-]	E_0 [eV]
Si-e^-	5.41	-0.51	1.51	8.15
Mg-e^-	2.03	-0.54	1.54	7.65
Fe-e^-	0.03	-0.63	1.63	7.87
Al-e^-	2.3	-0.51	1.51	5.99
Ca-e^-	2.87×10^{-6}	-0.85	1.85	6.11
Na-e^-	0.14	-0.57	1.57	5.14
K-e^-	1.43×10^{-3}	-0.67	1.67	4.34

tuning rotational or vibrational collision numbers. Also, the excitation of the electronic levels is not taken into account.

Free electrons are treated under the assumption of an ambipolar electric field, which is a standard approximation for low-density plasmas and leads to local charge neutrality [Carlson and Hassan, 1992, Boyd, 1997]. Also, ions are not affected by electric and magnetic fields, and they are characterised by straight ballistic trajectories like neutrals. Similarly, Dimant and Oppenheim [2017a] assumed charge neutrality to develop their kinetic model and neglected the effect of fields on the ions. This assumption was justified by comparing the electrostatic energy with the characteristic ion kinetic energy.

Finally, we do not consider three-body recombination reactions.

3.3.5. The SPARTA code

The SPARTA code (Stochastic PArallel Rarefied-gas Time-accurate Analyzer) by Gallis et al. [2014] is used here. Developed at Sandia Labs, this is an open-source DSMC-Boltzmann solver, and its object-oriented philosophy enables extensions (such as the implementation of the evaporation boundary condition) and its usage as an external library. The code can be freely downloaded at `https://sparta.sandia.gov/`.

3.4. Results and discussion

We start with a numerical test conceived to assess the degree of thermal nonequilibrium in a rarefied hypersonic flow at velocities and sizes relevant for the meteor phenomenon.

Then, as main study case, we investigate the flow around a 1 mm meteoroid, flying at 32 km/s, at three different altitudes: 80, 100, and 120 km, based on the fact that, in Figure 2.2, the altitude of detection roughly spans from 80 to 120 km. The surface temperature is set to 2000 K. This value is chosen

in agreement with the results of Chapter 2, in which, after the onset of the evaporation, the wall temperature reaches a plateau not far from the melting condition independent of the initial size and velocity. However, in this chapter, we examine the effect of the wall temperature on the flowfield at 80 km altitude, for the case in which $T_w = 3000$ K.

Lastly, in Section 3.4.4, we study the details of the ionisation process and extract global ionisation efficiencies from the simulations at different altitudes (80, 100, and 120 km) and flight velocities (12, 32, and 72 km/s), which could be used as input in classic synthetic models.

3.4.1. Details of the simulations

The simulations are performed in a two-dimensional axisymmetric configuration around a spherical body. The wall is assumed fully catalytic for ion-electron recombination. Freestream densities, compositions, and temperatures are computed according to the Naval Research Laboratory Mass Spectrometer Incoherent Scatter Radar (NRLMSISE-00) empirical atmospheric model developed by Picone et al. [2002].

In Figure 3.9, we show the equilibrium composition of the vapour in a relevant range of temperatures. At 2000 K, the ablated vapour is mainly composed of O, O_2, Fe, FeO, Na, and NaO, while SiO, SiO_2, Mg, and MgO appear only at higher temperatures. K, which is only present as a trace element in the liquid phase, is not considered in the simulations, given the difficulties to accurately track minor species in DSMC. Moreover, refractory elements such as Ca, Al, and Ti are excluded from the simulations as they do not significantly contribute to the evaporation process at these temperatures.

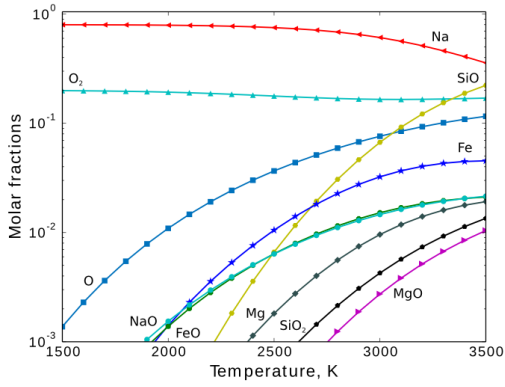

Figure 3.9.: *The composition of the ablated vapour in equilibrium with its condensed phase is shown for a range of temperatures characteristic of meteoroid melting. The results are obtained with the software MAGMA [Fegley and Cameron, 1987].*

For the three different altitudes, the timestep is equal to $\Delta t = 10^{-8}$ s, that

is sufficient to satisfy the DSMC numerical constraint for which the timestep has to be a fraction of the mean collision time. The domain sizes are reported in Table 3.5, along with the number of cells employed and the average number of particles present in the computational box throughout the simulations. The mesh is not uniform, as it is more refined in the proximity of the body and in the stagnation region, where the density is higher (we remind that the local mesh refinement should be a fraction of the local mean free path, as a rule of thumb $\Delta x < \tilde{\lambda}/3$). All the simulations took less than 24 hours, running on 64 processors (one node) of the VKI cluster. Only 5×10^3 timesteps were necessary to reach the steady state, while the remaining computational resources were used to collect the samples to average the macroscopic properties.

Table 3.5.: *Numerical parameters employed in the DSMC simulations. The wall temperature is 2000 K, the diameter of the body 1 mm, and its velocity 32 km/s.*

Altitude	Domain size - Number of diameters along x and r		Number of cells	Number of particles
[km]	[-]	[-]	[-]	[-]
80	760	5	25×10^3	2.6×10^6
100	270	20	150×10^3	3.6×10^6
120	200	100	65×10^3	12.1×10^6

3.4.2. Thermal nonequilibrium in the gas phase

We consider a 1 cm body, flying at 20 km/s. We extract the velocity distribution function (VDF) from DSMC simulations. The front region (Figure 3.10) shows a very high degree of nonequilibrium: the freestream particles (seen as a sharp peak at 20 km/s) are easily distinguished from the scattered molecules (with a Maxwellian distribution characterised by negative velocities). The effect of collisions is slightly visible, populating a region that connects the two families of particles. The resulting axial VDF has a bimodal shape, and the temperature anisotropy between the axial and radial translational modes can be appreciated.

3.4.3. Influence of the altitude on the dynamics of the gas phase

Now, we consider a 1 mm meteoroid at three different conditions: 80, 100, and 120 km. The comparison of translational temperatures and concentrations of the ablated vapour are shown in Figure 3.11. First of all, in Figure 3.11 (a), we see a rise in the temperature in front of the body. This growth becomes more and more diffuse as the freestream density decreases, and the bow shape, clearly

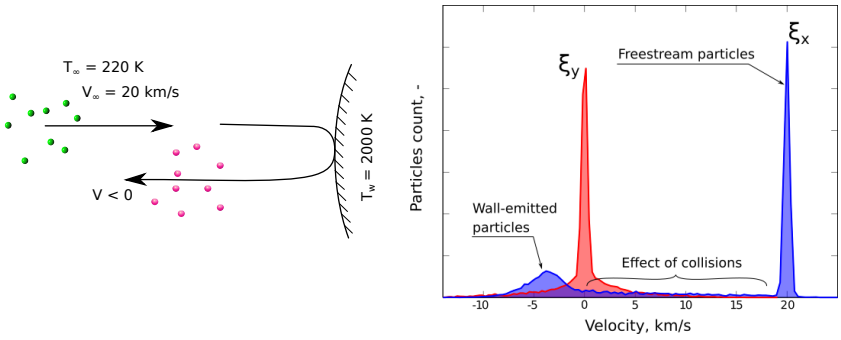

Figure 3.10.: *On the left, a schematic showing the mixing process of the two families of molecules in front of the body. On the right, VDF for the axial (ξ_x) and radial (ξ_y) velocities in front of a 1 cm body flying at 20 km/s. Two populations are visible in the axial VDF, shifted with respect to each other by a hypersonic velocity: the freestream and the wall scattered molecules. The same populations, with zero average velocity but the same temperature, can be distinguished from the radial VDF.*

visible at 80 km, gradually disappears. As a result of the thermal nonequilibrium, very high temperatures are computed. In DSMC, these temperatures are related to the width of the overall VDF which comes from the blending of the distributions of the two different classes of molecules. This effect has been described in Section 3.4.2 in terms of microscopic quantities for a non-ablating body, and it was already observed by Boyd [1998]. As a result, no particles are really characterised by such a temperature in the thermal sense. The small effect of collisions is also confirmed by the fact that the maximum value of the temperature seems insensitive to changes in the altitude: in fact, as the number of collisions decreases, internal molecular modes become less excited, and the gas starts behaving like a monatomic gas, characterised only by translational degrees of freedom.

At 120 km, the ablation phenomenon resembles a spherical expansion into the vacuum, with the ablated vapour able to travel upstream, only marginally interacting with the incoming jet. In this condition, a metal cloud forms all around the body, with almost spherical symmetry (see also Figure 3.12). The pressure of this vapour is higher than the stagnation pressure generated by the air molecules. At 100 km, the density profile of the ablated vapour along the stagnation line is very similar to the one at 120 km, but still different in terms of molar fraction (compare Figures 3.11 (b) and 3.12). On the other hand, at 80 km, the concentration of metals ahead of the body is lower and leads to two possible considerations. First, the vapour is taken away by the incoming jet. Second, the ablated atoms are immediately scattered back towards the wall where they can condense. In Figure 3.12, the metal vapour profiles are the same in the trail for all the tested conditions. This is because the close trail would be nearly in vacuum if it were not for the ablated vapour.

Finally, number density profiles along the radial direction r, at a given position in the rear of the body, are plotted in Figure 3.13 at an altitude of 80 km. In this picture, we have lumped the species into groups associated with the related chemical element, e.g., sodium (Na, Na^+, NaO) or silicon (Si, Si^+, SiO, SiO_2). The mixing layer at the edge of the trail ($r = D$) is evident if we look at the air species profiles, where a shadowing effect of the meteoroid can be appreciated. Concentrations reflect the vapour pressures computed by MAGMA. The ablated vapour fills the trail and diffuses in the background gas. Silicon and magnesium profiles are in close concentrations.

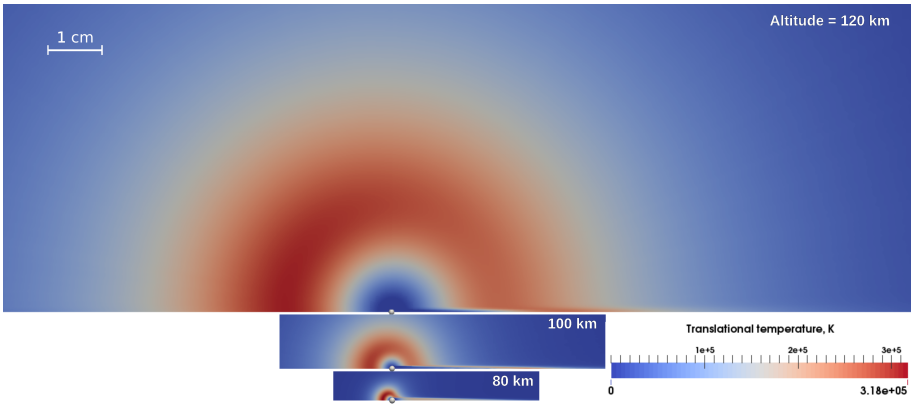

(a)

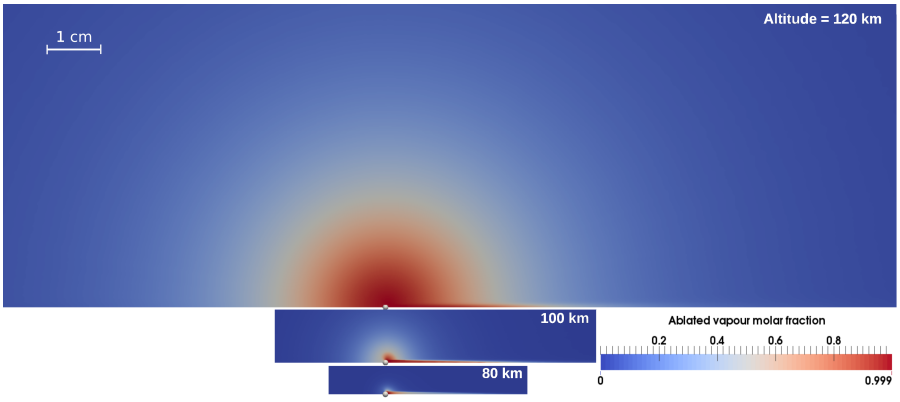

(b)

Figure 3.11.: *Fields for the translational temperature (a) and the ablated vapour molar fraction (b) for three different altitudes of detection: 80, 100, and 120 km. The wall temperature is 2000 K, the diameter of the body 1 mm, and its velocity 32 km/s. The freestream flows from left to right.*

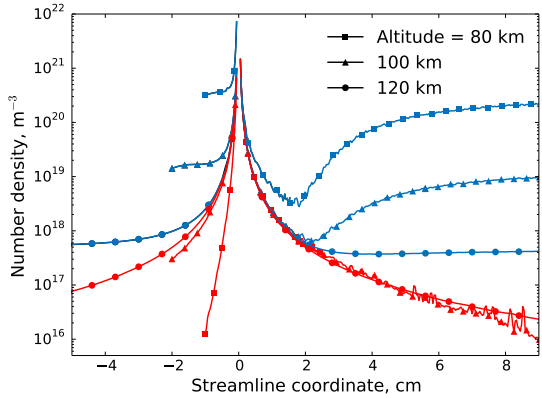

Figure 3.12.: *Density profiles along the axis of symmetry for three different altitude conditions. The reference system is centred at the stagnation point: air-vapour mixture* ——, *ablated vapour* ——.

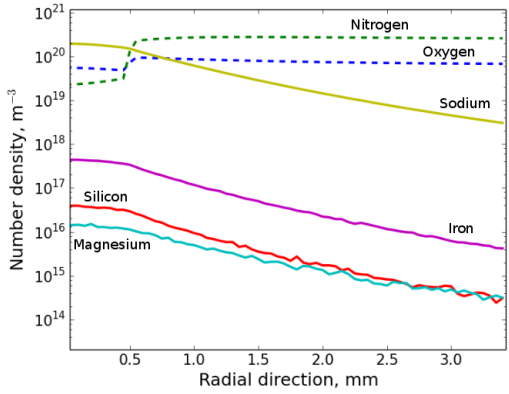

Figure 3.13.: *Density profiles in the radial direction in the rear of a 1 mm body flying at a speed of 32 km/s at 80 km altitude. Labels in the plot refer to the species associated with a single element, e.g., sodium (Na, Na^+, NaO), silicon (Si, Si^+, SiO, SiO_2), nitrogen (N, N^+, N_2, N_2^+), etc.*

Heat transfer coefficients

In order to assess the shielding effects by the ablated vapour, the heat transfer coefficient is computed as follows

$$\Lambda = \frac{q_{\mathrm{sp}}^{\mathrm{dsmc}}}{\frac{1}{2}\rho_\infty V_\infty^3}, \tag{3.31}$$

where q_{sp}^{dsmc} is the numerical heat flux computed by sampling the net energy balance at the stagnation point over all the impacts of DSMC particles with the wall. For all the conditions, we find that $\Lambda \approx 1$, meaning that the evaporation flux at 2000 K is not intense enough to partially screen the meteoroid from the energy of the incoming flow. The scenario will change radically in a condition of stronger evaporation, like the one we will analyse in Section 3.4.5.

3.4.4. Production of free electrons

A cylindrical volume of ionised plasma quasi-instantaneously forms upon the passage of the meteoroid. Literature refers to the radius of this cylinder as the *initial meteor radius*, which is usually defined as the half-width of the initial Gaussian distribution of electrons [Manning, 1958]. In the determination of r_0, Jones [1995] assumed that the vast majority of the metal atoms ionise after the first collision. However in DSMC, if the first collision is elastic, the ablated particle may experience a fully elastic thermalisation during subsequent interactions with the surrounding atmosphere, as the atom loses about one-third of its speed after each collision. Although we cannot say much about the length of this radius (our computational domain is only a few meteoroid diameters wide[2]), the conducted analysis provides insight into the formation of the plasma and its radial distribution.

Electrons are mainly produced ahead of the body and are advected around the meteoroid to the rear, where they start to dissipate by diffusing in the low-density surrounding (see Figure 3.20). We are assuming that recombination plays a significant role only in the long trail, which is not part of the simulated domain.

Up to 40 km/s, heavy-impact ionisation cross sections are smaller than those for electron-impact ionisation (the reader can compare Figures 3.4 with 3.5). However, the former process is necessary to trigger the electron avalanche. In Figure 3.14, we see that the contribution of Na to electron production is prevailing.

Between 80 and 120 km, a difference between 2 and 3 orders of magnitude exists in the number of free electrons (Figure 3.14). If we now look at a single element, we can appreciate the influence of the Knudsen number on the ionisation process. The number of generated ions is a strong function of the altitude of detection, although the number of their parent neutrals is the same for all the conditions, as it only depends on the wall temperature and meteoroid composition. However, Equation 1.2 cannot capture this behaviour as the electron density only depends on the energy of the collisions, through V_∞, and the ablation rate. In fact, in classical models, the effect of the density of the incoming jet enters the physical description only in the material energy balance. We will come back to this point later in the discussion about the ionisation coefficients.

In the same plot, we can compare the ionisation degree between metals and

[2]One of the main limitations in extending the size of the computational domain resides in the ability of the stochastic DSMC method to accurately track ablated metals far away from the body, where they become trace species strongly diluted in the background air.

air species. The number of ions coming from the air (N^+, O^+, N_2^+, O_2^+, and NO^+) is always comparable with those of Mg and Fe. This aspect is disregarded by standard models which assume metals only to be responsible for the plasma formation.

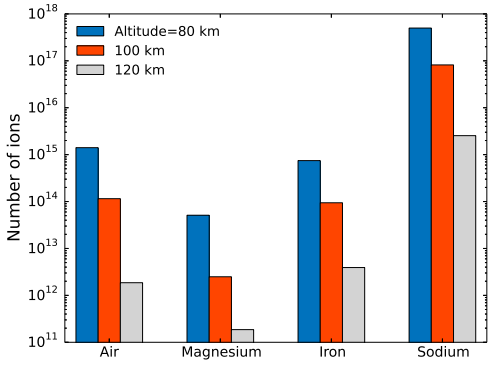

Figure 3.14.: *Number of ions generated by gas-phase collisions at different altitudes. The process is dominated by sodium. Air ions are always comparable with Mg^+ and Fe^+.*

Ionisation efficiency in the simulated domain

For each metal, we can now use the following definition

$$\beta_i = \frac{N_i^{\text{ions}}}{N_i^{\text{ions}} + N_i^{\text{neutrals}}}, \tag{3.32}$$

in order to extract the resulting equivalent efficiency of the ionisation process in the simulated domains.

Figure 3.15 shows that metals present similar ionisation coefficients at a given condition. On the other hand, efficiency is strongly dependent on the altitude. We have previously mentioned this effect in the count of the generated ions (Figure 3.14). To further investigate this, we perform nine simulations at different altitudes (80, 100, and 120 km) and flight velocities (12, 32, and 72 km/s).

Ionisation efficiencies for all the conditions are reported in Figure 3.16, along with the Knudsen number experienced by the evaporating molecules relative to the impinging jet

$$\text{Kn}_\text{r} = \sqrt{2}\frac{V_\text{t}}{V_\infty}\text{Kn}_\infty, \tag{3.33}$$

as proposed by Bronshten [1983], where V_t represents the thermal velocity of the ablated atoms leaving in equilibrium with the wall. The dependency of the ionisation efficiency on Kn_r is apparent. Flows with higher V_∞ experience

greater collisional frequencies for the same Kn_∞. In general, coefficients in Figure 3.16 appear to be much lower than those proposed by Jones [1997] with Equation 1.3. However, a direct comparison between Equation 1.3 and Figure 3.16 is not appropriate as it would require to simulate much wider domains. Independently from the degree of rarefaction, the metallic atoms may take a few mean free paths to ionise. Therefore, to obtain values that could be directly used for radio and radar observations, the collection of the electrons should be done from a domain of the order of the electromagnetic wavelength employed in the detection which, in turn, could be used to define a relevant macroscopic length for the Knudsen number.

Nonetheless, a severe discrepancy between his theoretical work and observational fits was found by Jones [1997], according to whom Equation 1.3 may be useful to interpret laboratory results in ionisation chambers at air densities higher than those of the upper atmosphere, but its use to investigate meteor observations could be improper.

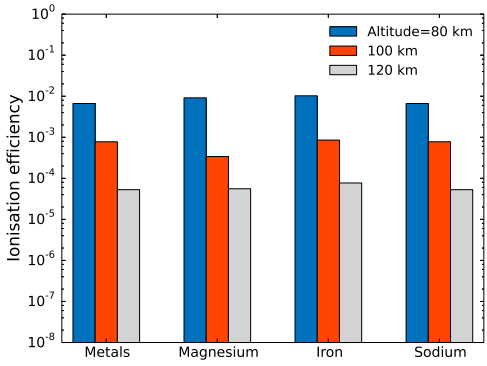

Figure 3.15.: *Global and species-specific ionisation efficiencies computed according to Equation 3.32 at different altitudes. The wall temperature is 2000 K. The resulting ionisation efficiency inside the computational domain is a strong function of the altitude.*

3.4.5. Influence of the wall temperature on the flowfield

In order to analyse the influence of the evaporation regime on the overall flowfield, we now perform a simulation for a 1 mm meteoroid flying at 32 km/s, at an altitude of 80 km, and ablating at a surface temperature of 3000 K.

Figure 3.18 shows that the ablation rate is preeminent in the outcome of the simulation. As the saturated vapour pressure varies exponentially with the wall temperature (Clausius-Clapeyron law), evaporation is much stronger at this condition and results in a region of perturbed atmosphere which is considerably wider than in the case previously studied.

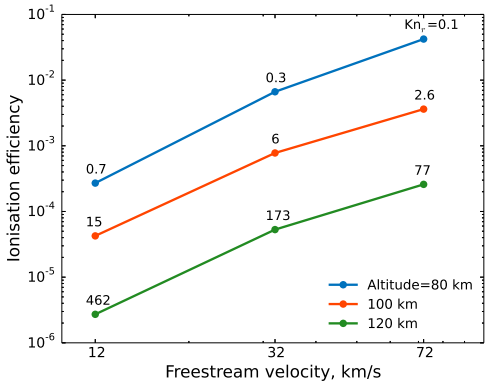

Figure 3.16.: *Global ionisation efficiencies computed inside the computational domain according to Equation 3.32, at different altitudes and freestream velocities. The wall temperature is 2000 K.*

Atomic sodium and its ion still dominate the ablated vapour, but all the other metal species are present in relevant concentrations (see Figure 3.17), except for Si which is not visible in our simulations as its saturated pressure is too low. In reality, however, the latter would be probably generated by the breaking of the bonds of SiO and SiO_2 molecules, whose dissociation reactions are not included in this work. Ion profiles plotted in Figure 3.17 present a similar behaviour in that they reach a maximum value just outside of the trail (now several diameters wide). This reinforces the idea that the ionisation process is mainly driven by the energetic collisions between the incoming air jet and the vapour.

In Figure 3.19, the excitation of the vibrational degrees of freedom of the molecules in the mixture is important (up to 6000 K) for both the situations, although for the case of intense evaporation, the region of excitation left behind by the meteoroid is much more extensive, and the vapour ablating from the sides of the body significantly contributes to the excitation process.

Similar conclusions can be drawn by analysing Figure 3.20, which shows contours for free electrons number densities. Here, electron densities reach peak values above 3×10^{20} $1/m^3$ at the stagnation point for $T_w = 3000$ K (compared to 1×10^{19} $1/m^3$ for the case of moderate evaporation), but high degrees of ionisation occur in the whole surrounding of the body, and they become remarkably significant at the sides of the meteoroid.

Finally, at this condition, the vapour relevantly screens the meteoroid from the incoming air, and this translates in low values of the heat transfer coefficient, $\Lambda \approx 0.25$.

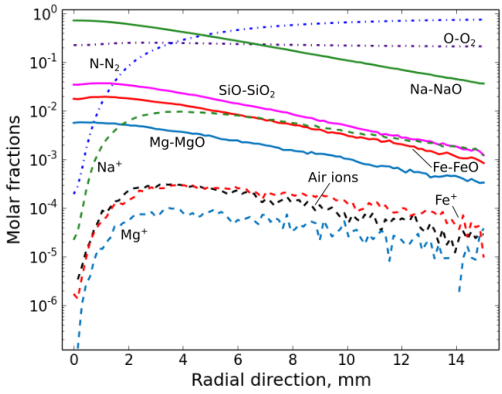

Figure 3.17.: *Concentration profiles in the radial direction in the rear of a 1 mm body flying at a speed of 32 km/s at 80 km altitude, and ablating at a surface temperature of 3000 K.*

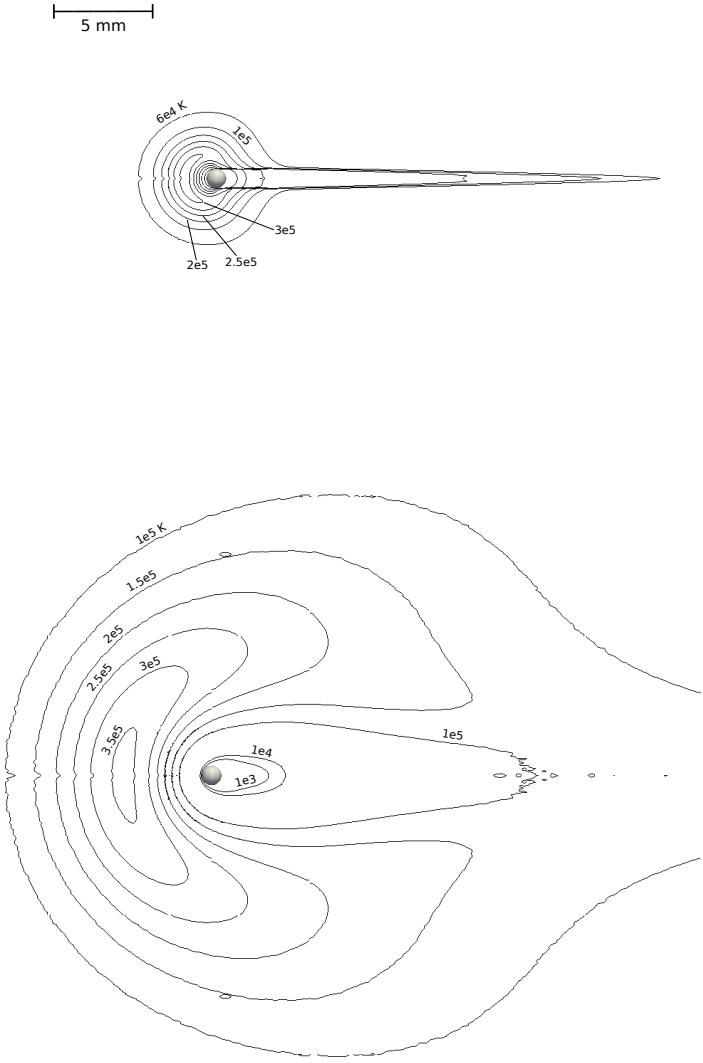

Figure 3.18.: *Translational temperature at 80 km altitude for 1 mm body flying at 32 km/s. Comparison between two different evaporation regimes,* $T_w =$ 2000 *K (upper) and 3000 K (lower). The freestream flows from left to right.*

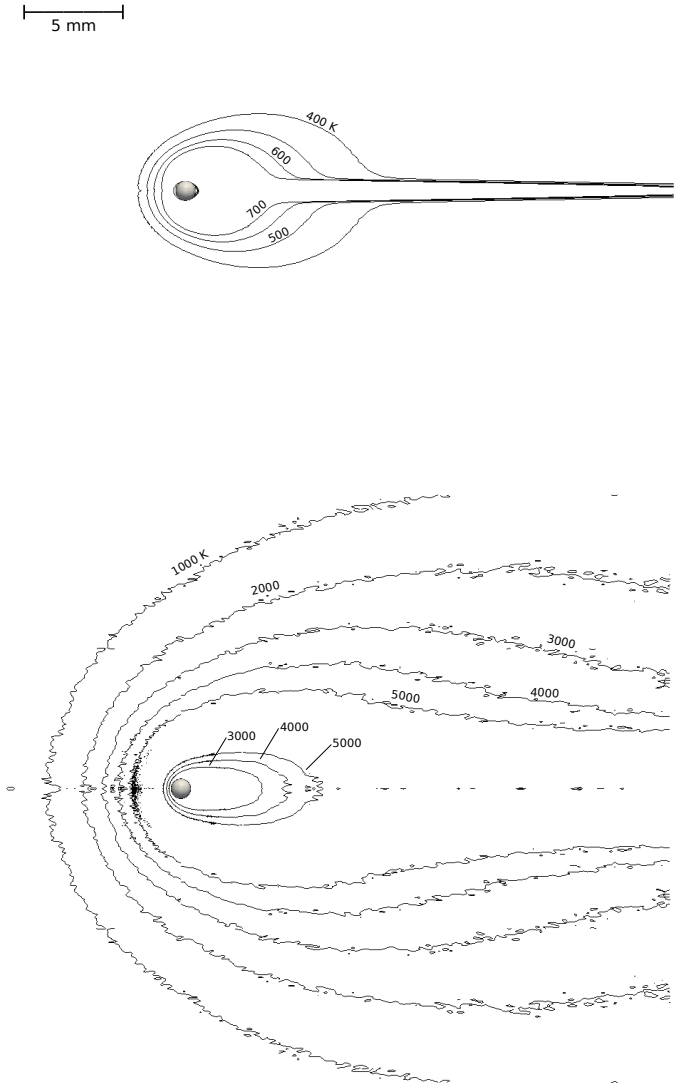

Figure 3.19.: *Vibrational temperature of the mixture at 80 km altitude for 1 mm body flying at 32 km/s. Comparison between two different evaporation regimes, $T_w = 2000$ K (upper) and 3000 K (lower). The freestream flows from left to right.*

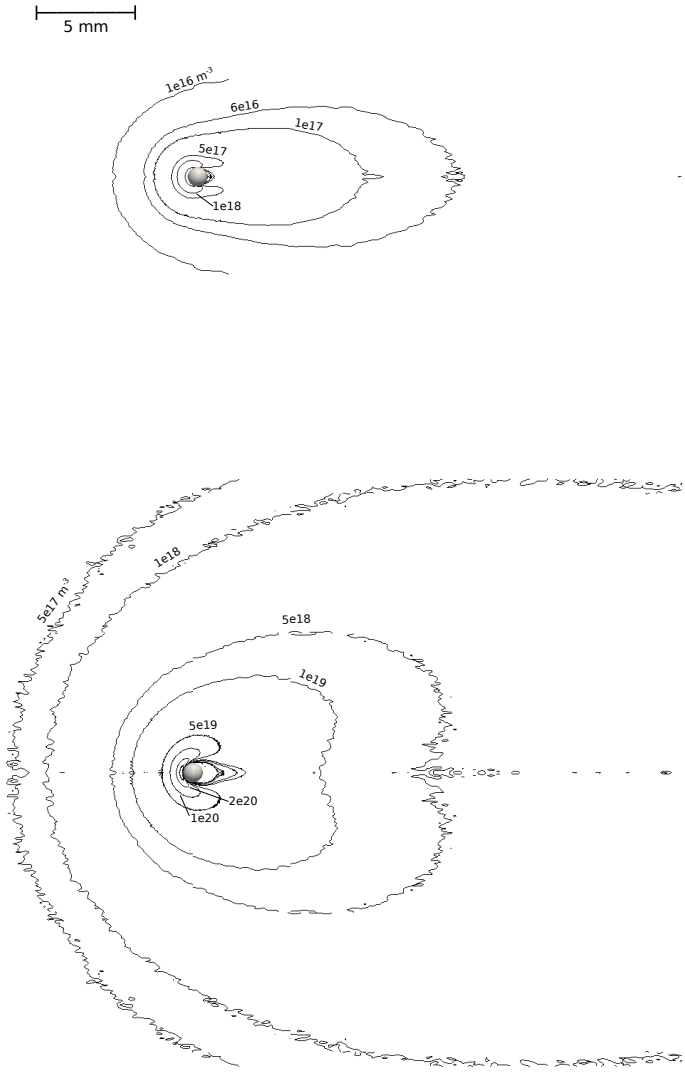

Figure 3.20.: *Electron number density at 80 km altitude for 1 mm body flying at 32 km/s. Comparison between two different evaporation regimes, $T_w = 2000$ K (upper) and 3000 K (lower). The freestream flows from left to right.*

3.5. Concluding remarks

We have used DSMC to analyse the detailed flowfield structure in the surroundings of a meteoroid at different conditions, spanning a broad spectrum of Knudsen and Mach numbers. For this purpose, an evaporation boundary condition has been employed relying on a multicomponent multiphase equilibrium solver. With respect to the usual approach, this boundary condition can take into account condensation fluxes and the backscattering of molecules at the wall. Secondly, we have computed the transport properties of the metals in the gas phase starting from Lennard-Jones potentials. This new data has enabled comparison with experimental values for viscosities and thermal conductivities available in the literature for some neutral alkali species. Moreover, DSMC inelastic cross sections have been derived based on Drawin's methodology, and a link with the classical theory on ionisation efficiencies has been provided. This set of data, comprised of elastic and inelastic cross sections, may be useful to scientists as a reference database for future theoretical and numerical studies and can be used independently of the DSMC method.

According to the preliminary trajectory analysis performed in Chapter 2, we have decided to model the flow around a 1 mm meteoroid evaporating, not far from its melting condition. A high level of thermal nonequilibrium has been measured in the head of the meteor. At higher altitudes, the vapour can travel upstream without interacting much with the incoming jet. On the other hand, the interaction between the vapour and the incoming jet is significant at 80 km, especially in the condition of intense evaporation.

The ionisation of sodium turned out to be the dominant process in the production of free electrons, and hyperthermal air-vapour collisions play the most important role in this process. The ionisation of air species, which is not considered by the classical theory of meteors, is always comparable, if not higher, to that of Mg and Fe. We have also proposed a methodology through which DSMC can be employed as a numerical experiment to provide ionisation coefficients to be used as input in synthetic models.

CHAPTER 4

Experimental Characterisation of Meteorite Ablation

"One of the greatest pains to human nature is the pain of a new idea."

– Walter Bagehot

4.1. Introduction

Meteoroids present many similarities with the Thermal Protection Systems (TPS)[1], and they can be studied taking advantage of the well established techniques in the field of heat shield characterisation. Ground experiments provide the opportunity to look at the meteor phenomenon in detail, with the possibility of focusing on the gas-surface interaction for well-defined flight conditions and material properties.

In this chapter, we present two distinct experiments, which have been performed in two different facilities: the VKI Plasmatron wind-tunnel [Bottin et al., 1999] and the NASA Ames Laser Hardened Materials Evaluation Laboratory (LHMEL) facility [Hull and Lander, 1996]. These setups are characterised by different working principles, allowing us to span a range of ablation

Parts of this chapter are the result of collaborative work and have been published in

1. B. Helber, B. Dias, F. Bariselli, L. F. Zavalan, L. Pittarello, S. Goderis, B. Soens, S. J. McKibbin, P. Claeys, T. E. Magin, **Analysis of meteoroid ablation based on plasma wind-tunnel experiments, surface characterization, and numerical simulations**, *The Astrophysical Journal*, 876(2):120-134, 2019

2. L. Pittarello, S. Goderis, B. Soens, S. J. McKibbin, G. Giuli, F. Bariselli, B. Dias, B. Helber, G. O. Lepore, F. Vanhaecke, C. Koeberl, T. E. Magin, P. Claeys, **Meteoroid atmospheric entry investigated with plasma flow experiments: Petrography and geochemistry of the recovered material**, *Icarus*, 331:170-178, 2019

[1] A TPS protects the astronauts and payload from severe heat loads to the spacecraft during its reentry.

conditions: from mild to intense evaporation; from convective- to radiative-dominated heat fluxes[2]. On the one hand, the subsonic 1.2 MW inductively-coupled plasma wind-tunnel at VKI can reproduce the aerothermodynamic environment of atmospheric entry in the boundary layer of a test object for a wide range of pressures (between 5 and 200 mbar), but relatively low heat fluxes (from 0.5 to 16 MW/m^2). On the other hand, the LHMEL laser ablation experiment guarantees high heat sources (from 40 to 160 MW/m^2 for the test campaign presented here), and it is suitable for detailed analysis of gas-surface interactions. Although a high-powered laser essentially fails in reproducing the intensively reactive plasma around the material, it provides significant radiative heat fluxes, such as those experienced by a meteoroid due to the incandescent shocked gas.

First of all, this chapter aims to yield insight into the mechanisms characterising meteoroid ablation. For this reason, experiments are followed by a multiscale analysis of the surface to gain a better understanding of the thermochemical mechanisms occurring during material degradation. Second, the experimental surface temperature data are used to build a thermal response model of the material by solving the heat conduction equation in a one-dimensional Cartesian domain. This provides a more detailed understanding of the surface energy balance and heterogeneous chemical reactions, and it allows us to test the evaporation sub-models introduced in Chapters 2 and 3.

The chapter is structured as follows. In the following section, we present a review of the literature on experimental meteorite characterisation. Section 4.3 and Section 4.4 are the core of the chapter. Section 4.3 is devoted to a description of the VKI plasma wind-tunnel experiment, while Section 4.4 deals with the analysis of the results from the NASA Ames laser ablation tests. For both of these sections, first, we present methodology, materials, and testing conditions. Second, we examine the acquired pictures, and we proceed to the chemical characterisation of the resulting materials, which highlight the main gas-surface interaction mechanisms. Finally, surface measurements are shown and discussed. These measurements are compared with simulations results obtained using a material response code. In Section 4.5, the conclusions are drawn.

4.2. Literature review on meteorite experiments

The first seminal experiments on meteorite ablation date back to the second half of the 19th century, when the French geologist and mineralogist Gabriel Auguste Daubrée tried to replicate physical features of meteorites by directing a jet of hot gas obtained from gunpowder onto millimetre-sized zinc pellets [Howarth, 2006]. However, we have to wait till the middle of the 20th century to witness the second wave of ground experiments.

[2]We have to remark that none of these two facilities can reproduce the low-pressure conditions experienced by radio meteors.

Thomas and White [1953] compared the atomic spectra of observed meteors with those obtained by ultra-speed pellets in a ballistic facility. Almost 10 years later, the interaction between a hypersonic flow and an axially symmetric ablator was investigated by Zotikov [1962] by ensuring the stagnation temperature of the flow exceeded the melting temperature of the body. The process of ablation was observed visually and photographed with a motion picture camera. Attention was paid to the shape and form of the samples after ablation. As a result, general laws of the process of body ablation were obtained, as well as quantitative data on heat transfer in the range of the parameters of the experiment.

The first experiments in an Arcjet facility at NASA Ames were performed by Shepard et al. [1967] who compared the luminous intensity of meteorite analogues, such as gabbro and basalt, with stony meteorites. The authors observed similar intensities from artificial and natural meteorites proposing the use of artificial samples to gain better knowledge of the ablation of asteroidal meteors. Using the same facility, Allen and Baldwin [1967] studied the effective density variation of potential cometary type meteors due to the frothing phenomenon, i.e. the formation of foam and small bubbles at the surface of the meteoroid.

These types of meteoroids are expected to include a high water content, which evaporates when certain conditions are reached resulting in a density anomaly. Bronshten [1983] conducted experiments on samples of stony and iron meteorites in an inductively-coupled plasma facility. After an initial stage during which the sample warms up, softens, and liquefies, the sample started to ablate. From the observations, it was possible to infer that melting and mechanical disintegration were probably dominant at altitudes lower than 100 km, with the direct vaporisation of material dominating only above 120 km. As the author admitted himself, however, it is questionable that the mentioned experiments had been able to replicate the extreme environment taking place during hypervelocity atmospheric entry, with realistic surface temperatures and heat fluxes. A series of experimental studies on ablation were also conducted by Blanchard and Cunningham [1974]. Experiments on a meteorite analogue, *olivine*, showed a similar fusion crust and oxidation level as the recovered carbonaceous chondrite meteorites. The authors pointed out that the elemental and mineralogical composition as well as the morphological and textural features must be taken into account.

More recently, three series of experiments have been performed making use of improved measurement and inspection techniques (see Table 4.1). In spring 2016, Helber et al. [2019] tested some alkali basalt samples and one H5 El Hammami meteorite sample in the VKI Plasmatron facility. The objective of this study was the characterisation of the gas-surface interaction processes occurring at the stagnation point, with focus on surface temperature measurements, spatially-resolved spectral features of the evaporating gases, visual observation of the surface, and sample recovery for a posteriori material analysis. The results of this work will be summarised in Section 4.3. In another recent work, Loehle et al. [2017b] tested an H4 chondrite and analogue samples at the Institut für Raumfahrtsysteme (IRS) with the objective of gaining a

better understanding on the ablation process and associated spectral features. Cylindrical-shaped samples were exposed to high heat flux to the point of complete disintegration. The spectra measured by Echelle spectroscopy gave a good comparison with flight data. The surface quickly reached a constant temperature at around 2400 K. In the work by Agrawal et al. [2018], the extreme entry conditions experienced by the Chelyabinsk meteorite during its entry were reproduced. Two samples of the H5 Tamdakht chondrite and one iron meteorite, all carved into spherical cone shapes, were exposed for few seconds to a plasma flow in the Arcjet Interaction Heating Facility of NASA Ames Research Center. The chondrite resisted for 2 s while the iron meteorite was completely destroyed after 2.5 s. For all samples, substantial removal of the melt by shearing effects was observed and values for the effective heat of ablation were derived leading to an improvement of the current models. However, the experimental replication of meteor entry in a clean plasma flow is a challenging procedure. For instance, the main disadvantage of Arcjet facilities is the presence of copper in the flow due to cathode erosion and degradation possibly catalysing surface reactions.

In parallel to the experiments in high-enthalpy facilities, intensive evaporation has been studied by directing a high-power laser beam towards the surface of meteorite test samples. This type of experiment is designed to reproduce the strong heating rate on the surface upon the entry of a bolide at high velocities. In Milley et al. [2007], the authors investigated the production of light during meteor ablation to better estimate the luminous efficiency. The expanding vapour was observed by CCD detectors used for meteor observations. The spectral features contained mainly neutral atoms and light production from the vapour was observed even in the absence of high-speed collisions with air constituents. The same technique was used by White and Stern [2017] at NASA Ames to study the thermo-chemical behaviour of the material when subjected to high heat fluxes. We will come back to this experiment in Section 4.4, where we will also present results from the chemical characterisation of the material recovered after the tests, and we will simulate the thermal response.

Ferus et al. [2018] developed a methodology to analyse and interpret real-time plasma spectra from meteor detections using a calibration-free method. The method was validated by comparison with laboratory experiments in which measurements, performed by using Laser-Induced Breakdown Spectroscopic (LIBS), allowed quantitative determination of elemental compositions and temperatures in Perseid and Leonid events. In the work of Bones et al. [2016], a novel facility (The Meteoric Ablation Simulator) was presented to study differential evaporation in interplanetary dust particles ($< 50\mu$m) in free molecular flow. The authors were able to produce a controlled heating rate to represent entry conditions and to measure impact ionisation coefficients for the interpretation of radio and radar observations. Gómez Martín et al. [2017] observed differential ablation effects showing that sodium is the major contributor for radio observation due to its high volatility and low ionisation energy.

Table 4.1.: *Comparison of recent meteoroid ablation test campaigns in different high-enthalpy facilities, in terms of chamber pressure p, cold-wall heat flux q_{cw}, enthalpy h_E, and configuration. References: (1) Helber et al. [2019] (Present work); (2) Loehle et al. [2017b]; (3) Agrawal et al. [2018].*

Facility	p hPa	q_{cw} MW/m^2	h_{E} MJ/kg	Configuration	Ref.
VKI Plasmatron	15-200	1-3	24-54	Stagnation point	1
IRS Arcjet	24	16	70	Cylindrical sample	2
Ames Arcjet	14	40	20	Full axisymmetric body	3

4.3. The VKI Plasmatron experiment

In this section, we present the results obtained in spring 2016, during an experimental campaign in the VKI inductively-coupled plasma wind-tunnel (Plasmatron). The experiments were performed by Dr Helber. The chemical and petrographic analysis of the virgin and recovered samples was performed by the AMGC research group led by Prof. Claeys at the Vrije Universiteit Brussel (VUB).

4.3.1. Facility, measurement techniques and methods

The experimental setup installed at the Plasmatron facility offers intrusive and non-intrusive (optical) measurement techniques. Instrumentation for the material analysis of this work consisted of a digital camera, a 2-colour pyrometer, a broadband radiometer, and three spectrometers as detailed below. During this investigation, the main data of interest comprised the surface response to the incoming air plasma in terms of temperature, mass loss, and species ejected into the boundary layer. The setup used for spectroscopy, and the collected spectroscopic data are not reported here and can be found in Helber et al. [2019].

Plasmatron facility description

The VKI Plasmatron facility has been used for the reproduction of the aerothermodynamic environment of atmospheric entry plasma flows, creating a high-enthalpy, highly dissociated subsonic gas flow [Bottin et al., 1999]. It is equipped with a 160 mm diameter Inductively Coupled Plasma (ICP) torch powered by a high-frequency, high-power, high-voltage (400 kHz, 1.2 MW, 2 kV) generator (MOS technology). The gas is heated by induction through a coil, creating a high purity plasma flow. Three probe holders are installed in the Plasmatron facility next to each other, which can be exchanged independently by a pneumatic mechanism. One holds the test sample, whilst the other two are used for heat flux and Pitot pressure measurements in the same experimental run as the ablation test. For the results presented throughout this section, the

time indication $t = 0$ s corresponds to the injection of the test sample into the plasma flow. The sample was attached to a sample holder located 445 mm downstream of the plasma jet exit. After reaching the target testing condition (testing chamber static pressure and heat flux), the sample was inserted using the pneumatic mechanism.

Experimental diagnostics and methods

A schematic of the experimental setup for in-situ ablation measurements can be found in Figure 4.1 [Helber et al., 2014, 2016], and it is reviewed below. We used a 2-colour pyrometer, employing a wide (0.75 to 1.1 µm) and narrow (0.95 to 1.1 µm) spectral band for the temperature determination at a 1 Hz acquisition rate (1300 to 3300 K). Using two narrow wavelength bands and assuming a constant emissivity over this wavelength range allows an emissivity-independent surface temperature determination. The pyrometer was pointed and focused at the stagnation area of the sample through a 1 cm thick glass window, at an angle of $\approx 35°$ with respect to the stagnation line. The instrument was calibrated up to 3300 K, which resulted in $\delta T_{\mathrm{w}} = \pm 15$ K in the observed temperature range.

A broadband infrared radiometer recorded the surface radiance in a broad spectral range ($0.6 - 39\mu$m). Assuming a test object following gray body behaviour, this instrument allows estimation of the hot wall emissivity by using the 2-colour pyrometer surface temperature as black body radiance reference and the in-band ($0.6 - 39\mu$m) radiance provided by the radiometer. For this work, the broadband radiometer was calibrated using a black body source up to 1770 K, assuming that emissivity is constant up to 10 µm. The integrated spectral radiance beyond 10 µm at this temperature only constitutes 2% of the total radiation and it is thus assumed that emission above 10 µm can be neglected.

The front surface was monitored by a 14 bit CCD camera providing snap shots throughout the experiment. Synchronised with the camera were Optical Emission Spectroscopy (OES) measurements, which consisted of three low-resolution, wide-range spectrometers, providing information of the emission spectrum upstream of the test specimen.

Full details of the instrumentation can be found in Helber et al. [2019].

Test samples

Two different samples were cut into a cylindrical shape with diameter $d = 16$ mm and length $l = 6$ mm using a commercial diamond-embedded drill bit. Each sample was embedded in a hemispherical holder of 50 mm diameter and 45 mm length made out of cork-composite ablative material (Figure 4.2). This sample holder had two main objectives: firstly, insulating the test sample from side-wall heating, allowing a one-dimensional heat conduction approach; and secondly, to provide a test shape of known geometry in order to be able to perform an extensive plasma flow characterisation by intrusive probes and numerical rebuilding. The employed cork composite material is highly insulating

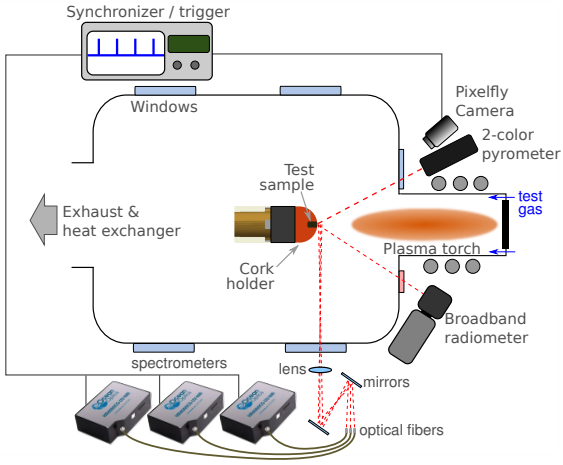

Figure 4.1.: *Schematic of the Plasmatron experimental setup (not to scale) with diagnostics for meteor ablation analysis.*

and the only source of heat delivered to the test sample can be assumed to be coming from the stagnation region. A graphite holder of the same geometry was also designed and employed in a second test campaign for which the results are presented in Pittarello et al. [2019]. The main disadvantage of the graphite configuration was a strong three-dimensional heating of the test sample due to the high thermal conductivity of graphite, making a numerical analysis of the experimental results difficult. By contrast, the main drawback of using a cork housing was the pollution of the boundary layer with cork ablation products as detected by the spectrometers. For future experiments, we suggest using a pure test sample, as done by Loehle et al. [2017b], without any additional interfaces that could contaminate the recorded data, such as a single sample in the desired test shape (e.g. hemisphere). However, meteorite samples for such destructive tests are difficult to obtain, especially of a reasonable size to be machined into the desired shape, and the strong sidewall heating in such case would make the thermal analysis more difficult compared to the one-dimensional approach we applied in this work. In addition, such a sample might be completely destroyed during the experiment because of the fast heating, hampering recovery and further analyses of the resulting material (no material remainders have been analysed in Loehle et al. [2017b]).

Two different materials were chosen as test samples: a fragment of alkali basalt (AB) serving as analogue meteoritic material; and a piece of the El Hammami H5 ordinary chondrite (OC). Their main characteristics are reported in Table 4.2. The densities were obtained by weighing the samples and assuming a perfectly cylindrical shape. Physico-chemical properties were determined by Pittarello et al. [2019] and are briefly presented below.

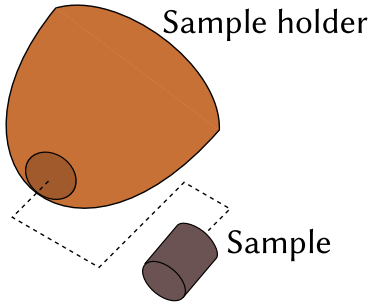

Figure 4.2.: *Schematic of the sample and its cork holder for the Plasmatron experiment. Material sample (ordinary chondrite or alkali basalt) of 16 mm diameter embedded in the sample holder in stagnation point configuration.*

Table 4.2.: *Characteristics of the two samples tested in the VKI Plasmatron facility.*

Material ID	l [mm]	d [mm]	m [g]	ρ [kg/m^3]
AB	6	16	2.74	2400
OC	6	16	3.65	3026

Alkali basalt Being a mineralogically simple material, basalt is one of the most common igneous rocks on Earth and its bulk composition roughly resembles that of chondrites and more closely matches stony achondrites. This specific sample is an alkali-basalt with approximately 50 wt. % of SiO_2. The chemical composition of the basalt was determined by the AMGC research group at VUB. They used μ-X-ray fluorescence (μ-XRF) and a Scanning Electron Microscope (SEM), coupled with Energy-Dispersive X-ray Spectroscopy (EDS). Results from this analysis are presented in Table 4.3. For details on the analytical conditions, we refer to Pittarello et al. [2019]. The semi-quantitative analysis shows a material particularly enriched in volatiles with SiO_2 and Al_2O_3 as major components, indicating a high feldspar content typical of mafic, basaltic rocks. Basalt densities commonly vary between 2700 and 3300 kg/m^3 making our sample slightly lighter (2400 kg/m^3) than average basalt. The equilibrium melting temperature of most basalts is generally in the range between 1273 and 1473 K, as average thermal conductivities vary between 1.69 and 2.11 W/m/K [Eppelbaum et al., 2014]. The specific heat of basalts is generally between 840 and 1230 J/kg/K with a heat of fusion of ≈ 500 kJ/kg [Kojitani and Akaogi, 1995].

Ordinary chondrite Ordinary chondrites represent the vast majority of all meteorites recovered on Earth. These meteorites are thought to come from a relatively small number of asteroids located in near-Earth orbits (e.g., Vernazza

et al. [2015]). They comprise a range of particle types, from fine dust-like matrix to millimetre-scale chondrules, which are solidified molten droplets after which chondrites are named. They are often considered the primary building blocks of most large solar system objects. Among these, class H ordinary chondrites have a relatively reduced chemical composition and therefore are suitable to highlight possible redox processes induced by interaction with atmospheric oxygen. The class H ordinary chondrite El Hammami (petrologic type 5) was selected. The petrologic type defines the thermal metamorphism experienced in the parent body, from 3 to 6 (or 7) for ordinary chondrites, for increasing chemical equilibration. A meteorite with a high petrologic type (5 to 6) will, therefore, exhibit homogeneous compositions for each mineral phase. The chemical characterisation of a silicate portion of the sample was performed by the AMGC research group at VUB. The results from Laser Ablation-Inductively Coupled Plasma-Mass Spectrometry (LA-ICP-MS) [Pittarello et al., 2019] are reported in Table 4.3, where the average composition of H chondrites reported by Jarosewich [1990] is also presented as a reference. In Yomogida and Matsui [1983], the authors computed bulk densities in a range between 3350 and 3690 kg/m^3 for H chondrites. In the same study, thermal conductivities were measured between 0.415 and 3.85 W/m/K. In the case of H chondrites, the specific heat range is 500 to 900 J/kg/K between 200 and 600 K [Yomogida and Matsui, 1983], while several studies show average values around 700 J/kg/K for temperatures close to 300 K [Consolmagno et al., 2013].

Table 4.3.: *Major species chemical composition before the experiments. Chemical composition was determined by means of μ-XRF for the alkali basalt (AB) and LA-ICP-MS for the ordinary chondrite (OC-silicate portion). For the latter, a reference value from literature is also provided [Jarosewich, 1990].*

Mat. ID	SiO_2	TiO_2	Al_2O_3	Na_2O	K_2O	CaO	FeO	MgO
				[wt %]				
AB	52.3	1.2	22.3	6.7	6.2	5.2	5.0	0.6
OC	50.7	0.1	1.7	1.6	0.1	2.3	15.9	26.0
OC-Ref.	36.6	0.1	2.1	0.8	-	1.7	11.9	23.1

4.3.2. Test parameters and rebuilding of flight conditions

The Local Heat Transfer Simulation (LHTS) methodology was originally developed by Kolesnikov [1993] and allows us to duplicate flight conditions at the stagnation point (reproducing the stagnation point convective heat flux), by matching the boundary layer edge total enthalpy h_E, pressure p_E, and the radial velocity gradient in radial direction at the wall β_E between ground experimental and flight conditions. Quantity β_E represents the inverse of the characteristic advection timescale at the stagnation point, and it permits to mimic flight chemical conditions in the ground test.

The subsonic Plasmatron flowfield was numerically simulated by solving the Navier-Stokes equations coupled with the Maxwell equations for the electromagnetic field created by the coil (VKI ICP code [Degrez et al., 2004, Vanden Abeele and Degrez, 2000, Magin and Degrez, 2004]). This provides the boundary layer velocity gradient β_E and boundary layer thickness, as well as an initial streamwise velocity for the characterisation of the boundary layer around the test sample under local thermodynamic equilibrium and axisymmetric flow assumptions [Barbante and Chazot, 2006]. The hydrodynamic boundary layer edge parameters (temperature T_E, density ρ_E, and velocity v_E) are determined through an iterative procedure using the VKI boundary layer code [Barbante et al., 2002], which takes as input conditions the flow quantities determined from the VKI ICP code, as well as the experimental heat flux and Pitot pressure measurements. The VKI boundary layer code consists of solving the chemically-reacting stagnation line boundary layer over a catalytic surface under chemical nonequilibrium conditions, assuming fixed wall catalytic properties for copper and a cold-wall temperature for the heat flux probe. A more detailed description of this procedure applied to ablation tests can be found in Helber et al. [2015].

We chose three test conditions, often used for TPS testing, which are characterised by a high level of confidence in terms of repeatability and flow behaviour. In addition, these experimental conditions were chosen to allow the recovery of the sample for surface characterisation analysis after the tests. The experimental conditions are listed in Table 4.4. In this chapter, we present results for Condition (1), whilst Conditions (2) and (3) are relevant for the surface characterisation presented in Pittarello et al. [2019]. Notice that the cold-wall heat flux q_{cw} was measured by means of a cylindrical calorimeter probe for Condition (1) and a hemispherical calorimeter probe for Conditions (2) and (3). The values presented in Table 4.4 are given for a hemispherical calorimeter, or its equivalent for Condition (1).

Table 4.4.: *Plasmatron test conditions. Data include experimentally measured static pressure p, generator electric power P_{el}, and mean cold-wall heat flux q_{cw}, as well as numerically rebuilt boundary layer edge values of enthalpy h_E, gas density ρ_E, gas temperature T_E, axial velocity v_E, and boundary layer gradient β_E.*

	Experimental			Numerical				
Cond. ID	p [hPa]	P_{el} [kW]	q_{cw} [MW/m^2]	h_E [MJ/kg]	ρ_E [g/m^3]	T_E [K]	v_E [m/s]	β_E [1/s]
(1)	200	206	1.2	24	7.0	6293	26	1230
(2)	220	310	3.0	42	4.3	8079	55	4480
(3)	15	373	3.1	54	0.3	9229	687	29 790

A numerical procedure was used to infer flight conditions from the experimental ones. We can write momentum and energy balances across the shock

wave that develops during flight in a continuum flow. These balances take the name of Rankine-Hugoniot jump relations and read as

$$p_\infty + \rho_\infty V_\infty^2 = p_\mathrm{E} \tag{4.1}$$

$$h_\infty + \frac{V_\infty^2}{2} = h_\mathrm{E}, \tag{4.2}$$

in approximated form. Quantities p_∞ and h_∞ represent the atmospheric pressure and enthalpy at the flight altitude, while post-shock quantities, which are denoted with subscript $_\mathrm{E}$, are equivalent to ground-test values, if we count on the LHTS assumption. By solving these relations for a thermally perfect gas, a contour map of post-shock enthalpy h_E and pressure p_E was defined for a range of freestream velocities and altitudes. An equivalent flight radius can also be computed by means of the modified Newtonian theory [Anderson, 2000]

$$R_\mathrm{fl} = \frac{1}{\beta_\mathrm{E}} \sqrt{\frac{2(p_\mathrm{E} - p_\infty)}{\rho_\mathrm{E,fl}}}, \tag{4.3}$$

where $\rho_\mathrm{E,fl}$ represents the flight boundary layer edge density obtained from Equations 4.1 and 4.2 and the perfect gas law.

The three experimental conditions are shown in Figure 4.3. For the experimental results reported here, Condition (1) corresponds to a 3.8 m diameter object ($2 \times R_\mathrm{fl}$), flying at a velocity of 6.9 km/s, at an altitude of 54.7 km. Fireball trajectories for two well-known events are also reported in Figure 4.3: one can observe that the range of velocities of the two bolides, Benešov and Chelyabinsk, are higher than our experimental conditions. For the sake of comparison, we also show the trajectory of one of the meteors detected by Jacchia and Whipple [1961] through Super-Schmidt cameras. This particular event was selected because of the low speed and altitude range, which makes this condition easier to replicate. In our experiments, we chose a lower heat flux condition than what can be assumed from existing meteor observations to avoid complete destruction of the samples and ensure successful recovery of the modified basaltic and chondritic materials. Recovery of modified experimental samples enabled us to set a further objective in this experimental campaign, which was a complete petrographic and geochemical characterisation and comparison with natural meteorite fusion crust. Future work may include testing at higher heat fluxes, reproducing smaller meteoroids at higher entry velocities.

4.3.3. Experimental results

In Table 4.5, we present an overview of the main results for both materials in terms of maximum surface temperature, test time, and total mass loss. In our tests, the basalt sample broke soon after injection into the plasma (after about 8 s), and the test run was aborted. The fracturing of the basalt can be ascribed to thermal fracturing, probably resulting from the mineral flow fabric (crystal alignment reflecting flow of the original lava before solidification) and

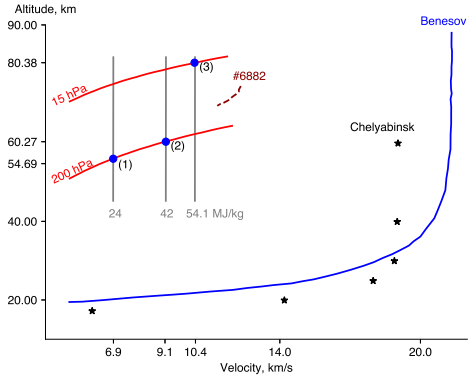

Figure 4.3.: *Duplication of the Plasmatron test conditions to flight conditions. The Benešov fireball reported by Borovička and Spurný [1996] has an estimated value at entry conditions of 2.3 m diameter body with 21.3 km/s velocity. The Chelyabinsk event is estimated to be 18 m in size, with an entry velocity of 19 km/s [Borovička et al., 2013]. The trajectory #6882 is one of the 413 photographic meteors reported by Jacchia and Whipple [1961] and Shepard et al. [1967]. The sizes of these bodies are not reported.*

strong, igneous crystalline texture. Anisotropies in the basalt result in internal stress during temperature increase, due to different thermal expansion coefficients among minerals or even preferred orientation of minerals. In contrast, the ordinary chondrite withstood the plasma flow during the entire test time of 21 s without fracturing, probably because of its predominantly granular metamorphic texture (rather than igneous). In fact, the ordinary chondrite sample only lost 3 mg during those 21 s, starting from an original weight of 3.65 g. This illustrates that, although the surface appeared to be boiling and frothing, only a little material volatilisation took place and not much mass was injected into the boundary layer, allowing the recovery of the ablated material.

Table 4.5.: *Overview of Plasmatron results for Condition (1). Data for alkali basalt (AB) and ordinary chondrite (OC) includes test sample exposure time τ, mean surface temperature T_w, total mass loss Δm, and surface emissivity ϵ. Due to the fracturing of the material, the total mass lost by the basalt sample could not be determined.*

Material ID	τ [s]	T_w [K]	Δm [mg]	ϵ [-]
AB	8	2280	n/a	0.74
OC	21	2360	3.0	0.69

Snap shots taken throughout the experiment indicate the formation of gas

bubbles on the surface shown in Figure 4.4 and Figure 4.5. The frothing appeared earlier for the basalt sample (after 2 s of plasma exposure) than for the ordinary chondrite (5 s after plasma exposure). A possible explanation for this observation may lie in the fast evaporation of the volatile elements for which the concentration is considerably higher in the basalt sample (see Table 4.3). In gases of solar composition, Na and K have 50% condensation temperatures of 958 and 1006 K respectively; for Fe this is 1334 K [Lodders, 2003]. One should note that during hypersonic flight this frothing layer can be removed by the aerodynamic forces as suggested by Allen and Baldwin [1967]. However, this aspect of the flow cannot be appreciated in the stagnation point configuration and, more in general, it cannot be taken into account by LHTS similarity rules.

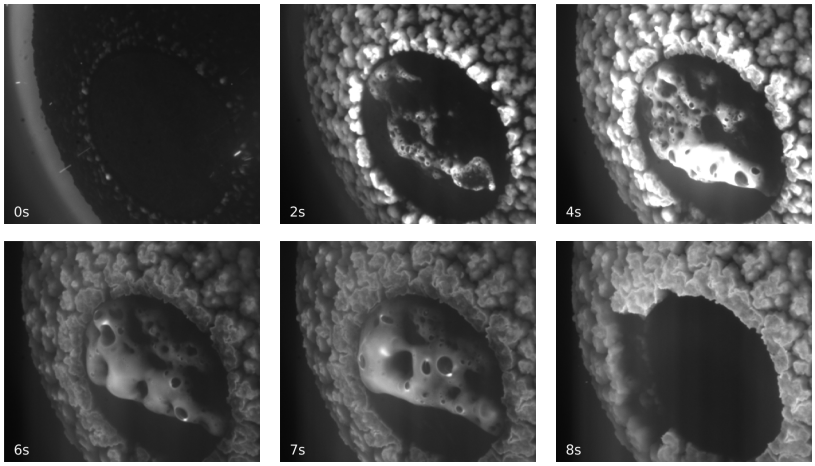

Figure 4.4.: *Snap shots (upper left to lower right) during alkali basalt test at 1.2 MW/m^2 and 200 hPa highlight boiling of the surface after 2 s (time from injection indicated in each image); the sample broke out of the sample holder after 8 s and the test was aborted.*

Photographs taken before and after each experiment are shown in Figure 4.6 and Figure 4.7. The alkali basalt had glassy features on its surface after resolidification upon cooling down. These glasses have roughly the same composition as the basalt, with apparent depletion of highly volatile elements (Na and K). The ordinary chondrite, however, displayed a reddish colour change, which probably indicates a change of the oxidation state of the high iron content with formation of *hematite* (Fe_2O_3) at the surface. Global oxidation of the sample is also suggested based on petrographic observations of the resulting material, which contains *magnetite* (Fe_3O_4) [Pittarello et al., 2019].

Surface temperature measurements

The plateau temperatures reached during these test conditions were 2280 K for the alkali basalt (Figure 4.8 (a)) and 2360 K for the ordinary chondrite

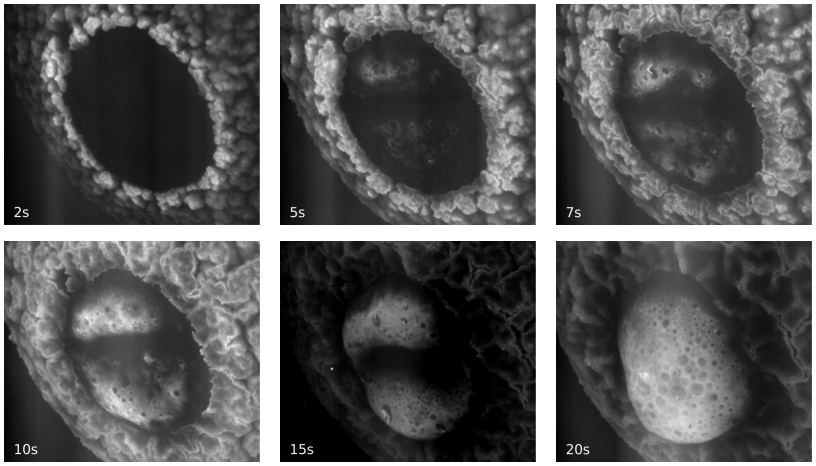

Figure 4.5.: *Snap shots (upper left to lower right) during ordinary chondrite test at 1.2 MW/m^2 and 200 hPa highlighting boiling of the surface after 5 s (time from injection indicated in each image); a melted surface state remained present throughout the remaining 15 s of the test.*

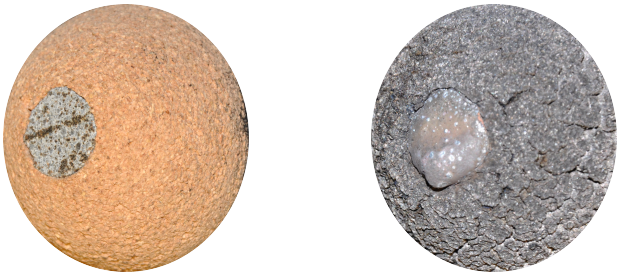

(a) *Pre-test* **(b)** *Post-test*

Figure 4.6.: *Ordinary chondrite samples before (a) and after (b) plasma exposure.*

(Figure 4.8 (b)). Although the pyrometers measuring surface areas of 11 mm diameter mostly covered the basalt and chondrite sample surfaces, some additional radiation, coming from the cork housing, may have been recorded by the pyrometer. This cork housing is likely to have resulted in a different surface temperature than the held samples, as well as in different apparent emissivities, affecting the measured temperatures to a small degree.

The delayed temperature rise of the pyrometer with respect to the radiometer in Figure 4.8 originated from a higher low-temperature limit for the pyrometer. Especially for the intact ordinary chondrite sample, the cooling curve due to surface radiation and internal conduction after the plasma was turned off can be well observed. In addition, the broadband radiometer measurement

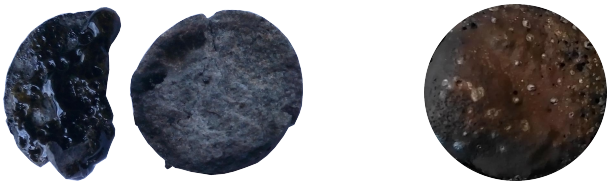

(a) *AB* **(b)** *OC*

Figure 4.7.: *Alkali basalt (a) and ordinary chondrite (b) samples after plasma exposure. In the former (a), glassy features formed after the resolidification. In the latter (b), the change of colour, probably a sign of the change in the oxidation state of iron, is visible.*

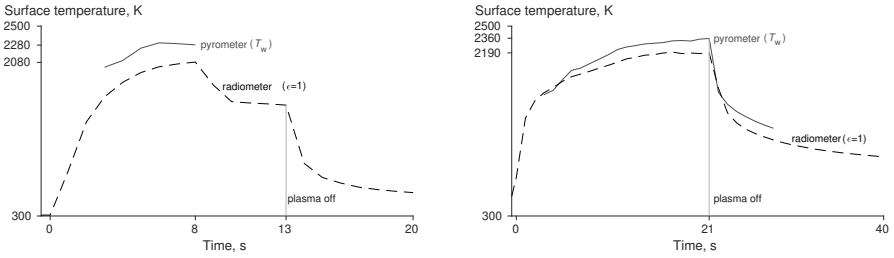

(a) *Alkali basalt (AB)* **(b)** *Ordinary chondrite (OC)*

Figure 4.8.: *Surface temperature evolution of alkali basalt (a) and ordinary chondrite (b); Radiometer measurements were recorded in a wider temperature range but for $\varepsilon = 1$ (see text); Once the plasma is switched off (AB: 13 s, OC: 21 s), the surface temperature drops immediately due to the high thermal radiation.*

served to provide an average apparent directional emissivity at those temperatures for both materials ($T^4_{\varepsilon=1,0.6-39\mu m}/T^4_{\mathrm{w}}$). This resulted in an emissivity of $\varepsilon_{0.6-39\mu m} = 0.69$ for the basalt sample and in $\varepsilon_{0.6-39\mu m} = 0.74$ for the ordinary chondrite. Those data will be used below in Section 4.3.4 for comparison to a one-dimensional numerical model.

Chemical and petrographic characterisation of the resulting material

Regarding the alkali basalt, the resulting material after the experiment mostly consisted of homogeneous glass. The chemical composition of the glass in comparison with that of the basalt before the experiment, showed apparent enrichment of the melt of Ti, Fe, and Mn and depletion of Na and K. The depletion of highly volatile alkali metals (Na and K) supports the optical emission spectroscopy measurements during the experiment. On the surface of the glass, spherical objects were observed, with an average composition rich in SiO_2, Na_2O, and K_2O, suggesting condensation from the vaporised material.

The melting of the ordinary chondrite, despite quite rapid quenching, resulted in extensive crystallisation after the experiment. A rough comparison between the bulk composition of the resulting material and the interior of the sample, unaffected by melting, showed that the melt was overall enriched in TiO, FeO, and Cr_2O_3. This apparent enrichment might result from the depletion of most volatile or moderately volatile elements. The crystallised phases are olivine and magnetite, suggesting oxidation of the Fe originally in the metal state. Detailed characterisation of the resulting material from both experiments is provided in Pittarello et al. [2019].

4.3.4. Material response modelling

The heat conduction code developed in Sections 2.2 and 2.3 is modified and tailored to study the thermal response of the OC sample in the experiment, by solving the heat conduction equation in a one-dimensional Cartesian domain

$$\frac{\partial T}{\partial t} = \frac{\lambda}{\rho c_\mathrm{p}} \frac{\partial^2 T}{\partial x^2}. \tag{4.4}$$

Numerical results are then compared with the experimental data obtained in Section 4.3.3. The choice of the one-dimensional approximation is supported by the good insulation properties of the cork holder. At the stagnation point, we applied a boundary condition constructed as a surface energy balance between the gas and the liquid phase:

$$q_\mathrm{w}^\mathrm{conv} + q_\mathrm{w}^\mathrm{chem} = \lambda \frac{\partial T}{\partial x}\bigg|_\mathrm{w} + \epsilon \sigma_\mathrm{S} (T_\mathrm{w}^4 - T_\infty^4) + \phi_\mathrm{e} L_\mathrm{e}. \tag{4.5}$$

The left hand side represents the heat due to the impinging plasma flow $q_\mathrm{w}^\mathrm{conv}$ and heterogeneous chemical reactions $q_\mathrm{w}^\mathrm{chem}$, while the right hand side comprises the energy loss due to the thermal conduction inside the material, re-radiation, and net evaporation of the surface. Concerning the physical properties, density ρ and emissivity ϵ were measured. The specific heat c_p and latent heat of vaporisation L_e were constrained to the values chosen by Vondrak et al. [2008] and Campbell-Brown et al. [2013] and are summarised in Table 4.6.

The convective contribution can be estimated by the Fay and Riddell [1958] formula:

$$q_\mathrm{w}^\mathrm{conv} = \frac{\mathrm{Nu}}{\sqrt{\mathrm{Re}}} \sqrt{\rho_\mathrm{w} \eta_\mathrm{w} \beta_\mathrm{E}} \left(\frac{h_\mathrm{E} - h_\mathrm{w}}{\mathrm{Pr}} \right), \tag{4.6}$$

where the non-dimensional parameters are the Nusselt Nu, Reynolds Re, and Prandtl Pr numbers. The Reynolds number is computed based on the equivalent radius. The subscript "w" is used to refer to the stagnation point condition at the wall, while "$_\mathrm{E}$" represents the edge of the boundary layer. More information about this approach can be found in Turchi et al. [2015]. Condition (1) reported in Table 4.4 corresponds to a cold-wall convective heat flux of 1.2 MW/m^2.

In Section 4.3.3, the change in composition of the ordinary chondrite was in-

terpreted as a possible change in the oxidation state of iron species, resulting in crystallisation from the melt of magnetite (Fe_3O_4) and of olivine richer in FeO than the original olivine. The formation of magnetite can be described using a hematite-like component (Fe_2O_3), which is diluted by FeO in the sample. Since oxidation is a strongly exothermic process, one cannot exclude the possibility of such reactions contributing to the energy balance by releasing their formation enthalpy at the wall. Genge [2016] showed, that oxidation is important for iron micrometeoroids because it proceeds faster than vaporisation. The author reports that for wüstite (FeO) dominated particles an increase in mass of up to 23% by reaction with atmospheric oxygen can occur. In this work, we consider reactions of the following type,

$$2\mathrm{FeO}_{(\mathrm{l})} + \frac{1}{2}\mathrm{O}_{2(\mathrm{g})} \rightarrow \mathrm{Fe_2O_{3(l)}} \tag{4.7}$$

and

$$\mathrm{Fe}_{(\mathrm{l})} + \frac{1}{2}\mathrm{O}_{2(\mathrm{g})} \rightarrow \mathrm{FeO}_{(\mathrm{l})}. \tag{4.8}$$

For example, the chemical heat flux related to the former reaction can be written as

$$q_{\mathrm{w}}^{\mathrm{chem}} = 2\gamma_{\mathrm{r}} p_{\mathrm{O_2}} \sqrt{\frac{\mu_{\mathrm{O_2}}}{2\pi k_{\mathrm{B}} T_{\mathrm{w}}}} \Delta h_{0,\mathrm{Fe_2O_3}} X_{\mathrm{FeO}}, \tag{4.9}$$

which is obtained by multiplying the impinging oxygen flux for the enthalpy of reaction, $\Delta h_{0,\mathrm{Fe_2O_3}}$, rescaled by the molar concentration X_{FeO} of FeO in the material. This was computed under the assumption of local thermodynamic equilibrium using the Plasmatron chamber pressure (which for this condition practically equals total pressure inside the flowfield) and test sample wall temperature T_{w}. In this formula, γ_{r} plays the role of a recombination probability for the impinging molecular oxygen at the surface and the factor 2 provides the correct stoichiometric constraint.

Now, we estimate the relative importance of the oxidation term with respect to the evaporation one in Equation 4.5. Since $\Delta h_{0,\mathrm{Fe_2O_3}} \approx L_{\mathrm{e}}$, then $q_{\mathrm{w}}^{\mathrm{chem}} = 2\phi_{\mathrm{ox}} L_{\mathrm{e}}$ and their net contribution to the global surface energy balance, $q_{\mathrm{w}}^{\mathrm{chem}} - \phi_{\mathrm{e}} L_{\mathrm{e}}$, can be written as follows:

$$2\phi_{\mathrm{ox}} L_{\mathrm{e}} - \phi_{\mathrm{e}} L_{\mathrm{e}} = \frac{1}{2} q_{\mathrm{w}}^{\mathrm{chem}} + (\phi_{\mathrm{ox}} - \phi_{\mathrm{e}}) L_{\mathrm{e}} \approx \frac{1}{2} q_{\mathrm{w}}^{\mathrm{chem}}, \tag{4.10}$$

where ϕ_{ox} is the input of the oxidation reactions to the overall mass balance. The term containing L_{e} is negligible when compared to the first one, as it is proportional to the small mass loss, $\frac{1}{\pi d^2} \frac{\Delta m}{\tau} L_{\mathrm{e}}$. This result is used as input in Equation 4.5.

In Figure 4.9, the comparison between the simulated and experimental values of the wall temperature is shown. Both measurements are presented, the emissivity-independent pyrometer measurement (blue bullets), as well as the emissivity dependent radiometer measurement (red triangles), accounting for the estimated emissivity (Section 4.3.3). This was done because the radiometer

Table 4.6.: *Physical properties assumed for the numerical modelling of the thermal response in the samples. Densities were measured by weighing the cylinders and emissivity calculated as described in Section 4.3.3.*

Material ID	ρ [kg/m^3]	λ [W/m/K]	ϵ [-]	c_p [J/kg/K]	L_e [J/kg]
AB	2400	0.7	0.69	800	6×10^6
OC	3026	3.0	0.74	1000	6×10^6

presents a wider temperature range and was able to capture the heating up of the material from room temperature, as well as the full cooling down for the ordinary chondrite test. For alkali basalt, the fracturing of the sample after 8 s did not allow us to compare the computational model to the measurements in the cooling phase of the material.

The heterogeneous exothermic reactions play an essential role in the energy balance and have a significant impact on the temperature profiles, as demonstrated by Figure 4.9, where the two simulations, with and without oxidation, are compared. Both the plateau after heating up and the cooling down are well captured with the values of recombination coefficient $\gamma_\mathrm{r} = 0.6$ ($\gamma_\mathrm{r} = 1$ being full recombination). An oxidation probability close to unity is in line with the works of Genge [2016] and Capek and Borovička [2017].

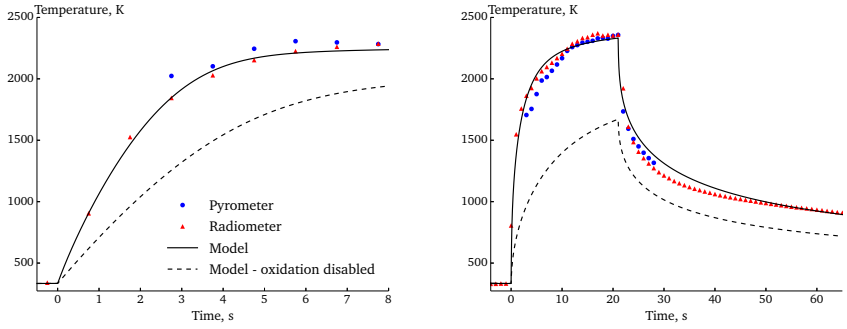

(a) *Alkali basalt (AB)* **(b)** *Ordinary chondrite (OC)*

Figure 4.9.: *Comparison of the surface temperature measurements with the numerical simulation of the thermal response of the alkali basalt (a) and ordinary chondrite (b). Exothermic heterogeneous reactions play an important role as discussed in Section 4.3.3 and have a significant impact on the simulations. We used the same parameter γ_r for modeling the basalt response as chosen for the ordinary chondrite.*

4.4. The NASA Ames laser ablation experiment

In this section, we analyse the results from a pathfinder laser ablation experiment on some meteorite samples. These experiments were designed and performed at LHMEL (NASA Ames Research Center) by White and Stern [2017] in the framework of the Asteroid Threat Assessment Project (ATAP). We examined the phenomenological aspects of the ablation process, and we modelled the thermal response of the sample, to enable comparison with the available experimental data. Also, the fusion crust was chemically characterised by means of SEM-EDS analysis and Raman spectroscopy.

4.4.1. Facility, setup and test conditions

A top-down schematic of the LHMEL setup can be seen in Figure 4.10. This is a simplified schematic, in which only the main elements of the setup are reported. In this diagram, a continuous-wave fibre laser beam (1.07 μm in wavelength) beam enters the test area from the upper left side. A small amount of the beam is siphoned off and redirected at a plate with the detector to the left. This enables real-time measurement of the actual beam power as well as the beam profile. The majority of the beam passes though and is directed at the target, labelled in the figure as "sample". From the upper right side, a wind-tunnel provides a nitrogen cross-flow stream during the test. For this pathfinder test, the cross-flow velocity was set at 1 m/s.

Also, in Figure 4.10, the locations of the high-definition cameras and the 4-colour pyrometer are visible. The pyrometer was employed to track the surface temperature evolution in time, enabling the comparison of the latter with a simple thermal response model.

On the right of Figure 4.10, a detailed picture of the sample and its holder is provided. The green spot is used to align the laser and corresponds approximately to the centre of the laser beam. To accommodate the irregular shape of the test coupons, a three point of contact spring-loaded sample holder was employed.

Test conditions

The test matrix for this experimental campaign was designed by White and Stern [2017] to achieve a range of radiative heat fluxes, which could be considered representative of flight conditions. Among all the performed tests, only a subset of them were selected and are reported in Table 4.7. Our investigation will only be focused on these conditions. As can be seen, the beam was operated at nominal powers ranging from 5 up to 20 kW, corresponding to approximate unblocked heat flux values from 46 to 157 MW/m^2, assuming a 1.1 cm laser spot diameter, and an adsorption coefficient around 0.9. All tests were carried out at ambient pressure.

Before testing the actual meteorite fragments, the exposure times were calibrated using basalt samples and tailored to ablate the sample up to half of its

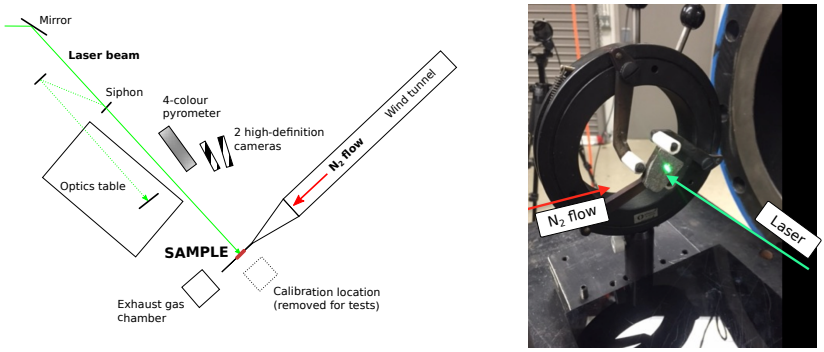

Figure 4.10.: *On the left, a schematic of the experimental setup employed for the NASA Ames laser ablation experiment. The layout shows incident laser, detectors, optics table, and wind tunnel. On the right, a picture of a Tamdakht sample in its holder. The green laser spot is the alignment beam. Credits of the NASA Ames Research Center.*

depth.

Table 4.7.: *Test matrix reporting the conditions selected from the full NASA Ames laser ablation experimental campaign.*

Cond. ID	P_{el} [kW]	q_w^{rad} [MW/m^2]	τ [s]
(1)	5	46	2.5
(2)	10	97	1.3
(3)	20	157	0.6

4.4.2. Test samples

On 20 December 2008, at 22:37 local time, the inhabitants of south-western and central Morocco witnessed an intensive long lasting fireball, descending in an almost horizontal trajectory from the west coast towards the High Atlas. The first fragments of a parent body estimated in 100 kg were found two weeks later in the vicinity of Tamdakht (Ouarzazate). The Tamdakht meteorite was found to be a class H ordinary chondrite (petrologic type 5). For a literature review on the chemical and physical properties of ordinary chondrites, the reader can refer to Section 4.3.1.

At NASA Ames, the investigators cut some of the original Tamdakht meteorite fragments into 1 cm thick slices using a diamond-edged saw blade. The flat cut surface was then ground lightly to remove any macroscopic grooves from the saw blade, as well as to try to create a uniform surface. This flat surface was exposed to the laser beam. The remaining edges were left in their original state.

Chemical characterisation of the virgin material for the Tamdakht meteorite

Some specimens of the Tamdakht meteorite were delivered to us to perform chemical characterisation and micrographs of the virgin material. This analysis was carried out at the SURF research group lab of the VUB.

We are interested in examining morphology and chemical composition of the original surface. This investigation is relevant for a proper understanding of the ablation process, and to constrain the chemical composition in the subsequent modelling phase of the thermal response. For this purpose, we employed an electron microscope coupled with EDS. EDS provides semi-quantitative chemical analysis of the investigated phases and qualitative distribution throughout the sample of selected chemical elements. In a second step, the identification of the investigated phases was performed with Raman spectroscopy, which characterises the vibrational stage of chemical bonds in the crystal lattice.

For the following analysis, no particular preparation was performed on the samples, whose surface was not polished or carbon coated to prevent charging of the surface.[3]

SEM-EDS analysis SEM produces high-resolution micrographs of the surface by scanning the sample with a narrow, high-energy beam of primary electrons. The interaction of the electrons with the atomic structure of the material leads to the elastic backscattering of primary electrons, production of secondary electrons, and photon emission from the surface. The number of electrons locally emitted by the surface is linked to its morphology, and it allows us to build up the final image. The emitted light in the form of X-rays has frequencies characteristic of the electronic structure of the excited atoms. It can be measured by EDS detectors, allowing the concentration of a particular element to be identified in a specific position and to show spatial variation of elements.

In Figure 4.11, we provide the image from the backscattered electron detector (working distance (WD) set to 16.3 mm and acceleration voltage (AV) of the electron gun set to 15 kV) which provides information related to the atomic number of the investigated phase. In particular, the higher the molecular weight, the brighter the surface appears. SEM analysis of the virgin material reveals irregular bands of a heavy species and spherical amoeboid formations. The surface is characterised by a crystalline structure and presents cracks and irregularities.

Species concentrations of the virgin material are reported in Table 4.8. EDS analysis detected Fe, Si and Mg in similar concentrations (around 15% each). Carbon fractions are also important (up to 10%). This can be attributed to contamination of the samples, occurring in the vacuum chamber upon the deposition on the surface of hydrocarbon molecules from the pumping system. Other refractory metals (Ca, Al, Ni, Cr, Mn, and Ti) were found in lower, but

[3]For example, in SEM, a conductive layer can be applied to improve the imaging of the samples.

still relevant, concentrations (in total around 3.5%). Volatile species, such as S (1.8%), Na (around 1%), and K (< 0.1%) were also detected.

Figure 4.12 shows a spatially resolved elemental map from EDS. The heavy species bands displayed in Figure 4.11 are found to be a metal iron phase. These bands are embedded in a *olivine-pyroxene* matrix. In Figure 4.12, some of the metallic bands show the presence of nickel and others of sulphur. Although EDS does not provide information on the nature of the lattice structure, the spatial correlation in these pictures may give an indication about the presence of ferronickel minerals (such as *kamacite* or *taenite*), and iron sulfide minerals, such as *troilite* (FeS). Finally, EDS highlighted similar patterns for aluminium, sodium, and calcium, elements that often bond together in rocks to form *plagioclases* minerals, i.e. $CaAl_2Si_2O_8$ and $NaAlSi_3O_8$. These speculations should be supported by further dedicated analysis.

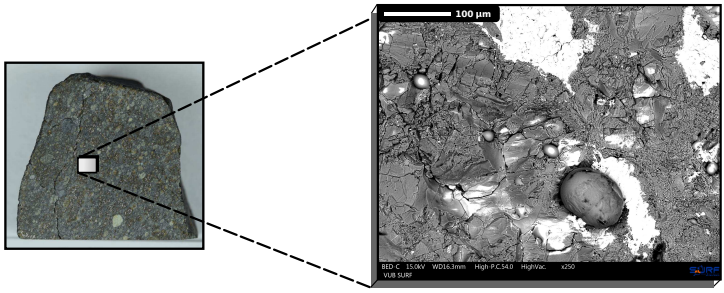

Figure 4.11.: *SEM pictures of the virgin material of the Tamdakht meteorite. The heavy species metal phase can be distinguished. On the left, we can see one of the samples before the test. Pictures are not in the same scale.*

Table 4.8.: *EDS analysis of the virgin surface on the Tamdakht meteorite. Elements sorted by melting point, from the highest to the lowest. Cr, Mn, and Ti are present as trace species (< 0.3 wt %).*

Surface region	C	Fe	Ni	Si	Ca	Al	Mg	S	Na	O
					[wt %]					
Virgin	9.9	14.4	0.8	16.0	1.2	1.2	14.4	1.8	0.9	38.7

Raman spectroscopy qualitative analysis This technique relies on the interaction of a monochromatic light beam with the lattice. In particular, the frequency of a fraction of the incident light is shifted upon the inelastic response of the molecules in the lattice. A Raman spectrum (Figure 4.13) presents a number of bands at different wavelengths, each of which corresponds to a change in colour of the scattered light. These shifts in energy are characteristic of specific

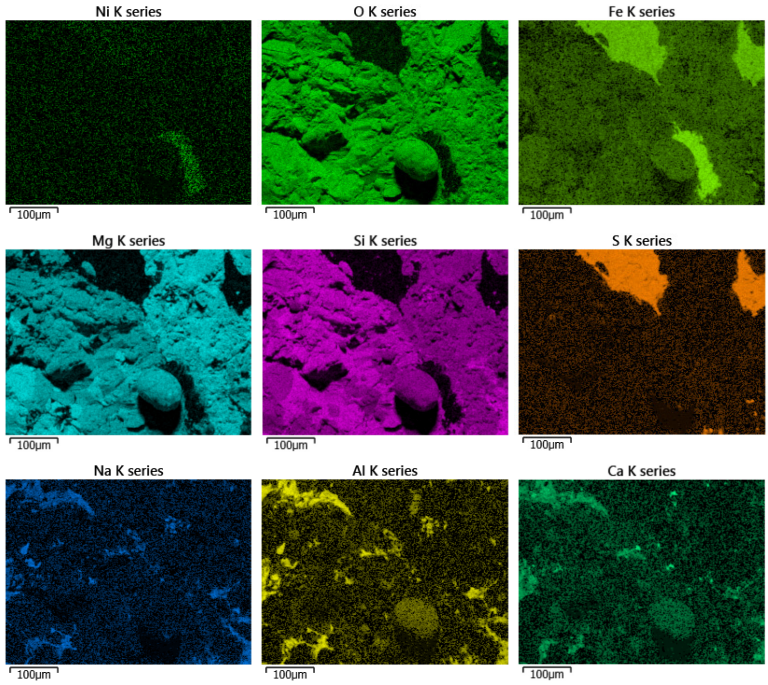

Figure 4.12.: *Elemental distribution of the virgin surface of the Tamdakht meteorite. Results obtained using EDS analysis. From the spatial correlation of the elements, we may infer the possible presence of troilite (FeS) and plagioclase minerals ($CaAl_2Si_2O_8$ and $NaAlSi_3O_8$).*

chemical bonds, therefore providing information about the mineral structure of the sample.

In order to detect specific minerals, we compared measured spectra with reference spectra from the RRUFF online database [Lafuente et al., 2015]. The shift of the peaks clearly reveals the nature of the silicate matrix: in Figure 4.13 (a), we can see the signature from olivine $(Mg, Fe)_2SiO_4$ (the spectrum of its endmember *forsterite* Mg_2SiO_4 is provided for comparison); in Figure 4.13 (b), the signature from pyroxene $(Fe, Mg)SiO_3$ is recognised. For comparison, we provide the signature of the pyroxene endmember *enstatite* ($MgSiO_3$).

4.4.3. Experimental results

In order to obtain a qualitative picture of the different mechanisms playing a role in the ablation process, we start analysing the results from the sequences obtained with the high-definition camera. In fact, going into this test campaign, an open question was whether vaporisation would dominate at the range of heating rates provided by the experiment.

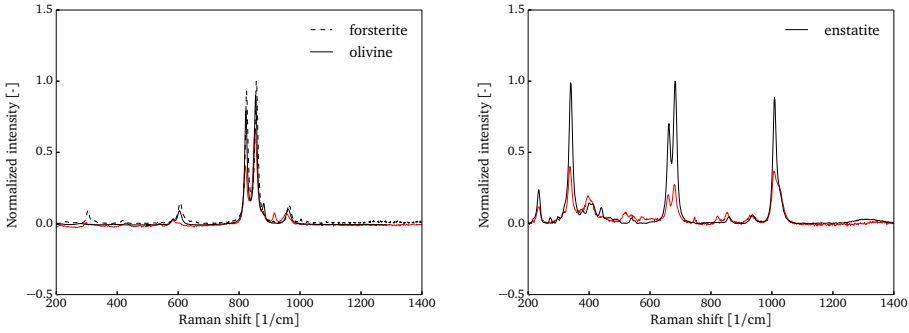

Figure 4.13.: *Raman spectra sampled from the virgin surface of the Tamdakht meteorite (measurement ——, RRUFF reference spectrum ——, - - -): (a) signature from the olivine phase; (b) signature from the pyroxene phase compared to that of enstatite.*

As soon as the laser beam hits the material, a thick and dense plume develops from the surface (Figure 4.14 - Frames 1 and 2). This process is extremely abrupt because of the fast rise of the temperature, as shown by the measurements collected by the 4-colour pyrometer and discussed later on in this section.

Contrary to the Plasmatron experiments previously presented in Section 4.3, vaporisation is the dominant process for all the tested heat sources. Nonetheless, a significant amount of liquid is observed during all the tests. For example, in Figure 4.14 (a) - Frame 4, we see liquid dripping from the exposed surface of the sample. The bright area near the bottom of the frame is a drop that is about to fall out of the field of view of the camera.

In Figure 4.15, we see ejection of droplets as consequence of the explosive boiling. The latter appears to be significant enough not to be neglected by modelling approaches.

Also, a multitude of bubbles escaping from the surface are observed (Figure 4.15), probably due to the presence of volatile elements in the matrix of the meteorite. This suggests that the vaporisation process has to be considered as a volume phenomenon rather than a surface process, as the existing modelling effort has tried to picture it.

Finally, Figure 4.16 shows pre- and post-test photographs of the Tamdakht samples. We see an opaque and homogeneous glassy coating on the post-test chondrite sample, which is typical of ordinary chondrite fusion crusts.

Surface temperature measurements

Steady-state surface temperatures are reported in Table 4.9 and are characterised by values in a range between 2900 and 3200 K. High heat source conditions resulted in surface temperatures way above the maximum temperatures

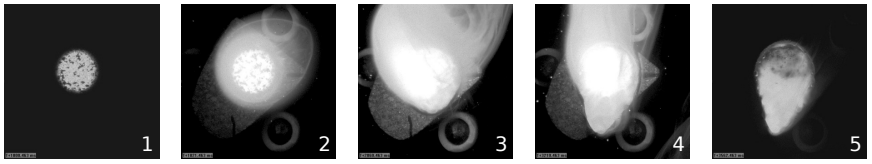

(a) $q_w^{rad} = 46\ MW/m^2$

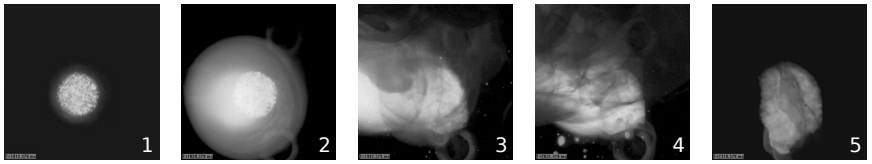

(b) $q_w^{rad} = 97\ MW/m^2$

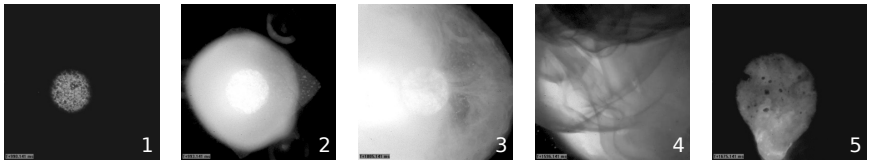

(c) $q_w^{rad} = 157\ MW/m^2$

Figure 4.14.: *Sequence of still frames caught by the high-speed camera in the laser ablation experiment for different heat source conditions. Credits of the NASA Ames Research Center.*

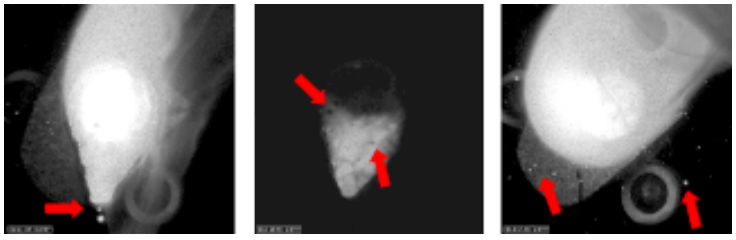

Figure 4.15.: *Details of three different ablation mechanisms in the laser ablation experiment: dripping of the molten layer (left), boiling of the liquid (centre), and ejection of droplets or particles (right). Credits of the NASA Ames Research Center.*

recorded during the Plasmatron tests (Figure 4.8). Although the variation in the imposed heat flux is significant from one condition to another, at these intense ablation regimes, evaporation acts as a dominant cooling mechanism, contributing in keeping the different plateaus in a relatively small range of temperatures. Moreover, for all conditions, the steady state at the surface was promptly reached as soon as the laser was activated (see Figure 4.22).

In Section 4.4.4, we will compare the 4-colour pyrometer evolution in time with the numerical model.

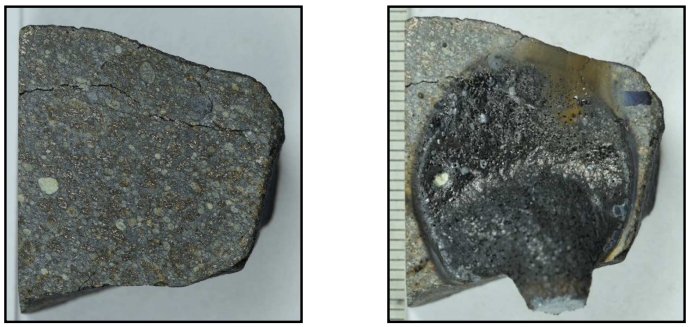

(a) (b)

Figure 4.16.: *Pre- (a) and post-test (b) samples of the Tamdakht chondrite exposed to $q_w^{rad} = 157\ MW/m^2$ laser heat flux. Credits of the NASA Ames Research Center.*

Table 4.9.: *Surface temperatures recorded in the LHMEL experiment at steady state. The plateaus are in a relatively small range of temperatures, although the difference in the imposed heat fluxes is significant from Condition (1) to (3) (from 46 to 157 MW/m^2).*

Cond. ID	q_w^{rad} [MW/m^2]	T_w [K]
(1)	46	2900-3000
(2)	97	3100-3150
(3)	157	3150-3200

Chemical characterisation of the resulting material

These measurements were carried out at the SURF research group lab of the VUB. Along the same lines of the analysis performed on the virgin material in Section 4.4.2, we investigated two regions: i) the surface of the molten crater formed by the laser beam; ii) the fusion crust along its thickness. These regions are highlighted in Figure 4.17, that shows a tomography performed at the NASA Ames Research Center of one of the ablated samples.

Samples were neither polished nor coated. Assuming contamination of the material in the chamber, carbon was excluded from quantification.

Surface analysis of the molten crater In Figure 4.18 (a, b)[4], the molten material appears with spherical inclusions spread in the silicate matrix. These inclusions were not present in the virgin material (Figures 4.11 and 4.12), they look bigger than the original metallic bands (as if they had coagulated), and much more regular in shape.

[4]Settings: (a) WD = 19.1 mm, AV = 20 kV; (b) WD = 22.5 mm, AV = 15 kV.

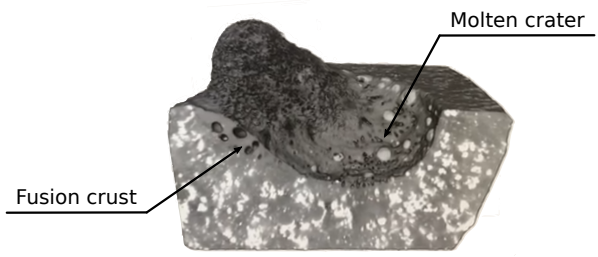

Figure 4.17.: *Topography of one of the ablated samples of the Tamdakht meteorite (cross section view). Credits of the NASA Ames Research Center.*

The silicate portion of the depression is covered by numerous vesicles of different size due to the boiling of the material. In Figure 4.18, we can also observe fractures probably formed during the cooling down and re-solidification process. These fractures travel inside the matrix until they reach a spherical inclusion, where they keep propagating along the interface between the inclusion and the matrix.

In Table 4.10, we report the quantitative analysis from EDS, where elemental concentrations for the molten surface and the comparison with the virgin material can be read. The presence of oxygen is increased from 43.2 to 53.6%, probably due to oxidation of metal iron or a change in the state of oxidation of other metal oxides. This conclusion may be also supported by a decrease in iron and silicon (from 16.1 to 12.8% and from 17.9 to 13%). On the contrary, the magnesium concentration does not change. Other refractory metals (Ni, Al, Ca, Cr, Mn, and Ti) are in lower, but still relevant, concentrations (in total 2.4%). In general, it seems that there is a decrease in the concentration of almost all the refractory elements, and an increase of sodium from 1 to 1.4%. This trend is misleading, and it can be plausibly attributed to the different WD used in the measurements of the virgin and the molten material. Different WDs were unavoidable because of the morphology of the depression. The opposite trend can be appreciated in Table 4.11, where we could sample three distinct areas over a flat region along the cross section of the specimen.

Table 4.10.: *EDS analysis of the surface of the molten crater in the Tamdakht meteorite. Comparison of elemental concentrations between virgin and molten material. Elements sorted by melting point, from the highest to the lowest. Cr, Mn, and Ti are present as trace species (< 0.3 wt %).*

Surface region	Fe	Ni	Si	Ca	Al	Mg	S	Na	O
					[wt %]				
Virgin	16.1	0.9	17.9	1.3	1.3	16.1	2.0	1.0	43.2
Molten	12.8	0.8	13.0	0.6	0.7	16.2	0.7	1.4	53.6

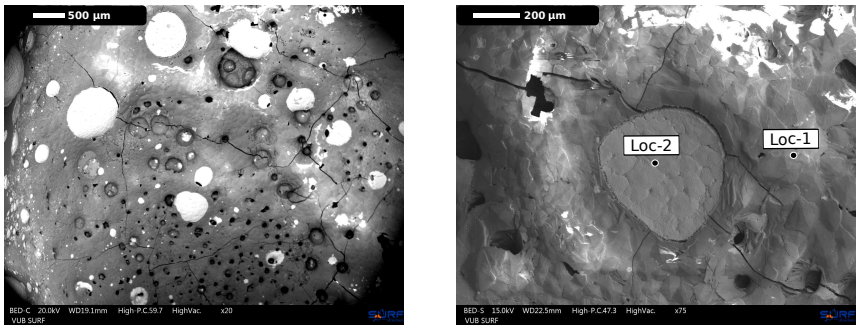

(a) (b)

Figure 4.18.: *SEM pictures of the surface of the molten crater in the Tamdakht meteorite. (a) The surface is covered by vesicles due to the boiling of the material. (b) The inclusions seem to become coagulated during the ablation process. For the correspondent elemental composition, the reader can refer to Figure 4.19.*

From the EDS elemental distributions in Figure 4.19, we can appreciate that spherical inclusions are composed mainly of iron and oxygen and in smaller parts by nickel and sulphur.

In addition, Raman spectroscopy was performed on the silicate molten matrix, at location "Loc-1" in Figure 4.18 (b). Figure 4.20 (a) presents a clear signature from the olivine phase (forsterite endmember Mg_2SiO_4 shown for comparison). Moreover, Figure 4.20 (b) reveals oxidation of metallic iron bands ("Loc-2" in Figure 4.18 (b)) with the atmospheric oxygen at ambient pressure. For comparison, we show a reference spectrum from hematite[5] (Fe_2O_3).

In-depth analysis of the fusion crust The formation of voids characterises the fusion crust due to the boiling of the material. In Figure 4.21 (a, b)[6], smaller bubbles are formed at the interface between the virgin and molten material, while bigger voids are present as we get closer to the external surface, similarly to what was obtained for OC in the Plasmatron experiment [Pittarello et al., 2019].

The elemental composition by EDS is reported in Table 4.11, and it reveals a clear depletion of the light species in the crust (S, Na, K, P), if compared with the original material (from 2.8 to 0.8%), and unchanged refractory metals (Ca, Al). On the other hand, by comparing the compositions sampled at position "Crust-A" versus "Crust-B" in Figure 4.21 (b), very little concentration gradients of the volatile species can be seen inside the solidified melt, probably mixed by intense boiling during the ablation process. Finally, as observed in

[5]Note that, in the Fe-O phase diagram, hematite is stable at high oxygen concentrations (see Genge et al. [2017]), such as those experienced by the molten meteorite at ambient pressure, but we cannot be sure of the oxidation state of iron from our qualitative analysis.

[6]Settings: (a) WD = 21.3 mm, AV = 20 kV; (b) WD = 20.1 mm, AV = 15 kV.

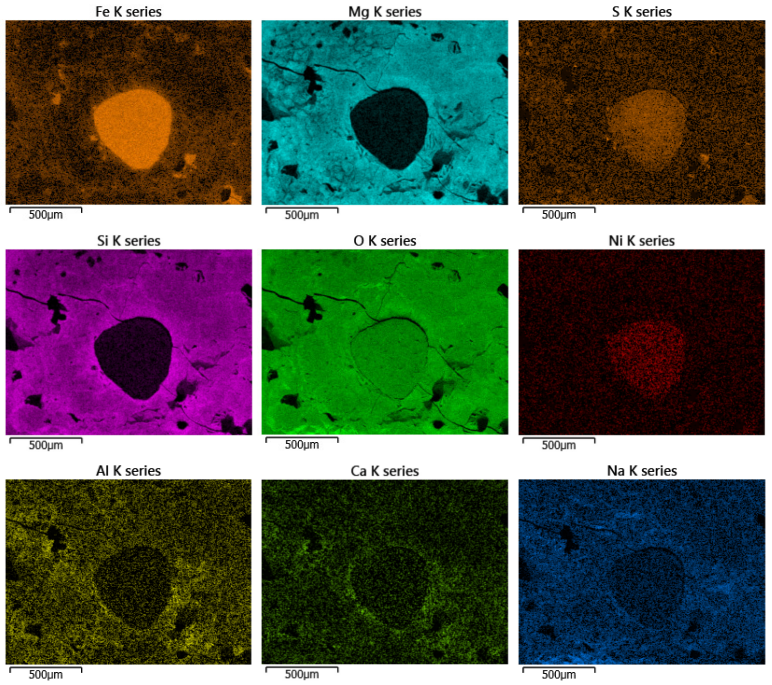

Figure 4.19.: *Elemental distribution of the surface of the molten crater in the Tamdakht meteorite. Results were obtained using EDS analysis. The oxidation of the iron metal phase is apparent.*

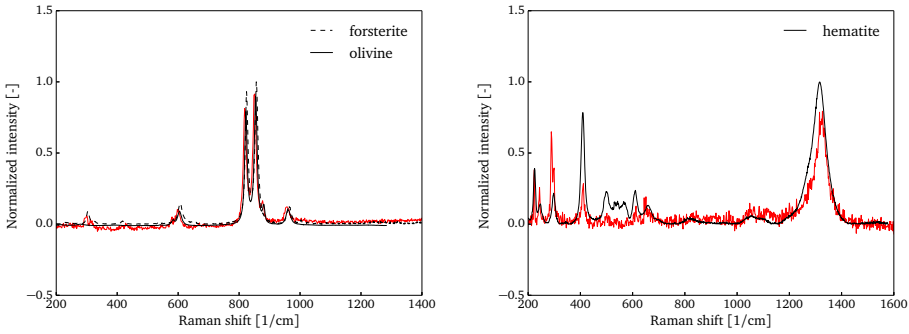

(a) **(b)**

Figure 4.20.: *Raman spectra sampled from the surface of the molten crater of the Tamdakht meteorite (measurement ——, RRUFF reference spectrum ——, - - -): (a) signature from the olivine phase; (b) signature from the oxidised iron metal phase compared to that of hematite (Fe_2O_3).*

the analysis of the surface of the molten crater, oxygen is strongly enhanced, whilst iron and silicon decrease, perhaps for a change in the oxidation state.

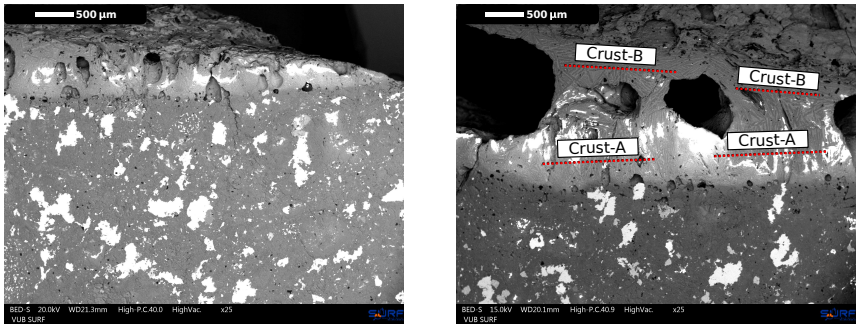

(a) **(b)**

Figure 4.21.: *SEM pictures of the fusion crust formed as a consequence of the ablation process of the Tamdakht meteorite. (a) A multitude of vesicles characterises the crust, that is placed in the upper part of the picture. (b) Lines along which the elemental composition was sampled via EDS analysis (see Table 4.11).*

Table 4.11.: *EDS analysis of the fusion crust: in-depth concentrations of chemical species. Regions "Crust-A" and "Crust-B" refer to Figure 4.21 (b). Elements sorted by melting point, from the highest to the lowest. Cr and Mn are present as trace species (< 0.3 wt %).*

Region	Fe	Ni	Si	Ca	Al	Mg	S	Na	K	P	O
						[wt %]					
Virgin	16.3	1.1	18.5	1.4	1.7	15.7	1.7	1.1	.1	.1	42.1
Crust A	8.6	<.1	15.5	1.3	1.7	16.8	0.4	0.4	<.1		55.1
Crust B	13.2	<.1	16.3	1.5	1.6	17.3	0.5	0.4	<.1		48.9

Analogies with natural fusion crusts The fusion crust obtained by laser ablation presents features that recall those of natural fusion crusts [Genge and Grady, 1999]. In particular, we could find the following similarities: i) presence of dispersed spherical vesicles; ii) high depletion of volatile elements (especially sulphur) due to evaporation and degassing; iii) increased amount of oxygen, likely due to interaction with atmospheric oxygen; iv) separation of immiscible Fe-Ni-S liquid droplets.

4.4.4. Material response modelling

This activity was performed at the NASA Ames Research Center during an internship in summer 2017. Analogously to what done in Section 4.3.4 for the Plasmatron experiment, we compute the thermal response of the ordinary chondrite samples, to enable comparison with the 4-colour pyrometer data in the three different conditions.

We modify the left-hand side of the surface energy balance in Equation 4.5, by substituting convective and chemical heat flux contributions with the nominal radiative heat flux provided by the laser beam $q_{\mathrm{w}}^{\mathrm{rad}}$. We assume an evaporation rate predicted via the Knudsen-Langmuir formula (Equation 3.7) that models vaporisation without accounting for condensation fluxes (see Section 3.2.2 for further discussion). Equilibrium vapour densities for the different species $n_{\mathrm{w}_i}^{\mathrm{eq}}$ are calculated at each timestep, in agreement with the updated surface temperature, using MAGMA code (see Section 3.2.2 for further details). Physical properties are considered equivalent to those used in Section 4.3.4, except for the density which was measured by weighing the sample. Properties are summarised in Table 4.12.

Table 4.12.: *Physical properties assumed for the numerical modelling of the thermal response of the Tamdakht meteorite. Density was measured by weighing the samples.*

ρ [kg/m^3]	λ [W/m/K]	ϵ [-]	c_{p} [J/kg/K]	L_{e} [J/kg]
3530	3.0	0.74	1000	6×10^6

In Figure 4.22, we show the comparison between the experimental surface temperature and the one computed by the simulations for Conditions (1)-(3). For all tests, the temperature is well estimated. In particular, the model obtains satisfying agreement at the steady state, and the decay in temperature, when the laser is switched off, is well predicted. It is remarkable to see such a good comparison since neither boiling nor melting removal is considered. Despite the energy losses due to mechanical removal, at these high evaporation rates, vaporisation governs the surface energy balance, where it represents the principal cooling mechanism. Here, the cooling effects provided by the Knudsen-Langmuir law (upper evaporation limit) are sufficient to justify the temperature plateaus observed. Figure 4.22 shows the evolution in time of the evaporation mass flux as predicted by the model. Finally, we should remark that the same law would overpredict the mass loss in the Plasmatron experiment, since it is not possible to accurately describe the low evaporation rates without modelling the gas phase.

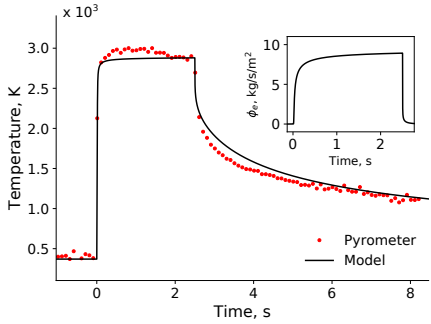

(a) $q_w^{rad} = 46\ MW/m^2$

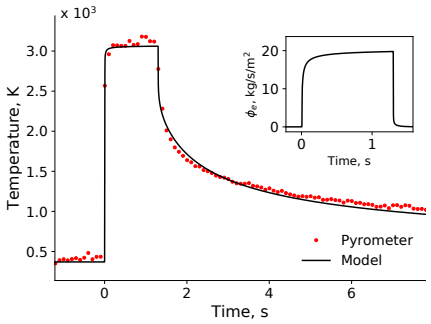

(b) $q_w^{rad} = 97\ MW/m^2$

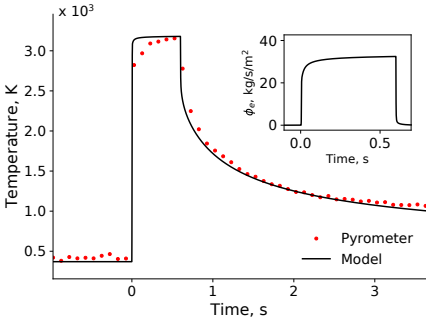

(c) $q_w^{rad} = 157\ MW/m^2$

Figure 4.22.: *Comparison of the surface temperature measurements with the numerical results in the LHMEL experiment for Conditions (1)-(3). For each condition, the evolution of the evaporation mass flux computed by the model is shown.*

4.5. Concluding remarks

We have presented the results from a couple of experiments carried out in two very diverse facilities, in order to yield insight into the ablation process for a broad range of conditions.

i) The VKI Plasmatron experiment produced convective and chemical heat fluxes coming from the interaction of a reactive air plasma with the sample, in a controlled pressure chamber. The pyrometer recorded surface temperatures between 2280 and 2360 K. At these temperatures, we did not observe a substantial mass loss of the ordinary chondrite due to evaporation or mechanical removal, although melting and boiling were evident. Frothing of the surface appeared to be more heterogeneous for the alkali basalt than for the ordinary chondrite. Also, exothermic oxidation reactions of iron may play an essential role in surface chemistry. This role was first inferred from the colour change of the OC sample after the experiment, but it was additionally supported by analysis of the recovered material. Finally, our numerical model, based on a one-dimensional heat balance, required a contribution to the chemical heat flux by iron oxidation reactions, in order to match the experimental surface temperature.

ii) The NASA Ames LHMEL setup generated an intense radiative heat source coming from a continuous-wave fiber gas laser at ambient pressure. The pyrometer measured temperature plateaus in the range between 2900 and 3200 K. Chemical analysis of the ablated material using SEM-EDS revealed a fusion crust which was depleted in volatile species and probably characterised by a change in the oxidation state of iron and silicon. Raman spectra showed hematite formation in the iron metal phase. Intense boiling resulted in voids after the re-solidification of the molten material. Finally, numerical prediction of the material response showed a good agreement with the experimental data by taking into account vaporisation into a vacuum as the primary source of cooling, without the need of including chemical oxidation in the surface energy balance.

In conclusion, these experiments confirm the contribution of boiling and iron oxidation to the ablation process, in addition to surface evaporation and melting. Fusion crusts resulting from the two experiments present similarities with those formed during atmospheric entry. Moreover, these experiments suggest that, even at high heating rates, mechanical removal of the melt phase can represent a significant mechanism of mass loss in real flight conditions. Hence, in Chapter 6, our effort to tackle this aspect of the modelling. In the never-ending discussion about the competition of vaporisation and mechanical removal in real flight conditions, we could infer that the liquid layer would be blown off as droplets, which would eventually evaporate.

CHAPTER 5

Plasma Evolution in Meteor Trails

> *"Geometry, which should only obey Physics, when united with it sometimes commands it. If it happens that the question which we wish to examine is too complicated for all the elements to be able to enter into the analytical comparison we wish to make, we separate the more inconvenient [elements], we substitute others for them, less troublesome but also less real, and we are surprised to arrive, notwithstanding a painful labour, only at a result contradicted by nature; as if after having disguised it, cut it short or altered it, a purely mechanical combination could give it back to us."*
>
> – Jean Le Rond D'Alembert (Essai d'une Nouvelle Théorie de la Résistance des Fluides)

5.1. Introduction

In this chapter, we present a self-consistent procedure in four steps to compute extensive meteor plasma trails resulting from the ablation process of meteoroid material in the rarefied segment of the entry trajectory. This procedure is a general and standalone methodology, which is able to provide meteor physical parameters at given trajectory conditions, without the need to rely on phenomenological lumped models (see the summary given in Bronshten [1983] or Ceplecha et al. [1998]). In particular, we focus our attention on the formation

Parts of this chapter have been published or are submitted for publication in

1. S. Boccelli, F. Bariselli, B. Dias, T. E. Magin, **Lagrangian diffusive reactor for detailed thermochemical computations of plasma flows**, *Plasma Sources Science and Technology*, 28(6):065002, 2019
2. F. Bariselli, S. Boccelli, A. Frezzotti, A. Hubin, T. E. Magin, **Aerothermodynamic modelling of meteor entry flows in the rarefied regime**, *2018 Joint Thermophysics and Heat Transfer Conference*, Atlanta, Georgia, USA, 2018-4180, 2018
3. F. Bariselli, S. Boccelli, B. Dias, A. Hubin, T. E. Magin, **A self-consistent method for the simulation of meteor trails with application to radio observations**, *Astronomy & Astrophysics*, 641, A100, 2020

and development of the trail generated by a 1 mm meteoroid flying at altitudes above 80 km.

We start from the DSMC solutions obtained in Chapter 3, for a domain spanning a few diameters in the nearby of the body. These solutions describe the evaporation process, the high level of nonequilibrium of the vapour in the shock layer, and the energetic collisions leading to the ionisation of air and metal species.

Second, we employ these simulations as initial conditions for performing detailed chemical and multicomponent diffusion calculations of the extended trail (up to several kilometres), to study the processes which lead to the extinction of the plasma. Specifically, we are interested in assessing the relative influence of detailed chemistry and differential diffusion in the neutralisation process. By exploiting the properties of the vapour column behind the body and the parabolised nature of the resulting hydrodynamic equations, an ad hoc diffusive Lagrangian reactor was developed by Boccelli et al. [2019]. The result is a lightweight solver able to produce detailed maps of chemicals and free electrons along the meteor trail. Our approach marches in time along the precomputed streamlines, calculating multicomponent mass diffusion in the radial direction, due to gradients in species concentration, the ambipolar electric field, and chemical reactions. For the latter, we will take advantage of the extensive knowledge that has been acquired on chemical processes of metal ions in the mesosphere and thermosphere in the last 20 years [Plane et al., 2015]. Some preliminary results on the presented methodology applied to meteor trails have been published in Bariselli et al. [2018].

Third, we retrieve the effective diffusion coefficient and the electron line density, and we compare the outcome of our computations with classical lumped model results and observational fittings.

Finally, we link the dissipation of the electrons to the reflected radio echo, so as to estimate the resulting signal in the framework of the classical underdense meteor theory [McKinley, 1961]. A schematic where we describe the procedure pursued in this work is presented in Figure 5.1.

This chapter is structured as follows. In Section 5.2, we explain the methodology. First of all, we discuss the morphology of the trail and the working assumptions. Second, we introduce the governing equations and the physicochemical models applied to the computation of the long trail. The tools employed are described in Section 5.3. Here, we also refer to the transport and kinetic data used for the calculations. In Section 5.4, we present the results, starting from the DSMC calculations in the nearby of the meteoroid, continuing with the long trail evolution. Also, we retrieve the diffusion coefficient and the electron line density. Finally, we discuss the link existing between the dissipation of the ionised products and the decay in time of the radio echo in relationship to plasma parameters.

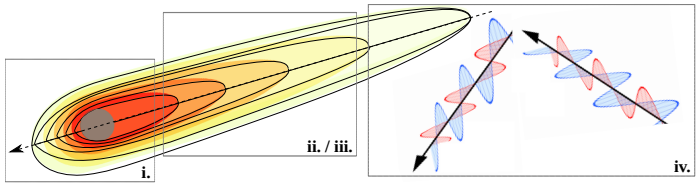

Figure 5.1.: *Schematic to describe the methodology pursued in this work. i) The expansion of the metal vapour in the background atmosphere and the consequent hyperthermal collisions are computed using the DSMC-Boltzmann method. ii) The long trail evolution is simulated by means of a Lagrangian diffusive reactor marching along the streamlines, which takes advantage of the parabolised nature of the equations. This solver accounts for ionic chemical reactions and radial diffusion. iii) The diffusion coefficient and electron line density are retrieved from the simulations. iv) The radio echo reflected by an underdense meteor is reconstructed at the receiver.*

5.2. Methodology

5.2.1. Phenomenology of the trail

The trail is composed of two regions (see Figure 5.2).

i) A near trail region, where density and velocity change considerably, and the temperature starts decreasing with respect to the hot bow-shock region. This first region, the *near trail*, is only a few to some hundred diameters long depending on the altitude and entry velocity, and it is entirely out of thermo-chemical equilibrium. This implies non-Maxwellian distribution functions for the velocity of molecules, and that the gas composition is to be found by finite rate chemistry. Its limited extent allows for the possibility of employing computationally intensive methods, such as DSMC [Boyd, 1998, Bariselli et al., 2019] or PIC [Oppenheim and Dimant, 2015, Sugar et al., 2018]. Nonetheless, due to their statistical nature, tracking minor chemical compounds with such methods could represent a crucial challenge. Therefore, one could wish to thermo-chemically refine the results obtained with these techniques a posteriori.

ii) A far trail region, where the fluid fields (density ρ_∞, velocity $\boldsymbol{v}_\infty$, and temperature T_∞) have reached freestream values. Diffusion processes in the near trail cause strong shear forces and heat exchange between the hot and high-velocity trail and the surrounding fluid at rest, such that fluid dynamic quantities soon reach equilibrium. This denotes the beginning of the *far trail*, which however remains highly out of equilibrium from the chemical point of view: in contrast with fluid quantities, chemistry is governed by collisions, which are rare in the high atmosphere. This region develops up to several kilometres (therefore, a few tenths of a second in the laboratory frame), and its evolution is governed by mass diffusion of chemical components and chemical

reactions. As opposed to the near trail, this region is too extended to be simulated by computationally intensive methods such as DSMC or PIC, and a more computationally efficient methodology must be applied.

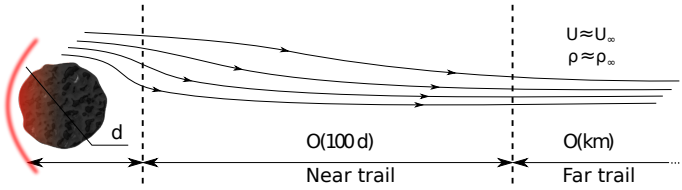

Figure 5.2.: *Regions composing the meteor trail. The near trail is only a few hundreds diameters long. The far trail has reached freestream values, but it is still in chemical nonequilibrium and can be several kilometres long. The drawing is not to scale.*

5.2.2. Working assumptions

In order to simplify the treatment of the problem, we have made a series of assumptions. We list them so that the range of validity of our simulations is clarified.

1. The body does not fragment.

2. The effect of the geomagnetic field on the diffusion process is not taken into account. However, as discussed in Section 1.3.1, the Earth magnetic field can lead to anisotropies in the transport properties [Jones, 1991, Robson, 2001, Dimant and Oppenheim, 2006].

3. Only molecular diffusion is modelled, while turbulent diffusion, whose scales are of the order of 300 m, is not included. For a numerical study of the effects of turbulence in the trail, see the work by Oppenheim and Dimant [2015].

4. We assume a two-dimensional axisymmetric configuration. Therefore, shear winds that could deform the plasma column and generate multiple reflection points are not considered [McIntosh, 1969, Hajduk et al., 1989].

5. The flow is steady.

6. Ozone concentration is kept constant. However, O_3 densities vary significantly between night and day, and this can substantially influence the decay time of the radio signal. The impact of atmospheric ozone was analysed by Baggaley and Cummack [1974].

7. Free electron temperature is considered in equilibrium with heavy species.

However, in general, the electrons cool less rapidly than the ions[1]. If the thermalisation process usually takes several tens of milliseconds for ions, according to Baggaley and Webb [1977], the electron cooling time varies from about 10^{-3} s at an altitude of 80 km to about 10^{-1} s at 115 km.

5.2.3. Governing equations

In Section 3.2.1, we have introduced Equation 3.1, the Boltzmann equation, that provides the model characterising the dynamics of dilute gases, both in and out of thermodynamic equilibrium [Ferziger and Kaper, 1972]. This equation describes the evolution in time of a probability distribution function $f_i(\boldsymbol{x}, \boldsymbol{\xi}, t)$ for species i over the velocity and physical space. Such a model holds for every rarefaction condition and constitutes a proper framework for an accurate description of the meteor phenomenon, as we have discussed in Chapter 3. The particle-based DSMC method (explained in Section 3.3) provides an accurate numerical solution to this equation [Bird, 1994].

Maxwell transfer equations

In Section 3.2.1, we have shown the link between microscopic and macroscopic variables. This link was established through Equation 3.2, by averaging microscopic quantities weighted by f_i over the velocity space $\boldsymbol{\xi}$, and summing over the species in the mixture. Similarly, by computing the moments of the Boltzmann equation, one can always write a set of species mass, momentum, and energy balances for a reacting flow at the macroscopic level [Ferziger and Kaper, 1972]. Considering one mass equation for each species and two other equations for the momentum and energy of the whole mixture, one obtains the so-called Maxwell transfer equations. At steady state these balances read as

$$\boldsymbol{\nabla} \cdot (\rho_i \boldsymbol{v}) + \boldsymbol{\nabla} \cdot (\rho_i \boldsymbol{V}_i^{\mathrm{d}}) \;=\; \dot{\omega}_i \quad i \in \mathcal{S} \tag{5.1}$$

$$\boldsymbol{\nabla} \cdot (\rho \boldsymbol{v} \otimes \boldsymbol{v}) + \boldsymbol{\nabla} \cdot \boldsymbol{\Pi} \;=\; 0 \tag{5.2}$$

$$\boldsymbol{\nabla} \cdot (\rho e \boldsymbol{v}) + \boldsymbol{\nabla} \cdot \boldsymbol{q} + \boldsymbol{\Pi} : \boldsymbol{\nabla} \boldsymbol{v} \;=\; 0. \tag{5.3}$$

where ρ_i is the density of the i-th species, $\boldsymbol{v}$ the hydrodynamic velocity, and e the mixture thermal energy per unit volume. Note that, inter-species friction and energy exchange do not appear, as these terms cancel out at the mixture level. The nonreactive collisional operator has no contribution to Equations 5.1-5.3, since the collisional invariants are in the kernel of this operator [Giovangigli, 1999]. Therefore, the right-hand side of the Boltzmann equation contributes only to the species mass conservation, through the chemical production rates

[1] This is due to the mass disparity between electrons and heavy species, that makes electron-heavy collisions less efficient in exchanging momentum and energy than likewise-particle collisions.

$\dot{\omega}_i$, resulting from the reactive collision operator $\mathcal{R}_i$ in Equation 3.1

$$\dot{\omega}_i = \int \mu_i \mathcal{R}_i \; d\boldsymbol{\xi}. \tag{5.4}$$

Equations 5.1-5.3 hold independently from the degree of nonequilibrium of the gas (i.e. collisional and collisionless regimes), as long as constitutive relations for the stress tensor

$$\boldsymbol{\Pi} = \sum_{i \in \mathcal{S}} \int \mu_i \; (\boldsymbol{\xi} - \boldsymbol{v}) \otimes (\boldsymbol{\xi} - \boldsymbol{v}) \; f_i \; d\boldsymbol{\xi}, \tag{5.5}$$

the heat flux

$$\boldsymbol{q} = \sum_{i \in \mathcal{S}} \int \frac{1}{2} \; \mu_i \; |\boldsymbol{\xi} - \boldsymbol{v}|^2 \; (\boldsymbol{\xi} - \boldsymbol{v}) \; f_i \; d\boldsymbol{\xi}, \tag{5.6}$$

and the diffusion velocities

$$\boldsymbol{V}_i^{\mathrm{d}} = \frac{1}{n_i} \int (\boldsymbol{\xi} - \boldsymbol{v}) \; f_i \; d\boldsymbol{\xi} \tag{5.7}$$

are not imposed. In the particular case of asymptotic solution, for small Knudsen numbers (small departures from translational equilibrium), one retrieves the Navier-Stokes equations [Giovangigli, 1999].

Diffusive Lagrangian reactor for parabolised equations

We can rework Equations 5.1-5.3, in order to tailor them to the solution of the flow in the trail. First, we can take advantage of a trail property: due to its elongated shape, gradients of fluid and chemical quantities are mainly directed in the radial direction. Since gradients are the main driving forces for mass and energy diffusion processes, this implies that radial diffusion dominates over streamwise diffusion, which can be disregarded.

Second, we can assume that chemistry is partially decoupled from the velocity field in the trail. The idea is that the mixture velocity and density obtained with a chemical model are not significantly influenced by the detailed chemistry of minor species, which can be added a posteriori into the problem. This thermochemical refinement approach was verified in several test cases by Boccelli et al. [2019].

Therefore, if velocity and density are given, then the set of mass and energy equations can be solved marching along such precomputed fields, with the initial species concentration and temperature picked from the beginning of the streamlines. In this sense, such precomputed fluid elements resemble a collection of variable volume chemical reactors (see Figure 5.3 for a graphical representation).

To do so, Equations 5.1-5.3 are recast into Lagrangian form. This implies reshaping the equations to allow to emerge the material derivative: $\boldsymbol{v} \cdot \boldsymbol{\nabla} \equiv V \mathrm{d}/\mathrm{d}s$, where s is the streamline curvilinear abscissa. After introducing the

mass fractions $Y_i = \rho_i/\rho$, the mass Equation 5.1 of the i-th species reads

$$\frac{\mathrm{d}Y_i}{\mathrm{d}s} = \frac{\dot{\omega}_i - \boldsymbol{\nabla}\cdot\left(\rho_i \boldsymbol{V}_i^{\mathrm{d}}\right)}{\rho V}, \tag{5.8}$$

where V is the hydrodynamic velocity module. A larger set of species with a more complete chemical mechanism is usually considered for the Lagrangian reactor.

The same procedure can be applied to the energy balance from which an equation for the temperature T is obtained

$$\frac{\mathrm{d}T}{\mathrm{d}s} = \left[\mathcal{Q} - \frac{1}{2}\frac{\mathrm{d}V^2}{\mathrm{d}s} - \sum_{i\in\mathcal{S}} h_i \frac{\mathrm{d}Y_i}{\mathrm{d}s}\right] \Big/ \left[\sum_{i\in\mathcal{S}} Y_i c_{\mathrm{p}_i}\right], \tag{5.9}$$

where h is the enthalpy, c_{p} the specific heat, and $\mathcal{Q}$ the variation of total enthalpy along the streamline which can be expressed, neglecting viscous stresses, as $\mathcal{Q} = -\boldsymbol{\nabla}\cdot\boldsymbol{q}/\rho V$, and it will be detailed later on.

Note that since the velocity is given, there is no need to solve for the momentum Equation 5.2. Besides, since the density comes directly from the velocity field through the mass equation, solving for the global mass equation is not necessary, and it is sufficient to import the assigned density.

Finally, once the density, velocity, and temperature fields have relaxed to freestream conditions (ρ_∞, $\boldsymbol{v}_\infty$, T_∞) in the far trail, the mass balances (Equation 5.8) are the main actors driving the trail evolution through radial gradients in the chemical concentrations. The importance of the energy balance (Equation 5.9) is marginal as the temperature is nearly uniform. The weight of this equation in the far trail lies in the diffusion of the energy produced or absorbed by chemical reactions.

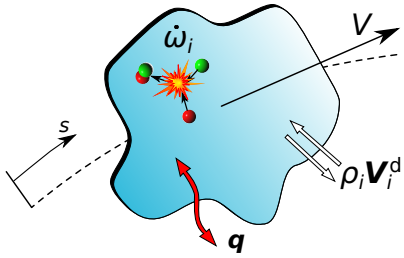

Figure 5.3.: *Cartoon of a Lagrangian fluid reactor marching along precomputed streamlines. Species concentrations and energy can evolve inside the reactor because of chemical processes and radial diffusion exchange among different fluid elements.*

5.2.4. Physico-chemical models

Thermodynamics

Equation 5.9 requires the evaluation of the species enthalpy h_i. Thermodynamic properties can be obtained by means of statistical mechanics, assuming that the energy modes follow a Maxwell-Boltzmann distribution at temperature T [Anderson, 2000].

At temperatures close to freestream values, such as the one characterising the far trail, only the contribution of the translational and rotational degrees of freedom of the molecules shall be considered, as the vibrational and electronic modes are not excited[2]. Moreover, for a chemically reacting flow, the input of the formation enthalpy h_0 should also be accounted for. Quantity h_i for the i-th species reads as follows

$$h_i = c_{\mathrm{p}_i} T + h_{0_i}, \tag{5.10}$$

where $c_{\mathrm{p}_i} = \frac{5}{2}\frac{k_\mathrm{B}}{\mu_i}$ for atoms and free electrons and $\frac{7}{2}\frac{k_\mathrm{B}}{\mu_i}$ for linear molecules, k_B and μ_i being respectively the Boltzmann constant and the mass of the species.

Hydrodynamic closure for mass and energy diffusion fluxes

Despite the high degree of rarefaction, the flow eventually thermalises as the trail develops. This aspect has been studied by different authors [Baggaley and Webb, 1977, Boyd, 1998, Bariselli et al., 2018]. This property allows us to employ near-equilibrium diffusion models based on gradients of thermodynamic quantities, such as the Fourier law and hydrodynamic mass diffusion.

For the quasi-Maxwellian trail, the expressions of the diffusive fluxes $\rho_i \boldsymbol{V}_i^\mathrm{d}$ and $\boldsymbol{q}$ can be obtained from the Chapman-Enskog theory [Giovangigli, 1999]. Diffusion velocities are written as a linear combination of the gradients of species concentration X_i, through the *multicomponent diffusion matrix* D_{ij}

$$\boldsymbol{V}_i^\mathrm{d} = -\sum_{j\in\mathcal{S}} D_{ij}\left[\boldsymbol{\nabla} X_j - \frac{X_j q_j}{k_\mathrm{B} T}\boldsymbol{E}\right] \quad i \in \mathcal{S}, \tag{5.11}$$

where the a priori unknown ambipolar electric field $\boldsymbol{E}$ acts as a restoring force to charge neutrality, and it is obtained by constraining the net electric current to zero

$$\sum_{i\in\mathcal{S}} n_i \boldsymbol{V}_i^\mathrm{d} q_i \;=\; 0, \tag{5.12}$$

q_i being the charge and n_i the number density of the i-th species[3]. Thermal and barodiffusion effects are neglected in this work. Heat fluxes include conduction,

[2] One may argue that the light emission of the trail is the proof that the vibrational and electronic degrees of freedom are excited. In fact, we are assuming that internal energy excitation and nonequilibrium is only significant in the near trail.

[3] Note that in this general formulation, the effects of the ambipolar electric field do not rely on the definition of an ambipolar diffusion coefficient. The ambipolar electric field can be

modelled with Fourier's law, and diffusion of enthalpy

$$\boldsymbol{q} = -\lambda \boldsymbol{\nabla} T + \sum_{i \in \mathcal{S}} \rho_i h_i \boldsymbol{V}_i^{\mathrm{d}}, \tag{5.14}$$

where the temperature gradients $\boldsymbol{\nabla} T$ and the heat conduction coefficient λ appear. Diffusion velocities transport the species enthalpy h_i.

Finally, the transport coefficients D_{ij} and λ, which appear in Equations 5.11 and 5.14, require the evaluation of the *collision integrals* resulting from the Chapman-Enskog solution procedure [Giovangigli, 1999]. These integrals link interatomic forces at the microscopic level to transport properties at the macroscopic scale. The choice of the potential depends on the nature of the interaction between two species in a given mixture [Capitelli et al., 2000, Bruno et al., 2010, Levin and Wright, 2004], as will be detailed in Section 5.3.

Chemical kinetics

Metal atoms, M, are produced during ablation, and they ionise as a result of the highly energetic collisions with the atmospheric molecules of the incoming stream [Dressler and Murad, 2001]. The chemical evolution of these ions influences the radio signal decay, at timescales which can be comparable with those of the diffusion process. In particular, the formation of metal oxide ions (MO^+ and MO_2^+) and clusters ($\mathrm{M}^+ \cdot \mathrm{N}_2$), by means of exchange reactions with the background atmosphere, regulate the free electron densities as they are efficiently depleted by fast dissociative recombination reactions [Plane et al., 2015].

If we consider a system of elementary reactions $r \in \mathcal{R}$, we can write

$$\sum_{i \in \mathcal{S}} \nu_{ir}^{'} \mathrm{X}_i \rightleftharpoons \sum_{i \in \mathcal{S}} \nu_{ir}^{''} \mathrm{X}_i, \tag{5.15}$$

where X_i is the chemical symbol for species $i \in \mathcal{S}$, and $\nu_{ir}^{'}$ and $\nu_{ir}^{''}$, the forward and backward stoichiometric coefficients for species i in reaction r. Then, the mass production rate for the i-th chemical component, $\dot{\omega}_i$, can be expressed through the *law of mass action* [Giovangigli, 1999], as follows

$$\dot{\omega}_i = M_i \sum_{r \in \mathcal{R}} \nu_{ir} \left[k_{\mathrm{f}} \prod_{i \in \mathcal{S}} \left(\frac{\rho_i}{M_i} \right)^{\nu_{ir}^{'}} - k_{\mathrm{b}} \prod_{i \in \mathcal{S}} \left(\frac{\rho_i}{M_i} \right)^{\nu_{ir}^{''}} \right], \tag{5.16}$$

where $\nu_{ir} = \nu_{ir}^{''} - \nu_{ir}^{'}$ and symbol M_i stands for the species molar mass. The

promptly evaluated a posteriori in the form

$$\boldsymbol{E}_{\mathrm{a}} = \frac{\sum_{i \in \mathcal{S}} X_i q_i \sum_{j \in \mathcal{S}} D_{ij} \boldsymbol{\nabla} X_j}{\sum_{i \in \mathcal{S}} X_i q_i \sum_{j \in \mathcal{S}} D_{ij} \frac{X_j q_j}{k_{\mathrm{B}} T}}, \tag{5.13}$$

by imposing zero net electric current. The multicomponent ambipolar matrix is retrieved by substituting the obtained electric field in Equation 5.11.

forward rate coefficients in Arrhenius form reads as

$$k_{\mathrm{f}}(T) = C_4 T^{C_5} \exp\left\{ -\frac{E_0}{k_{\mathrm{B}} T} \right\}, \tag{5.17}$$

in which the rate constants C_4, C_5, and E_0 are usually determined experimentally. Backward rates, k_{b}, are computed from *detailed balance*, starting from the available forward rate coefficients and equilibrium constants based on thermodynamic properties.

5.2.5. An additional note on the Lagrangian reactor

The Lagrangian reactor procedure that we have just introduced can be used for both the near and the far trail. In the first case, velocity and density fields are taken from a *baseline simulation*, to refine the chemical evolution of the ablated vapour by adding more detailed processes. In this region, exchange reactions leading to the formation of metal oxide ions and clusters may start playing a role already [Dressler and Murad, 2001], and an accurate description of the chemical mechanism would require a large number of species to be described, most of which are present only as traces. Chemical traces constitute a formidable challenge to DSMC and PIC simulations, as minor species suffer from very large statistical scatter [Hadjiconstantinou et al., 2003]. The approach of refining a DSMC baseline simulation, introducing detailed chemistry a posteriori, in the hypothesis that this will influence the flowfield only marginally, has shown to provide reliable results in the past [Boccelli et al., 2019], where a near trail DSMC computation was used as a baseline solution, and its chemistry was refined by the Lagrangian reactor method.

Regarding the far trail, velocity and density fields are constant and uniform as they have attained freestream values. Therefore, the streamlines do not vary any more and can be arbitrarily extended up to any length of interest, and these can be used as an input to the diffusive Lagrangian reactor.

In this work, we present results concerning the far trail only. We perform a DSMC simulation of the near trail, and the conditions at the end of the domain will be used as initial conditions for the Lagrangian reactor computation.

5.3. Numerical tools and dataset

5.3.1. The LARSEN code

At every position along the trail, Equations 5.8 and 5.9 are discretised radially using a finite volumes scheme [Boccelli et al., 2019] (see Figure 5.4). Therefore, at a given timestep, gradients of species concentration and temperature are evaluated. Note that, as each streamline can have different velocity, synchronisation would quickly be lost during the integration, posing an issue to the evaluation of transverse diffusion terms. In order to circumvent this problem, the streamwise derivatives $\mathrm{d}/\mathrm{d}s_k$ along each streamline k are converted

into derivatives along the symmetry axis x, by taking into account the local streamline slope θ_k

$$\mathrm{d}x = \cos\theta_k \, \mathrm{d}s_k \quad \Longrightarrow \quad \frac{\mathrm{d}}{\mathrm{d}x} = \frac{1}{\cos\theta_k} \frac{\mathrm{d}}{\mathrm{d}s_k}. \tag{5.18}$$

Once the radial discretisation is performed, the problem has become a system of ODEs in the only variable x, which is integrated using Rosenbrock-4 or Runge-Kutta schemes. Error estimation in the integrator allows the employment of an adaptive step.

The computational cost scales with the number of streamlines considered and depends on the number of species employed, the stiffness of the chemical mechanism, and the characteristic timescales for mass and energy diffusion processes. Overall, the Lagrangian procedure is highly efficient if compared to the DSMC computation of a trail. Typical simulation time for a 1 km trail is of the order of 20 minutes on a single-core laptop, while it would easily exceed a few weeks of computation time on several cores for the DSMC method.

A version of the LAgrangian Reactor for StrEams in Nonequilibrium (LARSEN) code, implemented by S. Boccelli during his MSc thesis at VKI, is freely available at `https://github.com/broderspp/brODErspp`, and more recent versions are available upon request to the authors.

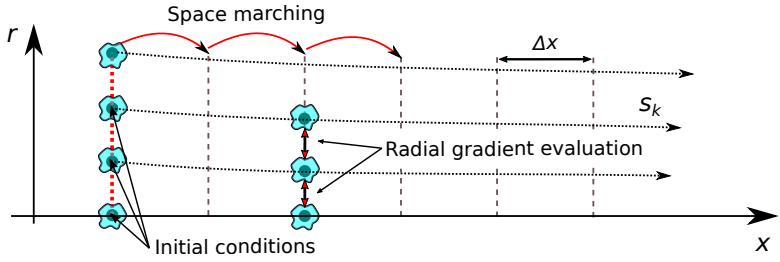

Figure 5.4.: *Schematic of the LARSEN numerical procedure along multiple streamlines.*

5.3.2. The MUTATION++ library

The MUTATION++ library (MUlticomponent Thermodynamic And Transport Properties for IoNized plasmas) was developed at VKI by Scoggins and Magin [2014] and provides thermodynamic, transport, and kinetic models and data to the LARSEN code for the closure of Equations 5.8 and 5.9. This library is available online at `https://github.com/mutationpp/Mutationpp`.

The library computes the diffusion velocities and the ambipolar electric field by solving the Stefan-Maxwell system [Magin and Degrez, 2004]. Transport coefficients for neutral-neutral interactions are derived according to Lennard-Jones (12-6) data available in Svehla [1962], McGee et al. [1998] and Capitelli et al. [2000]. Combination rules for those polyatomic species [André et al.,

2010], whose potential parameters are not available in the literature, are used. We employ the screened Coulomb (Debye-Hückel) potential shielded at the Debye length for charged-charged collisions. In terms of data, the evaluation of this potential only requires the mass and charge of the colliding species. Concerning ion-neutral interactions, a combination of the Tang-Toennies potential and the Langevin polarisation potential is used, respectively for air-air and metal-air collisions. In particular, air-air collision integrals are taken from the work of Levin and Wright [2004], whereas metal-air collisions are based on the Langevin potential, which necessitates polarisability parameters of the neutral species and the mass of the ion.

Finally, we employ the forward rate coefficients given by Park [1993] and Park et al. [2001] (see Appendix B) for air reactions and the one from Plane et al. [2015] for the thermalised chemical kinetics of metals. A brief review of the latter is given below.

Chemical mechanism for the neutralising trail

The chemistry in the thermalised trail has been widely studied, and the recombination of the metal ions is relatively well understood [Baggaley and Cummack, 1974, Baggaley, 1978]. The interested reader can consult the comprehensive review by Plane et al. [2015] on the topic, where both theoretical and experimental works are reported.

The ablated vapour of an ordinary chondrite mostly comprises iron, magnesium, sodium, and silicon species. In particular, an essential contribution to the production of ions is given by Na, because of its volatile nature and low ionisation potential. Species such as SiO_2 and SiO are present in relevant concentrations, contrary to atomic Si, which is characterised by low vapour pressures. For this reason, Si ionisation and its consequential chemical neutralisation will not be considered here.

Magnesium and iron (M = Mg, Fe) oxide ions are formed by means of charge exchange processes with the atmospheric ozone

$$\mathrm{M^+ + O_3 \rightarrow MO^+ + O_2}, \tag{5.19}$$

or, below 80 km, by three-body processes in two steps, such as

$$\mathrm{M^+ + 2O_2 \rightarrow MO_2^+ + O_2} \tag{5.20}$$

and

$$\mathrm{MO_2^+ + O \rightarrow MO^+ + O_2}. \tag{5.21}$$

The resulting oxide ion is efficiently depleted by the fast dissociative recombination reaction

$$\mathrm{MO^+ + e^- \rightarrow M + O}, \tag{5.22}$$

or, in the case of the iron dioxide ion, by

$$\mathrm{FeO_2^+ + e^- \rightarrow Fe + O_2}. \tag{5.23}$$

Furthermore, metal clusters can be created by reactions of the following type

$$M^+ + 2N_2 \rightarrow M^+ \cdot N_2 + N_2, \tag{5.24}$$

where the atmospheric nitrogen plays the role of third-body in the reaction. Magnesium clusters can recombine through dissociation, similarly to Reaction 5.22 or, in the case of iron, they recycle back to FeO^+.

The neutralisation process of sodium is different from the one of Mg and Fe. Na^+ has a complete outer electron configuration and can only form a cluster with N_2 in a three-body process of this type

$$Na^+ + 2N_2 \rightarrow Na \cdot N_2^+ + N_2 \tag{5.25}$$

with subsequent recombination

$$Na \cdot N_2^+ + e^- \rightarrow Na + N_2. \tag{5.26}$$

The reaction rates included in the chemical mechanism are reported in Table 5.1.

5.4. Results and discussion

We choose one of the conditions examined in Chapter 3, by considering a 1 mm diameter meteoroid, flying at 32 km/s, and evaporating at a surface temperature equal to 2000 K. We examine two detection points, one at $H = 80$ km and the other at 100 km, which represent typical values for radio detection of meteors. For the presented cases, Kn_r based on Equation 3.33 is between the value of 6 at the altitude of 100 km and the value of 0.3 at the altitude of 80 km, these conditions belonging to the transitional regime. Freestream densities, compositions, and temperatures are an input to our model, and computed according to the Naval Research Laboratory Mass Spectrometer Incoherent Scatter Radar (NRLMSISE-00) empirical atmospheric model developed by Picone et al. [2002] and are reported in Table 5.2, whereas abundances for ozone gas are roughly estimated according to values reported by Baggaley and Cummack [1974]. An ordinary chondrite is assumed, for which we assume the following prototypical mass concentrations: 36% SiO_2, 25% MgO, 38% FeO, and 1% Na_2O.

5.4.1. Chemical kinetics of metals in an isothermal reactor

We start investigating the chemical mechanism presented in Section 5.3.2, by studying the evolution of the species of meteoric origin independent from the diffusion process, as if the gas was constrained in an isothermal reactor. Freestream values of density and temperature from Table 5.2 are employed to set the conditions of the reactor, and the atmospheric background species are kept constant in time. As an initial condition, we consider a quasi-neutral mixture of a metal vapour diluted in air, in which the molar fractions are arbitrarily

Table 5.1.: *Reaction rates included in the chemical mechanism for the neutralising trail. Forward rates, k_f, are computed according to Equation 5.17. Backward rates, k_b, are computed starting from the available forward rates and thermodynamic equilibrium properties in order to satisfy equilibrium. References: (1) Plane and Whalley [2012]; (2) Feng et al. [2013]; (3) Plane [2004]; (4) Plane and Whalley [2012]; (5) Present work.*

Reaction	C_4 [m^3/mol/s]	C_5 [-]	E_0/k_B [K]	Reference
Charge exchange				
$Mg^+ + O_3 \rightleftharpoons MgO^+ + O_2$	7.23×10^8	0.0	0	1
$MgO^+ + O \rightleftharpoons Mg^+ + O_2$	3.55×10^8	0.0	0	1
$Mg^+ + N_2 + M \rightleftharpoons Mg^+ \cdot N_2 + M$	5.8×10^9	-1.72	0	1
$Mg^+ \cdot N_2 + O_2 \rightleftharpoons MgO_2^+ + N_2$	2.11×10^6	0.0	0	1
$Mg^+ + O_2 + M \rightleftharpoons MgO_2^+ + M$	5.44×10^9	-1.65	0	1
$MgO_2^+ + O \rightleftharpoons MgO^+ + O_2$	3.91×10^8	0.0	0	1
$MgO^+ + O_3 \rightleftharpoons Mg^+ + 2O_2$	1.08×10^8	0.0	0	1
$MgO^+ + O_3 \rightleftharpoons MgO_2^+ + O_2$	1.99×10^8	0.0	0	1
$Fe^+ + O_3 \rightleftharpoons FeO^+ + O_2$	4.58×10^8	0.0	241	2
$Fe^+ + N_2 + M \rightleftharpoons Fe^+ \cdot N_2 + M$	8.66×10^9	-1.52	0	2
$Fe^+ \cdot N_2 + O \rightleftharpoons FeO^+ + N_2$	3.01×10^7	0.0	0	2
$FeO_2^+ + O \rightleftharpoons FeO^+ + O_2$	3.01×10^7	0.0	0	2
$Fe^+ + O_2 + M \rightleftharpoons FeO_2^+ + M$	1.22×10^{11}	-1.86	0	2
$Na^+ + N_2 + M \rightleftharpoons Na \cdot N_2^+ + M$	2.01×10^{11}	-2.2	0	3
Dissociative recombination				
$MgO^+ + e^- \rightleftharpoons Mg + O$	2.55×10^{12}	-0.5	0	4
$Mg^+ \cdot N_2 + e^- \rightleftharpoons Mg + N_2$	2.55×10^{11}	-0.5	0	4
$FeO^+ + e^- \rightleftharpoons Fe + O$	2.55×10^{12}	-0.5	0	2
$FeO_2^+ + e^- \rightleftharpoons Fe + O_2$	2.55×10^{11}	-0.5	0	2
$Na \cdot N_2^+ + e^- \rightleftharpoons Na + N_2$	8.52×10^{11}	-0.5	0	3
Electron-impact ionisation				
$Mg + e^- \rightleftharpoons Mg^+ + 2e^-$	3.22×10^{11}	-0.5	88 696	5
$Fe + e^- \rightleftharpoons Fe^+ + 2e^-$	1.95×10^{11}	-0.5	91 246	5
$Na + e^- \rightleftharpoons Na^+ + 2e^-$	1.21×10^{11}	-0.5	59 594	5

Table 5.2.: *Simulated freestream conditions.*

Cond. ID	H [km]	V_∞ [km/s]	n_∞ [$1/m^3$]	T_∞ [K]	X_{N_2}	X_{O_2}	X_O	X_{O_3}
					[% mol]			
(1)	80	32	3.14×10^{20}	215	80.0	19.998	0.001	0.001
(2)	100	32	1.37×10^{19}	181	80.0	16.999	3.0	0.001

set as $Mg^+ = 0.1\%$, $Fe^+ = 0.1\%$, and $Na^+ = 1.0\%$.

For magnesium, the formation of oxide ions in trace concentrations, such as

MgO^+ and MgO_2^+, precedes the actual recombination of the free electrons, as is shown by Figure 5.5. In the same figure, the ion chemistry relevant to iron behaves similarly to the one of magnesium, but concentrations of FeO_2^+ are lower, if compared to MgO_2^+, because the former is directly lost by dissociation via Reaction 5.23. In Figure 5.6, recombination appears to be significantly dependent on the background pressure for both magnesium and iron, mainly because of the influence of Reaction 5.24 in the deionisation process.

With reference to sodium, the neutralisation mechanism is significantly different and controlled by the cluster $Na{\cdot}N_2^+$. Since it only relies on three-body collisions (Reaction 5.25), it is characterised by longer timescales. This effect is better shown in Figure 5.6, where timescales for recombination increase up to three orders of magnitude, moving from 80 to 100 km.

From this analysis, we can conclude that, at an altitude of 80 km, ion chemistry in the trail proceeds at rates which are likely to be comparable with the timescales of mass diffusion. On the other hand, we have to exclude that chemical reactions can play any role in the radio signal decay at 100 km.

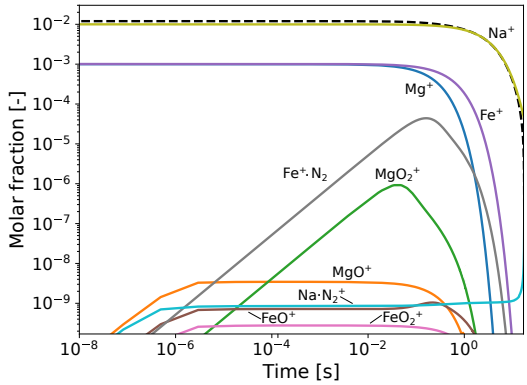

Figure 5.5.: *Evolution of the chemicals of meteoric origin involved in the deionisation process in the background atmosphere at an altitude of 80 km. Free electrons are represented with a dashed black line* **- - -**.

5.4.2. Trail analysis

We simulate the full trail with the methodology described in Section 5.2. Starting from the DSMC simulations performed in Chapter 3, we briefly discuss the main features of the near trail. This discussion allows us to examine the hypotheses introduced in Section 5.2, with regard to thermal equilibrium, velocity and density fields. In a second step, we employ the information at the outlet of the DSMC domain, and we march along the freestream streamlines with LARSEN, in order to compute the chemistry in the far trail.

Note that all the plots of the trail have to be considered in a frame of reference fixed to the meteoroid. Therefore, the reported simulations are to be

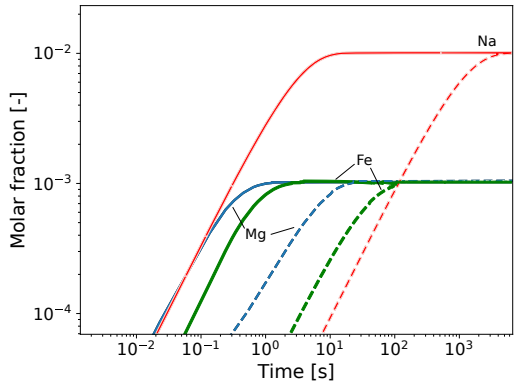

Figure 5.6.: *Influence of the atmospheric pressure in the neutralisation of the trail. Comparison between 80 and 100 km altitude. The effect of the background pressure is particularly evident for Na, whose recombination is fully driven by a three-body process. Dashed lines - - - refer to 80 km and solid lines ——— to 100 km.*

interpreted, by a ground-based observer, as simulations of one point of the trajectory. What an observer moving with the meteoroid sees as a trail, which relaxes to the freestream velocity and develops in space, is seen by a ground observer as the radial evolution of a trail, whose velocity relaxes to zero a few diameters after the meteoroid. In this way, the given plots can be interpreted as the radial evolution in one particular position of the sky, as time passes. Freestream density and temperature in the background atmosphere can thus be taken to be constant during the radial evolution, even for extensive simulations. The conversion between the indicated spatial position x and the ground-observer elapsed time t is obtained through the flight velocity V_∞ at the reflection point: $t = x/V_\infty$.

SPARTA DSMC-Boltzmann simulations of the near trail

For a detailed description of the DSMC simulations, the reader can refer to Chapter 3. Here, we are interested in examining i) the hypotheses pertinent to the relaxation to freestream conditions and ii) the initial condition profiles which are provided to the far trail simulations. We are assuming that metals are not involved in exchange reactions in the near trail so that metal oxide ions and clusters can only be produced in the far trail. Free electrons, whose diffusion is modelled under the ambipolar assumption, are expected to recombine later in the far trail.

The dynamics of the gas to the rear of the body can be best appreciated by plotting the development in the physical space of the velocity distribution function (VDF), as is done in Figure 5.7, for both the axial and the radial velocities. These distribution functions are obtained by sampling DSMC par-

ticles at different stations along the trail, in regions which are one meteoroid diameter in height.

In the near trail (from 0 to roughly 150 diameters in this test case), both the axial and radial VDFs are characterised by a bimodal shape, and the two families of particles, the metal vapour and the air, do not interact significantly. Indeed, thermalisation would push the two VDFs towards a common Maxwellian distribution. Also, Figure 5.7 shows that the near trail quickly assumes the freestream velocity condition as the trail is progressively filled by fast air molecules which, in a few diameters, take over the slow ablated vapour. Eventually, even in a low collisionality regime, this process leads to a Maxwellian distribution, at the end of the near trail.

The metal vapour diffuses in the surroundings, nearly in thermal equilibrium with the wall, with a law not far from the one describing an expansion into a vacuum ($\sim 1/r^2$) (see the metal vapour density field in Figure 5.8). Moreover, in Figure 5.8, we can see how the average density in the near trail region reaches the values of the freestream in nearly 100 diameters. Also, in Figure 5.9, similar relaxation times apply to the translational and internal temperatures. Here, translational and rotational degrees of freedom in the near trail take only a few microseconds to relax to the values of the freestream, confirming that the importance of Equation 5.9 is marginal in the far trail. In the near trail, the very high temperatures observed (up to 10^5 K) arise from the mixing of the two families of molecules, freestream and ablated vapour. This results in a global population strongly out of equilibrium, and whose dispersion - and therefore temperature - appears extremely high. Rather than the thermal content of the single population, this is to be interpreted as a *geometrical temperature*.

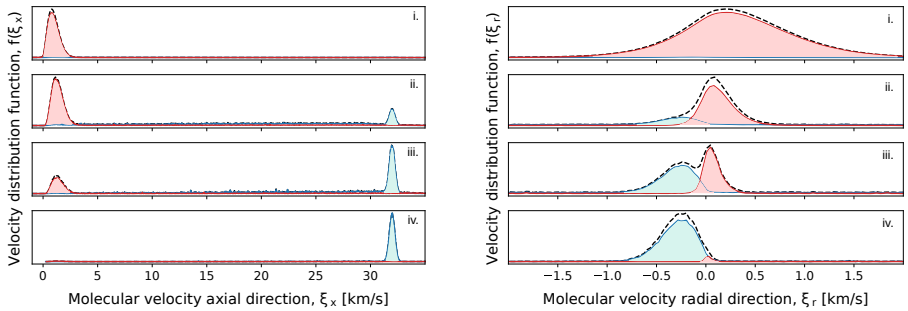

Figure 5.7.: *Evolution along the near trail of the axial VDF $f(\xi_x)$ (a) and the radial VDF $f(\xi_r)$ (b): i. $x = D/2$; ii. $x = 5/2D$; iii. $x = 5D$; iv. $x = 15D$. Air-vapour mixture - - -, air ——, and vapour contribution ——. Plots refer to Condition (1), at 80 km altitude.*

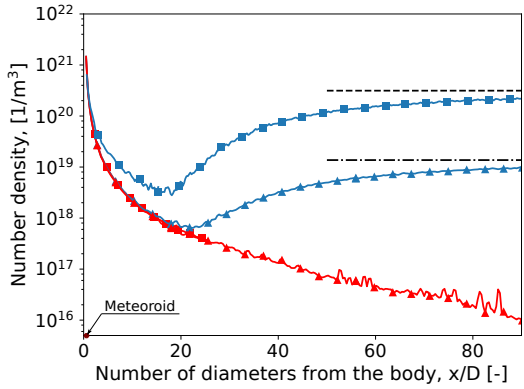

Figure 5.8.: *DSMC density profiles along the near trail for the two different altitude conditions, 80 km (marker ■) and 100 km (marker ▲). The reference system is centred at the stagnation point: air-vapour mixture ——, ablated vapour ——. Profiles are averaged in a width of one meteoroid diameter around the axis of symmetry.*

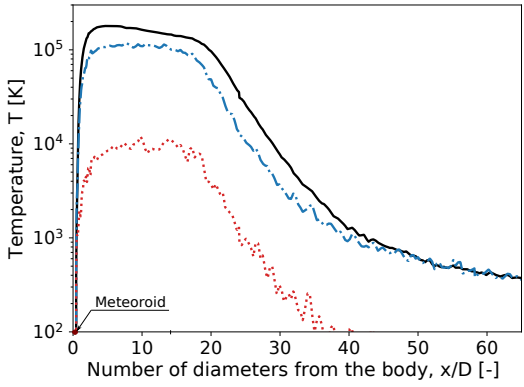

Figure 5.9.: *Translational and internal temperature profiles along the near trail at 80 km altitude. The reference system is centred at the stagnation point. In the near trail, T_{tr} —— and T_{rot} -·-· take only a few microseconds to relax to the values of the freestream. Vibrational temperature is marked with a dotted red line ····.*

LARSEN Lagrangian reactor simulations of the far trail

We start the computation of the far trail from the radial profiles obtained at the outlet of the DSMC domain. In Figure 5.10, we show these profiles at 80 km after a few steps of integration in LARSEN, which reduces considerably the noise characterising the chemical traces in DSMC.

If we look at the density profiles in Figure 5.11, chemical traces of sodium are present far behind the meteoroid. At high altitude, the trail tends to diffuse much more than at lower altitude: at 100 km, metal traces are detectable in a 10 m radius cone after 1 km.

At 80 km, exchange reactions are active and produce metal oxide ions and clusters. For these species, profiles at the axis of symmetry of the simulation domain are plotted in Figure 5.12. However, in the next section, we will show that their influence is marginal in the dynamics of the free electrons. Indeed, the evolution of radial profiles suggests a deionisation process dominated by diffusion. We will give a quantitative evaluation of this in the following section.

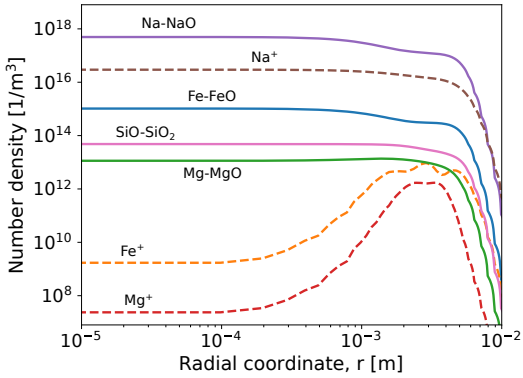

Figure 5.10.: *Radial profiles for species densities at the beginning of the far trail domain, at an altitude of 80 km. Profiles are reported after a few steps of integration in LARSEN. This reduces considerably the noise characterising chemical traces simulated in DSMC.*

Electron line density and ambipolar diffusion coefficient extracted from trail simulations

We can compare the present numerical result with the analytical solution for a problem of pure diffusion. In the case of a dilute solution at constant mixture density, Equation 5.1 reduces to

$$\frac{\partial n_e}{\partial t} = \boldsymbol{\nabla} \cdot (D_\mathrm{a} \boldsymbol{\nabla} n_e), \tag{5.27}$$

whose solution is given by Equation 1.4. From the electron number density n_e, the electron line density $\hat{n}_\mathrm{e}$ can be directly extracted from the simulations by numerical integration, as follows

$$\hat{n}_\mathrm{e}(t) = 2\pi \int_0^\infty n_\mathrm{e}(r,t)\ r\ dr, \tag{5.28}$$

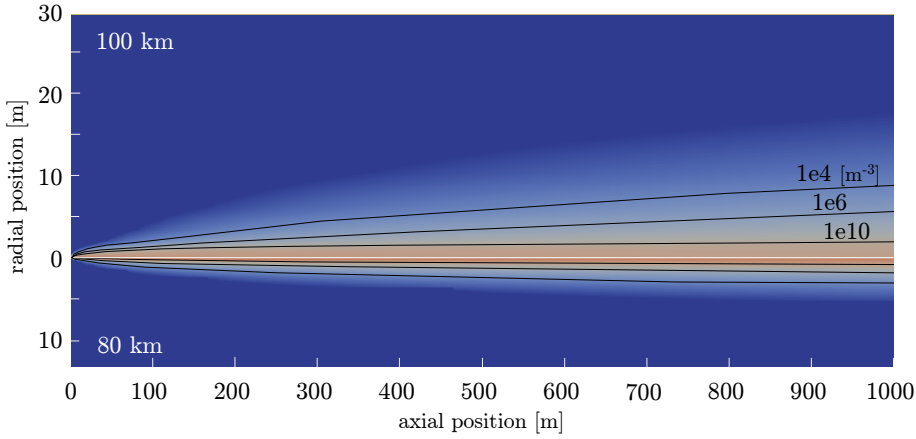

Figure 5.11.: *Ablated vapour expansion in the trail of the meteor. Number density contours at 80 and 100 km altitude show how much faster the vapour expands at higher altitudes. Contours are drawn for the Na species. The freestream flows from left to right.*

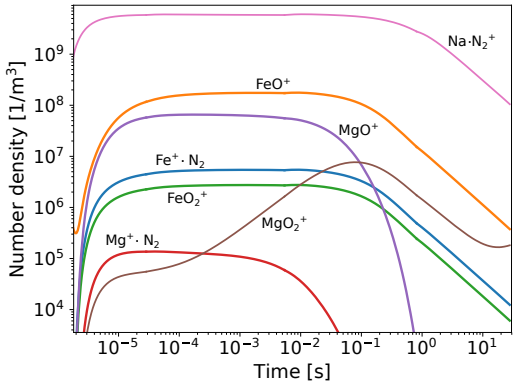

Figure 5.12.: *Evolution of the chemicals of meteoric origin involved in the deionisation process, at an altitude of 80 km. Reported values refer to the axis of symmetry. Exchange reactions are active at this condition, but their influence is marginal in predicting the evolution of the electrons.*

which is constant along the trail (therefore in time), if chemistry is not important. The initial meteor radius r_0 is taken equal to the radial width of the DSMC computational domain that is equal to 10 and 40 meteoroid radii respectively at 80 km and 100 km[4]. In this regard, we would like to point out

[4]The literature refers to the initial meteor radius as the span of the cylinder of ionised plasma that is quasi-instantaneously formed upon the passage of the meteoroid. In a consistent way, we are implying that only the processes occurring in the near trail can

that the employed DSMC domains are probably not large enough to contain the full ionisation profile, as an ablated atom may take several mean free paths before ionising. Therefore, it may be that we are underestimating the total free electron production.

For both our simulated conditions, the electron line density turns out to be nearly constant. Its values can be found in Table 5.3. In Figure 5.13, electron density profiles at an altitude of 100 km are seen to follow the analytical solution for radial diffusion closely, once the proper diffusion coefficient is chosen (the slight systematic discrepancy between the two solutions can be attributed to the numerical error or secondary effects played by chemistry). The close agreement confirms the importance of diffusion over chemistry for the current conditions and the fact that a constant diffusion coefficient represents a fair assumption. Diffusion coefficients are obtained by fitting Equation 1.4 over the numerical profiles. The ambipolar diffusion coefficients resulting from LARSEN simulations are reported in Table 5.3 and show that the trail expands faster at 100 km than 80 km altitude.

Table 5.3.: *Electron line densities and ambipolar diffusion coefficients resulting from the numerical simulations.*

Condition ID	$\hat{n}_e$ [e/m]	D_a [m^2/s]
(1)	1.3×10^{12}	0.96
(2)	9.05×10^{10}	19.1

5.4.3. Link of trail simulations to the radio-echo theory

When the density of the free electrons is weak, the incident radio wave can propagate in the ionised gas, where it is scattered by the individual electrons with scattering cross section

$$\sigma_e = 4\pi r_e^2 \sin^2 \gamma, \tag{5.29}$$

r_e and γ being respectively the radius of the electron and the angle between the electric field of the incoming wave and the line of sight of the receiver [McKinley, 1961]. Physicists refer to this condition as *underdense reflection*. In this case, the reflected signal is the sum of the contributions from independent electrons, with no secondary scattering and absorption effects. On the other hand, when the meteor is *overdense*, free electrons cannot behave as autonomous reflectors, and the physics of the wave-plasma interaction is more complicated.

be responsible for the production of free electrons. Consequently, we define the initial meteor radius according to the ionisation profile developed at the outlet of the DSMC computational domain.

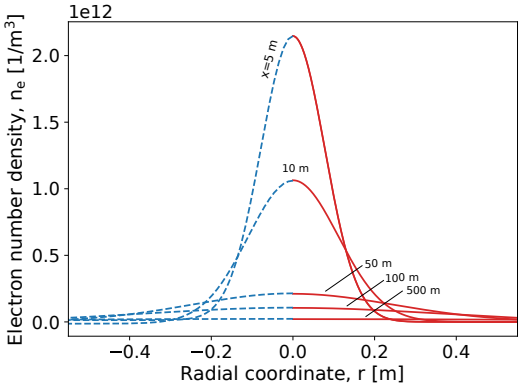

Figure 5.13.: *Comparison of the analytical* — *and numerical solutions* - - - *for the electron density profiles at different positions in the far trail at 100 km altitude.*

The underdense condition can be formally written as $n_e < n_{cr}$ [Foschini, 1999], where n_{cr} represents the critical density, which is reached when the *plasma frequency*

$$\omega_p = \sqrt{\frac{n_e q_e^2}{\epsilon_0 \mu_e}} \tag{5.30}$$

attains the value of the impinging radio wave frequency. In Equation 5.30, quantity q_e represents the electron charge, μ_e the mass of the electron, and ϵ_0 the permittivity of free space.

If we assume a wavelength $\lambda_\star = 6$ m, which corresponds to a radio frequency equal to 50 MHz, the overdense region extends up to 100 m along the axial direction and 5 cm in the radial one at 80 km altitude. The overdense region can be seen in Figure 5.14 for the 80 km case. On the other hand, at 100 km, the overdense region appears to be only a few centimetres long, and the underdense condition is fulfilled practically everywhere.

Reconstruction of the underdense radio echo

If underdense plasma theory applies, and the trail is regarded as a scattering cone (Equation 1.4) with a Gaussian density distribution, then an analytical treatment to the signal reconstruction exists [Verbeeck, 1995]. In the hypothesis of a plasma column dominated by diffusion, classical radio theory for the forward-scattering technique predicts a power delivered to the receiver which reads as

$$P_R(t) = \frac{c_0 \lambda_\star^3 r_e^2 \hat{n}_e^2}{32\pi^2 c_1} \exp\left\{\frac{-8\pi^2 c_2 (r_0^2 + 4D_a t)}{\lambda_\star^2}\right\} \times \frac{1}{2}[\mathcal{C}^2(t) + \mathcal{S}^2(t)] \tag{5.31}$$

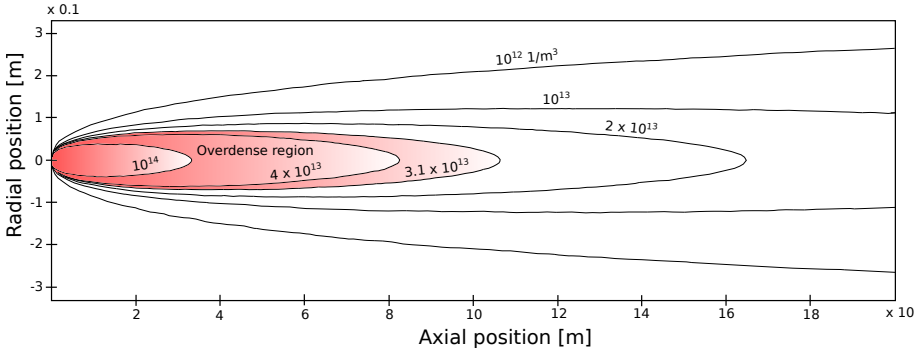

Figure 5.14.: *Contour plot of the electron number density for Condition (1), at 80 km altitude. The overdense region is highlighted ($n_{cr} = 3.1\times10^{13}$ $1/m^3$). We have assumed a wavelength $\lambda_\star = 6$ m, which corresponds to a radio frequency equal to 50 MHz. For this condition, the region extends up to 100 m in the axial direction and 5 cm in the radial direction. Axes are not to scale and the freestream flows from left to right.*

for $t > 0$ s. Constant c_0 depends on the apparatus, whereas c_1 and c_2 depend on the geometry of the detection. Quantity $\lambda_\star$ is the wavelength of the incident radio wave. Finally, $\mathcal{C}$ and $\mathcal{S}$ stand for the Fresnel integrals coming from diffraction phenomena[5].

Given the geometry of the detection (see Figure 5.15 for its graphical representation) and the technical parameters of the radio system, we can reconstruct an hypothetical radio echo, using the physical quantities of the plasma extracted from the simulations in Equation 5.31. In the BRAMS network [Lamy et al., 2011], a dedicated beacon is installed in Dourbes, Belgium. It emits a continuous waveform circularly polarised signal at a frequency of 49.97 MHz with a constant power $P_\mathrm{T} = 150$ W. In Equation 5.31, parameter c_0 is defined as

$$c_0 = P_\mathrm{T} G_\mathrm{T} G_\mathrm{R} \sin^2\gamma. \tag{5.32}$$

For the sake of simplicity, we assume the gains of the transmitter and the receiver, respectively G_T and G_R, equal to one, and we set $\sin^2\gamma = 1/2$ [Verbeeck, 1995].

Constants c_1 and c_2 fully depend on the geometry of the detection and respectively read as

$$c_1 = R_\mathrm{T} R_\mathrm{R} (R_\mathrm{T} + R_\mathrm{R})(1 - \sin^2\phi\cos^2\beta) \tag{5.33}$$

[5]Electromagnetic waves are scattered from an extended portion of the plasma column and not by a single specular reflection point. Along the trail, the closer we are to this point, the higher is the contribution to the received signal. Waves reflected by distinct portions of the trail are out of phase, as they travel different distances from the transmitter to the receiver. Doing so, they generate zones of constructive and destructive interference, which result in Fresnel oscillations.

and

$$c_2 = \frac{1}{\sec^2 \phi}, \tag{5.34}$$

where R_{T} and R_{R} are the distances of the transmitter and the receiver from the reflection point, ϕ is half of the angle between the transmitter and the receiver at the reflection point, and β the angle between the wave propagation plane, defined by the ellipse in Figure 5.15, and the meteor entry trajectory.

We imagine the reflected signal to be received by the BRAMS radio station in Overpelt, Belgium. We set $\beta = 0$ deg, and we consider that the wave propagation plane is not inclined with respect to the local normal to the surface. For both conditions, we simulate two different reflection points: one $x_{\mathrm{d}} = 70$ km and the other 117 km away from the transmitter. In Figure 5.16, we see that this distance influences the intensity of the signal (roughly by a factor $1/R^3$ according to Equation 5.33), but not its shape.

At 80 km altitude, the Fresnel oscillations are evident, whereas at 100 km, these fluctuations are significantly damped by the intense diffusion rate. Also, for the first case, the signal lasts up to 0.3 s, a much longer duration with respect to Condition (2), where the echo quickly disappears after 0.025 s. Finally, due to the higher electron densities characterising the plasma column, the intensity of the received power appears to be three orders of magnitude larger for the first case than in the second[6].

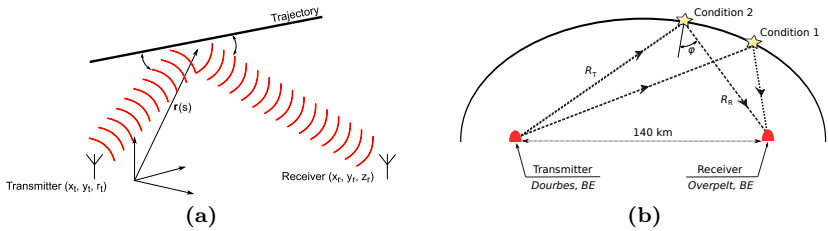

Figure 5.15.: *(a) Graphical representation of the radio signal forward-scattered by a meteor trail. The optical path of the reflection is specular. Reflections of the emitted signal from other segments of the trail can result in diffraction patterns, which are accounted in Equation 5.31 by the Fresnel integrals. (b) Two hypothetical detection points for Conditions (1) and (2). The transmitter in Dourbes, Belgium emits a continuous radio wave at a frequency of 49.97 MHz and constant power of 150 W. The reflected signal is received by the radio station in Overpelt, Belgium. The ellipse defines the wave propagation plane, and the two entry trajectories are tangential to the ellipse at the reflection points. Moreover, we assume that the trajectories lie in the plane of propagation of the wave, having set $\beta = 0$ deg.*

[6]Note that both the events are below BRAMS detection threshold, which is -140 dBm with a S/N > 10 dB, detectable by performing a Fast Fourier Transform on 16384 samples (approximately 3 s). In order to reach -157 dBm, 100 times more samples would be necessary.

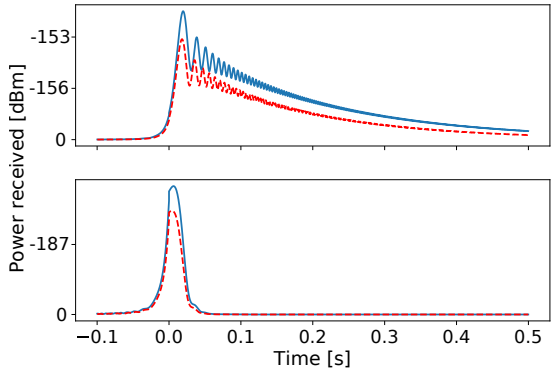

Figure 5.16.: *Simulated power profiles for Condition (1) (upper) and Condition (2) (lower). At $t = 0$ s, the meteor is at the reflection point. For both conditions, we simulate two different reflection points: one 70 km* ——— *and the other 117 km* - - - *away from the transmitter. Here, we are assuming that the wave propagation plane is not inclined with respect to the local normal to the surface.*

Comparison of the ambipolar diffusion coefficients with theory and radio/radar decay observations

We can now examine the diffusion coefficients extracted from the numerical simulations in the light of classical theoretical results and radio decay observations.

In a three-component thermalised plasma containing neutrals, ions, and electrons, a standard result [Kaiser, 1953, Ramshaw and Chang, 1993] predicts the ambipolar diffusion coefficient to be

$$D_{\mathrm{a}} = 2\mathcal{D}_{ij}, \tag{5.35}$$

$\mathcal{D}_{ij}$ being the ion-neutral *binary diffusion coefficient*, with index i and j respectively representing the ion and neutral species. Einstein's relation defines binary diffusion coefficients for ions in a neutral gas as

$$\mathcal{D}_{ij} = \mathcal{K}_{ij}\frac{k_{\mathrm{B}}T}{q_{\mathrm{e}}}, \tag{5.36}$$

where $\mathcal{K}_{ij}$ is the zero-field mobility factor [Mason and McDaniel, 1988]. Langevin's *theory of ionic mobilities* predicts a dependency of $\mathcal{K}_{ij}$ on the mass of the ion and the polarisability of the neutral molecule [Massey et al., 1971]. This theory has shown general good agreement with meteor decay times [Jones and Jones, 1990], and it is consistent with the approach adopted here, where ion-neutral binary diffusion coefficients $\mathcal{D}_{ij}$, arising from the Chapman-Enskog method

(see Appendix C), are computed using the Langevin potential. A comparison of the binary diffusion coefficients employed in this work with results obtained by means of Equation 5.36 and zero-field mobilities by Massey et al. [1971] is given in Figure 5.17, for some relevant ions diffusing in N_2. A difference exists in the data of N^+ and O^+, for which more accurate data have been used [Levin and Wright, 2004].

Also, ambipolar diffusion rates extracted from the simulations and reported in Table 5.3 are coherent with those predicted combining Equation 5.35 and 5.36, if we consider that Na^+ and Mg^+ are the most abundant ions in the simulations.

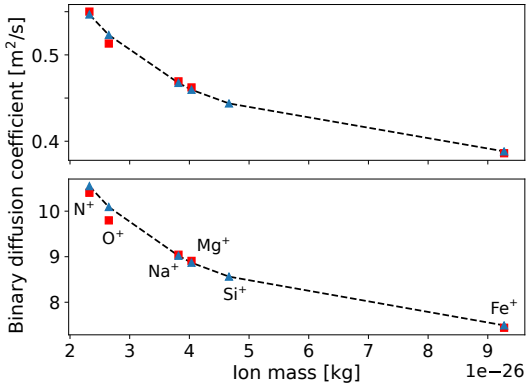

Figure 5.17.: *Binary diffusion coefficients for some relevant ion-N_2 collision pairs for Condition 1 (upper) and Condition 2 (lower). Marker ■ refers to the present work, marker ▲ to the work of Massey et al. [1971].*

Finally, we compare results from our numerical simulations with observations. Astronomers have proposed a variety of observational fittings to obtain the ambipolar diffusion coefficient from the exponential decay constant, which is given by

$$\tau = \frac{\lambda_\star^2}{32\pi^2 D_\mathrm{a}}, \tag{5.37}$$

and it is computed as the time that the echo intensity takes to decay by a factor $1/e$ [Herlofson, 1947]. In Figure 5.18, we consider some of these fits [Greenhow and Hall, 1961, Jones and Jones, 1990, Galligan et al., 2004]. We also report the data collected by the Advanced Meteor Orbit Radar (AMOR) [Baggaley et al., 2002], over which the fitting by Galligan et al. [2004] is based. Contour lines correspond to the number of detections. We find the diffusion of free electrons to be in good agreement with the ones retrieved by observations, even if simulations seems to slightly overpredict diffusion coefficients. Although scatters in the experimental data suggest caution in the comparison, possible reasons for this discrepancy could reside in: i) differences in the employed atmospheric model; ii) inhibition of diffusion by the geomagnetic field [Cervera and Reid, 2000]; iii) overestimated concentrations of Na^+ in the simulations,

with respect to Mg^+ and Fe^+. The far trail is computed in all its length, assuming a frozen composition of the meteoroid equal to its initial condition. However, a depletion in volatile elements in the first part of the entry path would lower sodium concentrations, and the vapour phase would start being dominated by refractory elements [McNeil et al., 1998, Janches et al., 2009].

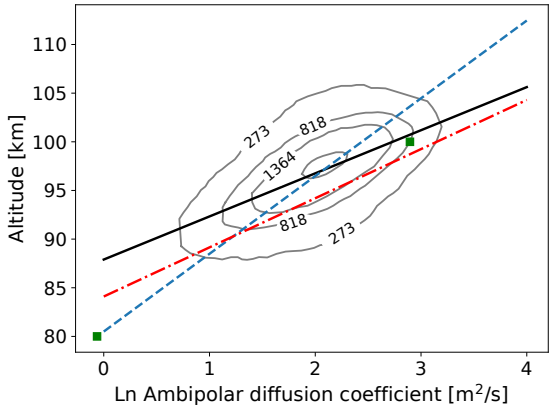

Figure 5.18.: *Base-10 logarithm of the ambipolar diffusion coefficient in function of the altitude. Comparison between numerical simulations from present work (marker ■) and fits to observed radio signal decays: Greenhow and Hall [1961] - - -, Jones and Jones [1990] -·-·-, Galligan et al. [2004] ——. Contour lines from the AMOR data correspond to the number of detections.*

5.5. Concluding remarks

We have introduced a method to model meteor plasma trails up to several kilometres in length, under rarefied conditions. This method is a general and self-consistent procedure that allows the computation of meteor physical parameters at given trajectory conditions, without the need to rely on phenomenological lumped models. In particular, we have analysed the main physico-chemical features of the near and far trail, and we have retrieved diffusion coefficient and electron line density, parameters of vital importance for the interpretation of radio-scattering.

As test case, we have investigated the formation and development of the trail generated by a 1 mm ordinary chondrite, flying at 32 km/s, at altitudes of 80 and 100 km. Starting from the DSMC computations of the evaporating meteoroid and the following ionisation reactions (Chapter 3), we have calculated the multicomponent diffusion, ambipolar electric field, and chemistry relevant to the dissipation of the plasma trail. In the near trail, translational and rotational degrees of freedom of heavy species take only a few microseconds to relax to the values of the freestream. In the far trail, ionic chemical reactions,

although active, have shown not to play a significant role in the neutralisation process, which is dominated by mass diffusion. Also, a common and constant diffusion coefficient was sufficient to reproduce the numerical profiles. The influence of chemistry and differential radial diffusion could be enhanced in overdense meteors, therefore this aspect deserves further investigation. Moreover, the extracted ambipolar diffusion coefficients have been compared with theoretical values and observations, finding a good agreement in both cases. As a last step, we have linked the dissipation of the free electrons in the trail to the classical radio-echo theory of underdense meteors, verifying whether applying this condition is legitimate or not for the tested conditions.

CHAPTER 6

Melting in Presence of Rarefied Gas Phase

"Il n'y a d'indispensable que les choses inutiles."

– Francis Picabia

6.1. Introduction

Chapter 4 has highlighted the mechanical removal of a liquid layer as a substantial ablation mechanism. In order to quantify its importance and to develop predictive tools, a description of the entrainment of the molten layer into a rarefied hypersonic flow is required. In this type of flow, the position of the phase boundaries is not known a priori, and a coupled treatment of the dynamic/thermal response of the material, along with the thermal nonequilibrium effects in the vapour, is necessary. Whereas solid and liquid can be dealt with as continuous media, a kinetic treatment is needed for the gas.

In this chapter, we present a methodology which considers the thermal and dynamic coupling of different phases by entirely relying on particle schemes. In our approach, the Smoothed Particle Hydrodynamics (SPH) method [Gingold and Monaghan, 1977] is employed for the solid and liquid phases, while the DSMC method introduced in Section 3.3 is used for the gas phase. If DSMC is the dominant technique for rarefied gas flow simulations, SPH has been selected, among other two-phase flow numerical techniques, because of its easier coupling with DSMC and its straightforward treatment of the free surface [Monaghan, 1994, Marrone et al., 2010].

In the SPH method, every particle represents a fluid parcel free to move in the domain, subject to pressure, viscous, and surface tension forces. The properties of one fluid particle depend on the properties of its neighbours through an interpolation kernel function. In comparison with mesh-dependent approaches,

Some of the results presented in this chapter have been obtained in the framework of H. Scandelli's MSc thesis, **Development of an ablation model for atmospheric entry flow in the framework of particle based solver**, Politecnico di Milano, 2017.

the SPH method significantly facilitates handling problems with free or interfacial surfaces, whose location is a priori unknown. Therefore, it is a particularly powerful tool for the study of multiphase fluid flow problems.

On the other hand, in the stochastic DSMC method, a microscopic particle simulates a large number of identical real molecules, and the dynamics of the gas is solved under the assumption that the streaming operator of the Boltzmann equation can be decoupled from the collision operator.

The approach adopted here is computationally more expensive than the one of Chapter 3, as it proposes to describe the dynamics of the different phases comprehensively. To the best of our knowledge, this is one of the first attempts to couple Boltzmann and Navier-Stokes equations in an unsteady simulation with a deformable gas-liquid interface. Ye et al. [2012] proposed a hybrid SPH-DSMC approach and employed it to study the flow in hydrogen separation membranes. The steady solution was obtained by an iterative process in which the two solvers were run separately over two different domains, and an overlapping buffer at their interface was used to update the freestream boundary conditions. Tiwari et al. [2013] coupled the Finite Pointset method, which is similar to SPH, to simulate a nanobubble in shear flow, keeping the interface fixed.

In the next section, we present the physico-mathematical models employed to simulate the different phases. In particular, specific attention is given to the description of the two interfaces, the solid-liquid and the liquid-vapour boundaries. In Section 6.3, the numerical methods employed for the solution are presented. After a description of the main features in SPH, we provide the details about the coupling procedure between this technique and DSMC. Section 6.4 briefly introduces the numerical tool, and Section 6.5 is dedicated to intermediate verification test cases of the computational model, in which the implementations of the two numerical methods are considered separately. Some verification test cases relevant to the SPH code are reported in Appendix D. Finally, results from thermally and dynamically coupled simulations are presented in Section 6.6.

6.2. Physico-mathematical models

6.2.1. Condensed phase

Navier-Stokes equations

The mathematical model for the condensed phase, liquid and solid, is based on the Navier-Stokes equations which can be derived by macroscopic local mass, momentum, and energy balances [Schlichting and Gersten, 1955]. In the case of a single component incompressible Newtonian phase, the Navier-Stokes equations reduce to

$$\boldsymbol{\nabla} \cdot \boldsymbol{v}_\mathrm{c} = 0 \tag{6.1}$$

$$\rho_\mathrm{c} \mathcal{D}_t \boldsymbol{v}_\mathrm{c} = \boldsymbol{\nabla} \cdot \boldsymbol{\Pi}_\mathrm{c} \tag{6.2}$$

$$\rho_{\mathrm{c}} c_{\mathrm{p,c}} \mathcal{D}_t T_{\mathrm{c}} + \boldsymbol{\nabla} \cdot \boldsymbol{q}_{\mathrm{c}} = 0, \tag{6.3}$$

where index "c" stands for the condensed phase and the operator $\mathcal{D}_t()$ is the material derivative $\partial_t() + \boldsymbol{v}_{\mathrm{c}} \cdot \boldsymbol{\nabla}()$, $\boldsymbol{v}_{\mathrm{c}}(\boldsymbol{x}, t)$ being the field velocity. Variables ρ_{c} and $c_{\mathrm{p,c}}(\boldsymbol{x}, t)$ are respectively the density and the specific heat, whereas $\boldsymbol{\Pi}_{\mathrm{c}}(\boldsymbol{x}, t)$ and $\boldsymbol{q}_{\mathrm{c}}(\boldsymbol{x}, t)$ are the stress tensor and the heat flux vector. In Equation 6.3, the viscous heating is assumed to be negligible. For an incompressible flow, this assumption results in a simplified energy equation, decoupled from the rest of the system [Faghri and Zhang, 2006]. The following relationships for the stress tensor and the heat flux

$$\boldsymbol{\Pi}_{\mathrm{c}} = -p_{\mathrm{c}} \mathbf{I} + \eta_{\mathrm{c}} (\boldsymbol{\nabla} \boldsymbol{v}_{\mathrm{c}} + \boldsymbol{\nabla} \boldsymbol{v}_{\mathrm{c}}^{\mathrm{T}}) \tag{6.4}$$

$$\boldsymbol{q}_{\mathrm{c}} = -\lambda_{\mathrm{c}} \boldsymbol{\nabla} T_{\mathrm{c}} \tag{6.5}$$

allow us to close the system, where $p_{\mathrm{c}}(\boldsymbol{x}, t)$ is the pressure in the fluid, $\eta_{\mathrm{c}}(\boldsymbol{x}, t)$ its dynamic viscosity, and $\lambda_{\mathrm{c}}(\boldsymbol{x}, t)$ the thermal conductivity.

For the solid phase, indicated with the index "s", the velocity field is zero everywhere so that only Equation 6.3 applies.

6.2.2. Vapour phase

Boltzmann equation

The model introduced in Section 6.2.1 can be applied to gases as long as a hydrodynamic closure of transport fluxes holds. However, when the low collision rate does not allow the molecules to reach local thermodynamic equilibrium, the gas has to be described at the kinetic scale using the Boltzmann equation, introduced in Section 3.2.1.

We can specialise Equation 3.1 to the case of a non-reacting dilute gas of hard spheres with mass μ, which reads as

$$\partial_t f_i + \boldsymbol{\xi} \cdot \boldsymbol{\nabla} f_i = \sum_{j \in \mathcal{S}_{\mathrm{g}}} \int d_{ij}^2 \left(f_i' f_j' - f_i f_j \right) |(\boldsymbol{\xi}_i - \boldsymbol{\xi}_j) \cdot \boldsymbol{n}| \, d\boldsymbol{n} \, d\boldsymbol{\xi}_j \quad i \in \mathcal{S}_{\mathrm{g}} \tag{6.6}$$

for a set of species $\mathcal{S}_{\mathrm{g}}$ in the gas phase. The streaming operator on the left-hand side describes the result of macroscopic gradients over the velocity distribution function evolution in the physical and molecular velocity space $(\boldsymbol{x}, \boldsymbol{\xi})$. At the right-hand side, the integral models the effect of the binary impacts with an effective diameter $d_{ij} = (d_i + d_j)/2$ (for a schematic of the binary interaction, see Figure 6.1), where d_i and d_j are the diameters of particles i and j.

Each collision is characterised by velocities $(\boldsymbol{\xi}_i, \boldsymbol{\xi}_j)$ and $(\boldsymbol{\xi}_i', \boldsymbol{\xi}_j')$ before and after the interaction, and by the unit vector $\boldsymbol{n}$. This vector defines the line of centres of the two spheres. Momentum and energy must be conserved by each elastic encounter, leading to the following relationships

$$\boldsymbol{\xi}_i' = \boldsymbol{\xi}_i - \boldsymbol{n}[\boldsymbol{n} \cdot (\boldsymbol{\xi}_i - \boldsymbol{\xi}_j)], \tag{6.7}$$

$$\boldsymbol{\xi}_j' = \boldsymbol{\xi}_j + \boldsymbol{n}[\boldsymbol{n} \cdot (\boldsymbol{\xi}_i - \boldsymbol{\xi}_j)]. \tag{6.8}$$

For the relative velocity $\boldsymbol{g}_{ij} = \boldsymbol{\xi}_i - \boldsymbol{\xi}_j$, this interaction results in a specular reflection around the line of centres, formally expressed as

$$\boldsymbol{g}_{ij}' = \boldsymbol{g}_{ij} - 2\boldsymbol{n}[\boldsymbol{n} \cdot \boldsymbol{g}_{ij}], \tag{6.9}$$

with the module of the relative velocity conserved through the impact, $|\boldsymbol{g}_{ij}'| = |\boldsymbol{g}_{ij}|$.

The effective diameter can depend on the relative velocity of the impact as follows

$$d_{ij} = d_{ij}^{\mathrm{ref}} \left(\frac{g_{ij}^{\mathrm{ref}}}{|\boldsymbol{g}_{ij}|} \right)^{\omega - \frac{1}{2}}, \tag{6.10}$$

where the quantities d_{ij}^{ref} and g_{ij}^{ref} are reference values for the effective diameter and the relative velocity evaluated at a temperature T_{ref}, whereas the exponent ω leads to a power law temperature dependence of the viscosity coefficient, $\eta_{\mathrm{g}} \propto T_{\mathrm{g}}^{\omega}$ [Bird, 1994].

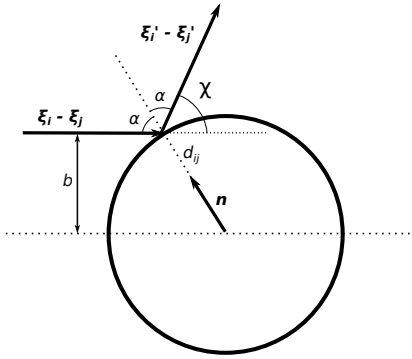

Figure 6.1.: *Schematic of the interaction between two hard spheres with an effective diameter d_{ij}. The encounter results in the symmetric scattering of the relative velocity around the line of centres, which is defined by the unit vector $\boldsymbol{n}$. Representation in the collision plane.*

Link between molecular and macroscopic scales

In Sections 3.2.1 and 5.2.3, we have already discussed the link existing between macroscopic and kinetic scales. Here, we recall this connection, as it is necessary to impose proper interface conditions between phases.

If we refer to the gas properties with the index "g", any quantity of interest at the macroscopic level $\Psi_{\mathrm{g}}(\boldsymbol{x}, t) = \{\rho_{\mathrm{g}}, \rho_{\mathrm{g}}\boldsymbol{v}_{\mathrm{g}}, \rho_{\mathrm{g}}E_{\mathrm{g}}\}$ is related to quantities at molecular scale $\theta_i(\boldsymbol{x}, \boldsymbol{\xi}, t) = \{\mu_i, \mu_i\boldsymbol{\xi}, \frac{1}{2}\mu_i|\boldsymbol{\xi}|^2\}$ as a moment of the probability

distribution function

$$\Psi_{\mathrm{g}} = \sum_{i \in \mathcal{S}_{\mathrm{g}}} \int \theta_i f_i \, d\boldsymbol{\xi}. \tag{6.11}$$

If we move from an absolute reference frame to the one moving with the local bulk velocity, we can define momentum and enery fluxes. The stress tensor for the gas $\boldsymbol{\Pi}_{\mathrm{g}}(\boldsymbol{x}, t)$ reads as follows

$$\boldsymbol{\Pi}_{\mathrm{g}} = \sum_{i \in \mathcal{S}_{\mathrm{g}}} \int \mu_i \, (\boldsymbol{\xi} - \boldsymbol{v}_{\mathrm{g}}) \otimes (\boldsymbol{\xi} - \boldsymbol{v}_{\mathrm{g}}) \, f_i \, d\boldsymbol{\xi}, \tag{6.12}$$

and similarly the energy flux $\boldsymbol{q}_{\mathrm{g}}(\boldsymbol{x}, t)$ as

$$\boldsymbol{q}_{\mathrm{g}} = \sum_{i \in \mathcal{S}_{\mathrm{g}}} \int \frac{1}{2} \, \mu_i \, |\boldsymbol{\xi} - \boldsymbol{v}_{\mathrm{g}}|^2 \, (\boldsymbol{\xi} - \boldsymbol{v}_{\mathrm{g}}) \, f_i \, d\boldsymbol{\xi}. \tag{6.13}$$

6.2.3. Interface conditions between phases

A complete description of the jump conditions which need to be applied at the interfaces between two phases and their derivation can be found in Guedon [2013]. Here, we consider an *ideal interface*, meaning that no entropy is generated during the change of phase, and viscous dissipation and kinetic energy can be considered negligible with respect to the heat flux and enthalpy.

Solid-liquid interface

At the interface between solid and liquid, $\boldsymbol{x} = \boldsymbol{X}_{\mathrm{sl}}(t)$, the following conditions can be applied

$$\rho_{\mathrm{c}} L_{\mathrm{m}} \boldsymbol{v}_{\mathrm{sl}} \cdot \boldsymbol{n}_{\mathrm{sl}} = [\boldsymbol{q}_{\mathrm{s}} - \boldsymbol{q}_{\mathrm{l}}] \cdot \boldsymbol{n}_{\mathrm{sl}} \tag{6.14}$$

$$T_{\mathrm{c}} = T_{\mathrm{m}} \tag{6.15}$$

$$\boldsymbol{v}_{\mathrm{c}} = 0, \tag{6.16}$$

$\boldsymbol{q}_{\mathrm{s}}$ and $\boldsymbol{q}_{\mathrm{l}}$ being respectively the heat flux vectors from the solid and liquid side. Temperature T_{m} is the melting condition of a pure substance[1], $\boldsymbol{n}_{\mathrm{sl}}(\boldsymbol{X}_{\mathrm{sl}}, t)$ the unit vector normal to the interface and $\boldsymbol{v}_{\mathrm{sl}}(\boldsymbol{X}_{\mathrm{sl}}, t)$ its velocity. The latent heat of melting L_{m} is defined as the jump in enthalpy between the two phases, $h_{\mathrm{l}} - h_{\mathrm{s}}$. Finally, Equation 6.16 represents the necessary boundary condition for the solution of the momentum balance (Equation 6.2).

Condensed phase-vapour interface

Let us consider the interface between the condensed phase and the vapour, $\boldsymbol{x} = \boldsymbol{X}_{\mathrm{cg}}(t)$, moving with velocity $\boldsymbol{v}_{\mathrm{cg}}(\boldsymbol{X}_{\mathrm{cg}}, t)$ and characterised by a normal

[1] As opposed to mixtures that are characterised by a range of temperatures over which the change of phase occurs.

unit vector, $\boldsymbol{n}_{\mathrm{cg}}(\boldsymbol{X}_{\mathrm{cg}}, t)$, pointing towards the vapour. Then, the two phases are coupled by means of surface mass, momentum, and energy balances

$$\rho_{\mathrm{c}} \left(\boldsymbol{v}_{\mathrm{c}} - \boldsymbol{v}_{\mathrm{cg}}\right) \cdot \boldsymbol{n}_{\mathrm{cg}} = -\rho_{\mathrm{v}} \left(\boldsymbol{v}_{\mathrm{v}} - \boldsymbol{v}_{\mathrm{cg}}\right) \cdot \boldsymbol{n}_{\mathrm{cg}} = \phi_{\mathrm{e}} \tag{6.17}$$

$$\phi_{\mathrm{e}} \left(\boldsymbol{v}_{\mathrm{c}} - \boldsymbol{v}_{\mathrm{v}}\right) = \left(\boldsymbol{\Pi}_{\mathrm{c}} - \boldsymbol{\Pi}_{\mathrm{g}}\right) \cdot \boldsymbol{n}_{\mathrm{cg}} - \epsilon_{\star} \kappa_{\mathrm{cg}} \boldsymbol{n}_{\mathrm{cg}} \tag{6.18}$$

$$\phi_{\mathrm{e}} \, L_{\mathrm{e}} = \left(\boldsymbol{q}_{\mathrm{c}} - \boldsymbol{q}_{\mathrm{v}}\right) \cdot \boldsymbol{n}_{\mathrm{cg}}, \tag{6.19}$$

in which we consider a constant surface tension coefficient $\epsilon_{\star}$, with $\kappa_{\mathrm{cg}}(\boldsymbol{X}_{\mathrm{cg}}, t)$ the mean local curvature of the interface, and $L_{\mathrm{e}} = h_{\mathrm{v}} - h_{\mathrm{l}}$ the latent heat of evaporation. Quantity ϕ_{e} represents the mass flux across the interface.

The conditions just defined link the condensed and vapour phases at the macroscopic level, but they do not provide the necessary information at the molecular scale. Therefore, some additional assumptions need to be made to assign the correct conditions to the velocity distribution function f_i at the interface. These conditions are those prescribed by the kinetic boundaries as defined in Section 3.2.2 (Equations 3.3-3.5). Moreover, ϕ_{e} can be determined via Equation 3.6.

6.3. Numerical methods

The DSMC method has been introduced in Chapter 3, and it will not be presented again in this section. The reader can refer to Section 3.3.

6.3.1. Smoothed Particle Hydrodynamics

The SPH method [Randles and Libersky, 1996, Ye et al., 2019] is a mesh-free, fully Lagrangian approach, used for the discretisation of partial differential equations. Initially developed for the solution of the Euler equations in the study of the dynamics of galaxies [Gingold and Monaghan, 1977], this method has been extended to simulate a wide variety of problems in computational physics, among which it has proven capabilities in simulating free surfaces [Monaghan, 1994, Marrone et al., 2010] and two-phase flows [Nugent and Posch, 2000, Shadloo and Yildiz, 2011, Wang et al., 2016].

In SPH, the fluid is represented by an ensemble of discrete particles $\mathcal{I}_{\mathrm{sph}}$, typically of fixed mass m, which move with the local fluid velocity of the consensed phase, $\boldsymbol{v}_{\mathrm{c}}(\boldsymbol{x}, t)$ and carry other fluid quantities specific to the given problem. Field variables in a certain point $\Psi_{\mathrm{c}}(\boldsymbol{x}, t)$ are calculated through an interpolation function (the *weighting smoothing kernel*) from the field variables of surrounding neighbour particles. Formally, this occurs in two steps, the integral function representation, or kernel approximation, and the particle approximation.

Smoothing kernel function

The smoothing kernel function $\mathcal{W}(\boldsymbol{x}-\boldsymbol{x}', h)$ is at the core of the SPH method and determines the way in which functions are approximated, assuring consistency and accuracy [Zhu et al., 2015]. In this work, we employ a quintic kernel of the following type

$$\mathcal{W} = \frac{7}{4\pi h^2}\left(2\frac{|\boldsymbol{x}-\boldsymbol{x}'|}{h}+1\right)\left(1-\frac{1}{2}\frac{|\boldsymbol{x}-\boldsymbol{x}'|}{h}\right)^4, \quad |\boldsymbol{x}-\boldsymbol{x}'| \leq 2h, \tag{6.20}$$

which is a positive and symmetric function, decreasing monotonically with the distance from the centre, and satisfying the following properties:

1. The support domain of the function is compact

$$\mathcal{W} = 0, \qquad |\boldsymbol{x}-\boldsymbol{x}'| \geq 2h, \tag{6.21}$$

   making the approximation a local operation. Quantity h is the smoothing length and is defined approximately as the radius of the circular support domain.

2. The function can be normalised over its support domain Ω

$$\int_\Omega \mathcal{W}\, d\boldsymbol{x}' = 1, \tag{6.22}$$

   ensuring the zero-th order consistency of the integral representation.

3. It satisfies the Delta function property

$$\lim_{h\to 0} \mathcal{W} = \delta(\boldsymbol{x}-\boldsymbol{x}') \tag{6.23}$$

   so that, as the smoothing length tends to zero, the approximation value approaches the function value.

Integral function representation

Starting from a continuous field $\Psi_c(\boldsymbol{x}, t)$, the integral function representation expresses the properties in a certain point of the domain as a weighted interpolation of the properties of its neighbourhood. This approximation reads as

$$< \Psi_c > \; = \; \int_\Omega \Psi_c \; \mathcal{W} \; d\boldsymbol{x}', \tag{6.24}$$

and is the denoted by the angle bracket <> operator. The same operation can be performed on the spatial derivative of the function

$$< \boldsymbol{\nabla}\Psi_c > \; = \; -\int_\Omega \Psi_c \; \boldsymbol{\nabla}\mathcal{W} \; d\boldsymbol{x}' \tag{6.25}$$

thank to which, the differentiation of the field is transmitted to a differentiation of the smoothing kernel[2].

Particle approximation

We divide the domain into a number of particles of mass m_i, and we move from an Eulerian to a Lagrangian description of the field. Particle i is characterised by position $\boldsymbol{x}_i(t)$ and discrete volume $d\boldsymbol{x}_i = m_i/\rho_{\mathrm{c}_i}$. In Equation 6.24, the continuous integral description can be converted into a discrete representation $\Psi_{\mathrm{c}_i} = \Psi_{\mathrm{c}}(\boldsymbol{x}_i)$, by summing over all the particles in the neighbourhood of $\boldsymbol{x}_i$, as if they were interpolation points in the support domain Ω_i

$$< \Psi_{\mathrm{c}_i} > \; = \; \sum_{j \in \Omega_i} \frac{m_j}{\rho_{\mathrm{c}_j}} \, \Psi_{\mathrm{c}_j} \, \mathcal{W}_{ij}, \tag{6.26}$$

where $\mathcal{W}_{ij} = \mathcal{W}(\boldsymbol{x}_i - \boldsymbol{x}_j, h)$. Similarly, for Equation 6.25, the spatial derivative of the field variable is written as

$$< \boldsymbol{\nabla} \Psi_{\mathrm{c}_i} > \; = \; - \sum_{j \in \Omega_i} \frac{m_j}{\rho_{\mathrm{c}_j}} \, \Psi_{\mathrm{c}_j} \, \boldsymbol{\nabla}_i \mathcal{W}_{ij}. \tag{6.27}$$

The spatial derivative can also be expressed as

$$< \boldsymbol{\nabla} \Psi_{\mathrm{c}_i} > \; = \; - \sum_{j \in \Omega_i} \frac{m_j}{\rho_{\mathrm{c}_j}} \, (\Psi_{\mathrm{c}_j} \pm \Psi_{\mathrm{c}_i}) \, \boldsymbol{\nabla}_i \mathcal{W}_{ij}, \tag{6.28}$$

and it is a direct consequence of Equation 6.22, which leads to

$$\sum_{j \in \Omega_i} \frac{m_j}{\rho_{\mathrm{c}_j}} \boldsymbol{\nabla}_i \mathcal{W}_{ij} \; = \; 0, \tag{6.29}$$

when derived. Equation 6.28 will be used for the discretisation of Equations 6.1-6.3, since it symmetrises (or anti-symmetrises) the formulation, and it reduces the error coming from the inconsistency of the particle approximation [Liu and Liu, 2003].

In Figure 6.2, the smoothing kernel function is represented schematically along with the particle approximation.

Space discretisation

By applying the approximation procedure just described, we can rework Equations 6.1-6.3 so to obtain a system of ordinary differential equations, which can be integrated in time. The resulting accuracy in space is $\mathcal{O}(h^2)$, when the number of particles in the compact support tends to infinity [Zhu et al., 2015].

[2]This characteristic property of the SPH method comes from applying Gauss's theorem to Equation 6.24, when $\nabla \Psi_{\mathrm{c}}$ is the continuous field that we want to represent, and it is is a direct consequence of Equation 6.21.

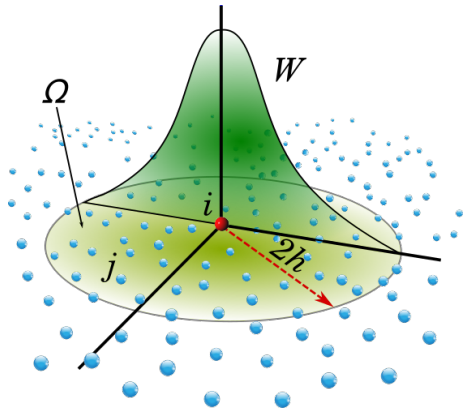

Figure 6.2.: *Representation of the smoothing kernel function and particle approximation idea. The properties of the red particle depend on the properties of all the blue particles close to it, in particular, the closer a blue particle is, the greater its contribution will be weighted.*

The detailed procedure can be found in Liu and Liu [2003] and the result reads as follows. For $i \in \mathcal{I}_{\text{sph}}$,

$$\mathcal{D}_t \rho_{\text{c}_i} = \sum_{j \in \Omega_i} m_j \, (\boldsymbol{v}_{\text{c}_i} - \boldsymbol{v}_{\text{c}_j}) \, \boldsymbol{\nabla}_i \mathcal{W}_{ij} \tag{6.30}$$

$$\begin{aligned} \mathcal{D}_t \boldsymbol{v}_{\text{c}_i} = & - \sum_{j \in \Omega_i} m_j \left(\frac{p_{\text{c}_i}}{\rho_{\text{c}_i}^2} + \frac{p_{\text{c}_j}}{\rho_{\text{c}_j}^2} \right) \boldsymbol{\nabla}_i \mathcal{W}_{ij} \\ & + \sum_{j \in \Omega_i} m_j \frac{\eta_{\text{c}_i} + \eta_{\text{c}_j}}{\rho_{\text{c}_i} \rho_{\text{c}_j}} \, (\boldsymbol{v}_{\text{c}_i} - \boldsymbol{v}_{\text{c}_j}) \, \frac{\boldsymbol{x}_i - \boldsymbol{x}_j}{|\boldsymbol{x}_i - \boldsymbol{x}_j|^2} \, \boldsymbol{\nabla}_i \mathcal{W}_{ij} \\ & + \epsilon_\star \kappa_{\text{cg}_i} \boldsymbol{n}_{\text{cg}_i} \delta_{\text{cg}_i} \; + \; \boldsymbol{a}_i \end{aligned} \tag{6.31}$$

$$\mathcal{D}_t T_{\text{c}_i} = \frac{1}{c_{\text{p,c}_i}} \sum_{j \in \Omega_i} m_j \frac{\lambda_{\text{c}_i} + \lambda_{\text{c}_j}}{\rho_{\text{c}_i} \rho_{\text{c}_j}} \, (T_{\text{c}_i} - T_{\text{c}_j}) \, \frac{\boldsymbol{x}_i - \boldsymbol{x}_j}{|\boldsymbol{x}_i - \boldsymbol{x}_j|^2} \, \boldsymbol{\nabla}_i \mathcal{W}_{ij} \; + \; l_i. \tag{6.32}$$

The pressure gradient (the first term in the right-hand side of Equation 6.31) is written in symmetrised form to conserve linear and angular momentum [Monaghan, 1994]. Formulations by Morris et al. [1997] and Monaghan et al. [2005] have been used for the diffusion terms in Equations 6.31 and 6.32 respectively. Term $\boldsymbol{a}_i$ represents a generic acceleration felt by the particle due to the presence of an external force, whereas quantity l_i is a generic energy source. The effect of the surface tension is taken into account by the *continuum surface force model* [Brackbill et al., 1992], according to which a volume term is added to the momentum equation. The Dirac delta function $\delta_{\text{cg}} = \delta(\boldsymbol{x} - \boldsymbol{x}_{\text{cg}})$ restrains the effects of the source term within the interface region. Finally, the local

curvature is computed as

$$\kappa_{\mathrm{cg}_i} = -(\boldsymbol{\nabla} \cdot \boldsymbol{n}_{\mathrm{cg}})_i = \sum_{j \in \Omega_i} \frac{m_j}{\rho_{\mathrm{c}_j}} \left(\boldsymbol{n}_{\mathrm{cg}_j} - \boldsymbol{n}_{\mathrm{cg}_i}\right) \cdot \boldsymbol{\nabla}_i \mathcal{W}_{ij}, \tag{6.33}$$

as derived by Morris [2000].

Time integration

In this work, integration in time of the system of Equations 6.30-6.32 is performed explicitly with a predictor-corrector scheme, $\mathcal{O}(\Delta t^2)$ accurate. The scheme is subject to the Courant-Friedrichs-Lewy (CFL) condition to guarantee stability. Details on the scheme are provided in Monaghan [1989]. The fluid is treated as weakly compressible with Tait's artificial equation of state used to compute the new pressure field at the updated particle position [Monaghan et al., 1999].

6.3.2. Coupling between phases

To model the transition between the solid and liquid phases, we use the *apparent heat capacity method* that has been introduced in Section 2.2.2. This method allows us to solve a single set of equations (Equations 6.30-6.32) for the whole condensed phase without the need to track the melting front, which can be obtained a posteriori by applying the condition in Equation 6.15. In the formulation provided by Hashemi and Sliepcevich [1967], the change of phase is accounted for by a temperature dependent specific heat $c_{\mathrm{p,c}}(\boldsymbol{x}_i)$ of the following type

$$c_{\mathrm{p,c}_i} = c_{\mathrm{p,s}} + (c_{\mathrm{p,l}} - c_{\mathrm{p,s}})\ \mathcal{Q}(T_{\mathrm{c}_i} - T_{\mathrm{m}}) + L_{\mathrm{m}}\ \mathcal{U}(T_{\mathrm{c}_i} - T_{\mathrm{m}}), \tag{6.34}$$

where function $\mathcal{Q}(T_{\mathrm{c}_i} - T_{\mathrm{m}})$ is the Heaviside step function and $\mathcal{U}(T_{\mathrm{c}_i} - T_{\mathrm{m}})$ is a Gaussian distribution centred in T_{m}

$$\mathcal{U} = \frac{1}{\sqrt{2\pi}\Delta T} \exp\left\{ -\frac{(T_{\mathrm{c}_i} - T_{\mathrm{m}})^2}{2\Delta T^2} \right\}, \tag{6.35}$$

which regularises the Dirac delta function $\delta(T_{\mathrm{c}} - T_{\mathrm{m}})$ in a finite temperature interval ΔT[3].

At each timestep, the solid phase is identified by $T_{\mathrm{c}_i} < T_{\mathrm{m}}$. Here, the velocity field is imposed as $\boldsymbol{v}_{\mathrm{c}_i} = 0$, whereas the liquid particles are allowed to move. The Dirichlet boundary condition in Equation 6.16 sets itself naturally at the interface.

[3] In alloys and multicomponents systems, the change of phase occurs over a range of temperatures where the two phases coexist (*mushy zone*) and ΔT assumes a physical meaning.

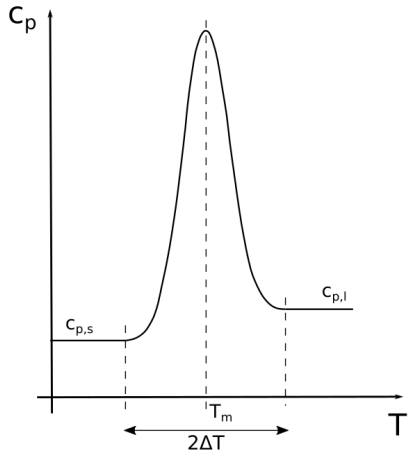

Figure 6.3.: *Schematic of the apparent specific heat function employed to model the latent heat of melting.*

SPH-DSMC coupling procedure

The SPH-condensed and the DSMC-vapour phase are integrated separately in time, and they are coupled by exchanging information at each timestep. The molecules of gas move in the physical space and intersect the boundaries with the condensed phase, which scatter them back. Gas-surface interactions result in momentum and energy exchange at the interface between the two phases and induce the physical properties of the condensed phase to evolve in time.

At each timestep, the coupling procedure consists of the following actions:

1. Physical quantities and positions of the SPH particles are updated in time following the numerical procedure described in Section 6.3.1. The cells of the DSMC background grid containing particles from the condensed phase are identified.

2. The SPH particles in the proximity of the surface are distinguished from the ones in the bulk of the condensed phase. In fact, the properties of the SPH particles near the free surfaces are characterised by a truncated particle approximation because of the absence of neighbours in their compact support (see Figure 6.5). The identification method used here was proposed by Doring [2005] and exploits the fact that the eigenvalues of the matrix $\mathbf{B}(\boldsymbol{x}_i)$

$$\mathbf{B}_i = \left[\sum_{j \in \Omega_i} \boldsymbol{\nabla}_i \mathcal{W}_{ij} \otimes (\boldsymbol{x}_j - \boldsymbol{x}_i) \, \frac{m_j}{\rho_{\mathrm{c}_j}} \right]^{-1} \tag{6.36}$$

used for the periodic renormalisation of the kernel gradient, depend on the spatial organisation of the particles in the neighbourhood of the con-

sidered parcel i. Note that the moment matrix $\mathbf{B}$ is equal to the identity matrix when parcel i is far from the free surface. Close to the boundaries, the distribution of particles around i is not symmetric anymore. Therefore, inside the bulk of the condensed phase, its minimum eigenvalue tends to 1, while it departs from unity as we approach the free surface. This allows us to determine the region of the fluid domain $\boldsymbol{X}_{\mathrm{cg}}$, where the free surface lies.

3. In order to account for evaporation, the SPH particles belonging to the interface are removed at the rate predicted by Equation 3.6. In the current implementation, an SPH particle is deleted only when its total mass has been lost. In this way, the evaporating front proceeds stepwise, advancing by a length equal to the spatial discretisation between SPH particles.

4. The unit vectors locally normal to the free surface $\boldsymbol{n}_{\mathrm{cg}}$ are necessary for the scattering of the DSMC molecules at the interface (see Equation 3.3) and must be computed. The idea is that the normal vector is aligned with the gradient of density of the SPH particles

$$\boldsymbol{\nabla}\rho_i = \sum_{j\in\Omega_i} m_j \boldsymbol{\nabla}_i \mathcal{W}_{ij}. \tag{6.37}$$

As shown by Randles and Libersky [1996], one can write that, for a parcel i in the bulk of the condensed phase, the sum over the gradients of the kernel function in its compact support is about zero. When a particle, instead, is near the free surface, such a sum is a good approximation of the vector locally normal to the interface. Since the accuracy of the evaluation of this vector depends on the particle disorder, it is possible to obtain a more accurate evaluation by using the renormalisation matrix introduced by Equation 6.36, as follows

$$\boldsymbol{n}_{\mathrm{cg}_i} = \frac{\boldsymbol{r}_i}{|\boldsymbol{r}_i|}, \tag{6.38}$$

where

$$\boldsymbol{r}_i = -\,\mathbf{B}_i \sum_{j\in\Omega_i} \frac{m_j}{\rho_{\mathrm{c}_j}}\, \boldsymbol{\nabla}_i \mathcal{W}_{ij}. \tag{6.39}$$

5. The DSMC molecules are moved in the physical space and are injected at the boundaries or at the vapour-liquid interface (see Section 3.3.1). When a molecule ends up in a cell in which the SPH phase is present, then gas-surface interactions routines are performed. The details of the procedure are explained in the following steps.

6. The intersection point of the DSMC molecules trajectories with the free surface of the liquid is computed. When one of the cells containing some condensed phase is crossed, the SPH particle which is the closest to the trajectory and belongs to the interface is selected. The intersection point is computed as the point of minimum distance between this SPH particle

and the DSMC particle trajectory. The full procedure is presented in the flowchart of Figure 6.4.

7. DSMC molecules can condense at the interface or are scattered back fully thermalised as specified by Equations 3.3 and 3.5. The unit vector normal the surface is chosen associated to the SPH particle selected on the interface at Step 6.

8. Momentum and energy are exchanged between the gas and the condensed phase. The net force and energy are included in the balances for the computation of the trajectories and thermal response of the SPH particles computed at Step 1 as follows. For $i \in \mathcal{I}_{\text{sph}}$,

$$\mathcal{D}_t \boldsymbol{v}_{\text{c}_i} = \boldsymbol{\chi}_i^{\text{sph}} + \boldsymbol{\chi}_i^{\text{dsmc}} \tag{6.40}$$

$$\mathcal{D}_t T_{\text{c}_i} = \Gamma_i^{\text{sph}} + \Gamma_i^{\text{dsmc}}, \tag{6.41}$$

where $\boldsymbol{\chi}^{\text{sph}}(\boldsymbol{x}_i)$ and $\Gamma^{\text{sph}}(\boldsymbol{x}_i)$ are nothing else than the right-hand sides in Equations 6.31 and 6.32, while $\boldsymbol{\chi}^{\text{dsmc}}(\boldsymbol{x}_i)$ and $\Gamma^{\text{dsmc}}(\boldsymbol{x}_i)$, which are different from zero only at the interface, are the net contribution resulting from momentum and energy exchange of the gas molecules impinging on the surface and can be expressed in the following way

$$\boldsymbol{\chi}_i^{\text{dsmc}} = \frac{W_{\text{p}} \sum_{j \in \mathcal{I}_i^{\text{s}}} \mu_j \ (\boldsymbol{\xi}_j^{\text{old}} - \boldsymbol{\xi}_j^{\text{new}})}{m_i \ N_{\text{s}} \ \Delta t} \tag{6.42}$$

and

$$\Gamma_i^{\text{dsmc}} = \frac{W_{\text{p}} \sum_{j \in \mathcal{I}_i^{\text{s}}} \frac{1}{2} \ \mu_j \ (|\boldsymbol{\xi}_j^{\text{old}}|^2 - |\boldsymbol{\xi}_j^{\text{new}}|^2)}{m_i \ c_{\text{p,c}_i} \ N_{\text{s}} \ \Delta t}, \tag{6.43}$$

where molecular velocities before and after the impact appear in the expressions, and the sum is accumulated over a collection of DSMC molecules $\mathcal{I}_i^{\text{s}}$, which have impinged the SPH particle i over N_{s} sampling timesteps.

9. The DSMC molecules belonging to the same cell can collide among themselves. The velocities are updated according to the local homogeneous relaxation equation, following the procedure illustrated in Section 3.3.1.

10. Macroscopic properties of the gas are computed in each DSMC cell as detailed in Section 3.3.1.

Finally, we recall that the timescales of the liquid and the gas are usually very different, the latter being much faster. Therefore, it is not always necessary to exchange the information between the two phases at each timestep. The possibility of averaging in a wider time window, i.e. $N_{\text{s}} >> 1$, can reduce the statistical noise introduced at Step 8 due to the stochastic nature of the DSMC methodology.

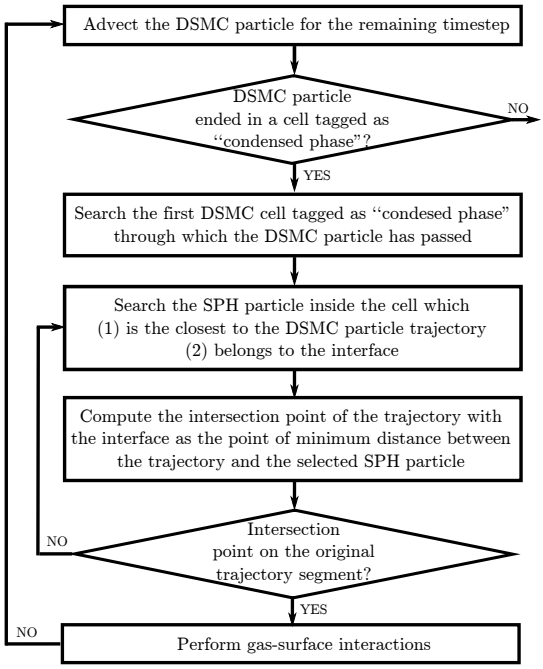

Figure 6.4.: *Details of the algorithm developed for Step 6 in the coupling procedure.*

6.4. Numerical tool

SPH routines from the open-source SPHysics software[4] [Gomez-Gesteira et al., 2012b], available online at `https://wiki.manchester.ac.uk/sphysics/index.php/Main_Page`, were embedded in the in-house DSMC code, TheGambler, developed for the purpose together with the coupling interface between the physical phases. SPHysics had been validated against experimental results in dam-break and sloshing flows [Gomez-Gesteira et al., 2012a]. We have taken advantage of the established capabilities of this tool, while others have been added and verified. In particular, in the SPH solver, the following features have been implemented:

1. the viscosity term in Equation 6.31;
2. the surface tension term in Equation 6.31;
3. the energy balance (Equation 6.32);

[4]Version 2.2.0, released under GNU General Public License version 3.

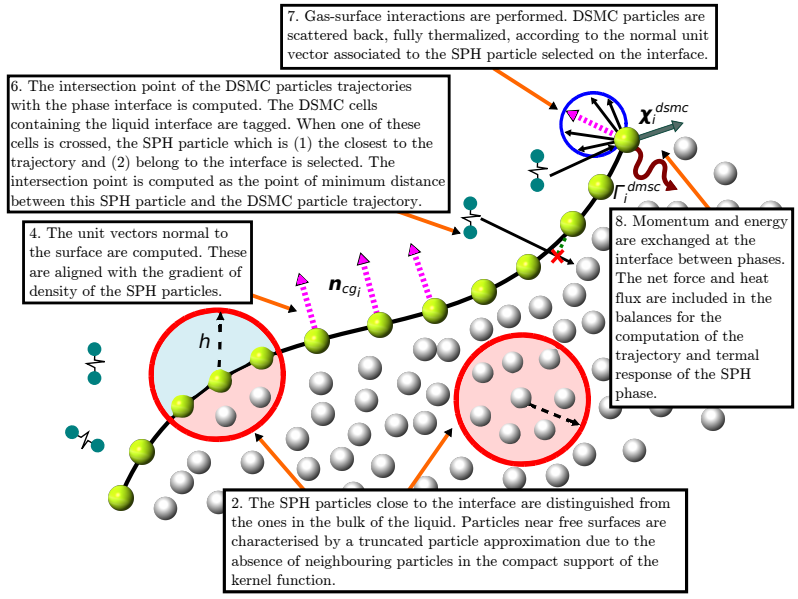

Figure 6.5.: *Schematic of the main steps in the SPH-DSMC coupling procedure presented in Section 6.3.2.*

4. the melting model detailed in Section 6.3.2;
5. the procedure for accounting for evaporation reported in Section 6.3.2.

In the following section, we present some intermediate verification cases, where the implementations of the two numerical techniques are tested separately. Other test cases are reported in Appendix D.

6.5. Model testing and intermediate verification cases

6.5.1. SPH-condensed phase

Melting of a slab with imposed external shear, pressure gradient, and heat flux

The effects of the gas phase are mimicked by means of an imposed pressure gradient $\partial p/\partial x = 10$ Pa/m, shear stress $\tau_{\mathrm{cg}} = 5 \times 10^{-6}$ Pa, and heat flux $q_{\mathrm{cg}} = 6$ MW/m^2 acting on a slab. A schematic representation of the problem is given in Figure 6.6, where the solid slab is at an initial temperature $T_0 = 240$ K below the melting temperature T_{m}. The lower boundary is kept at constant temperature equal to the initial one. At $z = D = 10^{-3}$ m, we impose the shear stress and the heat flux. The latter induces the slab to melt, and the formed

liquid layer is progressively set in motion by the combined action of the shear and pressure gradient. A periodic boundary condition is applied at the sides of the domain. Moreover, we implement the shear stress condition on the upper boundary by adding the following source term to interface SPH particles in Equation 6.31

$$a_i = \frac{\tau_{\mathrm{cg}}\ \Delta x_i}{m_i}\ \delta_{\mathrm{cg}_i}. \tag{6.44}$$

Also, Δt is fixed to 10^{-6} s and a uniform particle lattice ($\Delta x = \Delta z = 5 \times 10^{-6}$ m, with $h = 1.2\Delta x$) is employed. The physical parameters employed for this test case can be found in Table 6.1.

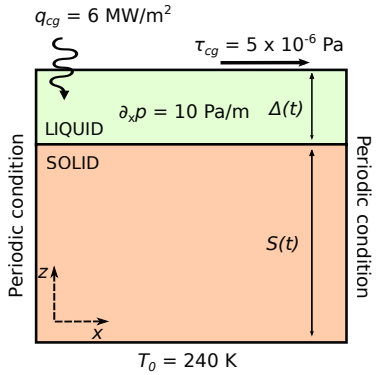

Figure 6.6.: *Schematic of the simulation. A Dirichlet boundary condition is applied at the lower wall, whereas Neumann conditions are used for the upper boundary. Periodicity is enabled at the sides of the domain.*

For this problem, an analytical solution exists only in steady state and in the solid reads as

$$T_{\mathrm{s}} = \frac{T_{\mathrm{m}} - T_0}{S_{\mathrm{eq}}} z + T_0 \tag{6.45}$$

and in the liquid as

$$T_{\mathrm{l}} = \frac{q_{\mathrm{cg}}}{\lambda_{\mathrm{l}}}(z - S_{\mathrm{eq}}) + T_{\mathrm{m}}, \tag{6.46}$$

where the position of the solid-liquid interface at equilibrium is

$$S_{\mathrm{eq}} = \frac{\lambda_{\mathrm{s}}(T_{\mathrm{m}} - T_0)}{q_{\mathrm{cg}}}. \tag{6.47}$$

Once the slab starts melting, a velocity profile develops in the liquid layer until it reaches the final steady state

$$v_{\mathrm{l}} = \frac{1}{\eta_{\mathrm{l}}}\left[\left(\tau_{\mathrm{cg}} - \Delta\frac{\partial p}{\partial x}\right) z_{\mathrm{l}} + \frac{1}{2}\frac{\partial p}{\partial x} z_{\mathrm{l}}^2\right], \tag{6.48}$$

where z_{l} coordinate has its origin at the $z = S_{\mathrm{eq}}$, and Δ is the thickness of

the liquid layer. A comparison between the SPH numerical solution and the exact steady states is shown in Figure 6.7 for both the temperature and velocity profiles, which appear to be in excellent agreement.

Also, a fictitious recession velocity v_r can be defined by integrating $v_\mathrm{l}(z_\mathrm{l})$ over the thickness of the molten layer Δ

$$v_\mathrm{r} = \int_0^\Delta v_\mathrm{l}\, dz = \frac{1}{\eta_\mathrm{l}}\left[\frac{1}{2}\Delta^2\tau_\mathrm{cg} - \frac{1}{3}\Delta^3\frac{\partial p}{\partial x}\right], \tag{6.49}$$

where we consider the slab of unitary length. A similar formula was derived by Bethe [1959] to model the mechanical removal of the liquid layer. Such a method describes the mass loss by considering a series of steady states and assumes the condensed phase to adapt instantaneously to changes of the external gas flow.

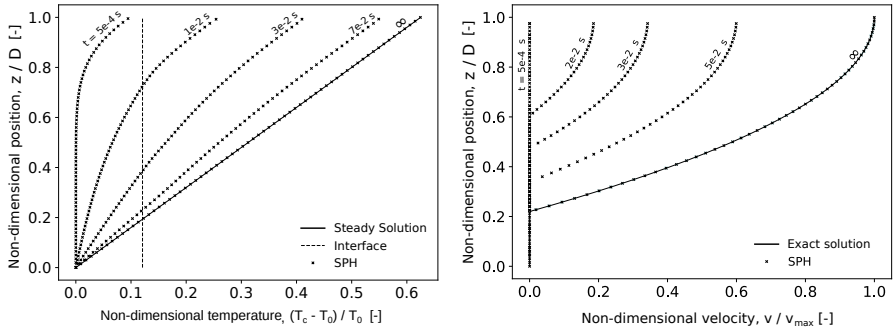

(a) **(b)**

Figure 6.7.: *Temperature (a) and velocity profiles (b) at different timesteps. At steady state (marked with ∞), the SPH solution is compared with the exact one.*

Table 6.1.: *Physical parameters employed for the test cases presented in Section 6.5.1. Quantity ν_l stands for the kinematic viscosity of the liquid phase, defined as η_l/ρ_c.*

ρ_c [kg/m^3]	ν_l [m^2/s]	λ_c [W/m/K]	$c_\mathrm{p,l}$	$c_\mathrm{p,s}$ [J/kg/K]	T_m [K]	L_m [J/kg]
1000	2×10^{-5}	40	4186	2220	273	3.3×10^4

6.5.2. DSMC-gas phase

Hypersonic gas flow about a cylinder

This test case consists in a hypersonic argon flow ($\mathrm{Kn}_\infty = 0.25$, $\mathrm{Ma}_\infty = 25$, and $T_\infty = 200$ K) developing around a solid cylinder, whose wall temperature is equal to 1500 K. The employed VHS data are given in Table 6.2. A comparison of the temperature field obtained with a classic DSMC boundary condition is shown in Figure 6.8. The solution is compared with the one reported by Lofthouse [2008], which is used as a reference. In the gas, around 50 simulated molecules are present in each cell. The mesh size is $\Delta x = 2 \times 10^{-4}$ m, which is enough to satisfy the DSMC accuracy condition $\Delta x < \tilde{\lambda}/3$, even at the stagnation point. This DSMC simulation takes only a few hours on a normal laptop.

Moreover, we compare the results obtained with a classic DSMC boundary condition with those attained through the DSMC-SPH boundary procedure, where SPH particles are kept at a fixed position in the domain. In the classic DSMC boundary condition, both the normal to the surface and the point of intersection of the DSMC molecule trajectory with the solid wall are computed analytically. Figure 6.9 shows gas temperature, number density, and velocity profiles along the stagnation line in the front and in the rear of the cylinder, for all the three cases, where the implemented boundary condition proves to perform well for the chosen conditions.

Table 6.2.: *VHS parameters used for argon.*

μ [kg]	T_{ref} [K]	d_{ref} [m]	ω [-]
66.335×10^{-27}	1000	3.595×10^{-10}	0.734

Subsonic Couette gas flow

We examine a subsonic Couette gas flow, and we compare the standard DSMC gas-surface interaction procedure with the strategy proposed in this work to deal with the SPH-DSMC interface.

A sketch of the simulation is provided on the right-hand side of Figure 6.10. At the beginning, the gas is at rest and in thermal equilibrium with the boundaries at $T_\mathrm{w} = 200$ K, as it is confined between two buffers of SPH particles, distance $D_\mathrm{g} = 0.1$ m apart. The upper buffer starts moving with a prescribed velocity $V_\mathrm{w} = 26.34$ m/s, which is low enough not to induce a significant thermal field in the gas. The lower buffer is static. Employed VHS parameters are reported in Table 6.2. The DSMC phase is discretised with 1000 cells along the height of the channel D_g, and about 200 simulated molecules are present in each cell.

After the initial transient phase, during which the gas inside the channel is accelerated by the moving wall, a steady state is gradually reached, and

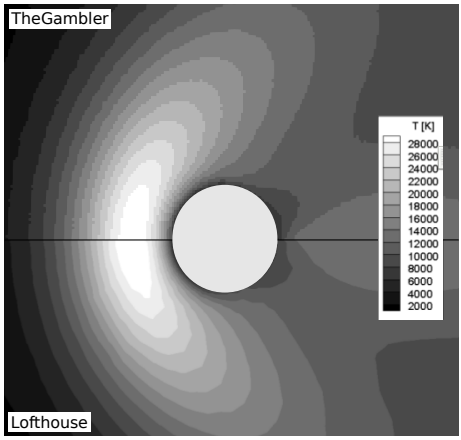

Figure 6.8.: *Temperature field for a hypersonicargon flow around a cylinder ($Kn_\infty = 0.25$ and $Ma_\infty = 25$). We compare the standard DSMC boundary procedure with Lofthouse [2008].*

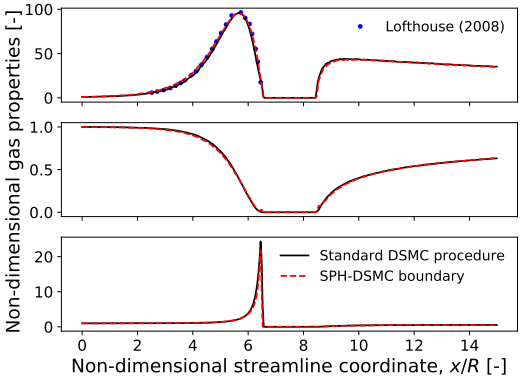

Figure 6.9.: *Gas properties along the stagnation line in front and in the wake of the body. The effect of the SPH-DSMC boundary procedure with respect to the standard one is examined.*

the final velocity profile is established. In Figure 6.10, the steady-state velocity profiles are plotted, and it can be seen that the proposed gas-surface interaction procedure is substantially equivalent to the standard one.

A parametric study is conducted to observe the behaviour of the system in function of the degree of rarefaction of the gas ($\mathrm{Kn} = 10^{-2}, 10^{-1}, 1$). Slip velocities of the gas at the interface with the SPH phase are more and more significant at high Knudsen numbers, when nonequilibrium effects cease to be confined in kinetic regions in the nearby of the interfaces, the so-called *Knudsen layers* [Kogan, 1969].

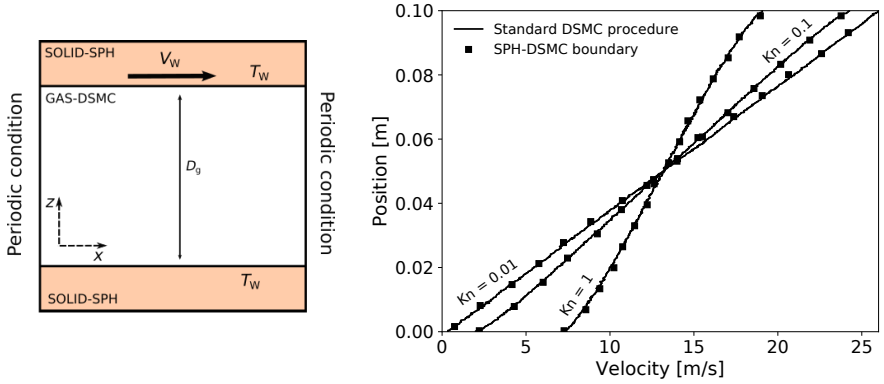

Figure 6.10.: *(a) A sketch of the simulation. The two walls are composed of SPH particles, and periodicity is enabled at the sides of the domain for both SPH and DSMC particles. (b) Velocity profiles in the gas phase at steady state for different Knudsen numbers. The proposed gas-surface interaction procedure proves to perform well for the tested conditions.*

6.6. Results and discussion

The thermal and dynamic coupling between the gas and the condensed phase is now taken into account. In this way, external forces and heat acting on the condensed phase are no more assigned boundary data, but they are obtained from the direct interaction between the DSMC-vapour and the SPH-solid/liquid phase.

6.6.1. Supersonic Couette gas flow over a melting slab

A gas is confined between an infinite wall and an infinite solid slab, distance $D_g = 0.1$ m apart. The gas is set in motion by the upper wall at temperature $T_u = 2000$ K, sliding at velocity $V_u = 832.95$ m/s. If the velocity of the wall is large enough, heat is transferred from the gas layer to the solid slab, which melts. A velocity and temperature profile forms in the liquid layer, resulting in a two-layer Couette flow, where the thickness of the liquid layer D_l is not known a priori. The slab is $D_c = 1.02 \times 10^{-3}$ m in height, and the temperature at its bottom is kept at a value equal to $T_0 = 300$ K. A schematic of the test case, along with reference axes is provided in Figure 6.11, whereas the properties of the gas and the condensed phase are provided in Tables 6.3 and 6.4.

We are interested in comparing a semi-analytical solution based on Navier-Stokes with the numerical result from the SPH-DSMC coupling. In this test case, the gas is characterised by a Knudsen number equal to 10^{-2}, based on the height of the channel. At these regimes, nonequilibrium effects are confined in

Table 6.3.: *Physical parameters used to model the condensed phase in the melting slab.*

ν_l	ρ_c	λ_l	λ_s	T_m
$[\mathrm{m}^2/\mathrm{s}]$	$[\mathrm{kg}/\mathrm{m}^3]$	$[\mathrm{W}/\mathrm{m}/\mathrm{K}]$		[K]
10^{-8}	10^{3}	10^{-4}	10^{-5}	900

Table 6.4.: *VHS parameters used for the supersonic Couette gas flowing over the melting slab.*

μ	T_ref	d_ref	ω
[kg]	[K]	[m]	[-]
66.335×10^{-27}	2000	3.595×10^{-10}	1.0

the Knudsen layers at the interfaces. This results in velocity and temperature jumps at the boundaries of the vapour phase that, if they are naturally accounted by the Boltzmann equation, need to be included in the hydrodynamic solution using proper jump conditions. This solution is described in detail in Appendix E, but we should note that the jump conditions introduce a dependence on the density field of the velocity and temperature profiles, which does not exist in the continuum limit. The comparison between the SPH-DSMC coupling shows a very good agreement with the presented semi-analytical approach as shown in Figure 6.11. The numerical solution is obtained by averaging in time, once the final steady state is reached. This simulation took around 20 days on a normal laptop to converge to a steady state, and a few days more were necessary to collect the sample used to average the profiles in the gas. The final solid fraction represents 4.44% of the total condensed phase. Velocity and temperature jumps are reported in Table 6.5.

Table 6.5.: *Velocity and temperature jumps predicted by the semi-analytical solution provided in Appendix E.*

Phase	Wall-vapour interface		Vapour-liquid interface	
	v	T	v	T
	[m/s]	[K]	[m/s]	[K]
Condensed	833.0	2000.0	72.6	2190.2
Vapour	821.4	2015.6	84.7	2195.4

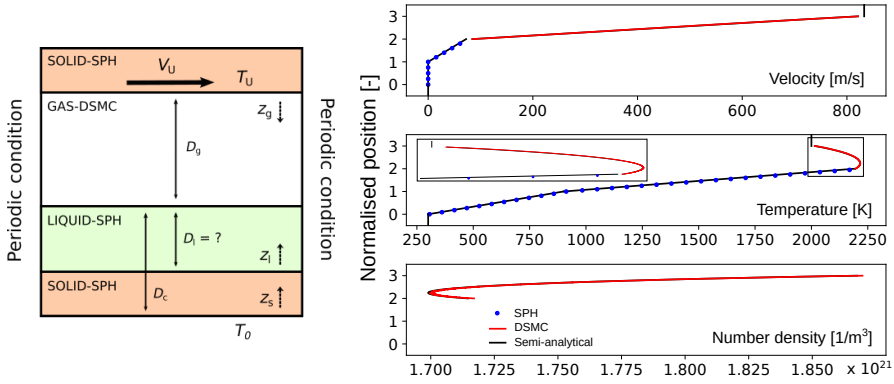

(a) **(b)**

Figure 6.11.: *(a) A sketch of the simulation is shown. (b) Semi-analytical and numerical profiles for velocity, temperature, and density in the gas and condensed phase at steady state. The position along the three coordinate systems is normalised with respect to the thickness of each phase.*

6.6.2. Thermal and dynamic coupling between a rarefied hypersonic gas flow and a melting cylinder

We examine the same argon flow around a cylinder that we have considered in Section 6.5.2 ($\mathrm{Kn}_\infty = 0.25$ and $\mathrm{Ma}_\infty = 25$, the latter being well below characteristic meteor conditions). This time we allow for energy exchange between the gas and the condensed phase. At first, momentum coupling between the gas and the liquid is not enabled, nor is evaporation. Physical properties of the cylinder are summarised in Table 6.6 and were arbitrarily chosen to shorten the timescale of the conjugate heat transfer problem. For the discretisation of the 0.01 m cylinder, we use nearly 35 000 SPH particles, immersed in a DSMC grid, whose cell size is $\Delta x = 2 \times 10^{-4}$ m. The calculations took around five days, running on a quad-core Intel Core i7-6820HQ processor at 2.7 GHz.

The initial temperature of the cylinder is set equal to 500 K and grows in time as the molecules of gas transfer their energy to the wall. As a result, the cylinder heats up until it melts. The progressive formation of the liquid layer is shown in Figure 6.12. Here, the cylinder is coloured according to the phase: grey stands for the solid, white for the mushy zone, taken as an interval ± 5 K across the melting point, and red for the liquid. For the gas phase, we show the field of translational temperature. It is possible to observe the evolution of the melting front, advancing faster in the forehead area than in the shoulders of the cylinder. Eventually, the heat wave reaches the rear of the object. The entire process lasts about one hundredth of a second.

In a second moment, the molten layer is allowed to move, by enabling the dynamic coupling between the phases. The liquid is set in motion by the action

of the external gas. In particular, in Figure 6.13, we present the evolution of the tangential velocity inside the liquid layer over time. Velocity profiles are plotted for different angular positions. These profiles are non-linear and seem to find a steady condition. The simulation were interrupted before the possible detachment of droplets from the molten surface. The formation of small liquid structures requires the local refinement of the DSMC grid, which is employed in the procedure detailed in Figure 6.4, for the detection of the vapour-liquid interface (in particular we use the DSMC cells to compute the intersection of the gas molecules with the liquid surface). Moreover, the implementation of local particle refinement techniques in the SPH phase is necessary to simulate the dynamics of fluid structures that are much smaller than the original cylinder.

Table 6.6.: *Physical parameters used to model the condensed phase in the cylinder. These properties were arbitrarily chosen to shorten the time scale of the conjugate heat transfer problem.*

ρ_c [kg/m^3]	ν_l [m^2/s]	λ_l	λ_s [W/m/K]	$c_{p,l}$	$c_{p,s}$ [J/kg/K]	T_m [K]	L_m [J/kg]
3000	3×10^{-3}	33.3	3.3	8.3	5.1	1923	3.33×10^5

6.7. Concluding remarks

We have presented a numerical procedure to model melting in the presence of a rarefied gas phase. Under the effect of external aerodynamic loads, the molten liquid is progressively taken away and eventually evaporates. We have tackled the problem by developing and implementing a tight coupling of the DSMC and the SPH techniques, respectively for the gas and the condensed phase.

After presenting the relevant mathematical and numerical models, we have dwelt on the coupling methodology between the two computational techniques. In particular, the treatment of the interfaces has been detailed. The solid-liquid interface can be dealt with the apparent heat capacity technique to account for the latent heat of melting. Concerning the gas-liquid boundary, thermal and dynamic coupling is achieved by applying classical kinetic boundary conditions for the vapour at the interface. Momentum and energy are exchanged between liquid and gas after the interaction of the molecules of gas with the free surface.

Some verification test cases have been examined to show the ability of the code to accurately solve for the vapour and the condensed phases separately. After, the thermal and dynamic coupling has been proven in some simplified configurations. The most significant one consists of a slab of material which melts under the effect of a supersonic Couette flow. For this case a semi-analytical solution has been found in the slip regime.

Finally, we have considered the melting of a solid cylinder immersed in a

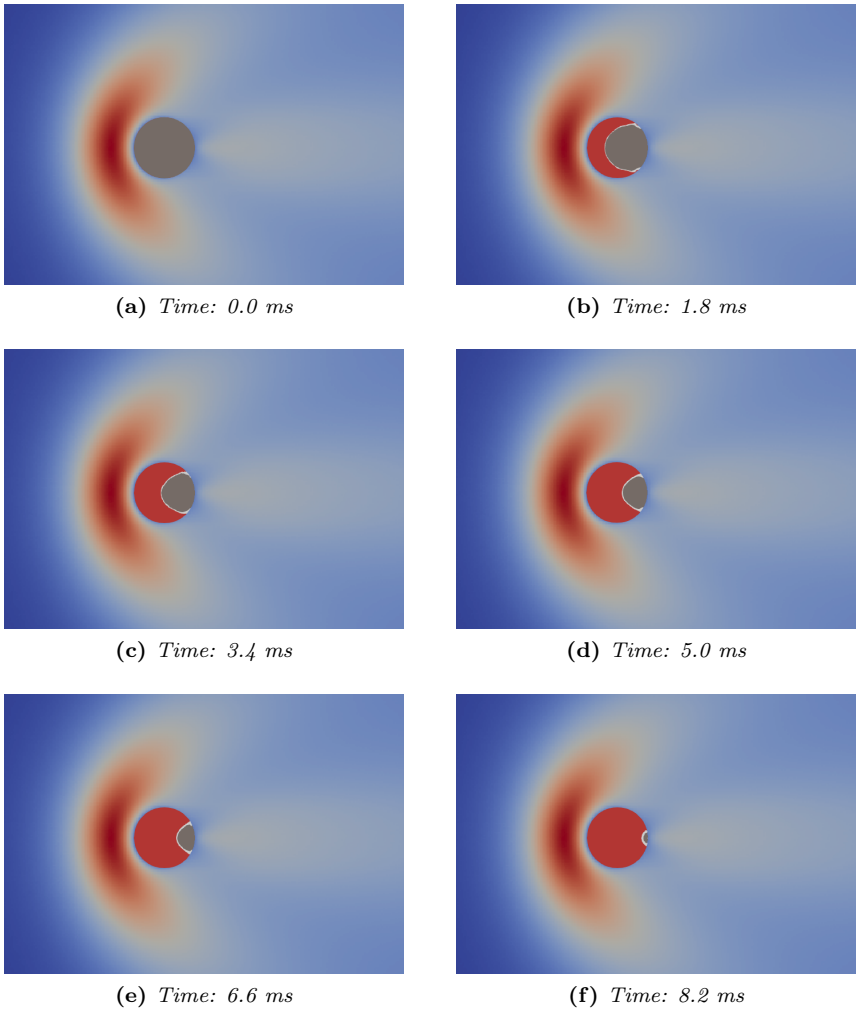

(a) *Time: 0.0 ms* **(b)** *Time: 1.8 ms*

(c) *Time: 3.4 ms* **(d)** *Time: 5.0 ms*

(e) *Time: 6.6 ms* **(f)** *Time: 8.2 ms*

Figure 6.12.: *From an initial solid state, the cylinder completely melts in about one hundredth of a second. The colours of the cylinder indicate the phase: grey stands for the solid, white for the mushy zone, and red for the liquid. For the gas phase, we show the field of translation temperature.*

rarefied hypersonic stream. The dynamics of the formed molten layer under the influence of the external flow has been analysed. A two-way coupling between phases has been pursued, at the expense of other possibly relevant phenomena such as evaporation or chemical nonequilibrium of the gas phase, which have not been taken into account. Moreover, at this stage, the code cannot address the formation of droplets detaching from the main body. In order to deal with large deformations of the interface, the code would require the implementation of local mesh/particle refinement techniques in the proximity

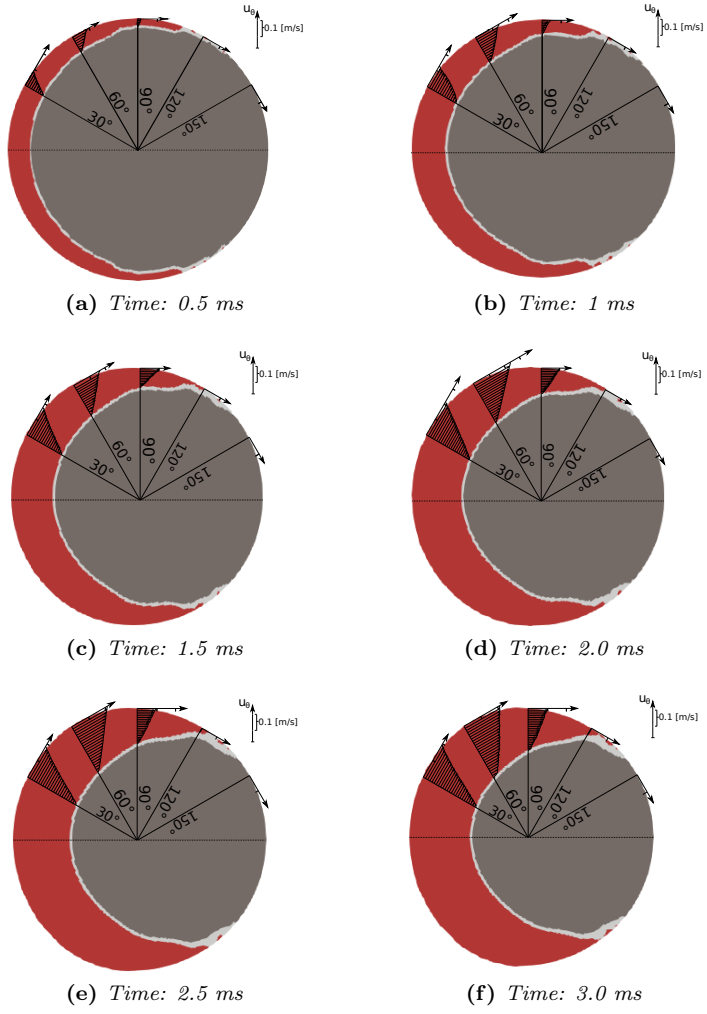

(a) *Time: 0.5 ms* **(b)** *Time: 1 ms*

(c) *Time: 1.5 ms* **(d)** *Time: 2.0 ms*

(e) *Time: 2.5 ms* **(f)** *Time: 3.0 ms*

Figure 6.13.: *A cylinder is immersed in a rarefied hypersonic flow. Due to the action of the gas, the cylinder first melts and then the molten layer deforms. The colours of the cylinder display the phase: grey stands for the solid, white for the mushy zone, and red for the liquid. Also, tangential velocity profiles, induced in the liquid, are plotted at different angular positions.*

of the free boundary.

Although our main results have been obtained neglecting the mass transfer between liquid and gas, we have proposed an approach to model evaporation. The step-wise SPH particle removal procedure has been tested in an exploratory test case to show its effectiveness, and it is ready to be assessed in more complex simulations.

CHAPTER 7

Conclusions and Perspectives

> *"All knowledge of reality starts from experience and ends in it. Propositions arrived at by purely logical means are completely empty as regards reality. Because Galileo saw this, and particularly because he drummed it into the scientific world, he is the father of modern physics - indeed, of modern science altogether."*
>
> – Albert Einstein

Since scientists have laid the foundations of the physical theory of meteors, in the first part of the 20th century, they have mainly focused on the development of synthetic models. These models are agile and based on algebraic relations, and they condense the complexity of the problem in a few free physical parameters. This intrinsic simplicity made them suitable for parametric studies and fitting of observational curves.

This type of approach has proved to be successful in explaining some of the macroscopic features of meteor observations. However, the latest progress in detection techniques has yielded drastic improvements in the quality and quantity of observational data. Most recent researches in the field have demonstrated that our understanding of plasma and hypersonic physics in the rarefied regime (between 70 and 130 km) is far from being complete since it is not adequate to explain observed phenomena.

Besides observations, from this moment forward, further progress in this discipline is likely to be achieved mainly via computer simulations. Studies relying on synthetic theories, exact approaches, and nondimensional analysis are of paramount importance, yet they struggle to lead to firm conclusions. Difficulties principally arise from the intercoupling of phenomena and multi-scale physics. Important factors risk being neglected solely for mathematical expediency.

Therefore, the goal of this work was to develop a rather general numerical methodology to describe the main physico-chemical processes characterising meteors. In particular, our focus was set on radio meteors, whose detection occurs in the rarefied segment of their entry trajectory.

In the next section, we will summarise the main contribution of this work. In Section 7.2, we will suggest possible improvements and promising research directions for future work.

7.1. Contribution of this work

At the beginning of this manuscript, we had identified two primary areas of improvement for current approaches, and we had distilled each of them into a technical objective: Objective 1. Modelling of the gas-surface interactions; Objective 2. Modelling of the ablated vapour and free electrons. What follows is the synthesis of the outcome of this dissertation into these two objectives. For each objective, we highlight the contribution provided, and we underline the limitations.

Modelling of the gas-surface interactions

Our knowledge of meteor gas-surface interactions mainly relies on the geochemical characterisation of meteorites or observations. However, a chemical inspection of the samples collected on the ground provides information about the outcome of the trajectory, without the possibility to understand which conditions these features are related to. Moreover, the interpretation of observational data is founded on lumped models that correlate the plasma signature to a radio signal from which size, velocity and composition of the body are inferred.

Hence, to gain a better understanding of the ablation process, we decided to develop devoted numerical models and to simulate the gas-surface interactions in ground experiments. This combined effort provided the opportunity to look at the degradation process in detail, with the possibility of focusing on well-defined flight conditions and material properties.

Modelling work relevant to gas-surface interactions was presented in Chapter 3, for evaporation, and in Chapter 6, for melting and mechanical removal. Both these chapters pertain to the framework of the DSMC method, but they were developed independently because they fulfil different roles in our investigation.

On the one hand, in Chapter 3, we studied the effect of the ablation process on the flowfield but not vice-versa. The evaporation boundary condition served as a modelling ingredient to investigate the formation of the plasma around the meteoroid (Objective 2.a). In the workflow of the thesis (see Figure 1.8), this is a necessary input to study the ion dissipation in the trail (Chapter 5, Objective 2.b). On the other hand, Chapter 6 was conceived to design a computational methodology for the study of the molten layer dynamics under the influence of the external flow. This task was set in the light of the experimental results obtained in Chapter 4, which underlined abundant melting and mechanical removal in the ablation process.

Chapters 3 and 6 are complementary in the level of complexity that they try to describe. In Chapter 3, a classical evaporation boundary condition was imposed on a fixed interface. The condensed phase was assumed to have constant and uniform temperature as well as constant chemical composition. The flowfield around the meteoroid is affected by evaporation, but the molten phase composition and temperature are not affected by the vapour (one-way cou-

pling). Chapter 6 was devoted to the development of a computational methodology. This methodology allows the study of melting when the gas phase is rarefied, the interfaces between phases are moving, and their position is a priori unknown. The approach adopted in Chapter 6 is computationally more intensive than the one of Chapter 3, as it proposes to describe the dynamics of the three phases comprehensively. In this case, a two-way coupling between phases was pursued, at the expense of other possibly relevant phenomena such as evaporation or chemical nonequilibrium of the gas phase, which were not taken into account.

Even given drawbacks and limitations, both the approaches represent evident advancements to the current state-of-the-art. The evaporation model in Chapter 3 is suitable for multicomponent mixtures and can take into account nonequilibrium condensation fluxes and the backscattering of molecules at the wall, phenomena that are usually disregarded in meteor analysis. This proved to be significant for events below 100 km, and it is expected to be even more meaningful for bigger meteoroids or higher ablation rates. To our best knowledge, the simulations presented in Chapter 6, where we considered a melting cylinder immersed in a rarefied hypersonic stream, are the first of their kind in the literature. However, while the implementation of the coupling procedure between phases was successfully verified, important limitations still exist when the free surface is significantly deformed. At the current stage, we cannot model the formation of droplets and their spraying from the surface, since it would require further development of the code (we will briefly address this issue in Section 7.2).

In Chapter 4, we presented two experimental campaigns, carried out in the VKI Plasmatron wind tunnel (low convective heat flux, mild evaporation) and in the NASA Ames laser ablation facility (high radiative heat flux and intense evaporation). Although both experiments failed in reproducing the rarefied environment of real-flight conditions, these tests were especially useful to yield insight into the ablation mechanisms: they confirmed strong degassing and volatilisation of light species, boiling of the material, and they gave indication that, in real flight, mechanical removal of the melt phase may represent the primary mechanism of mass loss, before complete vaporisation of the droplets. In addition, iron oxidation was observed.

Geochemical characterisation of the recovered material demonstrated the successful use of these type of facilities to reproduce fusion crusts similar to those collected on the ground. This paves the way for intensified analysis of meteor data by comparing ground-tested materials with collected meteorites and, therefore, may help to better characterise the composition and origin of meteors.

Finally, measurements of the surface temperatures coupled with thermal response modelling of the material helped in refining the understanding of the surface energy balance. Despite the simplicity of the numerical model, simulations and pyrometry data were found to agree reasonably well in laser experiments, while needed a tuned contribution of the oxidation heat flux in the Plasmatron tests. Under intense evaporation conditions, the cooling effect pro-

vided by the Knudsen-Langmuir law was sufficient to justify the temperature plateaus observed in laser tests. On the contrary, it is not possible to predict the low evaporation rates experienced by the samples in the Plasmatron without a two-way coupling simulation approach between gas and material.

Modelling of the ablated vapour and free electrons

Meteors are characterised by extensive spatial scales whose simulation constitute a formidable challenge. The ionisation process occurs in the space of a few mean free paths from the body, while the subsequent recombination and diffusion of ions takes place in trails that can develop for kilometres. In Chapters 3 and 5, we tried to tackle this problem.

In Chapter 3, collisional nonequilibrium processes related to the production of ions were addressed using the DSMC method. DSMC is an established method for the study of transitional flows, where the hydrodynamic regime does not hold, and analytical solutions cannot be found. Hence, it represents an excellent technique for the study of meteor flows, not least for the simplicity with which it is possible to include physico-chemical models in the algorithm. Detailed modelling of the dynamics of the rarefied gas in ablating meteoroids represents progress compared to the current literature.

In Chapter 5, the output of the DSMC simulations was used as an initial condition to compute the evolution of the metal compounds and ion dissipation with a Lagrangian approach. In this approach, a fluid element reactor marches along assigned streamlines, calculating multicomponent mass diffusion in the radial direction and detailed chemical reactions. Although we assumed (and verified) thermal equilibrium in the trail, the procedure is general and suitable for extensions. In future, one could include further nonequilibrium effects of the plasma, such a two-temperature model for ions and electrons.

Collisional processes and shielding effects investigated in Chapter 3 were shown to play a relevant role for some of the explored conditions, especially for intense evaporation and lower altitudes. Ionisation came mainly from the hyperthermal encounters between air and vapour, rather than from metal-metal collisions. The ionisation of air species, which is not considered by the classical theory of meteors, was always comparable to that of magnesium and iron atoms. In Chapter 5, recombination reactions had negligible effects in the neutralisation process of underdense trails, which were dominated by mass diffusion. Also, a common and constant diffusion coefficient, as used in standard models, was sufficient to reproduce the numerical profiles. The influence of chemistry and differential diffusion could be enhanced in overdense meteors, therefore this aspect deserves future investigation.

Transport and kinetic data provided in Chapters 3 and 5 should constitute a useful reference for future theoretical and numerical studies. In Chapter 3, although collision cross sections were derived under simplified assumptions, it is an attempt to address a complexity that had always been neglected. Among the critical issues that one could raise, we should mention that, in DSMC, we employed the Lennard-Jones potentials for all types of collision (including

those involving charged species), and that the model for reactive cross sections is semi-empirical and approximate in nature. In the former case, the choice was driven by simplicity, while in the latter, by the fact that a reliable theory and experimental data are still not available. In Chapter 5, where the diffusion process is driven by the interaction of the ions with neutral nitrogen, it was necessary to use the Langevin potential to reach diffusion rates close to those observed in meteor detections.

On the whole, the procedure presented in Chapters 3 and 5 represents a standalone methodology, which can provide meteor physical parameters at given trajectory conditions, without the need to rely on standard lumped models. To our knowledge, this is the first time that the radio signal of an underdense meteor has been reconstructed without relying on lumped models to describe either production or dissipation of the free electrons. Hence, we believe that this approach represents a useful addition to the field of meteor modelling in relation to radio-frequency technique and atmospheric chemistry.

General remarks on the methodology

The multiphysics nature of this phenomenon suggested not to restrict our focus on the study of a single aspect, but to embrace a heuristic approach, tackling this subject from different points of view. We employed a formal theoretical framework for the ablation process and the dynamics of the rarefied vapour, and we kept an explicit link between new developments and the classical approaches. For example, this link was shown discussing the relation between DSMC steric factors and ionisation efficiencies in Chapter 3, or the connection between the numerical simulations of the trail and the ambipolar diffusion coefficient in Chapter 5.

The developed tools and methodologies were verified with exact solutions for academic or reference test cases (e.g. in Chapter 2, the wall recession procedure was verified with an analytical test case, and the same was done for the SPH-DSMC coupling methodology developed in Chapter 6). When possible, the new data were compared with theoretical or experimental values from the literature. This was the case for some neutral alkali metals contained in the transport and kinetic database elaborated in Chapter 3. Other times, present results were compared with observations (e.g. the onset of evaporation in the entry trajectory analysis performed in Chapter 2 or the radio signal time decays obtained in Chapter 5).

Nevertheless, the proposed modelling approaches were not comprehensively validated. A critical review of modelling assumptions is challenging because the access to a number of the internal states of the target system is complicated, and observations are not always very detailed and rarely highly resolved. Epistemic uncertainties can be relevant sometimes because we do not have an adequate understanding of the processes (e.g. the excitation of the internal energy modes); sometimes because certain phenomena were deliberately neglected (e.g. boiling or oxygen accommodation on the melt). Also, we had to face a general lack of reliable data to use in the simulations, two for all, the

collision cross sections of the ablated vapours and the physical properties of the meteoroids that, especially at high temperature, are not well characterised in the literature. Advancements in meteor theory have been historically achieved through the method of trial and error. Therefore, the comparison with observational data and ground experiments represents a future vital validation step.

To conclude, we are confident that this dissertation has put together the fundamental tiles of a broader and ambitious modelling effort that will help astronomers to reduce uncertainties in the interpretation of radio echoes and meteor detection in general.

7.2. Recommendations and perspectives

Nowadays, computer modelling can provide a level of detail that is above that given by observations, considering that detected meteors reveal themselves only through a subset of observable states. However, further development of numerical simulations is limited by the scarcity of reliable and detailed observations. High-spatially resolved detections are difficult to realize, therefore scarce, nonetheless of vital importance to improve the accuracy of the simulations, and allow for validation of physical models. In addition, meteors are frequent events, and this makes data reduction and statistical treatment possible. The BRAMS network collects thousands of detections each year [Lamy et al., 2011]. The well-established Canadian Meteor Orbit Radar (CMOR) is able to record approximately 2500 meteoroid orbits per day [Jones et al., 2005]. Therefore, machine-learning algorithms could represent a new horizon to extract valuable knowledge about the physics involved.

Meteors have an enormous scientific potential, yet unexploited. Aerospace engineers and plasma physicists should look at meteors in the attempt to extend, train, and ultimately validate their models in the presence of a high degree of thermo-chemical nonequilibrium. Meteors provide a unique opportunity to validate theoretical models and engineering tools against natural free experiments, and measurements otherwise not available.

Finally, some of the key issues that were raised in this work lay on the boundaries between different disciplines. Research fields such as aerospace engineering, plasma physics, aeronomy, and geochemistry will have to establish tighter relations if a breakthrough in meteor science has to be achieved.

Possible modelling research directions

Modelling of the gas-surface interactions

In the light of the experimental results, the effects of oxygen accommodation on the molten phase deserve further investigation. Atmospheric oxygen reacts with the liquid, modifying the chemical composition and shifting its equilibrium condition. Doing so, it also affects the evaporation process and the surface energy balance.

Concerning the SPH-DSMC coupling procedure, in the presence of large deformations of the interface (e.g. to address formation of droplets and entrainment of the liquid phase in the gas flow), it will be necessary to implement a dynamic mesh refinement technique [Garcia et al., 1999, Zhang and Schwartzentruber, 2012] in the proximity of the SPH-DSMC boundary to accurately and efficiently solve for gradients in the gas phase. Moreover, one should consider the implementation of a SPH particle refinement technique [Barcarolo et al., 2014] or a particle shifting algorithm [Vacondio et al., 2013].

Modelling of the ablated vapour and free electrons

Accurate modelling of plasma effects in rarefied flows can be provided by coupling DSMC and PIC methods. As a future step, it would be interesting to relax the ambipolar assumption in the shock layer [Farbar and Boyd, 2010], and account for the Earth's magnetic field [Oppenheim and Dimant, 2015] in the trail. So far, no attempts have been made to include complex kinetics and proper ablation modelling in PIC simulations of meteors.

Moreover, radiative heat transfer may play a major role in the meteoric phenomenon. Most probably, the gas radiation has tremendous cooling effects: in the shock layer, where it could lead to photoionisation [Dias et al., 2018, Dias et al., 2020]; in the trail through radiative recombination processes [Plane et al., 2015]. At the same time, the emitted radiation reaches the surface of the object changing significantly the wall heat flux. Therefore, along with convective heating, radiative heat transfer must also be considered to make an accurate prediction of meteor degradation. Ambitious attempts to couple DSMC and radiative heat transfer codes are those by Ozawa et al. [2010] and Sohn et al. [2012].

Model validation

It will be desirable to examine the methodology against radio or radar observations, such as BRAMS or CMOR data, in order to compare experimental echoes with the ones synthetically generated through simulations. This procedure would provide validation of the models and further insight into the phenomena involved. Also, the electron fields obtained numerically open the possibility of employing more sophisticated methods to study in more detail the interaction of the plasma with the electromagnetic wave, e.g. Finite-Difference Time-Domain (FDTD) [Marshall and Close, 2015], optical ray tracing [Vecchi et al., 2004], or Volume-Surface Integral Equation (VSIE) [Sha et al., 2019] techniques.

A broader ambition: ablation modelling for artificial space debris

Meteoroids share a similar fate to that of artificial space debris as they undergo analogous degradation processes in their atmospheric entry. Therefore, the

ablation models developed and studied in this work could be further refined and extended to this field of aerospace science.

NASA estimates that the re-entry flux of orbital debris is nowadays superior to the flux of meteoroids[1]. Debris from launcher stages and satellites at end of life are increasingly becoming a threat for other space systems, but also a threat for mankind when, if not completely destroyed, they impact the Earth [Karrang et al., 2019]. To date, the exact mechanisms of the demise of space systems during their destructive re-entry are not understood.

While substantial progress has been made to model the physics of the flow and its interaction with materials at altitudes below 80 km, little progress has been made in the understanding of gas-surface interaction at higher altitudes [Koppenwallner and Lips, 2008, Liang et al., 2018]. Yet, during the initial phase of re-entry of space debris, significant processes like heating, melting and fragmentation take place. An accurate description of the ablation process during the re-entry of space debris is fundamental for the development of prediction tools for the evaluation of the risk at the ground and to infer the potential of survivability of the object [Lips and Fritsche, 2005, Wu et al., 2011].

[1] The number of artificial space debris in the Low-Earth Orbits (LEOs), which are at least 1 cm in size, exceeds 300 000 units.

Appendices

APPENDIX A

Verification of the FD tool for thermal response modelling

The developed numerical tool can model heat conduction in one-dimensional spherical and Cartesian domains, respectively for the solution of Equations 2.1 and 4.4. We verify the implementation for three different test cases. First, we consider the heat transfer inside a sphere with constant radius. Second, in Cartesian coordinates, we assess the methodology that allows the material to recede. Finally, we evaluate the accuracy with which the position of the melting front is computed through the apparent heat capacity method.

For all the cases, we employ 500 nodes for the spatial discretisation of the material, and we set a mesh Fourier number

$$\mathrm{Fo} = \frac{\lambda}{\rho c_\mathrm{p}} \frac{\Delta t}{\Delta x^2} \tag{A.1}$$

equal to 0.01 (we remind that Fo must be lower than 1/2 to satisfy the numerical stability). The employed physical properties are reported in Table A.1.

Table A.1.: *Physical parameters employed for the test cases presented.*

ρ [kg/m^3]	λ [W/m/K]	$c_{\mathrm{p,l}}$ [J/kg/K]	$c_{\mathrm{p,s}}$ [J/kg/K]	T_m [K]
1850	30	2000	3000	2000

Unsteady heat conduction in a sphere

We consider the thermal response of a sphere with radius $R = 0.2$ m and constant material properties. At the beginning, the temperature of the material is uniform at 0 K. When the surface of the sphere is exposed to a step in temperature till $T_\mathrm{w} = 4000$ K, an unsteady temperature profile $T(t, r)$ develops inside the body and satisfies the following relation

$$\Psi = \Psi_\mathrm{w}(1 - \mathrm{erf}\ \eta), \tag{A.2}$$

$\Psi(t, r)$ being a derived variable, defined as $\Psi = Tr$ (therefore $\Psi_w = T_w R$), and $\eta = \frac{x}{2\sqrt{\lambda/(\rho c_p)t}}$. The comparison between the numerical and exact solutions is provided in Figure A.1, for different instants in the simulation.

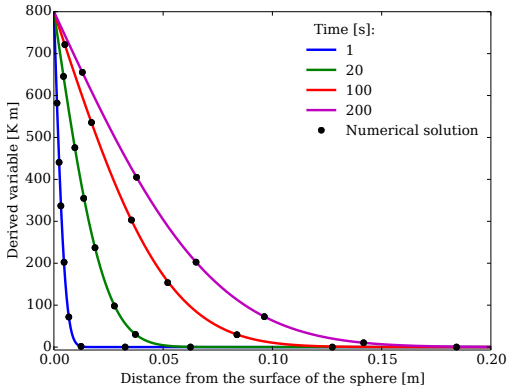

Figure A.1.: *Comparison between the exact and numerical temperature profiles to verify the solution of the heat equation in spherical coordinates.*

Steady-state recession in a semi-infinite slab

The effectiveness of the recession procedure is evaluated by comparing the numerical solution with an exact one for a one-dimensional semi-infinite slab, initially at a uniform temperature $T_0 = 300$ K. The slab is exposed to a step in the surface temperature $T_w = 4000$ K and in the surface recession velocity $V_w = 10^{-3}$ m/s. For constant properties, it can be shown that the temperature profile $T(r)$ approaches a quasi-steady form [Carslaw and Jaeger, 1959]

$$\frac{T - T_0}{T_w - T_0} = \exp\left\{ -\frac{\rho c_p}{\lambda} V_w r \right\}, \tag{A.3}$$

where the coordinate r has an origin that is tied to the receding surface. Therefore, one can write

$$r = x - V_w t, \tag{A.4}$$

x being the coordinate in a fixed reference frame. In other words, once the steady state is reached, the temperature profile does not change in shape, but it only translates in time with velocity V_w. Figure A.2 shows the comparison between the computed and exact profiles. For the numerical solution a finite slab of thickness $D = 0.2$ m is used, large enough to be sure that the heat wave cannot reach the final node during the computation. For the present conditions, after 100 s, the solution has reached the steady state, and the agreement between the profiles is excellent.

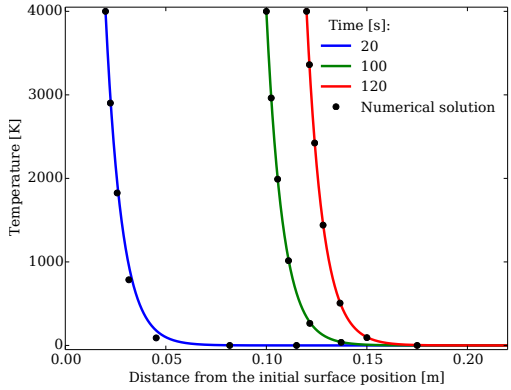

Figure A.2.: *Comparison between the exact and numerical temperature profiles for the verification of the receding wall procedure in Cartesian coordinates.*

Unsteady Stefan problem in a semi-infinite slab

Physicists refer to a free-boundary problem describing the temperature distribution in a medium that undergoes a phase change as *Stefan problem*. The classical solution to this problem can be obtained by solving two distinct heat conduction equations (one per phase), interfaced by a surface energy balance on the evolving boundary. An exact solution of the melting problem for a one-dimensional semi-infinite slab was obtained by Carslaw and Jaeger [1959]. In Figure A.3, we assess the accuracy of the equivalent capacity method by comparing the position of the melting front over time, $r_{\mathrm{sl}}(t)$, with the exact solution given by the following algebraic equation

$$\frac{T_0 - T_{\mathrm{m}}}{T_{\mathrm{w}} - T_{\mathrm{m}}} \sqrt{\frac{c_{\mathrm{p,l}}}{c_{\mathrm{p,s}}}} \frac{\exp\left\{ - c_{\mathrm{p,l}}/c_{\mathrm{p,s}}\ \eta^2 \right\}}{\operatorname{erfc}\left\{ - \sqrt{c_{\mathrm{p,l}}/c_{\mathrm{p,s}}}\ \eta \right\}} + \frac{\exp\{-\eta^2\}}{\operatorname{erf}\ \eta} - \frac{\sqrt{\pi}\ \eta\ L_{\mathrm{m}}}{c_{\mathrm{p,l}}} (T_{\mathrm{w}} - T_{\mathrm{m}}) = 0, \tag{A.5}$$

where variable $\eta = \frac{r_{\mathrm{sl}}}{2\sqrt{\lambda/(\rho c_{\mathrm{p,l}})t}}$ is its nondimensional root. We find a very good agreement between the two solutions ($T_{\mathrm{m}} = 2000$ K, $T_0 = 1000$ K, and $T_{\mathrm{w}} = 4000$ K). For the numerical solution, a finite slab of thickness $D = 0.2$ m is simulated. Also, the solution is plotted for different values of the latent heat, from which we can see how the melting front travels faster along the slab for lower values of L_{m}.

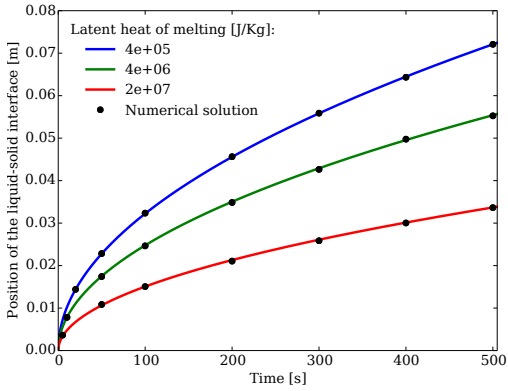

Figure A.3.: *Comparison between the exact and numerical position of the liquid-solid interface in the Stefan problem for the verification of the apparent heat capacity method.*

APPENDIX B

NASA Air-11 mixture: VSS model parameters and chemical mechanism

The NASA Air-11 mixture includes air neutrals and their ions, i.e. O_2, N_2, O, N, NO, O_2^+, N_2^+, O^+, N^+, NO^+, e^-. Table B.1 reports the employed VSS model coefficients that define the elastic cross sections in DSMC. Table B.2 shows the complete chemical mechanism in Arrhenius form [Park, 1993, Park et al., 2001].

Table B.1.: *VSS model parameters employed for the NASA Air-11 mixture. The reference temperature is 273.15 K.*

Interaction	d_{ref} [A]	ω [-]	α [-]
O_2-O_2	3.96	0.77	1.4
N_2-N_2	4.07	0.74	1.6
O-O	3.0	0.8	1.0
N-N	3.0	0.8	1.0
NO-NO	4.0	0.8	1.0
O_2^+-O_2^+	3.96	0.77	1.4
N_2^+-N_2^+	4.07	0.74	1.6
O^+-O^+	3.0	0.8	1.0
N^+-N^+	3.0	0.8	1.0
NO^+-NO^+	4.0	0.8	1.0
e^--e^-	7.0	0.5	1.0

Table B.2.: *Reaction rates included in the chemical mechanism for the NASA Air-11 mixture. Results obtained in Chapter 3 do not account for three-body reactions. References: (1) Park [1993]; (2) Park et al. [2001].*

Reaction	C_4 [m^3/mol/s]	C_5 [-]	E_0/k_B [K]	Reference
Heavy-impact dissociation				
$O_2 + X \rightleftharpoons 2O + X$ $X = O, N$	1.0×10^{15}	-1.5	59360	1
$O_2 + X \rightleftharpoons 2O + X$ $X = O_2, N_2, NO$	2.0×10^{15}	-1.5	59360	1
$N_2 + X \rightleftharpoons 2N + X$ $X = O, N$	3.0×10^{16}	-1.6	113200	1
$N_2 + X \rightleftharpoons 2N + X$ $X = O_2, N_2, NO$	7.0×10^{15}	-1.6	113200	1
$NO + X \rightleftharpoons N + O + X$ $X = O, N$	1.1×10^{11}	0.0	75500	1
$NO + X \rightleftharpoons N + O + X$ $X = O_2, N_2, NO$	5.0×10^{9}	0.0	75500	1
Exchange				
$NO + O \rightleftharpoons N + O_2$	8.4×10^{6}	0.0	19400	2
$N_2 + O \rightleftharpoons NO + N$	5.7×10^{6}	0.42	42938	2
Associative ionisation				
$N + O \rightleftharpoons NO^+ + e^-$	5.3×10^{6}	0.0	31900	2
$O + O \rightleftharpoons O_2^+ + e^-$	7.1×10^{-4}	2.7	80600	1
$N + N \rightleftharpoons N_2^+ + e^-$	44.0	1.5	67500	1
Charge exchange				
$NO^+ + O \rightleftharpoons N^+ + O_2$	1.0×10^{6}	0.5	77200	1
$N^+ + N_2 \rightleftharpoons N_2^+ + N$	1.0×10^{6}	0.5	12200	1
$O_2^+ + N \rightleftharpoons N^+ + O_2$	8.7×10^{7}	0.14	28600	1
$O^+ + NO \rightleftharpoons N^+ + O_2$	1.4×10^{-1}	1.9	26600	1
$O_2^+ + N_2 \rightleftharpoons N_2^+ + O_2$	9.9×10^{6}	0.0	40700	1
$O_2^+ + O \rightleftharpoons O^+ + O_2$	4.0×10^{6}	0.09	18000	1
$NO^+ + N \rightleftharpoons O^+ + N_2$	3.4×10^{7}	-1.08	12800	1
$NO^+ + O_2 \rightleftharpoons O_2^+ + NO$	2.4×10^{7}	0.41	32600	1
$NO^+ + O \rightleftharpoons O_2^+ + N$	7.2×10^{7}	0.29	48600	1
$O^+ + N_2 \rightleftharpoons N_2^+ + O$	9.1×10^{7}	0.36	22800	1
$NO^+ + N \rightleftharpoons N_2^+ + O$	7.2×10^{7}	0.0	35500	1
Electron-impact dissociation				
$N_2 + e^- \rightleftharpoons 2N + e^-$	3.0×10^{18}	-1.6	113200	2
Electron-impact ionisation				
$O + e^- \rightleftharpoons O^+ + 2e^-$	3.9×10^{27}	-3.78	158500	2
$N + e^- \rightleftharpoons N^+ + 2e^-$	2.5×10^{28}	-3.82	168200	2

APPENDIX C

Diffusion coefficients and interatomic potentials in MUTATION++

The diffusion velocities are solution of the Stefan-Maxwell system that requires the evaluation of the binary diffusion coefficients $\mathcal{D}_{ij}$. Details on this system and on its efficient solution can be found in the work of Magin and Degrez [2004]. Between species i and j, a coefficient reads as

$$\mathcal{D}_{ij} = \frac{3}{16n} \frac{k_\mathrm{B} T}{\mu_{ij}^\mathrm{R} \Omega_{ij}^{(1,1)}}, \tag{C.1}$$

where $\mu_{ij}^\mathrm{R} = \frac{\mu_i \mu_j}{\mu_i + \mu_j}$ is the reduced mass and $\Omega_{ij}^{(1,1)}$ the collision integral, defined as

$$\Omega_{ij}^{(1,1)} = \sqrt{\frac{2\pi k_\mathrm{B} T}{\mu_{ij}^\mathrm{R}}} \int_0^{+\infty} \int_0^{+\infty} e^{-\gamma_{ij}^2} \gamma_{ij}^5 (1 - \cos\chi)\ b db\ d\gamma. \tag{C.2}$$

Here, variable b is the impact parameter characterising the binary collision and $\gamma_{ij}^2 = \frac{\mu_{ij}^\mathrm{R} g_{ij}^2}{2 k_\mathrm{B} T}$ a reduced variable for the relative velocity g_{ij}. The scattering angle, $\chi = \chi(b, g, \psi)$, resulting from the dynamic of the binary collision, directly depends on the relevant interatomic potential, ψ.

For neutral-neutral collisions, we employ the Lennard-Jones (12-6) potential

$$\psi_{ij}(r) = 4\epsilon_{ij} \left[\left(\frac{\bar{\sigma}_{ij}}{r} \right)^{12} - \left(\frac{\bar{\sigma}_{ij}}{r} \right)^{6} \right], \tag{C.3}$$

where quantity ϵ_{ij} is the depth of the potential well, $\bar{\sigma}_{ij}$ is the finite distance at which the potential is zero, and r is the distance between the particles. Charged-charged interactions are treated according to the screened Coulomb (Debye-Hückel) potential

$$\psi_{ij}(r) = \frac{z_i z_j}{r} \frac{q_\mathrm{e}^2}{4\pi\epsilon_0} \exp\left\{ -\frac{r}{\lambda_\mathrm{D}} \right\}, \tag{C.4}$$

where z the elementary charge and λ_D the *Debye length* that reads as

$$\lambda_\mathrm{D} = \sqrt{\frac{\epsilon_0 k_\mathrm{B} T}{n_\mathrm{e} q_\mathrm{e}^2}}. \tag{C.5}$$

Finally, for neutral-ion interactions, where i is the neutral and j the charged species, we use the Langevin polarisation potential

$$\psi_{ij}(r) = -\frac{z_j^2 q_\mathrm{e}^2 \alpha_i}{8\pi\epsilon_0 r^4}, \tag{C.6}$$

where α_i is the dipole polarisability of the neutral species.

APPENDIX D

Verification test cases for SPH

Combined Couette-Poiseuille liquid flow

The liquid at rest is located between two infinite plates positioned at $z = 0$ m and $z = D = 10^{-3}$ m, and it is set in motion by the upper plate, which starts moving with a constant velocity $V_{\mathrm{u}} = 1.25 \times 10^{-5}$ m/s at time $t = 0$ s. A pressure gradient ($\Delta p = 10$ Pa) is applied in the same direction. In SPH, a uniform pressure gradient can be modelled as a mean acceleration field in the direction of the flow applied on each particle in Equation 6.31

$$a_i = \frac{\Delta p \Delta x_i \Delta z_i}{m_i}, \tag{D.1}$$

where $\Delta x = \Delta z = 5 \times 10^{-6}$ m. The timestep is set to $\Delta t = 10^{-6}$ s.

Analytical transient solutions for the Couette flow

$$v_{\mathrm{l}} = \frac{V_{\mathrm{u}}}{D} z + \sum_{n=1}^{\infty} \frac{2V_{\mathrm{u}}}{n\pi} (-1)^n \sin\left(\frac{n\pi}{D} z\right) \exp\left(-\nu_{\mathrm{l}} \frac{n^2\pi^2}{D^2} t\right) \tag{D.2}$$

and the Poiseuille flow

$$v_{\mathrm{l}} = \frac{a}{2\nu_{\mathrm{l}}} z(z-D) + \sum_{n=0}^{\infty} \frac{4aD^2}{\nu_{\mathrm{l}}\pi^3(2n+1)^3} \sin\left(\frac{\pi z}{D}(2n+1)\right) \exp\left(-\nu_{\mathrm{l}} \frac{(2n+1)^2\pi^2}{D^2} t\right) \tag{D.3}$$

are obtained by separation of variables, and the solutions can be combined by superposition of the effects. Quantity $\nu_{\mathrm{l}} = \eta_{\mathrm{l}}/\rho_{\mathrm{l}}$ is the kinematic viscosity of the liquid and a the acceleration due to the pressure gradient. In Figure D.1 (a), we report the comparison between the analytical and numerical solutions at different instants, which show an excellent agreement.

Heat conduction in a liquid slab as a result of a step variation in the wall temperature

The same set-up of the previous test case is now used to verify the ability of the code to correctly solve the implemented energy balance of Equation 6.32. A liquid at rest and uniform temperature $T_0 = 300$ K is located between two plates when, at time $t = 0$ s, the temperature of the upper plate is suddenly

changed to $T_\mathrm{u} = 400$ K. We use the same Δt and Δx as in the previous test case. The analytical solution reads as

$$T_\mathrm{l} = T_0 + \frac{T_\mathrm{u} - T_0}{D} z + \sum_{n=1}^{\infty} 2 \frac{T_\mathrm{u} - T_0}{n\pi} (-1)^n \sin\left(\frac{n\pi}{D} z\right) \exp\left(-\frac{k_\mathrm{l}}{\rho_\mathrm{l} c_\mathrm{p,l}} \frac{n^2\pi^2}{D^2} t\right). \tag{D.4}$$

The results are in excellent agreement with the exact solution, and the comparison is shown in Figure D.1 (b).

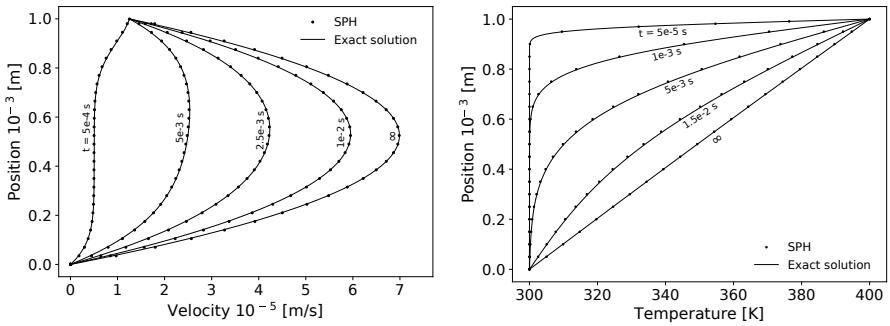

(a) **(b)**

Figure D.1.: *Comparison of analytical and numerical solutions for (a) a combined Couette-Poiseuille liquid flow; (b) the heat conduction in a liquid slab as a result of a step variation in the upper wall temperature.*

Heat conduction and melting in a two-dimensional solid slab

We consider the thermal evolution in a two-dimensional slab ($D_x = 10^{-3}$ m by $D_z = 2 \times 10^{-4}$ m, with $h = 1.2\sqrt{\Delta x^2 + \Delta z^2}$), where different combinations of boundary conditions are enforced. In the first configuration, Dirichlet boundary conditions are applied at the four boundaries; in the second, Dirichlet boundary conditions are enforced at three sides, while a Neumann conditions is applied at the upper one. In SPH, this type of condition can be implemented as a source term in Equation 6.32

$$l_i = \frac{q_\mathrm{cg}\ \Delta x_i}{m_i c_{\mathrm{p,l}_i}}\ \delta_{\mathrm{cg}_i}, \tag{D.5}$$

which is applied only to those particles belonging to the interface. Quantity $q_\mathrm{cg} = 45$ MW/m^2 represents the heat flux at the interface. The timestep and space discretisation are respectively equal to 5×10^{-8} s and 10^{-7} m.

The two configurations are shown in Figures D.2 (a) and D.2 (b) along with the comparison, at steady state, of the SPH solution with the numerical solutions obtained by means of time-explicit Finite Differences (FD) technique.

Temperature isolines are plotted and show a very good agreement between the two different techniques.

Also, we examine the second configuration for a test case in which the slab is allowed to melt (Figure D.2 (c)). The evolution of the melting front is plotted in Figure D.2 (c), from the initial condition until the steady state and shows a very good agreement with FD.

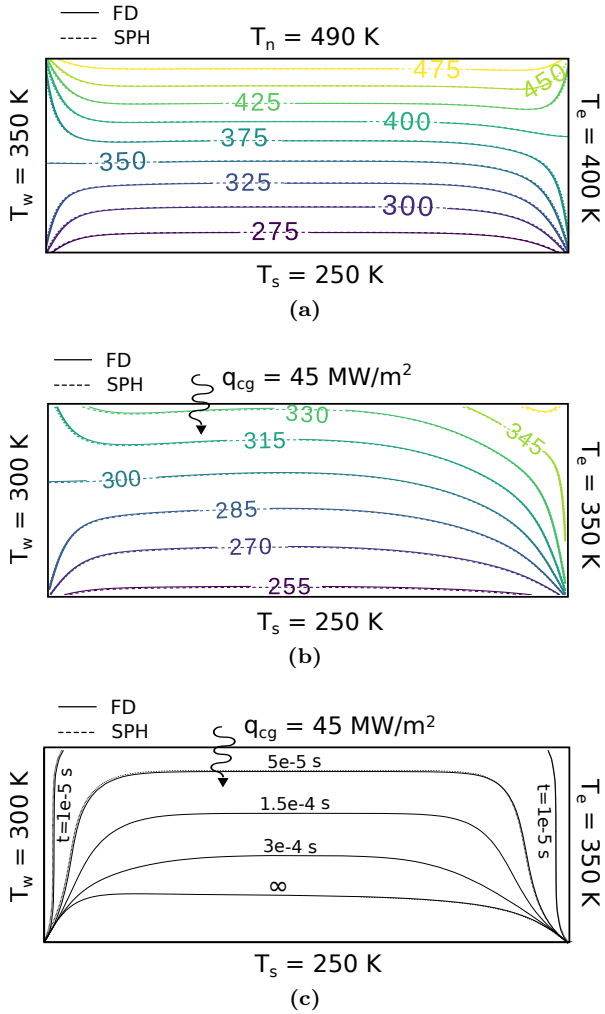

Figure D.2.: *Two-dimensional heat conduction problem with (a) Dirichlet boundary conditions enforced at all the four boundaries. Temperature isolines are plotted for the steady state; (b) Dirichlet boundary conditions enforced at three boundaries and a Neumann condition applied at the upper interface. Temperature isolines are plotted for the steady state; (c) Dirichlet boundary conditions enforced at three boundaries, and a Neumann condition applied at the upper interface. The evolution in time of the melting front is plotted.*

Evaporation in free molecular regime of a two-dimensional slab in the presence of a temperature gradient

We present an exploratory test case that has been performed to verify the SPH particle removal procedure implemented in order to simulate the mass transfer between the condensed and the gas phase. We examine a two-dimensional solid slab evaporating into vacuum, and we pose our attention on the evolution of the evaporation front. Here, the slab evaporates in free molecular regime, meaning no condensation flux is taken into account (Equation 3.7). Dirichlet boundary conditions are enforced everywhere, also at the upper moving boundary, where a linear temperature profile is imposed to link temperature values on the side walls (respectively T_w and T_e).

In order to evaluate the quality of the results, we compare SPH with FD. For the purpose of verification, an identical mass removal technique was implemented in the two codes. To set a reference solution, a much finer space and time discretisation was employed for FD. The evolution of the liquid-vacuum interface is plotted over time until the total evaporation of the system in Figure D.3 and the comparison of the two numerical techniques is found to be satisfactory.

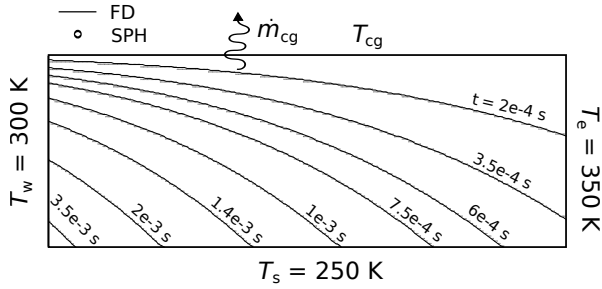

Figure D.3.: *Two-dimensional heat conduction problem with Dirichlet boundary conditions enforced at all the four boundaries. The evolution in time of the evaporating front is plotted.*

Table D.1.: *Physical parameters employed for the test cases presented.*

Figure	ρ_c [kg/m^3]	ν_l [m^2/s]	λ_c [W/m/K]	$c_\mathrm{p,l}$ [J/kg/K]	$c_\mathrm{p,s}$	T_m [K]	L_m [J/kg]
D.1 (a)	1000	2×10^{-5}	-	-	-	-	-
D.1 (b)	1000	-	40	4186	-	-	-
D.2 (a, b)	500	-	100		-	2220	-
D.2 (c)	500	-	100	4186	2220	273	3.3×10^4
D.3	500	-	100	4186	2220	-	-

APPENDIX E

Semi-analytical solution of a supersonic Couette gas flow over a melting slab

For a compressible Couette flow, an analytical solution can be found in the continuum regime [Liepmann and Roshko, 1957]. Here, we look for the hydrodynamic solution at steady state in the slip regime [Kogan, 1969], where rarefaction effects of the gas are confined at the gas-liquid boundaries, and a close solution to the problem can be found.

Gas layer

In the gas layer, the momentum equation in the direction of the flow x leads to a constant shear stress τ_{g} along z_{g}. Therefore, we can write

$$\tau_{\mathrm{g}} = \tau_{\mathrm{cg}}, \tag{E.1}$$

where τ_{cg} is the value of the shear stress at the gas-condensed phase interface. For a Newtonian fluid, we can relate the shear stress to the velocity gradient as follows

$$\eta_{\mathrm{g}} \frac{dv_{\mathrm{g}}}{dz_{\mathrm{g}}} = \tau_{\mathrm{cg}}, \tag{E.2}$$

where we have used Equation E.1. The velocity profile in the gas layer $v_{\mathrm{g}}(z_{\mathrm{g}})$ can be obtained by integrating Equation E.2 as follows

$$v_{\mathrm{g}} - v_{\mathrm{g}}(0) = \tau_{\mathrm{cg}} \int_0^{z_{\mathrm{g}}} \frac{dy}{\eta_{\mathrm{g}}}. \tag{E.3}$$

Note that velocity $v_{\mathrm{g}}(0)$ is different from V_{u} and has to be determined by applying proper slip boundary conditions. Moreover, the viscosity coefficient $\eta_{\mathrm{g}}(T_{\mathrm{g}})$ introduces a dependence on the temperature, which reads as

$$\eta_{\mathrm{g}} = \eta_{\mathrm{ref}} \left(\frac{T_{\mathrm{g}}}{T_{\mathrm{ref}}} \right)^{\omega}, \tag{E.4}$$

where, for a VHS gas,

$$\eta_{\mathrm{ref}} = \frac{15\ \sqrt{\pi\mu\ k_{\mathrm{B}}T_{\mathrm{ref}}}}{2\ (5-2\omega)(7-2\omega)\ \pi d_{\mathrm{ref}}^2}. \tag{E.5}$$

The energy balance in the gas phase

$$\frac{d}{dz_{\mathrm{g}}}(-q_{\mathrm{g}} + \tau_{\mathrm{g}} v_{\mathrm{g}}) = 0 \tag{E.6}$$

provides a second equation, which is necessary to obtain the temperature profile in the gas. For the heat flux, we employ Fourier law

$$q_{\mathrm{g}} = -\lambda_{\mathrm{g}} \frac{dT_{\mathrm{g}}}{dz_{\mathrm{g}}}, \tag{E.7}$$

where, from the Chapman-Enskog theory [Bird et al., 1960], we know that for a monatomic gas the following relationship between thermal conductivity and viscosity holds

$$\lambda_{\mathrm{g}} = \frac{15}{4} R\ \eta_{\mathrm{g}}. \tag{E.8}$$

Equation E.6 gives

$$\eta_{\mathrm{g}} \frac{d}{dz_{\mathrm{g}}}\left(\frac{c_{\mathrm{p,g}}}{\mathrm{Pr}} T_{\mathrm{g}} + \frac{v_{\mathrm{g}}^2}{2}\right) = -q_{\mathrm{cg}} + \tau_{\mathrm{cg}} v_{\mathrm{cg}}, \tag{E.9}$$

in which we have used the definition of Prandtl number

$$\mathrm{Pr} = \frac{\eta_{\mathrm{g}}\ c_{\mathrm{p,g}}}{\lambda_{\mathrm{g}}}, \tag{E.10}$$

that is constant and equal to 2/3 for a monatomic hard sphere gas.

Equation E.9 can be integrated with the help of Equation E.2 to obtain the temperature field $T_{\mathrm{g}}(z_{\mathrm{g}})$. The result reads as follows

$$c_{\mathrm{p,g}}\ [T_{\mathrm{g}} - T_{\mathrm{g}}(0)] + \frac{\mathrm{Pr}}{2}\ [v_{\mathrm{g}}^2 - v_{\mathrm{g}}^2(0)] = \mathrm{Pr}\left[-\frac{q_{\mathrm{cg}}}{\tau_{\mathrm{cg}}} + v_{\mathrm{g}}(D_{\mathrm{g}})\right][v_{\mathrm{g}} - v_{\mathrm{g}}(0)], \tag{E.11}$$

where the temperature at the upper boundary $T_{\mathrm{g}}(0)$ does not correspond to T_{u}, and its value must be determined using a suitable temperature jump condition. The same considerations apply to $v_{\mathrm{g}}(0)$ and $v_{\mathrm{g}}(D_{\mathrm{g}})$. If Equation E.11 is evaluated at $z_{\mathrm{g}} = D_{\mathrm{g}}$, we obtain the following expression

$$\boxed{\frac{q_{\mathrm{cg}}}{\tau_{\mathrm{cg}}} + \frac{c_{\mathrm{p,g}}}{\mathrm{Pr}} \frac{T_{\mathrm{g}}(0) - T_{\mathrm{g}}(D_{\mathrm{g}})}{v_{\mathrm{g}}(0) - v_{\mathrm{g}}(D_{\mathrm{g}})} + \frac{v_{\mathrm{g}}(0) - v_{\mathrm{g}}(D_{\mathrm{g}})}{2} = 0.} \tag{E.12}$$

Now, we can rework Equation E.11 as follows

$$\frac{T_{\mathrm{g}}}{T_{\mathrm{ref}}} = \frac{T_{\mathrm{g}}(0)}{T_{\mathrm{ref}}} - \mathrm{Pr}\left[-\frac{q_{\mathrm{cg}}}{\tau_{\mathrm{cg}}} + v_{\mathrm{g}}(D_{\mathrm{g}})\right]\frac{(\gamma-1)\ \mathrm{Ma}^2}{v_{\mathrm{g}}(0)}\left[1-\frac{v_{\mathrm{g}}}{v_{\mathrm{g}}(0)}\right] + \mathrm{Pr}\,\frac{(\gamma-1)\ \mathrm{Ma}^2}{2}\left[1-\frac{v_{\mathrm{g}}^2}{v_{\mathrm{g}}^2(0)}\right] \tag{E.13}$$

to express temperature as function of the velocity field, so that we can plug it into Equation E.4 and, in turn, Equation E.2. Here, the Mach number has been defined as

$$\mathrm{Ma} = \frac{v_{\mathrm{g}}(0)}{\sqrt{\gamma R T_{\mathrm{ref}}}}, \tag{E.14}$$

where $\gamma = c_{\mathrm{p,g}}/c_{\mathrm{v,g}} = 5/3$ is is the heat capacity ratio for a monatomic gas. From here on, we constrain our treatment to the case for which $\omega = 1$. This is not strictly necessary if not to simplify the computation of the following integral

$$\int_{v_{\mathrm{g}}(D_{\mathrm{g}})}^{v_{\mathrm{g}}(0)} \left(\frac{T_{\mathrm{g}}}{T_{\mathrm{ref}}}\right)^{\omega} dv_{\mathrm{g}} = \frac{\tau_{\mathrm{cg}} D_{\mathrm{g}}}{\eta_{\mathrm{ref}}}, \tag{E.15}$$

which otherwise would require numerical evaluation. Equation E.15 gives

$$\begin{aligned}\left\{\frac{T_{\mathrm{g}}(0)}{T_{\mathrm{ref}}} - \frac{\mathrm{Pr}}{v_{\mathrm{g}}(0)}\left[-\frac{q_{\mathrm{cg}}}{\tau_{\mathrm{cg}}} + v_{\mathrm{g}}(D_{\mathrm{g}})\right](\gamma-1)\ \mathrm{Ma}^2 + \mathrm{Pr}\,\frac{\gamma-1}{2}\,\mathrm{Ma}^2\right\} &\times [v_{\mathrm{g}}(0) - v_{\mathrm{g}}(D_{\mathrm{g}})] \\ + \left\{\frac{\mathrm{Pr}}{2v_{\mathrm{g}}^2(0)}\left[-\frac{q_{\mathrm{cg}}}{\tau_{\mathrm{cg}}} + v_{\mathrm{g}}(D_{\mathrm{g}})\right](\gamma-1)\ \mathrm{Ma}^2\right\}&[v_{\mathrm{g}}^2(0) - v_{\mathrm{g}}^2(D_{\mathrm{g}})] \\ - \left\{\frac{\mathrm{Pr}}{6v_{\mathrm{g}}^2(0)}(\gamma-1)\ \mathrm{Ma}^2\right\}&[v_{\mathrm{g}}^3(0) - v_{\mathrm{g}}^3(D_{\mathrm{g}})] \ = \ \frac{\tau_{\mathrm{cg}} D_{\mathrm{g}}}{\eta_{\mathrm{ref}}}.\end{aligned} \tag{E.16}$$

Equations E.12 and E.16 are a generalisation of the solution provided in Liepmann and Roshko [1957], when $v_{\mathrm{g}}(D_{\mathrm{g}})$ is different from zero. In the continuum limit, where no-slip boundary conditions apply, we have obtained a set of two equations in two unknowns, τ_{cg} and q_{cg}.

Finally, the momentum equation in z_{g} leads to constant pressure p_{g} across the channel. Thus, we can write the following relation for the number density of the gas $n_{\mathrm{g}}(z_{\mathrm{g}})$

$$\boxed{n_{\mathrm{g}}(0)\ T_{\mathrm{g}}(0) = n_{\mathrm{g}}(D_{\mathrm{g}})\ T_{\mathrm{g}}(D_{\mathrm{g}}),} \tag{E.17}$$

where we have used the law of perfect gases. Also, we can add

$$\boxed{n_{\mathrm{g}}(0) = \frac{p_{\mathrm{g}}}{k_{\mathrm{B}}\ T_{\mathrm{g}}(0)},} \tag{E.18}$$

where p_g is known. When comparing with a DSMC computation, the gas pressure can be constrained by the total number of particles N_0 present in the domain, which is constant throughout the simulation, since periodic boundary conditions are enforced along the sides. We write

$$N_0 = L_x \int_0^{D_g} n_g \, dz_g = \frac{p_g L_x}{k_B} \int_0^{D_g} \frac{dz_g}{T_g}, \tag{E.19}$$

where L_x is the length of the channel, and the integral can be evaluated by integrating the temperature field T_g given by Equation E.11.

Slip boundary conditions for the gas layer

Now, we account for rarefaction effects of the gas phase at the boundaries, writing down proper jump conditions for velocity and temperature fields [Sharipov, 2004]. If momentum and energy are fully accommodated at the boundary, the first-order slip condition for the velocity reads as follows

$$\Delta v_g = \frac{\sqrt{\pi}}{2} \frac{\eta_g}{n_g k_B T_g} \sqrt{2RT_w} \frac{dv_g}{dz}, \tag{E.20}$$

and for the temperature it is written in this way

$$\Delta T_g = \frac{\sqrt{\pi}\,\gamma}{(\gamma+1)\,\mathrm{Pr}} \frac{\eta_g}{n_g k_B T_g} \sqrt{2RT_w} \frac{dT_g}{dz}, \tag{E.21}$$

where T_w stands for the temperature of the wall. Therefore, for the upper wall, we can write

$$v_g(0) = V_u \pm \Delta v_g(0) \tag{E.22}$$

$$T_g(0) = T_u \pm \Delta T_g(0) \tag{E.23}$$

and, for the gas-liquid interface, we can write

$$v_g(D_g) = V_i \pm \Delta v_g(D_g) \tag{E.24}$$

$$T_g(D_g) = T_i \pm \Delta T_g(D_g), \tag{E.25}$$

where subscript "i" identifies the properties of the liquid at the interface. The gradient at the interface is evaluated with respect to a local reference system, where z exits the surface.

If we substitute Equations E.2 and E.4 in Equation E.20 and Equations E.7 and E.10 in Equation E.21, we end up with the following expressions

$$\boxed{v_g(0) = V_u \pm \frac{\tau_{cg}}{n_g(0)\; T_g(0)} \sqrt{\frac{\pi T_u}{2\mu k_B}}} \tag{E.26}$$

$$\boxed{T_{\mathrm{g}}(0) = T_{\mathrm{u}} \mp \frac{\gamma}{c_{\mathrm{p,g}}\ (\gamma+1)}\ \frac{q_{\mathrm{u}}}{n_{\mathrm{g}}(0)\ T_{\mathrm{g}}(0)}\ \sqrt{\frac{2\pi T_{\mathrm{u}}}{\mu k_{\mathrm{B}}}}} \tag{E.27}$$

$$\boxed{v_{\mathrm{g}}(D_{\mathrm{g}}) = V_{\mathrm{i}} \pm \frac{\tau_{\mathrm{cg}}}{n_{\mathrm{g}}(D_{\mathrm{g}})\ T_{\mathrm{g}}(D_{\mathrm{g}})}\ \sqrt{\frac{\pi T_{\mathrm{i}}}{2\mu k_{\mathrm{B}}}}} \tag{E.28}$$

$$\boxed{T_{\mathrm{g}}(D_{\mathrm{g}}) = T_{\mathrm{i}} \mp \frac{\gamma}{c_{\mathrm{p,g}}\ (\gamma+1)}\ \frac{q_{\mathrm{cg}}}{n_{\mathrm{g}}(D_{\mathrm{g}})\ T_{\mathrm{g}}(D_{\mathrm{g}})}\ \sqrt{\frac{2\pi T_{\mathrm{i}}}{\mu k_{\mathrm{B}}}},} \tag{E.29}$$

so that we attain four conditions, which link gas velocity and temperature fields at the boundaries, with those of the solid or liquid phase. These constraints can be used in Equation E.12 and Equations E.16-E.18. Finally, an expression for the heat flux at the upper boundary q_{u} can be obtained deriving Equation E.13 as follows

$$\boxed{q_{\mathrm{u}} = q_{\mathrm{cg}} + v_{\mathrm{g}}(0)\tau_{\mathrm{cg}} - v_{\mathrm{g}}(D_{\mathrm{g}})\tau_{\mathrm{cg}}.} \tag{E.30}$$

Liquid layer

For the incompressible liquid layer, we assume constant transport properties and decoupled momentum and energy equations. The integration of Navier-Stokes equations become trivial and leads to linear velocity $v_{\mathrm{l}}(z_{\mathrm{l}})$ and temperature $T_{\mathrm{l}}(z_{\mathrm{l}})$ profiles, respectively

$$v_{\mathrm{l}} = \mathcal{A}_{\mathrm{l}} z_{\mathrm{l}} \tag{E.31}$$

and

$$T_{\mathrm{l}} = T_{\mathrm{m}} + \mathcal{B}_{\mathrm{l}} z_{\mathrm{l}}, \tag{E.32}$$

At the solid-liquid interface, i.e. the melting front, $T_{\mathrm{l}}(0) = T_{\mathrm{m}}$ holds, and a no-slip boundary condition is used for the velocity. Quantities $\mathcal{A}_{\mathrm{l}}$ and $\mathcal{B}_{\mathrm{l}}$ are the integration constants.

When evaluated at the interface, Equations E.31 and E.32 provide two new conditions that can be plugged into Equations E.28 and E.29

$$\boxed{v_{\mathrm{l}}(D_{\mathrm{l}}) = \mathcal{A}_{\mathrm{l}} D_{\mathrm{l}} = V_{\mathrm{i}}} \tag{E.33}$$

and

$$\boxed{T_{\mathrm{l}}(D_{\mathrm{l}}) = T_{\mathrm{m}} + \mathcal{B}_{\mathrm{l}} D_{\mathrm{l}} = T_{\mathrm{i}}.} \tag{E.34}$$

Moreover, we can impose the continuity of the shear stress and heat flux at the interface between gas and liquid, as follows

$$\boxed{\tau_{\mathrm{l}} = \eta_{\mathrm{l}} \mathcal{A}_{\mathrm{l}} = \tau_{\mathrm{cg}}} \tag{E.35}$$

and

$$\boxed{q_\mathrm{l} = -\lambda_\mathrm{l}\mathcal{B}_\mathrm{l} = q_\mathrm{cg},} \tag{E.36}$$

which must be satisfied by Equations E.12 and E.16.

Solid layer

The solid phase is characterised by constant thermal conductivity. Similarly to the liquid phase, one obtains a linear temperature profile $T_\mathrm{s}(z_\mathrm{s})$, which reads as

$$T_\mathrm{s} = T_0 + \mathcal{B}_\mathrm{s} z_\mathrm{s}. \tag{E.37}$$

By imposing the continuity of the heat flux at the solid-liquid interface

$$\boxed{q_\mathrm{s} = -\lambda_\mathrm{s}\mathcal{B}_\mathrm{s} = -\lambda_\mathrm{l}\mathcal{B}_\mathrm{l} = q_\mathrm{l},} \tag{E.38}$$

we obtain an extra condition that, combined with the following one

$$\boxed{T_\mathrm{s}(D_\mathrm{s}) = T_0 + \mathcal{B}_\mathrm{s}(D_\mathrm{c} - D_\mathrm{l}) = T_\mathrm{m}} \tag{E.39}$$

closes the algebraic system with as many equations as unknowns.

Solution of the algebraic system

We have obtained a non-linear algebraic system of 15 equations in 15 unknowns. This system can be effectively solved with an iterative procedure of the following type:

1. Set $\Delta v_\mathrm{g}(0) = 0$, $\Delta T_\mathrm{g}(0) = 0$, $\Delta v_\mathrm{g}(D_\mathrm{g}) = 0$, and $\Delta T_\mathrm{g}(D_\mathrm{g}) = 0$;
2. Solve the non-linear system numerically;
3. Compute $\Delta v_\mathrm{g}(0)$, $\Delta T_\mathrm{g}(0)$, $\Delta v_\mathrm{g}(D_\mathrm{g})$, and $\Delta T_\mathrm{g}(D_\mathrm{g})$ using Equations E.26-E.29;
4. Go to Step 2 if the solution has not converged yet.

Bibliography

P. Agrawal, P. M. Jenniskens, E. Stern, J. Arnold, and Y.-K. Chen. Arcjet ablation of stony and iron meteorites. *AIAA Conference Proceedings*, AIAA 2018-4284, 2018. doi: 10.2514/6.2018-4284. 62, 63

C. M. O'D. Alexander. Exploration of quantitative kinetic models for the evaporation of silicate melts in vacuum and in hydrogen. *Meteoritics & Planetary Science*, 36(2):255–283, 2001. doi: 10.1111/j.1945-5100.2001.tb01870.x. 31

H. J. Allen and Jr. Baldwin, B. S. Frothing as an explanation of the acceleration anomalies of cometary meteors. *Journal of Geophysical Research*, 72(13): 3483, 1967. doi: 10.1029/JZ072i013p03483. 61, 71

J. D. Anderson. *Hypersonic and High Temperature Gas Dynamics*. AIAA, 2000. 4, 69, 100

P. André, J. Aubreton, S. Clain, M. Dudeck, E. Duffour, M. F. Elchinger, B. Izrar, D. Rochette, R. Touzani, and D. Vacher. Transport coefficients in thermal plasma. applications to mars and titan atmospheres. *European Physical Journal D*, 57(2):227–234, Apr 2010. doi: 10.1140/epjd/e2010-00036-5. 33, 103

W. J. Baggaley. The de-ionization of dense meteor trains. *Planetary and Space Science*, 26(10):979–981, October 1978. doi: 10.1016/0032-0633(78)90080-6. 10, 104

W. J. Baggaley. Meteors and atmospheres. *Symposium - International Astronomical Union*, 90:85–100, 1980. doi: 10.1017/S0074180900066535. 3

W. J. Baggaley. Radar observations. *In: Meteors in the Earth's Atmosphere*, edited by E. Murad and I. P. Williams, 2002. 3, 9, 10

W. J. Baggaley and C. H. Cummack. Meteor train ion chemistry. *Journal of Atmospheric and Terrestrial Physics*, 36(11):1759–1773, 1974. doi: 10.1016/0021-9169(74)90161-5. 10, 96, 104, 105

W. J. Baggaley and T. H. Webb. The thermalization of meteoric ionization. *Journal of Atmospheric and Terrestrial Physics*, 39(11):1399–1403, 1977. doi: 10.1016/0021-9169(77)90094-0. 11, 97, 100

W. J. Baggaley, R. G. T. Bennett, S. H. Marsh, G. E. Plank, and D. P. Galligan. Update on new developments of the advanced meteor orbit radar AMOR. *COSPAR Colloquia Series: Dust in the Solar System and other Planetary Systems*, 15:38–41, 2002. doi: 10.1016/S0964-2749(02)80321-3. 118

P. Barbante and O. Chazot. Flight extrapolation of plasma wind tunnel stagnation region flowfield. *Journal of Thermophysics and Heat Transfer*, 20(3): 493–499, 2006. doi: 10.2514/1.17185. 68

P. Barbante, G. Degrez, and G. S. R. Sarma. Computation of nonequilibrium high temperature axisymmetric boundary-layer flows. *Journal of Thermophysics and Heat Transfer*, 16(4):490–497, 2002. doi: 10.2514/2.6723. 68

D. A. Barcarolo, D. Le Touzé, G. Oger, and F. de Vuyst. Adaptive particle refinement and derefinement applied to the Smoothed Particle Hydrodynamics method. *Journal of Computational Physics*, 273:640–657, 2014. doi: 10.1016/j.jcp.2014.05.040. 153

F. Bariselli, S. Boccelli, A. Frezzotti, A. Hubin, and T. E. Magin. Aerothermodynamic modelling of meteor entry flows in the rarefied regime. *AIAA Conference Proceedings*, AIAA 2018-4180, 2018. doi: 10.2514/6.2018-4180. 94, 100

F. Bariselli, A. Frezzotti, A. Hubin, and T. E. Magin. Aerothermodynamic modelling of meteor entry flows. *Monthly Notices of the Royal Astronomical Society*, 492:2308–2325, 2019. doi: 10.1093/mnras/stz3559. 95

A. A. Berezhnoy and J. Borovička. Formation of molecules in bright meteors. *Icarus*, 210(1):150–157, 2010. doi: 10.1016/j.icarus.2010.06.036. 34

H. A. Bethe. A theory for the ablation of glassy materials. *Journal of the Aerospace Sciences*, 26(6):321–328, 1959. doi: 10.2514/8.8080. 137

G. A. Bird. Approach to translational equilibrium in a rigid sphere gas. *The Physics of Fluids*, 6(10):1518–1519, 1963. doi: 10.1063/1.1710976. 36

G. A. Bird. *Molecular Gas Dynamics and the Direct Simulation of Gas Flows*. Oxford University Press, 1994. 4, 9, 22, 36, 40, 97, 124

R. B. Bird, W. E. Stewart, and E. N. Lightfoot. *Transport Phenomena*. John Wiley & Sons, 1960. 32, 170

M. B. Blanchard and G. G. Cunningham. Artificial meteor ablation studies: Olivine. *Journal of Geophysical Research*, 79(26):3973–3980, 1974. doi: 10.1029/JB079i026p03973. 61

S. Boccelli, F. Bariselli, B. Dias, and T. E. Magin. Lagrangian diffusive reactor for detailed thermochemical computations of plasma flows. *Plasma Sources Science and Technology*, 28(6):065002, may 2019. doi: 10.1088/1361-6595/ab09b5. 94, 98, 102

C. A. Boitnott and H. F. Savage. Light Emission Measurements of Calcium and Magnesium at Simulated Meteor Conditions. II. Spectral Luminous Efficiencies. *The Astrophysical Journal*, 167:349, August 1971. doi: 10.1086/151037. 36

C. Bonacina, G. Comini, A. Fasano, and M. Primicerio. Numerical solution of phase-change problems. *International Journal of Heat and Mass Transfer*, 16(10):1825–1832, 1973. doi: 10.1016/0017-9310(73)90202-0. 15, 17

D. L. Bones, J. C. Gómez Martín, C. J. Empson, J. D. Carrillo Sánchez, A. D. James, T. P. Conroy, and J. M. C. Plane. A novel instrument to measure differential ablation of meteorite samples and proxies: The Meteoric Ablation Simulator (MASI). *Review of Scientific Instruments*, 87(9):094504, 2016. doi: 10.1063/1.4962751. 62

C. Borgnakke and P. S. Larsen. Statistical collision model for monte carlo simulation of polyatomic gas mixture. *Journal of Computational Physics*, 18 (4):405–420, 1975. doi: 10.1016/0021-9991(75)90094-7. 43

J. Borovička and P. Spurný. Radiation study of two very bright terrestrial bolides and an application to the comet S-L 9 collision with Jupiter. *Icarus*, 121(2):484–510, 1996. doi: https://doi.org/10.1006/icar.1996.0104. 70

J. Borovička, P. Spurný, P. Brown, P. Wiegert, P. Kalenda, D. Clark, and L. Shrbený. The trajectory, structure and origin of the Chelyabinsk asteroidal impactor. *Nature*, 503:235–237, 11 2013. doi: 10.1038/nature12671. 70

B. Bottin, O. Chazot, M. Carbonaro, V. van der Haegen, and S. Paris. The VKI Plasmatron characteristics and performance. Technical report, RTO-EN-008, 1999. 59, 63

I. D. Boyd. Monte Carlo simulation of nonequilibrium flow in a low-power hydrogen arcjet. *Physics of Fluids*, 9:3086–3095, October 1997. doi: 10.1063/1.869474. 44

I. D. Boyd. Computation of atmospheric entry flow about a Leonid meteoroid. *Earth, Moon, and Planets*, 82(0):93–108, Jan 1998. doi: 10.1023/A:1017042404484. 4, 9, 11, 47, 95, 100

J. U. Brackbill, D. B. Kothe, and C. Zemach. A continuum method for modeling surface tension. *Journal of Computational Physics*, 100(2):335–354, 1992. doi: 0.1016/0021-9991(92)90240-Y. 129

D. E. Briggs. *Thermal Conductivity of Potassium Vapor*. University of Michigan, PhD thesis, 1968. 33

V. A. Bronshten. *Physics of Meteoric Phenomena*. D. Reidel Publishing Co., 1983. 5, 6, 23, 35, 51, 61, 93

R. Brun. *Introduction to Reactive Gas Dynamics*. Oxford University Press, 2009. 4

D. Bruno, C. Catalfamo, M. Capitelli, G. Colonna, O. De Pascale, P. Diomede, C. Gorse, A. Laricchiuta, S. Longo, D. Giordano, and F. Pirani. Transport properties of high-temperature Jupiter atmosphere components. *Physics of Plasmas*, 17(11):112315, 2010. doi: 10.1063/1.3495980. 101

A. M. Bukhteev and Y. F. Bydin. Loss of electrons by fast Ca, Mg, Si and Fe atoms in encounters with N_2 and O_2. *Bulletin of the Academy of Science of the USSR, Physical Series*, 27(8):985, 1963. 36

Y. F. Bydin and A. M. Bukhteev. Ionization of fast Na, K, Rb, and Cs atoms in collisions with H_2, D_2, N_2, and O_2 molecules. *Soviet Physics-Technical Physics*, 5:512–519, 1960. 35, 36, 37

M. D. Campbell-Brown and D. Koschny. Model of the ablation of faint meteors. *Astronomy & Astrophysics*, 418(2):751–758, 2004. doi: 10.1051/0004-6361:20041001-1. 7, 19

M. D. Campbell-Brown, J. Borovička, P. G. Brown, and E. Stokan. High-resolution modelling of meteoroid ablation. *Astronomy & Astrophysics*, 557: A41, 2013. doi: 10.1051/0004-6361/201322005. 74

D. Capek and J. Borovička. Ablation of small iron meteoroids-First results. *Planetary and Space Science*, 143:159 – 163, 2017. doi: 10.1016/j.pss.2017.03.004. 76

M. Capitelli, C. Gorse, S. Longo, and D. Giordano. Collision integrals of high-temperature air species. *Journal of Thermophysics and Heat Transfer*, 14 (2):259–268, 2000. doi: 10.2514/2.6517. 101, 103

A. B. Carlson and H. A. Hassan. Direct simulation of re-entry flows with ionization. *Journal of Thermophysics and Heat Transfer*, 6(3):400–404, 1992. doi: 10.2514/3.374. 44

H. S. Carslaw and J. C. Jaeger. *Conduction of Heat in Solids*. Oxford at the Clarendon Press, 1959. 158, 159

Z. Ceplecha, J. Borovička, W. G. Elford, D. O. ReVelle, R. L. Hawkes, V. Porubčan, and M. Šimek. Meteor phenomena and bodies. *Space Science Reviews*, 84(3):327–471, 1998. doi: 10.1023/A:1005069928850. 3, 4, 5, 7, 15, 16, 93

C. Cercignani. *Mathematical Methods in Kinetic Theory*. Plenum Press, New York, 1969. 28

M. A. Cervera and I. M. Reid. Comparison of atmospheric parameters derived from meteor observations with CIRA. *Radio Science*, 35(3):833–843, 2000. doi: 10.1029/1999RS002226. 2, 118

G. J. Consolmagno, M. W. Schaefer, B. E. Schaefer, D. T. Britt, R. J. Macke, M. C. Nolan, and E. S. Howell. The measurement of meteorite heat capacity at low temperatures using liquid nitrogen vaporization. *Planetary and Space Science*, 87:146–156, 2013. doi: 10.1016/j.pss.2013.07.009. 67

J. F. Cuderman. Ionization of K Atoms in Collision with H_2, N_2, O_2, and CO. *Physical Review A*, 5:1687–1694, Apr 1972. doi: 10.1103/PhysRevA.5.1687. 35, 36, 37

G. Degrez, D. P. Vanden Abeele, P. F. Barbante, and B. Bottin. Numerical simulation of inductively coupled plasma flows under chemical non-equilibrium. *International Journal of Numerical Methods for Heat and Fluid Flow*, 14(4): 538–558, 2004. doi: 10.1108/09615530410532286. 68

B. Dias, F. Bariselli, A. Turchi, A. Frezzotti, P. Chatelain, and T. E. Magin. Development of a melting model for meteors. *AIP Conference Proceedings*, 1786(1):160004, 2016. doi: 10.1063/1.4967661. 17

B. Dias, J. B. Scoggins, and T. E. Magin. Shock layer radiation of an evaporating meteor. *European Planetary Science Congress*, 12:495, September 2018. 153

B. Dias, J. B. Scoggins, and T. E. Magin. Luminosity calculation of meteor entry based on detailed flow simulations in the continuum regime. *Astronomy & Astrophysics*, 635:A184, 2020. doi: 10.1051/0004-6361/202037498. 153

Y. S. Dimant and M. M. Oppenheim. Meteor trail diffusion and fields: 1. Simulations. *Journal of Geophysical Research: Space Physics*, 111(A12312), 2006. doi: 10.1029/2006JA011797. 11, 96

Y. S. Dimant and M. M. Oppenheim. Formation of plasma around a small meteoroid: 1. Kinetic theory. *Journal of Geophysical Research: Space Physics*, 122(4):4669–4696, 2017a. doi: 10.1002/2017JA023960. 10, 24, 44

Y. S. Dimant and M. M. Oppenheim. Formation of plasma around a small meteoroid: 2. Implications for radar head echo. *Journal of Geophysical Research: Space Physics*, 122(4):4697–4711, 2017b. doi: 10.1002/2017JA023963. 10

M. Doring. *Développement d'une méthode SPH pour les applications à surface libre en hydrodynamique*. Université de Nantes, PhD thesis, 2005. 131

H. W. Drawin and F. Emard. Atom-atom excitation and ionization in shock waves of the noble gases. *Physics Letters A*, 43(4):333–335, 1973. doi: 10.1016/0375-9601(73)90331-9. 36

R. A. Dressler and E. Murad. The gas-phase chemical dynamics associated with meteors. *The gas-phase chemical dynamics associated with meteors in Chemical Dynamics in Extreme Environments*, edited by R. A. Dressler, 2001. 2, 34, 35, 101, 102

L. Eppelbaum, I. Kutasov, and A. Pilchin. *Applied Geothermics*. Springer Berlin Heidelberg, 2014. 66

A. Faghri and Y. Zhang. *Transport Phenomena in Multiphase Systems*. Elsevier, 2006. 123

E. D. Farbar and I. D. Boyd. Modeling of the plasma generated in a rarefied hypersonic shock layer. *Physics of Fluids*, 22(10):106101, 2010. doi: 10.1063/1.3500680. 153

J. A. Fay and F. R. Riddell. Theory of stagnation point heat transfer in dissociated air. *Journal of the Aeronautical Sciences*, 25:73–85, 1958. doi: 10.2514/8.7517. 74

A. V. Fedkin, L. Grossman, and M. S. Ghiorso. Vapor pressures and evaporation coefficients for melts of ferromagnesian chondrule-like compositions. *Geochimica et Cosmochimica Acta*, 70(1):206–223, 2006. doi: 10.1016/j.gca.2005.08.014. 31

B. Fegley and A. G. W. Cameron. A Vaporization Model for Iron/Silicate Fractionation in the Mercury Protoplanet. *Earth and Planetary Science Letters*, 82(3):207–222, 1987. doi: 10.1016/0012-821X(87)90196-8. 7, 31, 45

W. Feng, D. R. Marsh, M. P. Chipperfield, D. Janches, J. Höffner, F. Yi, and J. M. C. Plane. A global atmospheric model of meteoric iron. *Journal of Geophysical Research: Atmospheres*, 118(16):9456–9474, 2013. doi: 10.1002/jgrd.50708. 106

M. Ferus, J. Koukal, L. Lenža, J. Srba, P. Kubelík, V. Laitl, E. M. Zanozina, P. Vána, T. Kaiserová, A. Knížek, P. Rimmer, E. Chatzitheodoridis, and S. Civiš. Calibration-free quantitative elemental analysis of meteor plasma using reference laser-induced breakdown spectroscopy of meteorite samples. *Astronomy & Astrophysics*, 610:A73, 2018. doi: 10.1051/0004-6361/201629950. 62

J. H. Ferziger and H. G. Kaper. *Mathematical Theory of Transport Processes in Gases*. Elsevier Science Publishing, 1972. 28, 97

G. J. Flynn. Extraterrestrial dust in the near-Earth environment. *Meteors in the Earth's Atmosphere*, edited by E. Murad and I. P. Williams, Cambridge University Press, 2002. 4

P. A. Forsyth and E. L. Vogan. Forward-scattering of radio waves by meteor trails. *Canadian Journal of Physics*, 33(5):176–188, 1955. doi: 10.1139/p55-023. 2

L. Foschini. On the interaction of radio waves with meteoric plasma. *Astronomy & Astrophysics*, 341:634–639, 1999. 114

A. Frezzotti. Boundary conditions at the vapor-liquid interface. *Physics of Fluids*, 23(3):030609, 2011. doi: 10.1063/1.3567001. 29

J. F. Friichtenicht, J. C. Slattery, and D. O. Hansen. Ionization from fe atoms incident on various gas targets. *Phys. Rev.*, 163:75–80, Nov 1967. doi: 10.1103/PhysRev.163.75. 35

D. P. Galligan, G. E. Thomas, and W. J. Baggaley. On the relationship between meteor height and ambipolar diffusion. *Journal of Atmospheric and Solar-Terrestrial Physics*, 66(11):899–906, 2004. doi: 10.1016/j.jastp.2004.03.002. 118, 119

M. A. Gallis, J. R. Torczynski, S. J. Plimpton, D. J. Rader, and T. Koehler. Direct Simulation Monte Carlo: The Quest for Speed. *AIP Conference Proceedings*, 1628(1):27–36, 2014. doi: 10.1063/1.4902571. 44

A. L. Garcia, J. B. Bell, W. Y. Crutchfield, and B. J. Alder. Adaptive mesh and algorithm refinement using Direct Simulation Monte Carlo. *Journal of Computational Physics*, 154(1):134–155, 1999. doi: 10.1006/jcph.1999.6305. 153

M. J. Genge. Igneous rims on micrometeorites. *Geochimica et Cosmochimica Acta*, 70(10):2603–2621, 2006. doi: 10.1016/j.gca.2006.02.005. 6

M. J. Genge. The origins of I-type spherules and the atmospheric entry of iron micrometeoroids. *Meteoritics & Planetary Science*, 51(6):1063–1081, 2016. doi: 10.1111/maps.12645. 75, 76

M. J. Genge. Vesicle dynamics during the atmospheric entry heating of cosmic spherules. *Meteoritics & Planetary Science*, 52(3):443–457, 2017. doi: 10.1111/maps.12805. 6

M. J. Genge and M. M. Grady. The fusion crusts of stony meteorites: Implications for the atmospheric reprocessing of extraterrestrial materials. *Meteoritics and Planetary Science*, 34(3):341–356, 1999. doi: 10.1111/j.1945-5100.1999.tb01344.x. 6, 88

M. J. Genge, C. Engrand, M. Gounelle, and S. Taylor. The classification of micrometeorites. *Meteoritics & Planetary Science*, 43(3):497–515, 2008. doi: 10.1111/j.1945-5100.2008.tb00668.x. 6

M. J. Genge, B. Davies, M. D. Suttle, M. van Ginneken, and A. G. Tomkins. The mineralogy and petrology of I-type cosmic spherules: Implications for their sources, origins and identification in sedimentary rocks. *Geochimica et Cosmochimica Acta*, 218:167–200, 2017. doi: 10.1016/j.gca.2017.09.004. 86

M. H. Ghatee and F. Niroomand-Hosseini. Hard-wall potential function for transport properties of alkali metal vapors. *Journal of Chemical Physics*, 126(1):014302, 2007. doi: 10.1063/1.2403879. 32, 33

R. A. Gingold and J. J. Monaghan. Smoothed Particle Hydrodynamics - Theory and application to non-spherical stars. *Monthly Notices of the Royal Astronomical Society*, 181:375–389, 1977. doi: 10.1093/mnras/181.3.375. 121, 126

V. Giovangigli. *Multicomponent Flow Modeling. Modeling and Simulation in Science, Engineering and Technology.* Birkähuser Boston Inc., Boston, MA, 1999. 28, 97, 98, 100, 101

O. G. Girin. A hydrodynamic mechanism of meteor ablation - the melt-spraying model. *Astronomy & Astrophysics*, 606:A63, 2017. doi: 10.1051/0004-6361/201629560. 1, 21

M. Gomez-Gesteira, A. J. C. Crespo, B. D. Rogers, R. A. Dalrymple, J. M. Dominguez, and A. Barreiro. SPHysics - Development of a free-surface fluid solver - Part 2: Efficiency and test cases. *Computers & Geosciences*, 48: 300–307, 2012a. doi: 10.1016/j.cageo.2012.02.028. 134

M. Gomez-Gesteira, B. D. Rogers, A. J. C. Crespo, R. A. Dalrymple, M. Narayanaswamy, and J. M. Dominguez. SPHysics - Development of a free-surface fluid solver - Part 1: Theory and formulations. *Computers & Geosciences*, 48:289–299, 2012b. doi: 10.1016/j.cageo.2012.02.029. 134

J. C. Gómez Martín, D. L. Bones, A. D. Carrillo Sánchez, J. D.and James, J. M. Trigo-Rodríguez, Jr. Fegley, B., and J. M. C. Plane. Novel experimental simulations of the atmospheric injection of meteoric metals. *The Astrophysical Journal*, 836(2):212, 2017. doi: 10.3847/1538-4357/aa5c8f. 62

J. S. Greenhow and J. E. Hall. The importance of initial trail radius on the apparent height and number distributions of meteor echoes. *Monthly Notices of the Royal Astronomical Society*, 121(2):183–196, 1960. doi: 10.1093/mnras/121.2.183. 10

J. S. Greenhow and J. E. Hall. The height variation of the ambipolar diffusion coefficient for meteor trails. *Planetary and Space Science*, 5(2):109–114, 1961. doi: 10.1016/0032-0633(61)90085-X. 118, 119

G. R. Guedon. *Two-phase heat and mass transfer modeling: flexible numerical methods for energy engineering analyses*. Politecnico di Milano, PhD thesis, 2013. 125

N. G. Hadjiconstantinou, A. L. Garcia, M. Z. Bazant, and G. He. Statistical error in particle simulations of hydrodynamic phenomena. *Journal of Computational Physics*, 187(1):274–297, 2003. doi: 10.1016/S0021-9991(03)00099-8. 102

A. Hajduk, J. Stohl, and G. Cevolani. Multiple reflections from meteor trails and small-scale wind structure. *Il Nuovo Cimento*, 12:315–334, 05 1989. doi: 10.1007/BF02507203. 96

H. T. Hashemi and C. M. Sliepcevich. A numerical method for solving two-dimensional problems of heat conduction with change of phase. *Chemical engineering progress Symposium Series*, 63:34–41, 1967. 130

A. Hashimoto. Evaporation metamorphism in the early solar nebula-evaporation experiments on the melt FeO-MgO-SiO_2-CaO-Al_2O_3 and chemical fractionations of primitive materials. *Geochemical Journal*, 17(3):111–145, 1983. doi: 10.2343/geochemj.17.111. 31

A. Hashimoto. Evaporation kinetics of forsterite and implications for the early solar nebula. *Nature*, 347:53–55, 09 1990. doi: 10.1038/347053a0. 31

B. Helber, C. O. Asma, Y. Babou, A. Hubin, O. Chazot, and T. E. Magin. Material response characterization of a low-density carbon composite ablator in high-enthalpy plasma flows. *Journal of Material Science*, 49(13):4530–4543, 2014. doi: 10.1007/s10853-014-8153-z. 64

B. Helber, O. Chazot, A. Hubin, and T. E. Magin. Microstructure and gas-surface interaction studies of a low-density carbon-bonded carbon fiber composite in atmospheric entry plasmas. *Composites: Part A*, 72:96–107, 2015. doi: 10.1016/j.compositesa.2015.02.004. 68

B. Helber, O. Chazot, A. Hubin, and T. E. Magin. Emission spectroscopic boundary layer investigation during ablative material testing in Plasmatron. *Journal of Visualized Experiments*, 112(e53742), 2016. doi: 10.3791/53742. 64

B. Helber, B. Dias, F. Bariselli, L. F. Zavalan, L. Pittarello, S. Goderis, B. Soens, S. J. McKibbin, Claeys P., and T. E. Magin. Analysis of meteoroid ablation based on plasma wind-tunnel experiments, surface characterization, and numerical simulations. *The Astrophysical Journal*, 876(2):120, 2019. doi: 10.3847/1538-4357/ab16f0. 61, 63, 64

N. Herlofson. The theory of meteor ionization. *Reports on Progress in Physics*, 11:444–454, 1947. 118

W. K. Hocking, T. Thayaparan, and J. Jones. Meteor decay times and their use in determining a diagnostic mesospheric temperature-pressure parameter: Methodology and one year of data. *Geophysical Research Letters*, 24(23):2977–2980, 1997. doi: 10.1029/97GL03048. 2

W. K. Hocking, B. Fuller, and B. Vandepeer. Real-time determination of meteor-related parameters utilizing modern digital technology. *Journal of Atmospheric and Solar-Terrestrial Physics*, 63(2):155–169, 2001. doi: 10.1016/S1364-6826(00)00138-3. 2

R. J. Howarth. Understanding the nature of meteorites: the experimental work of Gabriel-Auguste Daubrée. *Geological Society, London, Special Publications*, 256(1):101–122, 2006. doi: 10.1144/GSL.SP.2006.256.01.05. 60

R. J. Hull and M. L. Lander. Laser Hardened Materials Evaluation Laboratory (LHMEL). *Journal of Laser Applications*, 8(3):161–168, 1996. doi: 10.2351/1.4745418. 59

M. S. Ivanov, G. N. Markelov, S. F. Gimelshein, L. V. Mishina, A. N. Krylov, and N. V. Grechko. High-altitude capsule aerodynamics with real gas effects. *Journal of Spacecraft and Rockets*, 35(1):16–22, 1998. doi: 10.2514/3.26992. 36

L. G. Jacchia and F. L. Whipple. Precision orbits of 413 photographic meteors. *Smithsonian Contributions to Astrophysics*, 4:97–129, 1961. 69, 70

D. Janches, L. P. Dyrud, S. L. Broadley, and J. M. C. Plane. First observation of micrometeoroid differential ablation in the atmosphere. *Geophysical Research Letters*, 36(6), 2009. doi: 10.1029/2009GL037389. 20, 119

E. Jarosewich. Chemical analyses of meteorites: A compilation of stony and iron meteorite analyses. *Meteoritics*, 25(4):323–337, 1990. doi: 10.1111/j.1945-5100.1990.tb00717.x. 67

J. Jones, P. Brown, K. J. Ellis, A. R. Webster, M. Campbell-Brown, Z. Krzemenski, and R. J. Weryk. The Canadian Meteor Orbit Radar: system overview and preliminary results. *Planetary and Space Science*, 53(4):413–421, 2005. doi: 10.1016/j.pss.2004.11.002. 152

W. Jones. Theory of diffusion of meteor trains in the geomagnetic field. *Planetary and Space Science*, 39(9):1283–1288, 1991. doi: 10.1016/0032-0633(91)90042-9. 9, 96

W. Jones. Theory of the initial radius of meteor trains. *Monthly Notices of the Royal Astronomical Society*, 275(3):812–818, 1995. doi: 10.1093/mnras/275.3.812. 10, 50

W. Jones. Theoretical and observational determinations of the ionization coefficient of meteors. *Monthly Notices of the Royal Astronomical Society*, 288(4):995–1003, 1997. doi: 10.1093/mnras/288.4.995. 7, 8, 42, 43, 52

W. Jones and J. Jones. Ionic diffusion in meteor trains. *Journal of Atmospheric and Terrestrial Physics*, 52(3):185–191, 1990. doi: 10.1016/0021-9169(90)90122-4. 11, 117, 118, 119

E. Josyula and J. Burt. Review of Rarefied Gas Effects in Hypersonic Applications. Technical report, RTO-EN-AVT-194, 2011. 28

T. R. Kaiser. Radio echo studies of meteor ionization. *Advances in Physics*, 2(8):495–544, 1953. doi: 10.1080/00018735300101282. 1, 9, 117

P. Karrang, T. Lips, and T. Soares. Demisability of critical spacecraft components during atmospheric re-entry. *Journal of Space Safety Engineering*, 6(3):181–187, 2019. doi: 10.1016/j.jsse.2019.08.003. 154

J. Kero, C. Szasz, A. Pellinen-Wannberg, G. Wannberg, A. Westman, and D. D. Meisel. Three-dimensional radar observation of a submillimeter meteoroid fragmentation. *Geophysical Research Letters*, 35(4):L04101, 2008. doi: 10.1029/2007GL032733. 6

M. N. Kogan. *Rarefied Gas Dynamics*. Springer, 1969. 22, 139, 169

H. Kojitani and M. Akaogi. Measurement of heat of fusion of model basalt in the system Diopside-forsterite-anorthite. *Geophysical Research Letters*, 22(17):2329–2332, 1995. doi: 10.1029/95GL02064. 66

A. F. Kolesnikov. Conditions of simulation of stagnation point heat transfer from a high-enthalpy flow. *Fluid Dynamics*, 28(1):131–137, 1993. doi: 10.1007/BF01055676. 67

G. Koppenwallner and T. Lips. Influence of rarefied gas flow on re-entry survivability of space debris. *American Institute of Physics Conference Series*, 1084:740–747, 2008. doi: 10.1063/1.3076574. 154

J. A. Kunc and W. H. Soon. Analytical Ionization Cross Sections for Atomic Collisions. *Journal of Chemical Physics*, 95(8):5738–5751, 1991. doi: 10.1063/1.461622. 36

B. Lafuente, R. T Downs, H. Yang, and N. Stone. The power of databases: the RRUFF project. *In: Highlights in Mineralogical Crystallography*, edited by T. Armbruster and R. M. Danisi, 2015. 81

H. Lamy, S. Ranvier, J. Keyser, E. Gamby, and S. Calders. BRAMS: The Belgian RAdio Meteor Stations. *Meteoroids Conference Proceedings*, NASA/CP-2011-216469:351–356, 2011. doi: 10.1109/URSIGASS.2011.6050925. 2, 115, 152

G. J. LeBeau. A Parallel Implementation of the Direct Simulation Monte Carlo Method. *Computer Methods in Applied Mechanics and Engineering*, 174(3-4):319–337, 1999. doi: 10.1016/S0045-7825(98)00302-8. 36

D. I. Lee and C. F. Bonilla. The viscosity of the alkali metal vapors. *Nuclear Engineering and Design*, 7(5):455–469, 1968. doi: 10.1016/0029-5493(68)90083-6. 33

M. A. Lennon, K. L. Bell, H. B. Gilbody, J. G. Hughes, A. E. Kingston, M. J. Murray, and F. J. Smith. Recommended data on the electron impact ionization of atoms and ions: Fluorine to nickel. *Journal of Physical and Chemical Reference Data*, 17(3):1285–1363, 1988. doi: 10.1063/1.555809. 36, 37

E. Levin and M. J. Wright. Collision integrals for ion-neutral interactions of nitrogen and oxygen. *Journal of Thermophysics and Heat Transfer*, 18(1):143–147, 2004. doi: 10.2514/1.2552. 101, 104, 118

J. Liang, Z. Li, X. Li, and W. Shi. Monte Carlo simulation of spacecraft reentry aerothermodynamics and analysis for ablating disintegration. *Communications in Computational Physics*, 23(4):1037–1051, 2018. doi: 10.4208/cicp.OA-2016-0213. 154

H. W. Liepmann and A. Roshko. *Elements of Gasdynamics*. John Wiley & Sons, 1957. 169, 171

T. Lips and B. Fritsche. A comparison of commonly used re-entry analysis tools. *Acta Astronautica*, 57(2):312–323, 2005. doi: 10.1016/j.actaastro.2005.03.010. 154

G. R Liu and M. B. Liu. *Smoothed Particle Hydrodynamics: A meshfree particle method*. World Scientific Publishing, 2003. 128, 129

K. Lodders. Solar system abundances and condensation temperatures of the elements. *The Astrophysical Journal*, 591(2):1220, 2003. doi: 10.1086/375492. 71

S. Loehle, P. Jenniskens, H. Böhrk, T. Bauer, H. Elsäßer, D. W. Sears, M. E. Zolensky, and M. H. Shaddad. Thermophysical properties of Almahata Sitta meteorites (asteroid 2008 TC3) for high-fidelity entry modeling. *Meteoritics & Planetary Science*, 52(2):197–205, 2017a. doi: 10.1111/maps.12788. 19

S. Loehle, F. Zander, T. Hermann, M. Eberhart, A. Meindl, R. Oefele, J. Vaubaillon, F. Colas, P. Vernazza, A. Drouard, and J. Gattacceca. Experimental simulation of meteorite ablation during Earth entry using a plasma wind tunnel. *The Astrophysical Journal*, 837(2):112, 2017b. doi: 10.3847/1538-4357/aa5cb5. 61, 63, 65

A. J. Lofthouse. *Nonequilibrium Hypersonic Aerothermodynamics using the Direct Simulation Monte Carlo and Navier-Stokes Models*. University of Michigan, PhD thesis, 2008. 138, 139

S. G. Love and D. E. Brownlee. Heating and thermal transformation of micrometeoroids entering the Earth's atmosphere. *Icarus*, 89(1):26–43, 1991. doi: 10.1016/0019-1035(91)90085-8. 7

S. G. Love and D. E. Brownlee. A direct measurement of the terrestrial mass accretion rate of cosmic dust. *Science*, 262(5133):550–553, 1993. doi: 10.1126/science.262.5133.550. 1

T. E. Magin and G. Degrez. Transport algorithms for partially ionized and unmagnetized plasmas. *Journal of Computational Physics*, 198(2):424–449, 2004. doi: 10.1016/j.jcp.2004.01.012. 68, 103, 163

L. A. Manning. The initial radius of meteoric ionization trails. *Journal of Geophysical Research*, 63(1):181–196, 1958. doi: 10.1029/JZ063i001p00181. 7, 10, 50

S. Marrone, A. Colagrossi, D. Le Touzé, and G. Graziani. Fast free-surface detection and level-set function definition in SPH solvers. *Journal of Computational Physics*, 229(10):3652–3663, 2010. doi: 10.1016/j.jcp.2010.01.019. 121, 126

R. A. Marshall and S. Close. An FDTD model of scattering from meteor head plasma. *Journal of Geophysical Research: Space Physics*, 120(7):5931–5942, 2015. doi: 10.1002/2015JA021238. 153

E. A. Mason and E. W. McDaniel. *Transport Properties of Ions in Gases*. John Wiley & Sons, 1988. 117

H. S. W. Massey, E. H. S. Burhop, and H. B. Gilbody. *Electronic and Ionic Impact Phenomena: Vol. III.* Clarendon Press, Oxford, 1971. 117, 118

B. C. McGee, M. L. Hobbs, and M. R. Baer. Exponential 6 Parameterization for the JCZ3-EOS. Technical report, Sandia National Labs., Albuquerque, NM, SAND98-1191, 1998. 34, 103

B. A. McIntosh. The effect of wind shear on the decay constant of meteor echoes. *Canadian Journal of Physics*, 47(13):1337–1341, 1969. doi: 10.1139/p69-171. 96

D. W. R. McKinley. *Meteor Science and Engineering.* McGraw-Hill, 1961. 1, 2, 8, 94, 113

W. J. McNeil, S. T. Lai, and E. Murad. Differential ablation of cosmic dust and implications for the relative abundances of atmospheric metals. *Journal of Geophysical Research: Atmospheres*, 103(D9):10899–10911, 1998. doi: 10.1029/98JD00282. 7, 20, 119

G. Menees and C. Park. Nitric oxide formation by meteoroids in the upper atmosphere. *Atmospheric Environment*, 10:7:535–545, 1976. doi: 10.2514/6.1974-591. 41

E. P. Milley, R. L. Hawkes, and J. M. Ehrman. Meteor luminosity simulation through laser ablation of meteorites. *Monthly Notices of the Royal Astronomical Society: Letters*, 382(1):67–71, 2007. doi: 10.1111/j.1745-3933.2007.00390.x. 62

J. J. Monaghan. On the problem of penetration in particle methods. *Journal of Computational Physics*, 82(1):1–15, 1989. doi: https://doi.org/10.1016/0021-9991(89)90032-6. 130

J. J. Monaghan. Simulating free surface flows with SPH. *Journal of Computational Physics*, 110(2):399–406, 1994. doi: 10.1006/jcph.1994.1034. 121, 126, 129

J. J. Monaghan, R. A. F. Cas, A. M. Kos, and M. Hallworth. Gravity currents descending a ramp in a stratified tank. *Journal of Fluid Mechanics*, 379:39–69, 1999. doi: 10.1017/S0022112098003280. 130

J. J. Monaghan, H. E. Huppert, and M. G. Worster. Solidification using Smoothed Particle Hydrodynamics. *Journal of Computational Physics*, 206(2):684–705, 2005. doi: 10.1016/j.jcp.2004.11.039. 129

M. Moreno-Ibáñez, E. A. Silber, M. Gritsevich, and J. M. Trigo-Rodríguez. Verification of the flow regimes based on high-fidelity observations of bright meteors. *The Astrophysical Journal*, 863(2):174, 2018. doi: 10.3847/1538-4357/aad334. 23, 24

J. P. Morris. Simulating surface tension with Smoothed Particle Hydrodynamics. *International Journal for Numerical Methods in Fluids*, 33(3):333–353, 2000. doi: 10.1002/1097-0363(20000615)33:3<333::AID-FLD11>3.0.CO;2-7. 130

J. P. Morris, P. J. Fox, and Y. Zhu. Modeling low Reynolds number incompressible flows using SPH. *Journal of Computational Physics*, 136(1):214–226, 1997. doi: 10.1006/jcph.1997.5776. 129

S. Nugent and H. A. Posch. Liquid drops and surface tension with smoothed particle applied mechanics. *Physical Review E*, 62:4968–4975, 2000. doi: 10.1103/PhysRevE.62.4968. 126

Y. Ogasawara, S. H. Tabaian, and M. Maeda. Rates of Evaporation in a Vacuum in Liquid Ni-Ti Alloys. *ISIJ International*, 38:789–793, 01 1998. doi: 10.2355/isijinternational.38.789. 31

E. Öpik. Researches on the physical theory of meteor phenomena. III. Basis of the physical theory of meteor phenomena. *Publications of the Tartu Astrofizica Observatory*, 29:1–69, 1936. 6

E. Öpik. *Physics of Meteor Flight in the Atmosphere*. Interscience Publishers, London, 1958. 6

M. M. Oppenheim and Y. S. Dimant. First 3-D simulations of meteor plasma dynamics and turbulence. *Geophysical Research Letters*, 42(3):681–687, 2015. doi: 10.1002/2014GL062411. 11, 95, 96, 153

T. Ozawa, D. A. Levin, A. Wang, and M. Modest. Development of coupled particle hypersonic flowfield - Photon Monte Carlo radiation methods. *Journal of Thermophysics and Heat Transfer*, 24(3):612–622, 2010. doi: 10.2514/1.44645. 153

C. Park. Review of chemical-kinetic problems of future NASA missions. I - Earth entries. *Journal of Thermophysics and Heat Transfer*, 7(3):385–398, 1993. doi: 10.2514/3.431. 41, 104, 161, 162

C. Park and G. P. Menees. Odd nitrogen production by meteoroids. *Journal of Geophysical Research: Oceans*, 83(C8):4029–4035, 1978. doi: 10.1029/JC083iC08p04029. 41

C. Park, R. L. Jaffe, and H. Partridge. Chemical-kinetic parameters of hyperbolic Earth entry. *Journal of Thermophysics and Heat Transfer*, 15(1):76–90, 2001. doi: 10.2514/2.6582. 41, 104, 161, 162

J. M. Picone, A. E. Hedin, D. P. Drob, and A. C. Aikin. NRLMSISE-00 empirical model of the atmosphere: Statistical comparisons and scientific issues. *Journal of Geophysical Research: Space Physics*, 107(A12):SIA 15–1–SIA 15–16, 2002. doi: 10.1029/2002JA009430. 18, 45, 105

L. Pittarello, S. Goderis, B. Soens, S. J. McKibbin, G. Giuli, F. Bariselli, B. Dias, B. Helber, G. O. Lepore, F. Vanhaecke, C. Koeberl, T. E. Magin, and P. Claeys. Meteoroid atmospheric entry investigated with plasma flow experiments: Petrography and geochemistry of the recovered material. *Icarus*, 331:170–178, 2019. doi: 10.1016/j.icarus.2019.04.033. 65, 66, 67, 68, 71, 74, 86

J. M. C. Plane. The chemistry of meteoric metals in the Earth's upper atmosphere. *International Reviews in Physical Chemistry*, 10(1):55–106, 1991. doi: 10.1080/01442359109353254. 1

J. M. C. Plane. A time-resolved model of the mesospheric Na layer: constraints on the meteor input function. *Atmospheric Chemistry and Physics*, 4(3):627–638, 2004. doi: 10.5194/acp-4-627-2004. 106

J. M. C. Plane and C. L. Whalley. A new model for magnesium chemistry in the upper atmosphere. *Journal of Physical Chemistry A*, 116(24):6240–6252, 2012. doi: 10.1021/jp211526h. 106

J. M. C. Plane, W. Feng, and E. C. M. Dawkins. The Mesosphere and metals: Chemistry and changes. *Chemical Reviews*, 115(10):4497–4541, 2015. doi: 10.1021/cr500501m. 1, 35, 94, 101, 104, 153

O. P. Popova, S. N. Sidneva, V. V. Shuvalov, and A. S. Strelkov. Screening of meteoroids by ablation vapor in high-velocity meteors. *Earth, Moon, and Planets*, 82-83:109–128, 2000. doi: 10.1023/A:1017063007210. 23

O. P. Popova, A. S. Strelkov, and S. N. Sidneva. Sputtering of fast meteoroids' surface. *Advances in Space Research*, 39(4):567–573, 2007. doi: 10.1016/j.asr.2006.05.008. 6

J. D. Ramshaw and C. H. Chang. Ambipolar diffusion in two-temperature multicomponent plasmas. *Plasma Chemistry and Plasma Processing*, 13(3):489–498, 1993. doi: 10.1007/BF01465878. 117

P. W. Randles and L. D. Libersky. Smoothed Particle Hydrodynamics: Some recent improvements and applications. *Computer Methods in Applied Mechanics and Engineering*, 139(1):375–408, 1996. doi: 10.1016/S0045-7825(96)01090-0. 126, 132

R. Robson. Dispersion of meteor trails in the geomagnetic field. *Physical review E*, 63:026404, 03 2001. doi: 10.1103/PhysRevE.63.026404. 9, 96

L. A. Rogers, K. A. Hill, and R. L. Hawkes. Mass loss due to sputtering and thermal processes in meteoroid ablation. *Planetary and Space Science*, 53(13):1341–1354, 2005. doi: 10.1016/j.pss.2005.07.002. 9

L. Schaefer and B. Fegley. A thermodynamic model of high temperature lava vaporization on Io. *Icarus*, 169(1):216–241, 2004. doi: 10.1016/j.icarus.2003.08.023. 7, 31

H. Schlichting and K. Gersten. *Boundary-Layer Theory*. McGraw-Hill New York, 1955. 122

J. B. Scoggins and T. E. Magin. Development of Mutation++: Multicomponent Thermodynamic and Transport Properties for Ionized Plasmas written in C++. *11th AIAA/ASME Joint Thermophysics and Heat Transfer Conference*, AIAA 2014-2966, 2014. doi: 10.2514/6.2014-2966. 103

Y. Sha, H. Zhang, X. Guo, and M. Xia. Analyses of electromagnetic properties of a hypersonic object with plasma sheath. *IEEE Transactions on Antennas and Propagation*, 67(4):2470–2481, 2019. doi: 10.1109/TAP.2019.2891462. 153

M. S. Shadloo and M. Yildiz. Numerical modeling of Kelvin-Helmholtz instability using Smoothed Particle Hydrodynamics. *International Journal for Numerical Methods in Engineering*, 87(10):988–1006, 2011. doi: 10.1002/nme.3149. 126

F. Sharipov. Data on the velocity slip and temperature jump coefficients. *5th International Conference on Thermal and Mechanical Simulation and Experiments in Microelectronics and Microsystems*, pages 243–249, 2004. doi: 10.1109/ESIME.2004.1304046. 172

C. E. Shepard, H. A. Stine, J. W. Vorreiter, and W. Winovich. A study of artificial meteors as ablators. Technical report, NASA Ames Research Center, Moffett Field, CA, NASA-TN-D-3740, 1967. 61, 70

E. A. Silber, W. K. Hocking, M. L. Niculescu, M. Gritsevich, and R. E. Silber. On shock waves and the role of hyperthermal chemistry in the early diffusion of overdense meteor trains. *Monthly Notices of the Royal Astronomical Society*, 469(2):1869–1882, 2017. doi: 10.1093/mnras/stx923. 23

E. A. Silber, M. Boslough, W. K. Hocking, M. Gritsevich, and R. W. Whitaker. Physics of meteor generated shock waves in the Earth's atmosphere - A review. *Advances in Space Research*, 62(3):489–532, 2018a. doi: 10.1016/j.asr.2018.05.010. 23

E. A. Silber, M. L. Niculescu, P. Butka, and R. E. Silber. Nitric oxide production by centimeter-sized meteoroids and the role of linear and nonlinear processes in the shock bound flow fields. *Atmosphere*, 9(5), 2018b. doi: 10.3390/atmos9050202. 9, 23, 41

I. Sohn, Z. Li, D. A. Levin, and M. F. Modest. Coupled DSMC-PMC Radiation Simulations of a Hypersonic Reentry. *Journal of Thermophysics and Heat Transfer*, 26(1):22–35, 2012. doi: 10.2514/1.T3633. 153

D. I. Stefano, D. L. Timorot, and Y. Y. Totski. Viscosity and thermal conductivity of the vapors of sodium and potassium. *High Temperature Thermophysics*, 4:131, 1966. 33

H. C. Stenbaek-Nielsen and P. Jenniskens. A "shocking" Leonid meteor at 1000 fps. *Advances in Space Research*, 33(9):1459–1465, 2004. doi: 10.1016/j.asr.2003.06.003. 4, 5

E. Stokan and M. D. Campbell-Brown. Transverse motion of fragmenting faint meteors observed with the Canadian Automated Meteor Observatory. *Icarus*, 232:1–12, 2014a. doi: 10.1016/j.icarus.2014.01.002. 6

E. Stokan and M. D. Campbell-Brown. A particle-based model for ablation and wake formation in faint meteors. *Monthly Notices of the Royal Astronomical Society*, 447(2):1580–1597, 2014b. doi: 10.1093/mnras/stu2552. 10, 24

G. Sugar, M. M. Oppenheim, Y. S. Dimant, and S. Close. Formation of plasma around a small meteoroid: Simulation and theory. *Journal of Geophysical Research: Space Physics*, 123(5):4080–4093, 2018. doi: 10.1002/2018JA025265. 10, 95

R. A. Svehla. Estimated Viscosities and Thermal Conductivities of Gases at High Temperatures. Technical report, NASA Lewis Research Center, Cleveland, OH, NASA-TR-R-132, 1962. 34, 103

K. Swaminathan-Gopalan and K. A. Stephani. Calibration of DSMC parameters for transport processes in ionized air mixtures. *AIAA Conference Proceedings*, AIAA 2015-3373, 2015. doi: 10.2514/6.2015-3373. 40

R. N. Thomas and W. C. White. The physical theory of meteors. IV. Inquiry into the radiation problem-A laboratory model. *The Astrophysical Journal*, 118:555, 1953. doi: 10.1086/145783. 60

S. Tiwari, A. Klar, S. Hardt, and A. Donkov. Coupled solution of the Boltzmann and Navier-Stokes equations in gas-liquid two phase flow. *Computers & Fluids*, 71:283–296, 2013. doi: 10.1016/j.compfluid.2012.10.018. 122

J. M. Trigo-Rodríguez. The flux of meteoroids over time: meteor emission spectroscopy and the delivery of volatiles and chondritic materials to Earth. *Hypersonic Meteoroid Entry Physics*, edited by G. Colonna, M. Capitelli and A. Laricchiuta, 2019. 4

A. Turchi, S. Matesanz, J. Juan, T. E. Magin, and O. Chazot. On the flight extrapolation of stagnation-point ablative material plasma wind tunnel tests. *8th European Symposium on Aerothermodynamics for Space Vehicles*, 2015. 74

R. Vacondio, B. D. Rogers, P. K. Stansby, P. Mignosa, and J. Feldman. Variable resolution for SPH: A dynamic particle coalescing and splitting scheme. *Computer Methods in Applied Mechanics and Engineering*, 256:132–148, 2013. doi: 10.1016/j.cma.2012.12.014. 153

D. Vanden Abeele and G. Degrez. Efficient computational model for inductive plasmas flows. *AIAA Journal*, 38(2):234–242, 2000. doi: 10.2514/2.977. 68

N. B. Vargaftik, Y. K. Vinogradov, V. I. Dolgov, V. G. Dzis, I. F. Stepanenko, Y. K. Yakimovich, and V. S. Yargin. Viscosity and thermal conductivity of alkali metal vapors at temperatures up to 2000 K. *International Journal of Thermophysics*, 12(1):85–103, 1991. doi: 10.1007/BF00506124. 33

C. Vecchi, M. Sabbadini, R. Maggiora, and A. Siciliano. Modelling of antenna radiation pattern of a re-entry vehicle in presence of plasma. *IEEE Antennas and Propagation Society Symposium, 2004.*, 1:181–184, 2004. doi: 10.1109/APS.2004.1329583. 153

C. Verbeeck. The first Fresnel zone and the power profile throughout the forward scatter reflection surface. *14th International Meteor Conference, Brandenburg, Germany*, pages 83–98, 1995. 114, 115

P. Vernazza, B. Zanda, T. Nakamura, E. R. D. Scott, and S. Russell. The formation and evolution of ordinary chondrite parent bodies. *Asteroids IV*, edited by Michel, P. and DeMeo, F. E. and Bottke, W. F.:617–634, 2015. 66

F. Verniani and G. S. Hawkins. On the Ionizing Efficiency of Meteors. *The Astrophysical Journal*, 140:1590, November 1964. doi: 10.1086/148062. 35

D. Vinković. Thermalization of sputtered particles as the source of diffuse radiation from high altitude meteors. *Advances in Space Research*, 39(4):574–582, 2007. doi: 10.1016/j.asr.2005.08.035. 9

D. Vinković, M. Gritsevich, V. Srećković, B. Pečnik, G. Szabó, V. Debattista, P. Škoda, A. Mahabal, J. Peltoniemi, S. Mönkölä, A. Mickaelian, E. Turunen, J. Kákona, J. Koskinen, and V. Grokhovsky. Big data era in meteor science. *International Meteor Conference, Egmond, the Netherlands*, page 319, 2016. 9

T. Vondrak, J. M. C. Plane, S. Broadley, and D. Janches. A chemical model of meteoric ablation. *Atmospheric Chemistry and Physics*, 8(23):7015–7031, 2008. doi: 10.5194/acp-8-7015-2008. 1, 7, 18, 19, 74

Z. B. Wang, R. Chen, H. Wang, Q. Liao, X. Zhu, and S. Z. Li. An overview of Smoothed Particle Hydrodynamics for simulating multiphase flow. *Applied Mathematical Modelling*, 40(23):9625–9655, 2016. doi: 10.1016/j.apm.2016.06.030. 126

R. J. Weryk and P. G. Brown. Simultaneous radar and video meteors-II: Photometry and ionisation. *Planetary and Space Science*, 81:32–47, 2013. doi: 10.1016/j.pss.2013.03.012. 2

S. M. White and E. C. Stern. Laser ablation experiments on the Tamdakht H5 chondrite. *80th Annual Meeting of the Meteoritical Society*, 80:6130, 2017. 62, 77

Z. Wu, R. Hu, X. Qu, X. Wang, and Z. Wu. Space debris reentry analysis methods and tools. *Chinese Journal of Aeronautics*, 24(4):387–395, 2011. doi: 10.1016/S1000-9361(11)60046-0. 154

J. Ye, J. Yang, J. Zheng, X. Ding, I. Wong, W. Li, and C. Chen. A multi-scale flow analysis in hydrogen separation membranes using a coupled DSMC-SPH method. *International Journal of Hydrogen Energy*, 37(1):894–902, 2012. doi: 10.1016/j.ijhydene.2011.03.163. 122

T. Ye, D. Pan, C. Huang, and M. Liu. Smoothed Particle Hydrodynamics (SPH) for complex fluid flows: Recent developments in methodology and applications. *Physics of Fluids*, 31(1):011301, 2019. doi: 10.1063/1.5068697. 126

K. Yomogida and T. Matsui. Physical properties of ordinary chondrites. *Journal of Geophysical Research*, 88(B11):9513–9533, 1983. doi: 10.1029/JB088iB11p09513. 19, 67

C. Zhang and T. E. Schwartzentruber. Robust cut-cell algorithms for DSMC implementations employing multi-level Cartesian grids. *Computers & Fluids*, 69:122–135, 2012. doi: 10.1016/j.compfluid.2012.08.013. 153

Q. Zhu, L. Hernquist, and Y. Li. Numerical convergence in Smoothed Particle Hydrodynamics. *The Astrophysical Journal*, 800(1):6, 2015. doi: 10.1088/0004-637x/800/1/6. 127, 128

Q. Zhu, R. Dinsmore, B. Gao, and J. D. Mathews. High-resolution radar observations of meteoroid fragmentation and flaring at the Jicamarca Radio Observatory. *Monthly Notices of the Royal Astronomical Society*, 457(2):1759–1769, 2016. doi: 10.1093/mnras/stw070. 6

J. Zinn, O. P. Judd, and D. O. Revelle. Leonid meteor ablation, energy exchange, and trail morphology. *Advances in Space Research*, 33:1466–1474, 2004. doi: 10.1016/j.asr.2003.04.001. 11

I. A. Zotikov. Experimental investigation of the ablation of bodies by hypersonic flow. Technical report, NASA, N71-71474, 1962. 61